

**STUDYING DNA-DIRECTED NANOASSEMBLY, HYBRIDIZATION  
AND MISMATCH-DISCRIMINATION VIA PLASMON SCATTERING  
OF GOLD NANOPARTICLES**

**FONG KAH EE**

**NATIONAL UNIVERSITY OF SINGAPORE**

**2012**

**STUDYING DNA-DIRECTED NANOASSEMBLY, HYBRIDIZATION  
AND MISMATCH-DISCRIMINATION VIA PLASMON SCATTERING  
OF GOLD NANOPARTICLES**

**FONG KAH EE**

**(B. Eng. Hons., University of Science Malaysia)**

**A THESIS SUBMITTED FOR  
THE DEGREE OF DOCTOR OF PHILOSOPHY  
NATIONAL UNIVERSITY OF SINGAPORE**

**2012**

To Ben.J Lee Kuang Hawe

## ACKNOWLEDGEMENTS

I would like to express my deepest gratitude to everyone who contributes a lot in the completion of my PhD study.

My thanks to ....

..... my parents, Mr. Fong Poo Meng & Mdm. Mah Poh Yin, for their love and perseverance that has constantly motivated me.

..... my late fiancé, Ben.J Lee Kuang Hawe, for his encouragement and understanding that has always supported me.

..... National University of Singapore, for the Research Scholarship that was granted for me to pursue the PhD study.

..... my supervisor, A/P Lanry Yung Lin-Yue, for his valuable guidance, patience and positive approach that has made the completion of this study possible.

..... my godparents and friends, for their meticulous care and concern that has brightened me up during the lowest tide of my life.

..... the fellow post-docs and graduate students in A/P Lanry's lab, past and present, for their help and knowledge that was given to me generously.

..... the professional officers and lab technologists, for their experience and practical skills that has allowed me to handle various instrumentations properly.

..... last but not least, to the Buddha, for His Dhamma, delivered by the Sangha has lead me to the noble path

## TABLE OF CONTENTS

<b>ACKNOWLEDGEMENTS .....</b>	<b>i</b>
<b>TABLE OF CONTENTS .....</b>	<b>ii</b>
<b>DECLARATION.....</b>	<b>v</b>
<b>SUMMARY .....</b>	<b>vi</b>
<b>LIST OF ABBREVIATIONS .....</b>	<b>ix</b>
<b>LIST OF FIGURES .....</b>	<b>xi</b>
<b>LIST OF TABLES .....</b>	<b>xvii</b>
<b>CHAPTER 1: PROLOGUE.....</b>	<b>1</b>
1.1 Background .....	1
1.2 Objectives.....	3
<b>Chapter 2: LITERATURE REVIEW .....</b>	<b>6</b>
2.1 Optical properties of noble metal nanoparticles.....	6
2.1.1 Localized surface plasmon resonance (LSPR) .....	6
2.1.1.1 Chemical compositions.....	8
2.1.1.2 Size.....	10
2.1.1.3 Shape.....	13
2.1.1.4 Effect of the surrounding environment .....	16
2.1.2 Plasmon coupling between two noble metal nanoparticles .....	18
2.2 Synthesis of noble metal nanoparticles .....	24
2.3 Principles of dark field microscopy (DFM) .....	25
2.4 Nucleic acids .....	26
2.5 Application of LSPR in nucleic acid sensing.....	31
<b>CHAPTER 3: SYNTHESSES OF SPHERICAL GOLD NANOPARTICLES (nAu).....</b>	<b>47</b>
3.1 Experimental Section .....	47
3.1.1 Materials .....	47
3.1.2 Synthesis of 10 nm nAu.....	47
3.1.3 Synthesis of 50 nm nAu.....	48
3.1.4 Characterization of nAu.....	48
3.2 Results and Discussion.....	49
3.2.1 Syntheses and characterization of nAu.....	49
3.3 Conclusion.....	56
<b>CHAPTER 4: ANALYSIS OF METALLIC NANOPARTICLE-DNA ASSEMBLY FORMATION IN BULK SOLUTION VIA LOCALIZED SURFACE PLASMON RESONANCE SHIFT .....</b>	<b>57</b>
4.1 Introduction .....	57

4.2 Experimental Section .....	59
4.2.1 Materials .....	59
4.2.2 Syntheses and characterization of nAu.....	60
4.2.3 Fabrication of nAu-DNA probes .....	60
4.2.4 Formation and analysis of nAu-DNA assemblies .....	61
4.2.5 DFM and FESEM mapping of nAu and nanoassemblies.....	63
4.3 Results and Discussion.....	64
4.3.1 Analysis of nAu-DNA assemblies.....	64
4.3.2 Probe Concentration & Hybridized Duplex Length Study (Scheme 4.1) .....	67
4.3.3 Size Effect Study (Scheme 4.1 vs. Scheme 4.2).....	74
4.3.4 Surface-ssDNA Density Study (Scheme 4.2).....	78
4.4 Conclusion.....	80
<b>CHAPTER 5: HEAD-TO-TAIL: HYBRIDIZATION AND SINGLE-MISMATCH DISCRIMINATION IN METALLIC NANOPARTICLE-DNA ASSEMBLY .....</b>	<b>82</b>
5.1 Introduction .....	82
5.2 Experimental Section .....	85
5.2.1 Materials .....	85
5.2.2 Synthesis and characterization of nAu .....	86
5.2.3 Fabrication of nAu-DNA probes .....	87
5.2.4 Detection of ssDNA targets.....	87
5.3 Results and Discussion.....	90
5.3.1 Probes and hybridization design.....	90
5.3.2 Perfectly match vs. single-mismatch targets DNA (Scheme 5.1) .....	91
5.3.3 Target DNA with different single-mismatch sites correspond to tail-probe / nAu-T (Scheme 5.2).....	94
5.3.4 Target DNA with non-hybridizing sequence elongation (Scheme 5.3) .....	97
5.4 Conclusion.....	100
<b>CHAPTER 6: MAGNETIC PARTICLE-ASSISTED SINGLE-MISMATCH DNA DETECTION VIA PLASMONIC SCATTERING OF GOLD NANOPARTICLES ...</b>	<b>101</b>
6.1 Introduction .....	101
6.2 Experimental Section .....	108
6.2.1 Materials .....	108
6.2.2 Syntheses and characterization of nAu.....	110
6.2.3 Fabrication of nAu-DNA probes .....	110
6.2.4 Surface functionalization of MMP .....	110
6.2.5 Detection of target ssDNA .....	111
6.2.6 Quantification of nAu-DNA.....	112
6.3 Results and Discussion.....	113
6.3.1 Design of target ssDNA detection.....	113

6.3.2 Analytical performance .....	114
6.3.3 Issues on cross-linking .....	131
6.3.4 Suggested improvements .....	134
6.4 Conclusion.....	138
<b>CHAPTER 7: CONCLUSIONS AND FUTURE PROSPECT.....</b>	<b>140</b>
7.1 Conclusions .....	140
7.2 Future Prospect.....	143
<b>BIBLIOGRAPHY .....</b>	<b>146</b>
<b>APPENDICES .....</b>	<b>156</b>
Dark field micrographs, TEM micrographs, DFM-FESEM mappings and relevant statistics in Chapter 4 and Chapter 5.....	156
Publications .....	165

## **DECLARATION**

I hereby declare that this thesis is my original work and it has been written by me in its entirety.

I have duly acknowledged all the sources of information which have been used in this thesis.

This thesis has also not been submitted for any degree in any university previously.

---

FONG, Kah Ee

28 December 2012



## SUMMARY

Metallic nanoparticles are promising tools in plasmonic circuits, chemical sensors and biological assays due to the uniqueness of their localized surface plasmon resonance (LSPR). In biological detections, the prospects of utilizing these particles in drilling the precision and accuracy down to the single biomolecular sensitivity are encouraging. This has driven many scientists to pursue the development of a new generation of DNA sensing by employing these nanoparticles. This doctoral study attempts to combine the exquisite plasmon properties of spherical gold nanoparticles (nAu) and the specific recognition attributes of deoxyribonucleic acid (DNA) to study the nanoassembly formation, and to improve the sensitivity and selectivity of DNA detection. On that basis, the research directions presented in this thesis are outlined as follows.

The first part of the work focuses on the formation of DNA-modified gold nanoparticle (nAu-DNA) nanoassemblies in bulk solution from two-component hybridization of complementary nAu-DNA probes. Subsequently the nanoassemblies were bound on a glass substrate to study correlations among the LSPR wavelength shift, the plasmon colour change, and the nanoassembly structure. We observed that the hybridization percentage of the complementary 50 nm nAu increased with rising nAu concentration, longer hybridization time, and longer complementary duplex DNA length. In addition, due to lower scattering yield and smaller surface area from 10 nm nAu, the 50nm/10nm hetero-size system displayed limited observable LSPR shift compared to 50nm/20nm hetero-size system, which in turn was inferior to the 50nm/50nm homo-size system. For the hetero-size systems, reducing the surface density of ssDNA on the 20 nm and 10 nm nAu also significantly reduced the hybridization percentages. Overall, this study allows us to understand how different

experimental parameters can impact the assembly of nAu-DNA probes, particularly the limitation in using smaller size nAu (10 nm) for LSPR study.

The second part of the work investigates the influence of a head-to-tail nAu-DNA alignment on the detection of target single-stranded DNA (ssDNA) as well as on the single-base mismatch (SBM) discrimination. Due to the bulk size of nAu, it is envisaged that the alignment would render the tail nAu-DNA probe to hybridize to the target DNA at a higher efficiency than that of the head-probe. The progress of hybridization is deciphered through the LSPR coupling of nAu via a simple dark field microscopy. Our findings prove that the tail-probe exhibits considerably greater mismatch-discrimination than head-probe. Next, analysis of single-mismatch loci on the tail-probe shows that the GC-mismatch located at the middle of recognition site gives the greatest distinction against perfectly match targets. Finally, the head-to-tail assay is extended to perform hybridization on targets with non-hybridizing elongated sequences. The results show that while the non-hybridizing elongated sequence reduces the nanoassembly formation efficiency, it enhances the single-mismatch discrimination.

The third part of the work examines the appropriateness of employing magnetic microparticles (MMP) which exhibit superparamagnetism in the LSPR-assisted target ssDNA detection, in order to improve the sensitivity and selectivity against single-base mismatch (SBM). A simple DNA detection scheme is employed, in which the non-bleaching nAu plasmonic scattering is used directly as the signal to quantify the assay sensitivity by limit of detection (LOD) and the selectivity by SBM. No further amplification on the detected signal is carried out. The current system shows the LOD and SBM at 2 pM and 20 pM respectively. There are two main factors affecting the detection sensitivity and selectivity, i.e. the nonspecific adsorption along with the inefficient probe ssDNA immobilization onto the MMP surface. These two major issues have yet to be completely resolved. Further optimization

should bring the sensitivity and selectivity to a lower level compared to the current reported values. Therefore, the combination of superparamagnetic MMP and LSPR scattering is a potentially useful recipe in the DNA sensing and hence deserves more in-depth study.

## LIST OF ABBREVIATIONS

A	Adenine
AuNR	Gold nanorods
A15	Spacer comprising 15 deoxyadenosine triphosphates
$a_n, b_n$	Scattering coefficients expressed by Ricatti-Bessel functions
bp	Base-pair (s)
C	Cytosine
CCD	Charge-coupled device
CDA	Coupled Dipole Approximation
CID	Chemical interface damping
CRDC	Concentric ring/disk cavity
$C_{abs}$	Absorbance cross-section
$C_{ext}$	Extinction cross-section
$C_{sca}$	Scattering cross-section
$C_x/C_y$	Ratio of nanoassemblies formed by perfectly match to single-mismatch targets
D	Interparticle gap
DDA	Discrete Dipole Approximation
DFM	Dark field microscopy
DNA	Deoxyribonucleic acid
dsDNA	Double-stranded DNA
dT <sub>5</sub>	Thiolated ssDNA with 5 thymine bases
$d_{eff}$	Effective radius of 2 particles
$d_g$	Diameter of grown-nAu
$d_s$	Diameter of seed-nAu
$d_x$	Diameter of a metal nanoparticle of type x (x = 1, 2, 3, ..., n)
EBL	Electron-beam-lithography
EELS	Electron energy-loss spectroscopy
FDTD	Finite-difference-time-domain
FESEM	Field-emission scanning electron microscope
FIB	Focused-ion-beam
FRET	Förster Resonance Energy Transfer
f	Distance between focusing plane & objective lens
G	Guanine
GO	Graphene oxide
H	Hamaker constant
ITO	Indium-tin-oxide
$I_{abs}$	Mean absorbance intensity
$I_o$	Incident light intensity
$I_{sca}$	Mean scattering intensity
K	Arbitrary constant
LNA	Locked nucleic acid
LOD	Limit of detection
LSPR	Localized surface plasmon resonance
MMP	Magnetic microparticles
MSA	2-mercaptosuccinic acid
$[M]_s$	Gold ion concentration in seeds
$[M]_a$	Gold ion concentration in the added HAuCl <sub>4</sub>
m	Relative refractive index of nAu to medium

mOEG <sub>6</sub>	Thiolated methoxy-hexa(ethylene glycol)
NA	Numerical aperture
NCRDC	Nonconcentric ring/disk cavity
NEase	Nicking endonuclease
NIR	Near-infrared
NSL	Nanosphere lithography
n	Orders of oscillation mode
nAu	Spherical gold nanoparticles
nAg	Spherical silver nanoparticles
n <sub>med</sub>	Refractive index of a nanoparticle surrounding medium
n <sub>m</sub>	Complex refractive index of metal
OEG	Oligo(ethylene glycol)
PCR	Polymerase chain reaction
PNA	Peptide nucleic acid
PRET	Plasmon Resonance Energy Transfer
R	Aspect ratio of a metal nanorod
RNA	Ribonucleic acid
r	Radius of a nanoparticle
r <sub>eff</sub>	Effective radius
S	Interparticle centre-to-centre separation distance
SBM	Single-base mismatch
SERS	Surface-enhanced Raman scattering
SERRS	Surface-enhanced resonant Raman scattering
SMAD	Solvated Metal Atom Dispersion
SNOM	Scanning near-field optical microscopy
SNP	Single nucleotide polymorphisms
SP	Surface plasmon
SPP	Surface plasmon polariton
ssDNA	Single-stranded DNA
T	Thymine
TEM	Transmission electron microscopy
T15	Spacer comprising 15 deoxythymidine triphosphates
UV	Ultraviolet
V	Volume of a nanoparticle
x	Size parameter of a nanoparticle
ε <sub>m</sub>	Complex dielectric function of metals
ε <sub>real</sub>	Real component of metal dielectric function
ε <sub>im</sub>	Imaginary component of metal dielectric function
ε <sub>med</sub>	Dielectric function of a nanoparticle surrounding medium
λ <sub>med</sub>	Incident field wavelength in the nanoparticle surrounding medium
λ <sub>max</sub>	LSPR peak wavelength of nanoparticles
ρ	Density of a nanoparticle
ψ <sub>n</sub> (x), ξ <sub>n</sub> (x)	Ricatti-Bessel functions for a nanoparticle with size parameter x
ω	Incident wavelength in vacuum

## LIST OF FIGURES

Figure 2.1: The real and imaginary parts of the dielectric function in the binary Ag-Au alloy as a function of wavelength <sup>[19]</sup> .....	9
Figure 2.2: Extinction of a 20 nm spherical silver (blue line) and gold (green line) nanoparticle showing LSPR at 380 nm and 520 nm respectively <sup>[20]</sup> .....	10
Figure 2.3: Schematic representation of a dipolar plasmon oscillation in a gold nanoparticle, showing the displacement of the conduction electron cloud relative to the nuclei <sup>[22-23]</sup> .....	11
Figure 2.4: Mie theory prediction for scattering (black) and absorption (red) cross-sections as functions of nAu size at wavelength of 532 nm and medium refractive index of 1.25. Inset: Ratio of scattering and absorption cross-sections as a function of nanoparticle size. The dashed lines show how simplified power dependences are only accurate for nanoparticle sizes below 80 nm <sup>[24]</sup> .....	12
Figure 2.5: Extinction spectra of colloidal gold nanoparticles: (a) 23 nm spheres, (b) 70 nm spheres, (c) hexagons, (d) cubes, (e) rods (R = 4.4) and (f) rods (R = 16) <sup>[41]</sup> .....	15
Figure 2.6: Dark-field light scattering images from gold nanoparticles and (inset) corresponding TEM images: (a) 23 nm spheres, (b) 70 nm spheres, (c) hexagons, (d) cubes, (e) rods (R = 4.4) and (f) rods (R = 16). Scale bars represent 2 mm in light scattering images and 100 nm in TEM images <sup>[41]</sup> .....	16
Figure 2.7: Qualitative energy level diagram for plasmon hybridization in two interacting nAu of similar radius r. S = interparticle centre-to-centre separation distance. The dipole plasmons of the individual particles are 3-fold degenerate (i.e., the surface plasmon frequency is independent of polarization along x, y, and z axes) <sup>[22]</sup> .....	20
Figure 2.8: Working principles of dark field microscopy showing the light path (John Innes Centre, <a href="http://www.jic.ac.uk">http://www.jic.ac.uk</a> ) .....	26
Figure 2.9: Basic principles of DNA self-assembly in anti-parallel direction (5' to 3' coupled with 3' to 5'). The Watson-Crick base-pairing rules mean that adenine (A, green) pairs with thymine (T, purple) and guanine (G, pink) pairs with cytosine (C, orange) <sup>[93]</sup> .....	28
Figure 2.10: The double helix structure of DNA in its B-form, with its relevant dimensions and the main interactions. Adapted and modified <sup>[103]</sup> .....	30
Figure 2.11: (a) ssDNA-modified colloidal AuNS assembled into aggregated structure upon the addition of complementary linker DNA. The assembly took place gradually, forming oligomers of AuNS initially and later massive aggregates. The assembled nanoparticles could be reversibly annealed by applying external heating. Δ represents heating above the dissociation temperature of the duplex; (b) The observed colour change from red (monodisperse particles) to purple (aggregated particles) <sup>[125]</sup> .....	33

Figure 2.12: Aggregation behaviours of nAu-DNA at various NaCl concentrations at room temperature: (A) without target DNA, (B) with complementary target DNA, and (C) with target DNA possessing single base mismatch at 5' terminus. The final concentrations of nAu, immobilized probe DNA, and the free target DNA were 2.3 nM, 500 nM, and 500 nM respectively <sup>[120]</sup> .....37

Figure 2.13: Colorimetric method using unmodified colloidal nAu for differentiating between (a) ssDNA and dsDNA, <sup>[153]</sup> (b) dsDNA and triplex DNA, <sup>[156]</sup> and using (c) ssDNA-adsorbed AuNR <sup>[155]</sup> and (d) ssPNA-adsorbed nAu <sup>[141]</sup> for target detection .....39

Figure 2.14: Surface-confined heterogeneous array coupled with dark field microscopy (a) Multiplex detection: captured DNA probes, 50 nm and 100 nm nAu-DNA probes and the unlabelled target DNA co-hybridized in a three-component sandwich format according to the specific recognition sequences. Washing at elevated temperature removed the single-mismatch targets <sup>[118]</sup> (b) Ligated products bound to microarray spot containing capture DNA complementary to extension sequence of discrimination DNA. Wash step at elevated temperature removed the non-ligated detection DNA. The quantity of nAg-labelled detection DNA was then counted <sup>[83]</sup> .....41

Figure 2.15: (A) Photographs of white gene region in *Drosophila* X chromosome specifically labelled with gold-silver core-shell nanoparticles via *in situ* hybridization. Both the SYBR Green fluorescence of the stained polytene chromosome and the blue light scattered by the nanoparticles were imaged simultaneously. The large number of parallel-aligned copies of DNA present in the polytene chromosome provided multiple target sites for the nanoparticle hybridization (B) A close-up view of the white gene region from another sample, illustrating the large density of nanoparticles that can be clustered yet still be readily identified as individual target site labels. The typical distance between plasmonic nanoparticles is about 2µm. <sup>[29]</sup> .....42

Figure 2.16: Single hybridization event detection (a) 80 nm nAu-DNA probe immobilized on APTES (3-aminopropyltriethoxysilane) surface hybridized to a complementary target ssDNA and 40 nm nAu-DNA probe forming a sandwich structure <sup>[114]</sup> (b) Geometric extension motif for DNA sensing by dimeric 100 nm - 60 nm nAu joined by a probe ssDNA hairpin; 100 nm nAu was anchored to the substrate via aminosilane chemistry; the protein molecules depicted non-specific binding <sup>[116]</sup> (c) 40 nm nAu or nAg homodimer linked by a flexible probe ssDNA aided the sensing of single target ssDNA <sup>[117]</sup> .....43

Figure 2.17: Signalling concept of molecular beacon based on surface-enhanced resonant Raman scattering (a) SERRS signal was observed when an nAg-DNA probe formed hairpin, exposing Raman label close to the nAg surface (closed conformation), whereas (b) SERRS signal diminished when target DNA hybridized to the hairpin, pushing the label far from the plasmon decay distance (open conformation) <sup>[121]</sup> .....45

Figure 3.1: TEM images of (a) nAu with mean diameter 51.5 nm ± 3.7 nm on a wide field view, (b) its magnified view, and (c) nAu with mean diameter 10.03 nm ± 1.0 nm, which also serves as seed for the fabrication of 50 nm nAu. ....52

Figure 3.2: Statistical particle diameter analysis. Size distribution of (a) 10 nm nAu with an average diameter of  $10.03 \pm 1.03$  nm and (b) 50 nm nAu with an average diameter of  $51.5 \pm 3.69$  nm by measuring 114 and 159 nanoparticles in the TEM images, respectively.....52

Figure 3.3: UV-visible extinction spectra of nAu solution with mean diameters 10 nm (dashed line) and 50 nm (solid line). Both are normalized to their extinction peak maxima. The bandwidth (FWHM,  $\Pi$ ) for  $51.5 \pm 3.7$  nm nAu is 78 nm. ....53

Figure 3.4: Dark field image of as-synthesized nAu with mean diameter  $51.5 \pm 3.7$  nm. The solution was diluted many-fold from the as-synthesized solution to avoid over-crowding and to improve clarity. Each bright dot represents the optical scattering from single nAu. ....55

Figure 4.1: Typical light scattering spectra of the particles/nanoassemblies categorized as ‘green’, ‘yellow’, and ‘orange’ showed in Table 4.2, on glass-slides and in buffer (140 mM Tris, 140 mM NaCl, 2 mM  $\text{MgCl}_2$ ). The spectra were obtained with a dark field microscope, and exposure time 40 s - 100 s on the EMCCD-monochromator. The ranges of peak maxima for each category are around 550 nm, 570-580 nm, and 610-650 nm. ....67

Figure 4.2: Probe Concentration & Hybridized Duplex Length Study (Scheme 4.1). Dark field micrographs on (a) complementary probes nAu-P/nAu-cP<sub>27</sub> hybridized at constant ratio of 1/1 and concentration 400 fM, (b) control comprises only single type of probe, both recorded after 1 h-hybridization. The scattering colour of control remains more than 95% green even after 24 h. Images were taken from the bottom plane of liquid chamber, to which particles settled. Buffer: 140 mM Tris, 140 mM NaCl, 2 mM  $\text{MgCl}_2$ . ....69

Figure 4.3: Probe Concentration & Hybridized Duplex Length Study (Scheme 4.1). The charts summarize the hybridization percentage between complementary probes nAu-P/nAu-cP<sub>27</sub> (red bars), nAu-P/nAu-cP<sub>18</sub> (yellow bars), and nAu-P/nAu-cP<sub>14</sub> (blue bars), at decreasing concentration of (a) 400 fM, (b) 100 fM, and (c) 10 fM while the ratio is kept at 1/1. The analysis is performed by counting the hybridized-clusters (categorized as ‘yellow’ & ‘orange’ due to their distinct LSPR plasmon shift) vs. the individual probes (categorized as ‘green’). The corresponding controls are illustrated in (d) for 400 fM (black bars), 100 fM (grey bars), and 10 fM (light-grey bars) where only a single type of probe exists, thus no hybridization take place. Each set of data in (a)-(d) consists of three repeats. Buffer: 140 mM Tris, 140 mM NaCl, 2 mM  $\text{MgCl}_2$ . ....71

Figure 4.4: Size Effect Study (Scheme 4.1 vs. Scheme 4.2) at 1 h, 6 h, and 24 h. Hybridization percentage between nAu-P/nAu-cP<sub>27</sub> for (a) homo-size system with same probe size (50nm/50nm), (b) hetero-size system with different probe sizes (50nm/20nm), and (c) hetero-size system with different probe sizes (50nm/10nm). Ratio of complementary probes: 1/1; concentrations of all species: 800 fM. Data for homo-size system is the average of three repeats; for hetero-size system, each data reported consists of four repeats, two with 50 nm nAu-P / 20 nm or 10 nm nAu-cP<sub>27</sub>, and the other two with 20 nm or 10 nm nAu-P / 50 nm nAu-cP<sub>27</sub>. Images are quantified by counting the hybridized-clusters (‘yellow’ & ‘orange’) vs. the individual probes (‘green’). The corresponding controls for (a) homo-size system



comprises single type of 50 nm probe at 1.6 pM, and for (b) hetero-size system , comprises 800 fM 50 nm probe & 800 fM 20 nm or 10 nm probe, both carrying the same type of ssDNA sequences. Buffer: 140 mM Tris, 140 mM NaCl, 2 mM MgCl<sub>2</sub>. ..... 75

Figure 4.5: Surface-ssDNA Density Study (Scheme 4.2) at 1 h, 6 h, and 24 h. Hybridization percentage between nAu-P/nAu-cP<sub>27</sub> for (I) 50nm/20nm hetero-size system with the 20 nm nAu (a) fully saturated with ssDNA, or (b) bearing only 5 ssDNA, and for (II) 50nm/10nm hetero-size system with the 10 nm nAu (a) fully saturated with ssDNA, or (b) bearing only 5 ssDNA. Ratio of complementary probes: 1/1; concentrations of all species: 800 fM. Each data reported consists of four repeats, two with 50 nm nAu-P / 20 nm or 10 nm nAu-cP<sub>27</sub>, & the other two with 20 nm or 10 nm nAu-P / 50 nm nAu-cP<sub>27</sub>. Images are quantified by counting the hybridized-clusters ('yellow' & 'orange') vs. the individual probes ('green'). The corresponding controls comprise 800 fM 50 nm probe & 800 fM 20 nm or 10 nm probe, both carrying the same type of ssDNA sequences, for (a) fully saturated and (b) 5-ssDNA-bearing 20 nm or 10 nm nAu. Buffer: 140 mM Tris, 140 mM NaCl, 2 mM MgCl<sub>2</sub>. ..... 79

Figure 5.1: (Scheme 5.1) The counted nanoassemblies formed by hybridizing nAu-T and nAu-H to 28 b targets of perfect-match P (red bar), 'head'-single-mismatch MH (yellow bar), and 'tail'-single-mismatch MT (blue bar) at 4 pM target concentration. The control (pink bar) was taken at 24 h in the absence of target. Each sample contains 1 pM of nAu-T and 1 pM of nAu-H. Each set of data consists of three repeats. Buffer: 140 mM Tris, 140 mM NaCl, 2 mM MgCl<sub>2</sub>. ..... 92

Figure 5.2: The counted nanoassemblies formed by hybridizing nAu-T and nAu-H to 28 b targets of perfect-match P (red bar), end-AT-mismatch MT1 (orange bar), near-end-GC-mismatch MT2 (light blue bar), middle-GC-mismatch MT3 (yellow bar), middle-AT-mismatch MT4 (purple bar), near-end-GC-mismatch MT5 (pink bar), and end-GC-mismatch MT6 (green bar). The data of control (grey bar) is taken in the absence of target. The counts are measured after (a) 1 h, and (b) 24 h of hybridization. Each sample contains 1 pM of nAu-T, 1 pM of nAu-H and 4 pM of target ssDNA. Each data consists of three repeats. Buffer: 140 mM Tris, 140 mM NaCl, 2 mM MgCl<sub>2</sub>. ..... 96

Figure 5.3: The nanoassemblies formed at (a) 1 h and (b) 24 h, by hybridizing nAu-T and nAu-H to targets with non-hybridizing sequences elongated towards nAu-T (P60 - perfect-match, red bar; MT60 & MH60 - single-mismatches, orange & yellow bars respectively), targets with non-hybridizing sequences elongated towards nAu-H (P61 - perfect-match, green bar; MT61 & MH61- single-mismatches, blue & light blue bars respectively), with non-hybridizing sequences elongated towards both nAu-T and nAu-H (P90- perfect-match, purple bar), and with 100 b non-complementary target (grey bar). The data of control (pink bar) is taken in the absence of target. All the targets are at 40 pM while 100 b non-complementary target are at 400 pM. Each of the samples contains 1 pM of nAu-T and 1 pM of nAu-H. Each data consists of three repeats. Buffer: 140 mM Tris, 140 mM NaCl, 2 mM MgCl<sub>2</sub> ..... 99

Figure 6.1: Nanoassembly formation based on Scheme 6.1a using 2 pM of target (a) P and (b) MH; (c) the image for control was acquired in the absence of any target DNA. Collective mode condition: incubate 0.172 mg MMP-H<sub>M</sub> with the desired target, together with 3 nM of 10 nm nAu-T·C in 40 μL 200 mM NaCl + 10 mM phosphate + 0.005% Tween-20 for 5 h. The samples were then washed five times with 60 μL of the buffer, and the magnetically-collected precipitates redispersed in 8 μL of water. Dehybridization was performed by heating the mixture at 65 °C for 5 min under vigorous shaking. 1.7 pM nAu-rC was then added to hybridize with the released nAu-T·C. .... 116

Figure 6.2: Effect of (I) tail-to-tail vs. (II) head-to-tail hybridization conformation based on Scheme 6.1b & c respectively. Stepwise mode condition: incubate 0.2125 mg (I) MMP-H<sub>M</sub> or (II) MMP-T<sub>M</sub> with 333 fM target (Ia) P (Ib) MH (IIa) P (IIb) MT in 60 μL 140 mM Tris + 140 mM NaCl + 2 mM MgCl<sub>2</sub> + 0.005% Tween-20 for 3 h, followed by washing twice with 150 μL of the buffer, and subsequent 3 h incubation with 1.5 pM of (I) nAu-T·C or (II) nAu-H·C in 30 μL of the buffer. The samples were then washed twice with 150 μL of the buffer, and the magnetically-collected precipitates redispersed in (I) 20 μL (II) 15 μL of water. Dehybridization was performed by heating the mixture at 70 °C for 5 min under vigorous shaking. 1 pM nAu-rC was then added to hybridize with the released nAu-T·C or nAu-H·C. .... 118

Figure 6.3: Nanoassembly formation based on Scheme 6.1b using (a) 200 pM, (b) 20 pM, and (c) 2 pM of target P; (d) the image for control was acquired in the absence of any target DNA. Collective mode condition: incubate 0.125 mg MMP-H<sub>M</sub> with the desired targets, together with 2 pM of 50 nm nAu-T·C in 25 μL 140 mM Tris + 140 mM NaCl + 2 mM MgCl<sub>2</sub> + 0.005% Tween-20 for 7 h. The samples were then washed thrice with 40 μL of the buffer, and the magnetically-collected precipitates redispersed in 10 μL of water. Dehybridization was performed by heating the mixture at 65 °C for 5 min under vigorous shaking. 2.5 pM nAu-rC was then added to hybridize with the released nAu-T·C. .... 120

Figure 6.4: Dark field micrographs showing the varied amount of nAu-T released from the sandwich MMP-target-nAu based on Scheme 6.2a using (a) 200 pM, (b) 20 pM, and (c) 2 pM of target P; (d) the image for control was acquired in the absence of any target DNA. Collective mode condition: incubate 0.125 mg MMP-H<sub>M</sub> with (a) 200 pM, (b) 20 pM, and (c) 2 pM of target P, together with 2 pM of 50 nm nAu-T in 25 μL 140 mM Tris + 140 mM NaCl + 2 mM MgCl<sub>2</sub> + 0.005% Tween-20 for 7 h. The samples were then washed thrice with 40 μL of the buffer, and the magnetically-collected precipitates redispersed in 20 μL of water. Dehybridization was performed by heating the mixture at 65 °C for 5 min under vigorous shaking. .... 122

Figure 6.5: Effect of sonication based on Scheme 6.2a (I) without and (II) with sonication for 5 s using (a) 0.2 pM of P and (b) control. Stepwise mode condition: incubate 0.25 mg MMP-H<sub>M</sub> with the desired targets in 200 μL 100 mM Tris + 600 mM NaCl + 2 mM MgCl<sub>2</sub> + 0.005% Tween-20 for 3 h, followed by washing twice, and subsequent 4 h incubation with 10 pM of 50 nm nAu-T in 50 μL 140 mM Tris + 140 mM NaCl + 2 mM MgCl<sub>2</sub> + 0.005% Tween-20. The samples were then washed with 100 μL of the buffer for (I) 5 times without sonication or (II) 4 times with 5 s sonication, and the magnetically-collected precipitates redispersed in 10 μL of water. Dehybridization was performed by heating the mixture at 65 °C for 5 min under vigorous shaking. .... 124

Figure 6.6: (a, b) Dark field micrographs showing the amount of nAu-T adsorbed nonspecifically onto MMP-COOH using experimental condition similar to Figure 6.8..... 125

Figure 6.7: Effect of formamide based on Scheme 6.2a (I) with 20% formamide and (II) without formamide using (a) 0.2 pM P and (b) control. Stepwise mode condition: incubate 0.125 mg MMP-H<sub>M</sub> with the desired targets in 200  $\mu$ L 100 mM Tris + 600 mM NaCl + 2 mM MgCl<sub>2</sub> + 0.005% Tween-20 for 3 h, followed by washing once, and subsequent 3 h incubation with 10 pM of 50 nm nAu-T in 25  $\mu$ L 140 mM Tris + 140 mM NaCl + 2 mM MgCl<sub>2</sub> + 0.005% Tween-20 (I) with and (II) without 20% formamide. The samples were then washed 5 times with 100  $\mu$ L of the buffer, and the magnetically-collected precipitates redispersed in 10  $\mu$ L of water. Dehybridization was performed by heating the mixture at 65 °C for 5 min under vigorous shaking..... 127

Figure 6.8: Dark field micrographs showing the varied amount of nAu-T released from the sandwich MMP-target-nAu based on Scheme 6.2b using (a) 20 pM PM, (b) 20 pM SM, (c) 2 pM PM, and (d) 2 pM SM; (e) the image for control was acquired in the absence of any target DNA. Stepwise mode condition: incubate 0.25 mg MMP-H<sub>M</sub> with the desired targets in 200  $\mu$ L 100 mM Tris + 600 mM NaCl + 2 mM MgCl<sub>2</sub> + 0.005% Tween-20 at 37 °C for 2 h, followed by washing twice, and subsequent 6 h incubation with 10 pM of 50 nm nAu-T in 50  $\mu$ L 140 mM Tris + 140 mM NaCl + 2 mM MgCl<sub>2</sub> + 0.005% Tween-20 at 33 °C. The samples were then washed 4 times with 100  $\mu$ L of the buffer with 2 min vigorous shaking. The magnetically collected precipitates were finally redispersed in 10  $\mu$ L of water. Dehybridization was performed by heating the mixture at 65 °C for 5 min under vigorous shaking. .... 129

Figure 6.9: The amount of nAu-T released from MMP surface during dehybridization, for 20 pM and 2 pM of perfectly match (PM, blue bar) and single-mismatch (SM, red bar) captured target DNA, counted from total of ten frames of dark field micrographs for each sample. The data of control (green bar) is taken in the absence of any DNA target. The experimental condition is as described in Figure 6.8. The asterisk symbol (\*) denotes statistical difference ( $p < 0.05$ ) between two data. .... 131

## LIST OF TABLES

Table 4.1: List of DNA sequences used to conjugate nAu surface in this study. The underlined portions represent complementary sequences that hybridize. P denotes the main ssDNA probes; cP<sub>27</sub>, cP<sub>18</sub>, and cP<sub>14</sub> denote complementary ssDNA strands which will hybridize with 27 bases, 18 bases, and 14 bases of P to form 27 bp-, 18 bp-, and 14 bp-duplexes. ....60

Table 4.2 (Scheme 4.1): Correlation between the plasmon observed under dark field microscope with the inherent structure of the nanoassemblies. The sample is prepared by hybridizing 800 fM of complementary probes nAu-P/nAu-cP<sub>27</sub>, for 1 h at 1/1 molar ratio, in buffer 140 mM Tris, 140 mM NaCl, 2 mM MgCl<sub>2</sub>. FESEM image confirms the change in plasmon colour from green to yellow/yellowish-red when the gold nanoparticles form nanoassemblies due to hybridization. Note that dark field micrographs are taken after the solution dried-up; therefore, the plasmon scattering intensities as well as the plasmon shifts owing to hybridization are not as significant as the dark field micrographs demonstrated in the main article, which are captured with the particles residing in buffer. ....66

Table 5.1: List of DNA sequences used in this study. The underlined portions represent complementary sequences that hybridize. T and H denote the main ssDNA probes that were conjugated on nAu surface. P denotes unmodified ssDNA targets that are complementary to a portion of T and H. The bold characters indicate the single-mismatch bases. ....85

Table 6.1: DNA detection strategies with the aid of MMP and noble-metal nanoparticles .. 103

Table 6.2: List of DNA sequences used in this study. The similar underlined portions represent complementary sequences that hybridize. T, H, C and rC denote the probes ssDNA that were conjugated on nAu, whereas H<sub>M</sub> and T<sub>M</sub> was immobilized on the MMP surface. P denotes unmodified ssDNA that is fully-complementary to T and H<sub>M</sub> or H and T<sub>M</sub>, PM denotes unmodified ssDNA that is fully-complementary to T and H<sub>M</sub>, while MH & MT and SM are single-mismatch variants to P and PM respectively..... 109

## CHAPTER 1: PROLOGUE

### 1.1 Background

Upon excitation by incident electromagnetic field, the highly confined conduction electrons within a nanoscale clump of noble metal atom (sub-100 nm dimension) oscillate collectively and contribute to a substantially enhanced and confined electromagnetic field compared to the bulk metal. When the coherent oscillation of the conduction electrons is in resonance with the incident light frequency, an exclusive localized surface plasmon resonance (LSPR) is produced as the maximum field enhancement. Consequently, the optical cross-section of a noble metal nanoparticle at its resonant frequency is many folds larger than its absolute size. The resulting strong extinction properties give rise to significant plasmonic scattering under highly oblique illumination, enabling the far-field observation of individual nanoparticle that is originally forbidden in the diffraction-limited conventional ‘bright field’ optical microscopy. The resonance frequency at which plasmon can be excited is sensitive to the local dielectric environment. For instance, nanoparticle clustering couples their plasmons and alters the collective electromagnetic field considerably. The noble metal nanoparticles have attracted numerous studies on their optical characteristics as well as their potential and practical applications in both plasmonic circuits and in biological assays.

From the oldest known prokaryote in the Archean Eon to the earliest known eukaryote (algae) in the Proterozoic Eon, and to the modern mammals in Cenozoic Era, nucleic acids have been, and will most certainly continue to be the genetic information transmitter from which life builds on and ensures inheritance. Therefore, identifying the accurate deoxyribonucleic acid (DNA) and ribonucleic acid (RNA) with proper sequences is of high importance in DNA diagnostics, pathogenic and viral detection, medical genetics,

forensics, antisense and antigene therapies etc. For the last two decades, metallic nanoparticles have witnessed their growing and broadly expanded applications in nucleic acid detection along with nucleic acid-controlled self-assembly.

In-depth knowledge on the structure of single-stranded DNA (ssDNA) and their hybridization to form helical double-stranded DNA (dsDNA) has allowed researchers to create 1- to 3-dimensional ordered assemblies of nanoparticles based on the programmable nature of DNA. One of the most studied examples is the DNA-guided organization of gold nanoparticles with (an)isotropic geometries e.g. spheres, triangular nanoprisms, nanorods, rhombic dodecahedra and octahedra into crystallographic lattices or macroscopic frameworks.

Importantly, the plasmons of gold and silver nanoparticles can function as inorganic reporter or energy source/sink to account for the hybridization between probe DNA and synthetic or genomic complementary target DNA. It is particularly essential to accomplish the detection with high selectivity, i.e. the ability to distinguish the correct DNA from the single-base mismatch ones is extremely valuable in sequence-specific detection. This can, in one part, aid in the sensing of single nucleotide polymorphisms (SNP) which are the most abundant and stable type of genetic variations found in human genome. In fact, non-synonymous SNP can greatly affect the disease immunity level of each individual or alter the response to drug treatments; and genetic variations have been the culprits for many genetic disorders such as diabetes, schizophrenia, rheumatoid arthritis, hepatocellular carcinoma, Alzheimer's and Parkinson's diseases. Over the years, gold nanoparticles coupled to DNA probes have become a popular platform in the development of novel DNA sensors, because nanomaterials constructed from gold offer biocompatibility, easy functionalization, and are relatively stable in many solutions including the biological matrices. These sensory platforms often exploit the unique LSPR concentrated around the individual nanoparticles in a broad

spectrum of colorimetric, plasmonic scattering, luminescence, Raman scattering, and electronic nucleic acid detections.

## 1.2 Objectives

In this research, we exploit the powerful and versatile plasmonic scattering in three different hybridization-related studies. We use both the plasmon coupling event as well as the sole scattering signal from spherical gold nanoparticles (nAu) to describe the hybridization. Probe ssDNA could be facilely immobilized on the nAu by means of strong covalent bonding, and the resulting ssDNA-modified gold nanoparticle conjugates will be known as nAu-DNA henceforth. The doctoral research described in this thesis, specifically, aims to meet the following objectives:

**Objective 1:** To investigate the formation of nAu-DNA nanoassemblies in bulk solution by ensemble two-component hybridization based on the LSPR shift (Chapter 4)

While most of the existing studies have focused on the heterogeneous (surface-bound) hybridization system, herein, we use a homogenous (in bulk solution) system to circumvent the interference arising from glass-aqueous interface encountered by most of the chip-based heterogeneous hybridization. This would enable a more accurate and statistical representation of the ensemble hybridization behaviour for the whole populations of nAu-DNA probes. The hybridized nanoassemblies, as observed via plasmon scattering under the dark field microscopy, are correlated to their respective LSPR wavelength shift, plasmon colour change, and the structure of nanoassemblies. The main parameters affecting the hybridization between the complementary nAu-DNA probes are analyzed systematically and the nanoassembly formation efficiency is quantified in terms of the LSPR shift.

**Objective 2:** To examine the robustness of nAu-DNA probes in detecting unmodified target ssDNA and discriminating single-mismatches via a three-component assembly of nAu-DNA in head-to-tail alignment (Chapter 5)

The least restricted and the most thermodynamically favourable tail-to-tail nAu-DNA structure has been exploited extensively in nucleic acid sensing. Judging by its asymmetry construct, we hypothesize that nAu-DNA aligned in the head-to-tail orientation would render the head- and tail-probes different recognition dominance towards target ssDNA bearing single-mismatches at different location. Therefore, we inspect the competency of a three-component nAu-DNA assembly in head-to-tail alignment to discriminate single nucleotide mismatch at sites correspond to the head- and tail-probes, respectively. Our findings validate the hypothesis in which tail-probe exhibits considerably greater mismatch-discrimination ability than the head-probe. Specifically, the influence of mismatch loci and the type of base-pair mismatch on the nanoassembly formation are analyzed for single-mismatches against the tail-probe. Additionally, the head-to-tail assay is assessed for its hybridization efficiency with target ssDNA having non-hybridizing elongated sequences, which is common in the detection of endogenous nucleic acids extracted from cells and as functional DNA. Results from this study may offer a new approach to enhance the mismatch-discriminations.

**Objective 3:** To improve the sensitivity and selectivity in plasmonic scattering-based DNA detection with the assistance of magnetic microparticles (MMP) (Chapter 6)

The optical LSPR scattering phenomenon, which has been studied comprehensively, appears to receive comparatively little application in the superparamagnetic MMP-assisted DNA sensing. Therefore, we explore the levels of sensitivity and single-base mismatch selectivity that can be achieved in MMP-assisted DNA detection by employing the non-bleach LSPR scattering from nAu as the sole signal reporter. A simple and direct DNA



detection scheme is designed, in which the detected signal is not subjected to further complex development e.g. enzymatic amplification or metallic stripping, and does not require additional barcode DNA or chip-based hybridization (without additional amplification). The system which has not been fully optimized yet shows good prospect and presents the limit of detection (LOD) and single-base mismatch (SBM) selectivity at 2 pM and 20 pM respectively. Further optimization would be able to bring the sensitivity and selectivity even lower than the current obtained values.

## CHAPTER 2: LITERATURE REVIEW

This chapter provides fundamental understanding in the research area/work described in this thesis. The review encompasses six main topics: (1) the basic optical properties of noble metal nanoparticles, (2) the common methodologies in nanoparticle synthesis, (3) the working principle of dark field microscopy, (4) the basics of nucleic acids, and (5) the applications of LSPR in nucleic acid sensing. A nanoparticle is defined as any particle that has at least one dimension in the sub-100 nm scale and behaves as a whole unit in terms of its properties.

(Parts of paper reprints from *Nanoscale*, accepted 2013)

### 2.1 Optical properties of noble metal nanoparticles

#### 2.1.1 Localized surface plasmon resonance (LSPR)

Surface plasmon (SP) is highly versatile electromagnetic wave that is trapped on the metal surface at metallic-dielectric interface at the optical wavelength region. SP exhibits unique characteristics due to the oscillation of the conduction electrons near the metal surface upon excitation by incident light. At nanometre range, metallic nanoparticles possess high surface areas to volume ratio and show distinctly different optical, electronic, magnetic, and chemical properties compared to their bulk and molecular counterparts.<sup>[3-4]</sup> SP strongly confined on the surface of metallic nanoparticles is termed localized surface plasmon resonance (LSPR)<sup>[5]</sup> to differentiate them from surface plasmon polariton (SPP), which is propagating on the metallic-dielectric interface of metal thin films when excited by external photon with sufficient in-plane momentum.<sup>[6]</sup> When incident electromagnetic field interacts with a metal nanoparticle, conduction electrons near the metal surface oscillate collectively & coherently in resonance with the light frequency with respect to the nanoparticle lattice, due

to the coulombic attraction between electrons and metallic nuclei. This collective oscillation of electrons in resonance with incident light frequency then creates a strongly enhanced electromagnetic field on the metal nanoparticle surface, which is known as localized surface plasmon resonance (LSPR).

LSPR strongly affects the optical properties in both the near-field and far-field response of metal nanoparticles. Optical interaction between a metal nanoparticle with its surrounding medium and between metal nanoparticles in close proximity (e.g. in close-packed arrays) is governed by the near-field properties. The electromagnetic near-field bounded to the surface of metal nanostructures can be mapped by scanning near-field optical microscopy (SNOM),<sup>[7]</sup> and more recently, using cathodoluminescence<sup>[8-10]</sup> and electron energy-loss spectroscopy (EELS)<sup>[10-11]</sup> performed within electron microscopes with nanometer spatial resolution. On the other hand, the absorption and scattering (the summation of both is named extinction) in colloidal metal nanoparticle solution are ruled by the far-field optics. In essence, the optical absorption and scattering of spherical nanoparticles can be predicted with the following Mie theory, an analytical solution to Maxwell's equations that was developed by Gustav Mie:<sup>[12-13]</sup>

$$\text{Scattering cross-section, } C_{sca} = \frac{2}{x^2} \sum_{n=1}^{\infty} (2n+1) (|a_n|^2 + |b_n|^2) \quad (\text{Eq. 1})$$

$$\text{Extinction cross-section, } C_{ext} = \frac{2}{x^2} \sum_{n=1}^{\infty} (2n+1) [\text{Re}(a_n + b_n)] \quad (\text{Eq. 2})$$

$$\text{Absorption cross-section, } C_{abs} = C_{ext} - C_{sca} \quad (\text{Eq. 3})$$

in which  $x$  defines the size parameter,  $x = 2\pi r n_{med} / \omega$  ( $r$  is the particle radius,  $n_{med}$  is the real refractive index of the surrounding medium,  $\omega$  is the incident wavelength in vacuum),  $n$  are the integers representing the orders of oscillation mode ( $n = 1, 2, 3 \dots$  for dipole, quadrupole, octapole...),  $a_n$  and  $b_n$  are the scattering coefficients expressed by Ricatti-Bessel functions:

$$a_n = \frac{m\psi_n(mx)\psi_n'(x) - \psi_n'(mx)\psi_n(x)}{m\psi_n(mx)\xi_n'(x) - \psi_n'(mx)\xi_n(x)}, b_n = \frac{\psi_n(mx)\psi_n'(x) - m\psi_n'(mx)\psi_n(x)}{\psi_n(mx)\xi_n'(x) - m\psi_n'(mx)\xi_n(x)} \quad (\text{Eq. 4})$$

$\psi_n(x)$  and  $\xi_n(x)$  are Ricatti-Bessel functions,  $m = n_m/n_{\text{med}}$  ( $n_m$  is the complex refractive index of the metal). From the preceding equations, the LSPR of individual metal nanoparticles is controlled by their respective sizes, shapes, chemical compositions (which determine their dielectric constants), as well as the refractive index of the embedding environment.

### 2.1.1.1 Chemical compositions

The complex dielectric functions of metals,  $\epsilon_m$ , are functions of the wavelength,  $\omega$ , according to the equation  $\epsilon_m(\omega) = \epsilon_{\text{real}}(\omega) + i\epsilon_{\text{im}}(\omega)$ . The real component of the dielectric functions,  $\epsilon_{\text{real}}$ , governs the frequency position of the electron oscillation resonance. Whereas the imaginary component of the dielectric functions,  $\epsilon_{\text{im}}$ , incorporates the broadening and absorptive dissipation of the resonance due to damping and dephasing of the electron oscillations.<sup>[12]</sup> In this regard, dielectric constants for nanoparticles at different wavelengths are assumed to be the same as that of bulk metal,<sup>[14]</sup> and the experimental results generally agree well with the assumption, except for much complicated particle morphologies.

Other than  $\epsilon_{\text{im}}$  of several alkali and noble metals,  $\epsilon_{\text{im}}$  for most metals are too large to be neglected and this suppresses the excitation of the surface plasmon in the visible wavelength region.<sup>[15]</sup> In addition, while  $\epsilon_{\text{real}}$  for the aforementioned alkali and noble metals are negative due to d-d intraband transitions, conduction-d interband transitions in the non-noble metals contribute positively to their  $\epsilon_{\text{real}}$ , preventing the excitation of surface plasmon modes in the small metal spheres.<sup>[16]</sup> Therefore, most metals possess bulk plasmon resonance in the ultraviolet (UV) region, while noble metals (Au, Ag, and Cu) support distinctly sharper bulk plasmon resonances than non-noble metals in the visible-near-infrared (visible-NIR) region. The absorption and scattering cross-sections of gold and silver nanoparticles are

many-fold larger than their geometrical sizes, thanks to the enormously intense LSPR of these noble metal nanoparticles.<sup>[17]</sup> Consequently, changes in their resonance behaviours lead to visible colour change.

Due to the much smaller  $\epsilon_{im}$  value (Figure 2.1), silver nanoparticles suffer lower losses than gold and possess greater scattering quantum yield (higher ratio of scattering to extinction).<sup>[12]</sup> The smaller  $\epsilon_{im}$  and the steeper slope (hence greater magnitude) of  $\epsilon_{real}$  result in the narrower bandwidth and therefore sharper LSPR peak. These make the silver nanoparticles more efficient scatterers of light than gold nanoparticles in the visible-NIR spectrum (Figure 2.2). In general, both gold and silver nanoparticles have very high light-scattering powers in the visible-NIR spectrum compared to copper.<sup>[18]</sup>

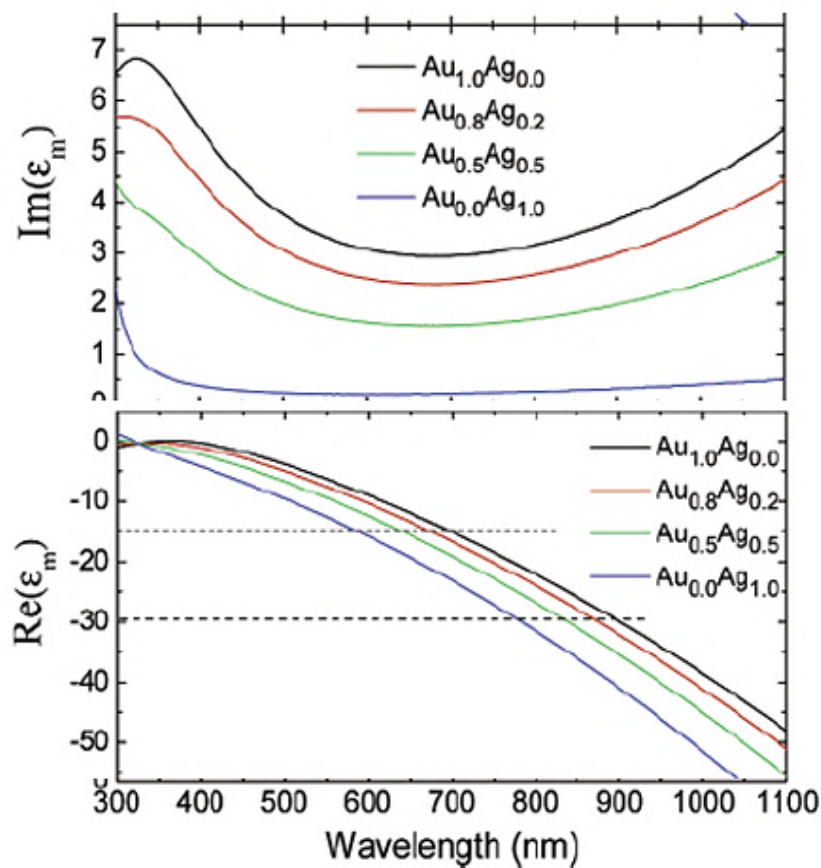


Figure 2.1: The real and imaginary parts of the dielectric function in the binary Ag-Au alloy as a function of wavelength<sup>[19]</sup>

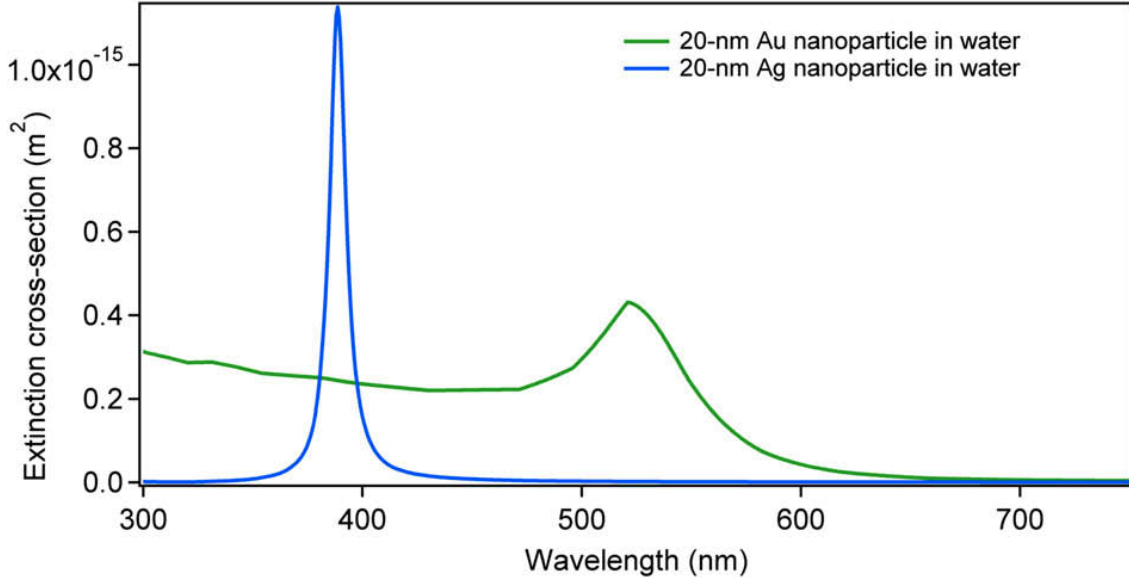


Figure 2.2: Extinction of a 20 nm spherical silver (blue line) and gold (green line) nanoparticle showing LSPR at 380 nm and 520 nm respectively <sup>[20]</sup>

### 2.1.1.2 Size

For a spherical metal nanoparticle with size much smaller than the wavelength of light, the optical properties follow the Mie theory that reduces to Rayleigh theory. The surface plasmon oscillation is dominated by the dipolar mode because all the electrons sense the same phase and move in same frequency with external electric field (Figure 2.3). Within this size range, the dipolar LSPR mode do not differ significantly, and the extinction cross-section (Eq. 2) simplifies to

$$C_{ext} = \frac{18\pi\epsilon_{med}^{1.5}V}{\omega} \frac{\epsilon_{im}(\omega)}{[\epsilon_{real}(\omega) + 2\epsilon_{med}]^2 + \epsilon_{im}^2(\omega)} \quad (\text{Eq. 5})$$

in which  $V$  is the particle volume,  $\epsilon_{med}$  is the dielectric function of the surrounding medium,  $\omega$  is the incident wavelength in vacuum. For  $\epsilon_{im}$  that is small or depends weakly on  $\omega$ , when the denominator in Eq. 5 is at its minimum (i.e. when  $\epsilon_{real} = -2\epsilon_{med}$ ), the extinction cross-section is maximized and the nanoparticle is at its resonance.<sup>[12-13]</sup> The plasmon excitation either (a) decays non-radiatively into electron-hole pair excitations (intraband excitation

within metal conduction band or interband excitation between d bands and conduction band), and constitutes the light absorption by particle; or (b) decays radiatively by radiating the electromagnetic energy at same frequency with surface plasmon oscillations, and constitutes the elastic/Rayleigh scattering by particle. Mean scattering and absorbance intensities ( $I_{\text{sca}}$  &  $I_{\text{abs}}$ ) are proportional to the sixth and third powers of the nanoparticle radius respectively.<sup>[18]</sup> Consequently, as the nanoparticle size increases in this size range, the enhancement of scattering component is faster than that of absorbance component, which eventually cause a net increase in the  $I_{\text{sca}}$ .<sup>[1,21]</sup>

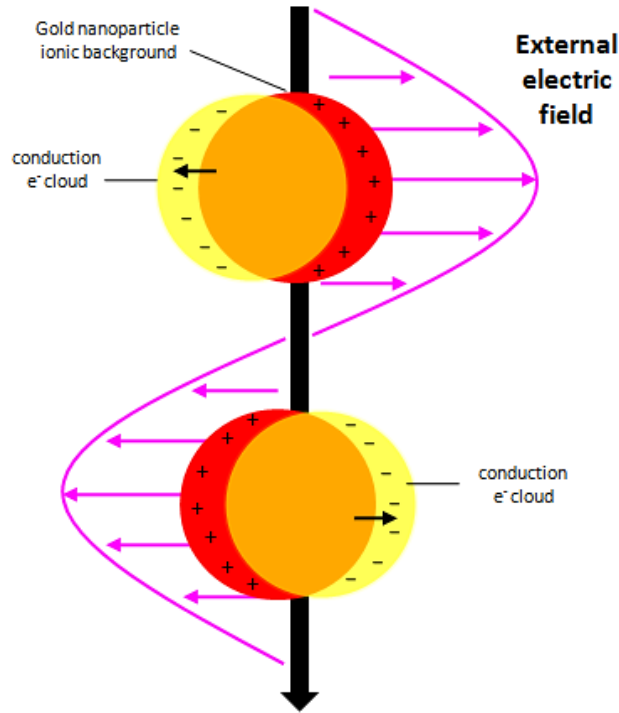


Figure 2.3: Schematic representation of a dipolar plasmon oscillation in a gold nanoparticle, showing the displacement of the conduction electron cloud relative to the nuclei<sup>[22-23]</sup>

For large spherical metal nanoparticles with radius  $R \approx 0.1 \lambda_{\text{med}}$  ( $\lambda_{\text{med}}$  represents the incident field wavelength in the nanoparticle surrounding medium), the optical properties follow the Mie theory. Indeed, the optical behaviour of spherical gold nanoparticles ( $\text{nAu}$ )  $> 80 \text{ nm}$  has been shown to deviate from the simple scaling laws (Figure 2.4).<sup>[24]</sup> Increasing the

nanoparticle volume enhances the radiative coupling (due to Mie scattering), thereby increase the scattering quantum yield. In addition, the electromagnetic wave retardation in larger nanoparticles also results in increased dipolar LSPR wavelength and the appearance of quadrupoles & higher-order multipole mode resonance on shorter wavelength.<sup>[24]</sup> While the period of dipole oscillation increases to accommodate the increased phase delay in the excited plasmon, the multipole mode resonances produce more nodes in polarization charges distribution induced on particle surface with shorter effective interaction distance. These eventually broaden the scattering spectra.<sup>[18]</sup>

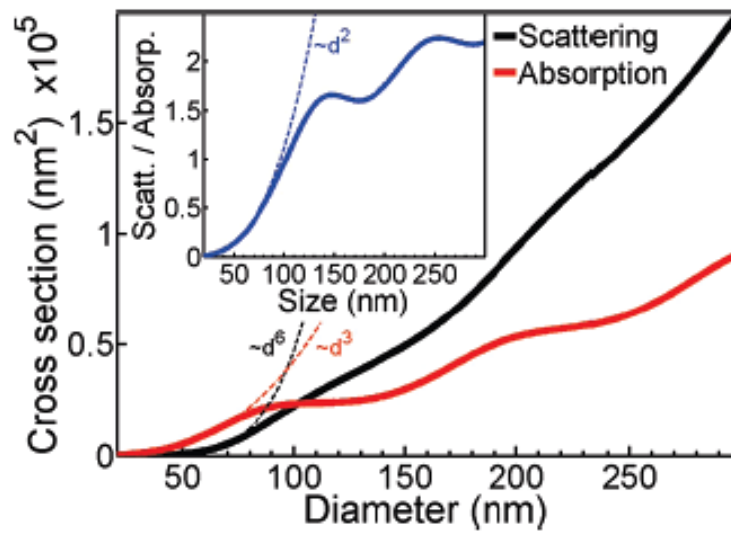


Figure 2.4: Mie theory prediction for scattering (black) and absorption (red) cross-sections as functions of nAu size at wavelength of 532 nm and medium refractive index of 1.25. Inset: Ratio of scattering and absorption cross-sections as a function of nanoparticle size. The dashed lines show how simplified power dependences are only accurate for nanoparticle sizes below 80 nm<sup>[24]</sup>

For particle smaller than about 10 nm, however, description of metal through bulk permittivity  $\epsilon_m$  fails dramatically as the particle size now reduces to similar or less than the mean free path of conduction electron. This additional surface damping or electron-surface scattering is the non-locality prevailing in small particles that broadens the LSPR spectra significantly.<sup>[25-27]</sup>



Scattered light flux from a single 60 nm spherical gold nanoparticle (nAu) has been estimated to be equivalent to the fluorescence light flux from approximately  $3 \times 10^5$  co-localized, individual fluorescein molecules.<sup>[18,28-30]</sup> In addition, the light scattered from gold or silver nanoparticles lies within the visible portion of the electromagnetic spectrum in accordance to their respective plasmon bands. Therefore, although they have dimensions smaller than the diffraction limit of light, the outstanding light scattering characteristic of individual gold & silver nanoparticles is still strong enough to allow the direct imaging of individual nanoparticle under dark field microscopy (DFM) setup (Section 2.3, *vide infra*).

At optical frequencies (*circa* 380 nm - 750 nm), the properties of small metal nanoparticles are predominantly influenced by the electric field, whereas magnetic contribution to scattering only produce (broad) resonances for particle sizes close to the incident wavelength.<sup>[22]</sup>

### 2.1.1.3 Shape

The LSPR of metal nanoparticles are controlled by their intrinsic shapes.<sup>[1,19,23]</sup>

Metal nanorods support two types of plasmon oscillations, i.e. a transverse mode excited relative to the rod width, and a longitudinal mode excited along the rod length. Due to its origin, longitudinal mode shows greater tunability than the transverse mode. Hence, metal nanorods can be aptly defined by two important parameters, effective radius ( $r_{\text{eff}} = (3V/4\pi)^{1/3}$ , where  $V$  is the total rod volume), and aspect ratio ( $R = \text{long-axis magnitude} / \text{short-axis magnitude}$ ). Gold nanorods (AuNR) show significantly greater optical cross-sections than the spherical gold nanoparticles at comparable effective radius.<sup>[1]</sup> Increasing either the effective radius or the aspect ratio red shifts the longitudinal LSPR, because the restoring force due to charge separation weakens when the charge is separated over longer distances.<sup>[31]</sup> This, in turn, enhances the local field. For gold, the Fermi energy level is 1.8 eV. The longitudinal

resonance energy which is less than the Fermi level suppresses interband damping (and therefore suppresses non-radiative decay), which results in drastic reduction in the plasmon dephasing rate.<sup>[32]</sup> High scattering contribution to total extinction can be achieved by increasing the aspect ratio of nanorods at fixed  $r_{\text{eff}}$  (which suppress the interband damping and thus reduce the non-radiative decay)<sup>[32]</sup> or by increasing the  $r_{\text{eff}}$  at fixed  $R$  (which increase the radiative decay).<sup>[1]</sup>

Core-shell silica-gold spherical nanoparticles show interesting optical properties that can be manipulated easily compared to solid gold nanoparticles.<sup>[1,33]</sup> The nanoshell plasmon resonance is the result of interaction between the plasmon supported by the metallic outer layer and the metallic inner cavity, and the strength of this interaction is sensitive to the metal shell thickness.<sup>[34]</sup> The shell thickness smaller than the mean free path of electron determines the amount of electron surface scattering.<sup>[33]</sup> Nevertheless, gold nanoshell with shell thickness smaller than the mean free path of electron can still exhibits multipolar resonances when the total outer diameter is large enough.<sup>[1]</sup> Depending on their ratios of core-to-shell radii, these nanostructures depict optical cross-sections comparable to or higher than solid nAu. Their plasmons can be tuned towards the longer wavelength region either by increasing the core-to-shell ratio at fixed total size, or by increasing the total nanoshell size at fixed ratio. However, higher core-to-shell ratio reduces the scattering contribution to total extinction, whereas larger total nanoshell size increases the scattering-to-absorption ratio.<sup>[1]</sup>

Nanoparticles with sharp edges/tips experience red shift in the plasmon resonance, as in nanopentagons,<sup>[35]</sup> nanotriangles,<sup>[35]</sup> nanocubes,<sup>[36]</sup> nanooctahedron,<sup>[36]</sup> nanostars,<sup>[37]</sup> and nanocrescents.<sup>[12]</sup> This is true even when the gold nanoparticles are described by the similar plasmon length (the length over which the plasmon oscillations take place), in which nanoparticles of more isotropic shapes showed modest blue shift in the dipolar plasmon frequency, i.e. truncated bitetrahedra < cubes < decahedra < icosahedra < octahedra.<sup>[38]</sup>

Multiple core-shell nanostructures, such as concentric ring/disk cavity (CRDC)<sup>[39]</sup> and nonconcentric ring/disk cavity (NCRDC)<sup>[39-40]</sup> have been built to tune the optically active plasmon resonances for showing Fano resonance and providing greater LSPR sensitivity.

The plethora of extinction spectra and dark field images of gold nanoparticles shows that 23 nm nAu (Figure 2.5a & 2.6a,  $\lambda_{\text{max}} = 522$  nm) scattered green light; upon size-increment to 70 nm, the scattered light turned yellow (Figure 2.5b & 2.6b,  $\lambda_{\text{max}} = 539$  nm). Hexagonal and cubic gold nanoparticles scattered bright yellow and orange-red respectively (Figure 2.5c-d & 2.6c-d, both  $\lambda_{\text{max}} = 540$  nm). While AuNR with length 62 nm & width 14 nm & aspect ratio 4.4 have pale-green scattering (Figure 2.5e & 2.6e, transverse and longitudinal  $\lambda_{\text{max}} = 520$  nm & 800 nm), those with length 372 nm & width 23 nm & aspect ratio 16 appeared dark-yellow (Figure 2.5f & 2.6f, transverse and longitudinal  $\lambda_{\text{max}} = 520$  nm & >1200 nm).<sup>[41]</sup>

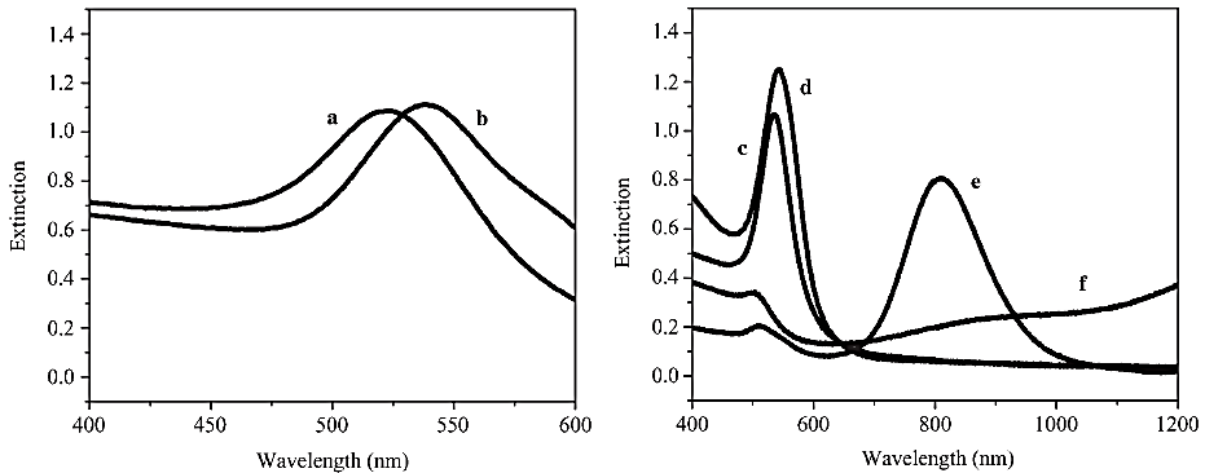


Figure 2.5: Extinction spectra of colloidal gold nanoparticles: (a) 23 nm spheres, (b) 70 nm spheres, (c) hexagons, (d) cubes, (e) rods ( $R = 4.4$ ) and (f) rods ( $R = 16$ )<sup>[41]</sup>

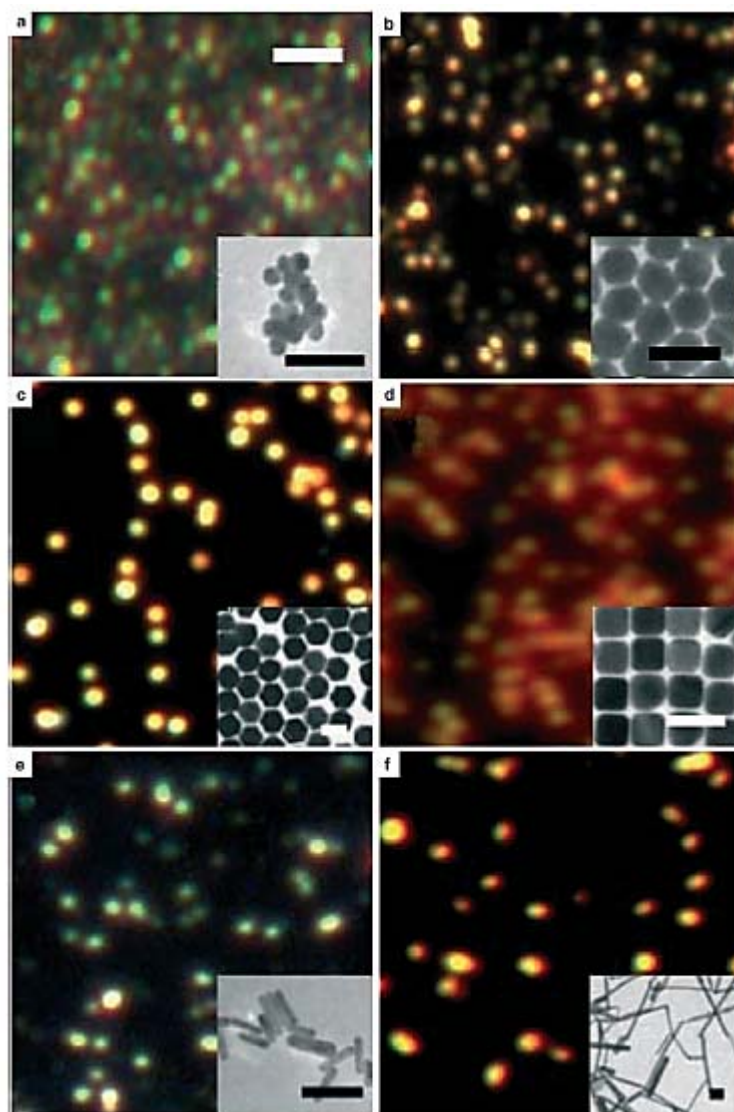


Figure 2.6: Dark-field light scattering images from gold nanoparticles and (inset) corresponding TEM images: (a) 23 nm spheres, (b) 70 nm spheres, (c) hexagons, (d) cubes, (e) rods ( $R = 4.4$ ) and (f) rods ( $R = 16$ ). Scale bars represent 2 mm in light scattering images and 100 nm in TEM images<sup>[41]</sup>

#### 2.1.1.4 Effect of the surrounding environment

Apart from its own size, shape, and dielectric properties, the resonance condition of a metallic nanoparticle (Eq. 5) also depends on the dielectric properties of its local environment ( $\epsilon_{\text{med}}$ ) including the influence from solvent, adsorbing molecules, and substrate.<sup>[23,42]</sup> The scattering spectrum of a nanoparticle in response to its surrounding medium has been studied by immersing the nanoparticle in solvent of various refractive indices ( $n_{\text{med}}$ )<sup>[43-44]</sup> as well as

electrodynamic simulation of the nanoparticle scattering spectra.<sup>[45]</sup> The sensitivity to changes in  $n_{\text{med}}$  is governed by the slope of real component of dielectric function for the constituent metal ( $\epsilon_{\text{real}}$ ) in the observed wavelength range.<sup>[12,46]</sup> As the slope of  $\epsilon_{\text{real}}$  vs. wavelength (Figure 2.1) for silver is just slightly steeper than that for gold, the magnitudes of their LSPR peak shifts at different  $n_{\text{med}}$  are almost the same. Consequently, the silver and gold composition effect on refractive index sensitivity is negligible.<sup>[19]</sup> Regardless of size and shape, the resonance peak shifts to longer wavelength with respect to an increase in refractive index of the surrounding medium due to a delayed plasmon oscillation.<sup>[43-44]</sup> Bigger particles or particles with larger effective radius exhibit greater sensitivity to  $n_{\text{med}}$  change.<sup>[19,45]</sup> Deviation from geometrical uniformity often associates with greater  $n_{\text{med}}$  sensitivity.<sup>[46-47]</sup> In this regard, nanoparticle with the highest aspect ratio, i.e. longer rods displayed the greatest sensitivity to changes in the  $n_{\text{med}}$ , consistent with the Mie theory.<sup>[16]</sup>

Besides, the adsorbing molecules can alter the plasmon resonance of their adsorbent nanoparticles. For example, alkanethiol monolayer self-assembled on a silver nanotriangle depicted linear correlation between the LSPR  $\lambda_{\text{max}}$  shift and the alkyl chain length for each addition of methylene unit.<sup>[43]</sup>

Charge transfer across the metal-solid interface has an indispensable effect in the metal nanoparticle plasmon resonance. For example, silver nanoparticles deposited on SiO<sub>2</sub>-glass substrate exhibited widen and red-shifted LSPR compared to a freestanding nanoparticle in vacuum. Likewise, silver nanoparticles embedded in SiO<sub>2</sub> matrix showed even greater extent of broadened and red-shifted peaks.<sup>[48]</sup> The qualitative mechanism underlying the observed phenomena was proposed as follows: Upon collision with the metal-substrate interface, the excited electrons are transferred temporarily to the substrate medium. The touching/embedding matrix functions as efficient heat bath that dissipates the momentum and energy of the transferred electrons. Thus, the back-transferred electrons suffer from

lagging of plasmon phase coherence. This translates into inelastic scattering of the electrons and broadening of the plasmon peaks, *a.k.a.* chemical interface damping (CID) effect. This effect is universal for all sizes and shapes, e.g. for gold prisms and decahedra dispersed on the glass surface embedded in a polymer matrix, the near-field sensitivity is reduced pronouncedly from that observed in a non-embedded nanoparticles.<sup>[49]</sup>

Importantly, AuNR deposited on 2 nm ultrathin titanium layer on glass demonstrated drastic LSPR amplitude reduction with pronounced red shift. This is attributed to the dissipative  $\epsilon_{im}$  of titanium and the CID effect (conduction electrons transfer across Au-Ti interface) that decrease significantly both the plasmon dephasing time as well as the plasmon scattering amplitude.<sup>[50]</sup> nAu deposited on polarisable/conductive substrates (e.g. silicon wafer, thin gold film) showed plasmon red-shift and doughnut-shaped scattering patterns, again emphasizing the near-field effect arising from the substrate.<sup>[6,51]</sup>

### **2.1.2 Plasmon coupling between two noble metal nanoparticles**

The potential in utilizing the near-field interaction between metal nanoparticles as optical waveguides,<sup>[52]</sup> biosensors,<sup>[53]</sup> molecular rulers,<sup>[54]</sup> and in surface-enhanced Raman scattering (SERS),<sup>[55-56]</sup> plasmonic circuit elements,<sup>[57]</sup> and building blocks for metamaterials<sup>[58]</sup> has spur growing interest and numerous investigations on 1-dimensional and 2-dimensional nanoparticles chain arrays,<sup>[59]</sup> and nanoparticle aggregates etc. While the most basic coupled nanostructure, *viz.* dimeric nanoparticles, may not be the optimal configuration for electromagnetic field enhancements, they serve as a simple prototypical model for the deeper understanding of the important physical factors underlying the electromagnetic field enhancements.

When two identical spherical gold nanoparticles (nAu) are in close proximity, their surface plasmons interfere, in which the three dipolar modes of each particle hybridize in the

dimer to form 4 plasmon orbitals<sup>[60]</sup> (Figure 2.7). Two of the plasmon orbitals have dipole moments oriented parallel to the dimer long axis. Among them, the symmetric bonding mode has the lowest resonance frequency/energy owing to the weakened dipole in each particle,<sup>[61]</sup> which gives a net dipole moment and couples best to the external light, whereas the dipoles of asymmetric anti-bonding mode cancel out each other. The other two plasmon orbitals have dipoles oriented perpendicular to the dimer long axis, with the symmetric anti-bonding mode and the asymmetric bonding mode having net and zero dipole moments respectively.<sup>[22,60]</sup> For homodimer, only the coupled modes with net dipoles interact with incident light (bright plasmon), while those having zero do not (dark plasmon). The far-field optical properties of the dimeric structure are thus governed dominantly by the symmetric bonding mode, which in turn, is dependent on the particle size, interparticle separation, and polarization with respect to the dimer axis. The bigger the size of the interacting nanoparticles and the smaller the separation distance, the more prominent is the coupling effect. In brief, the near-field interaction between the nanoparticles modulates the frequency of the coupled-nanoparticle LSPR to be viewable using far-field optics. This effect can be observed readily under the simple dark field microscopy (DFM, Section 2.3, *vide infra*). The near-field interaction leads to red-shifting of both the particle scattering spectrum, and sometimes, colorimetric changes in the scattered light if the red-shift is significant enough. The scattering cross-section also increases because of the increased scattering intensities.<sup>[13,31,37]</sup>

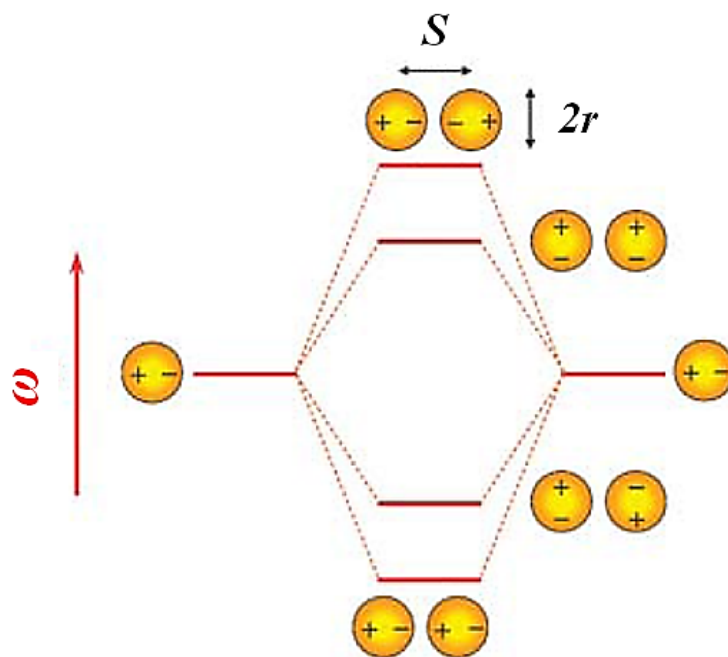


Figure 2.7: Qualitative energy level diagram for plasmon hybridization in two interacting nAu of similar radius  $r$ .  $S$  = interparticle centre-to-centre separation distance. The dipole plasmons of the individual particles are 3-fold degenerate (i.e., the surface plasmon frequency is independent of polarization along  $x$ ,  $y$ , and  $z$  axes) <sup>[22]</sup>

A number of studies on the coupling effect of discrete pairs of plasmon resonant nanoparticles have been reported recently. Yim et al.<sup>[62]</sup> used organic-aqueous interface methodology & later thiol ligand-exchange reaction to produce 60 nm nAu dimers with a gap of 2 nm and achieved 24% yield. Spectrum of single nAu monomer contained one plasmon resonance peak at 540 nm, while spectrum of single nAu dimer contained two plasmon resonance peaks. Red-shifted peak at 680 nm is due to the hybridized LSPR mode parallel to the longitudinal direction of the dimer axis, whereas shorter wavelength peak at 540 nm corresponds to hybridized LSPR mode perpendicular to the longitudinal direction of the dimer axis (corresponds to symmetric bonding and symmetric anti-bonding modes in Figure 7 respectively). All the single dimers have much stronger dark field scattering intensity than that seen from single monomers, at both 540 and 680 nm. This phenomenon is not surprising,



considering that the gap between two nAu is so small, meaning that the degree of LSPR coupling can be very significant and even remarkable at the transverse mode.

Reinhard et al.<sup>[54]</sup> used pairs of 42 nm nAu and pairs of 87 nm nAu to measure the interparticle distance based on the strength of their respective plasmon coupling. Their experimental measurements agreed very well with the simulated data (T-matrix method) for 42 nm nAu dimers, taking into account the average effect of wave vectors and light polarization in actual experimental geometry. 42 nm nAu dimer is more suitable for distance measurement, whereas the use of larger nAu (i.e. 87 nm) is more practical for polarization sensitive applications where it can be used to determine the relative orientation of a plasmon ruler with respect to the polarization of the illumination light (via the relative height and position of the two plasmon peaks). However, as the accuracy is a matter for concern, their results are limited by the nanoparticle size and shape heterogeneity, as well as the multiple tether formation. Apart from this, Reinhard et al.<sup>[63]</sup> also exploited pairs of 40 nm nAu as plasmon rulers based on the dependence of their light scattering on interparticle distance. They substantiated that plasmon rulers enabled the measurement of dynamical biophysical processes by applying the ruler to a DNA cleavage system using restriction enzyme EcoRV.

Seeing that there is a correlation between the red-shifted resonance spectrum with the interparticle separation, Reinhard's group<sup>[64]</sup> ventured further to resolve the simultaneous distance and orientation change by compacting the DNA linked dimeric nAu with a fourth generation polyamidoamine (PAMAM) dendrimer. They used polarization anisotropy to measure the change in the interparticle separation in the bathing medium, rather than the conventional scattering intensity alone, since polarization anisotropy is less susceptible to any changes in the medium refractive index. This work was particularly useful whenever the particles in question reside in a solution.

Tamaru et al.<sup>[65]</sup> used finite-difference-time-domain (FDTD) calculations to compare with the experimental light scattering of individual spherical silver nanoparticle (nAg, 100 nm diameter) pairs, spaced 1.1 nm in between them. There was good qualitative agreement between the simulated and experimental data, provided particle shape anisotropy and substrate effect were well accounted for.

Su et al.<sup>[66]</sup> used electron-beam-lithography (EBL) technique to place 2 gold elliptical disks on an indium-tin-oxide (ITO) substrate and studied the short axis plasmon coupling of the particles. The red-shifted peak decayed rapidly with increasing particle spacing, reaching zero when the particle spacing exceeded certain distances, reflecting the diminishing near-field plasmon coupling. The experimental and simulated Discrete Dipole Approximation (DDA) results had good correspondence with each other. They found that this exponential decay was universal for particular shape when the peak shift and particle gap were scaled appropriately, though different geometrical nanoparticles resulted in different decay length.

Rechberger et al.<sup>[61]</sup> used DDA theoretical estimation to investigate the optical properties for EBL-fabricated pairs of spherical gold nanodisks. Increasing the gap distance between the nanodisk pairs gave red-shifted peak for incident electric field parallel to the dimer long axis whereas a blue shift was observed for incident electric field orthogonal to the dimer long axis.

Gunnarsson et al.,<sup>[67]</sup> however, delved into greater details about the applicability of DDA compared to Coupled Dipole Approximation (CDA). Experimental measurement showed that strong red-shifted peaks took place at separation gap  $\approx$  nanodisk diameter, which was in good quantitative agreement with the previous findings.<sup>[61,66]</sup> It was found that the experimental scattering spectra of single silver nanodisk and silver nanodisk pairs separated by more than one particle radius could be well described by CDA, where the particles were approximated as point dipoles using modified dipole polarizability for oblate spheroids. For

smaller particle separations ( $\frac{\text{separation gap}}{\text{nanodisk diameter}} < 0.25$ ), the simple dipole model severely underestimated the particle near-field interaction. DDA, which is a finite-element method, described the experimental results well even at  $\frac{\text{separation gap}}{\text{nanodisk diameter}} < 0.25$ , including particles that had metallic bridges. They also verified the universal exponential decay for the red-shifted longitudinal LSPR in the silver nanodisk system.

All the studies above indicated that there is a continuous and exponential red shift in the LSPR as the interparticle distance between 2 nanoparticles in a dimer is decreased, especially when the incident light is polarized parallel to the dimer long axis. In addition, by using linear parallel and orthogonal excitation, polarization mapping could help to identify the unknown orientation of a particle pair.<sup>[68]</sup> Schmeits et al.<sup>[69]</sup> also reported that the surface plasmon modes of interacting spherical particles were function of the particle radii, the separation distance, and the dielectric constant of the surrounding medium.

Instead of using the scattered light to measure the coupling in gold nanodisks, Atay et al.<sup>[70]</sup> used a transmitted light measurement and successfully showed the strong dipole-dipole interaction between the particle pairs which was on dielectric separation, i.e. air. The work by Prikulis et al.<sup>[71]</sup> was a perfect exemplary demonstration of the LSPR colour change of individual spherical silver nanoparticles (nAg) pair with respect to individual nAg, when they were paired using an optical laser as trapping tweezers.

All the aforementioned investigations showed that the plasmonic coupling between two noble metal nanoparticles can be used as reliable molecular rulers as well as indicators for biomolecular interaction event. This kind of plasmonic readout has higher time resolution, longer lifetime and longer detection distance than dye-based Förster Resonance Energy Transfer (FRET) techniques.<sup>[72-74]</sup> Exploiting the unique optical plasmonic properties of noble metal nanoparticles, they can be applied as optical nanoprobe and plasmonic nano-rulers for

quantitative analysis of the dynamic and kinetic parameters of biomolecule detection processes with resolution down to nanometer scale, or even single molecular level.

## **2.2 Synthesis of noble metal nanoparticles**

Noble metal nanoparticles have been fabricated by a wide variety of protocols, which are essentially belonging to two classes: physical (top-down) method and chemical (bottom-up) method.

To date, several top-down approaches have been used to fabricate nanostructures.<sup>[31]</sup> Electron-beam-lithography (EBL) produces nanostructures of varied shapes with flat surfaces. Focused-ion-beam (FIB) etching is normally applied to create nano-size holes in metal films due to its slower rate. Nanosphere lithography (NSL) only fabricates triangular nanoprism array via the metal vapor deposition through the gaps of nanospheres monolayer.<sup>[42]</sup> Soft Interference Lithography is able to fabricate metal nanoparticles in much greater quantity (areas:  $1\ \mu\text{m}^2$  -  $10\ \text{cm}^2$ ) than EBL and FIB. Solvated Metal Atom Dispersion (SMAD) is suitable in industry for the preparation of large amount of colloidal metal nanoparticle solution with reproducible quality in the desired solvents. A top-down approach, SMAD vaporizes the bulk metal in vacuum and co-deposits the metal atoms with solvent vapours. The nanoparticles are later stabilized both sterically (via solvation) and electrostatically (via incorporation of negative charge).<sup>[75]</sup> A good advantage of SMAD is that the final product only contains pure colloidal metal nanoparticle without the presence of by-products as in the metal salt reduction methods. However, it is difficult to produce features with dimensions below 5 nm - 10 nm using EBL or FIB techniques. In addition, the metal evaporation results in nanoparticles that possess multiple crystal domains<sup>[76]</sup> with uncontrolled size and orientation, which is critical in catalysis as well as plasmonics, because electron scattering at grain boundaries attenuates the surface plasmon.

The shortcomings of the physical approach can largely be overcome by using the chemical approach, which involves the reduction of metal salt ion by reducing agent, and then capped the formed nanoparticles by a suitable surfactant/capping agent for stabilization in solution. Among the appeals of bottom-up method are excellent control over size, shape, composition, surface chemistry and the crystalline structure of the prepared nanoparticles owing to the wide range of synthesis parameters that can be tuned easily.<sup>[77]</sup> Furthermore, chemical synthesis does not require costly experimental equipment and chemicals. Most importantly, the production of nanoparticles in dispersed colloidal solution format allows facile downstream processing of the nanoparticles in many applications. Turkevitch introduced a simple synthesis of colloidal gold in 1951.<sup>[78]</sup> To date, the common wet-chemical reductions include sol process, micelle-assisted synthesis, sol-gel process, hydrothermal synthesis, pyrolysis, and chemical precipitation.<sup>[3]</sup> Depending on the further development involved, each method has its own advantages over the other and vice versa.<sup>[79]</sup>

### **2.3 Principles of dark field microscopy (DFM)**

Zsigmondy first reported the use of a dark-field immersion microscope to see colloidal gold,<sup>[80]</sup> and this technique has received wide applications in biological and material sciences.<sup>[16,28,44,81-83]</sup>

Dark field microscopy creates contrast between the object and the surrounding field of view. As the name implies, the background is dark and the object (here, nanoparticle) is bright. In principle, a white light beam is guided through a high numerical aperture ( $NA = n \sin \theta$ , where  $n$  &  $\theta$  represent the medium refractive index and angular aperture respectively, Figure 2.8) dark field condenser to illuminate the metal nanoparticles deposited on glass substrate. The condenser lens, fitted with a circular opaque blocker at the light path, produces a hollow cone of light at an extremely oblique angle to the sample. The objective lens, with

an NA smaller than that of condenser, prevents directly transmitted light from entering it. Therefore, only the light that is scattered by the sample can enter the objective lens, forming the 'dark field' configuration. The scattered light collected from dark field microscope is then sent to a CCD camera and spectrometer, of which Rayleigh scattering imaging and spectral analysis can be readily studied.<sup>[16,28,81]</sup>

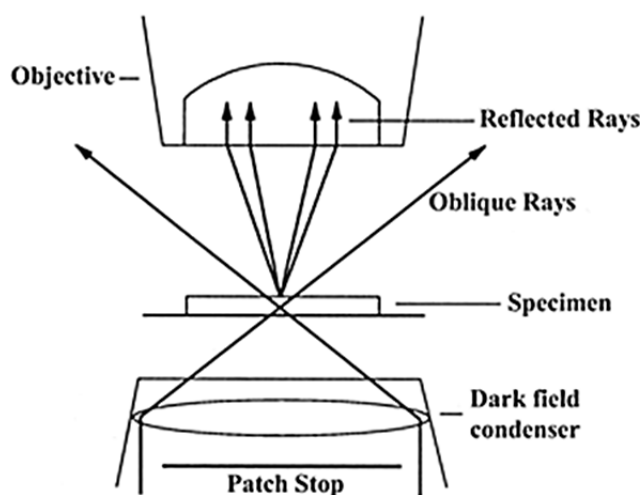


Figure 2.8: Working principles of dark field microscopy showing the light path (John Innes Centre, <http://www.jic.ac.uk>)

## 2.4 Nucleic acids

Nucleic acids are molecules storing and coding the genetic information in all known living organisms and some viruses. They resemble the blueprints that are used to construct cellular components and to mediate various biological metabolisms.

The monomers of nucleic acids are nucleotides.<sup>[84-85]</sup> A nucleotide consists of a nitrogenous nucleobase and a phosphate group tethered to a pentose through the sugar 1st- and 5th-carbon (Figure 2.9). Nucleoside refers to a nucleobase attached to the pentose sugar without the phosphate group. The four bases in the nucleic acid, namely adenine (A), thymine (T), guanine (G), and cytosine (C), can be classified into two groups - purines and

pyrimidines. While purine bases (A, G) are fused five- and six-heterocyclic rings, pyrimidine bases (T, C) are mono six-heterocyclic rings. The sugar can be 2-deoxyribose or ribose, and the resulting nucleic acids are termed deoxyribonucleic acid (DNA) and ribonucleic acid (RNA), respectively.<sup>[86]</sup> Uracil (U) is a pyrimidine base that resembles thymine chemical structure without a methyl group and it replaces the position of thymine in RNA.

A nucleic acid can be visualized as a linear polymer (polynucleotide) joining the nucleotides in series by phosphodiester bonds, forming the alternate sugar-phosphate backbone with the free nucleobases protruding in one direction. The asymmetric phosphodiester bonding (between 3rd- and 5th-carbons of two nucleotides) dictates the direction for a nucleic acid, wherein the end with a terminal phosphate on the 5th-carbon of the pentose is defined as 5', and the end with a terminal hydroxyl on the 3rd-carbon of the pentose is defined as 3' (Figure 2.9). An intriguing property of DNA molecules is their existence as either single-stranded DNA (ssDNA) or double-stranded DNA (dsDNA). The process of forming dsDNA is named DNA hybridization, in which two ssDNA strands in anti-parallel direction couple to each other through hydrogen bonding between the protruding oxygen- and nitrogen-rich bases. Due to the chemical structures and the dsDNA conformation, purine pairs with pyrimidine, i.e. A with T and G with C, via two and three hydrogen bonds respectively (Watson-Crick rules, Figure 2.9).<sup>[87]</sup> The hydrogen bonding ensures the reversibility of DNA hybridization: above the melting temperature or at low salt concentration, dsDNA separates into two ssDNA (denaturation) whereas ssDNA recombine at temperature below the melting point or at high salt concentration (renaturation/hybridization) on regions of sequence complementarities.<sup>[88]</sup> Generally, dsDNA with longer sequence and higher percentage of GC base-pair (bp) is more stable. In essence, dsDNA is stabilized by non-covalent interactions e.g. hydrogen bonding between nucleotides, and van der Waals base stacking between heterocyclic nucleobases.<sup>[89]</sup> Apart from Watson-

Crick base-pairings, nucleic acids can also exist in triple helical form and as G-quadruplex in telomeres.<sup>[90]</sup> For the former, an ssDNA bind to the purine bases of B-DNA in major grooves via Hoogsteen or reversed Hoogsteen hydrogen bonds;<sup>[91]</sup> for the later, a guanine-rich ssDNA binds in tetrad and is stabilized by a central potassium ion.<sup>[92]</sup>

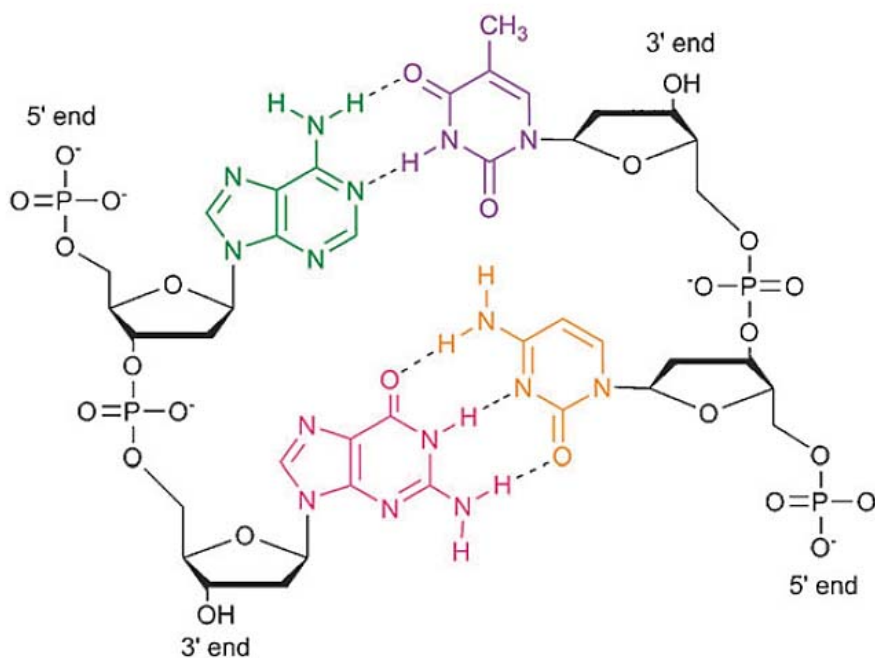


Figure 2.9: Basic principles of DNA self-assembly in anti-parallel direction (5' to 3' coupled with 3' to 5'). The Watson-Crick base-pairing rules mean that adenine (A, green) pairs with thymine (T, purple) and guanine (G, pink) pairs with cytosine (C, orange)<sup>[93]</sup>

Three major forms of dsDNA exist: B-DNA, A-DNA, and Z-DNA.<sup>[94]</sup> Biologically, right-handed spiral B-DNA is the most common as it is the favoured conformation in aqueous system. The width of such a double helical DNA is 2.2 nm - 2.6 nm, the length of one nucleotide base-pair is 0.33 nm, and a full helical turn contains 10 bp (Figure 2.10).<sup>[87,95]</sup> The DNA strands curling around each other expose gaps between the sugar-phosphate backbones, forming two alternate grooves: deep wide major grooves (2.2 nm wide), and shallow narrow minor grooves (1.2 nm wide). The major grooves are particularly useful for proteins like



transcription factors as they can bind to the side of specific base-sequences revealed by the grooves in order to regulate biological mechanisms.<sup>[96]</sup> A-DNA is a right-handed helix (wider than B-DNA) that present in dehydrating conditions, in hybrids of DNA-RNA pairs and in DNA-enzyme complexes. In contrast, Z-DNA is a left-handed helix observed in conditions of high salt concentrations.

For dsDNA shorter than its persistence length (50nm, *circa* 150bp),<sup>[97]</sup> it is rigid while dsDNA longer than this is very flexible, and this ensures the thin long dsDNA can be packed into the compact chromosomes in living cells. Supercoiling of dsDNA has been observed in the nucleus of eukaryote cells, as in transcriptions<sup>[98-101]</sup> and during the initiation of replication process.<sup>[98-100]</sup> On the other hand, ssDNA is even more flexible as its persistence length is short (1 nm, *circa* 1-3 bases).

The DNA is crucial to lives as some base sequences encode the myriad of proteins essential for living organisms (coding DNA), while some sequences regulate the various gene expression levels by serving as binding sites for initiators, enhancers, repressors or insulators (non-coding DNA). DNA segments that carry genetic information of peptide-coding are termed genes, and to function, these genes are copied into RNA by transcription process. Because of the base-pair complementarities and reversibility, all the sequences of dsDNA helices are duplicated during DNA replication (cell division) and RNA transcription (peptide coding).<sup>[102]</sup>

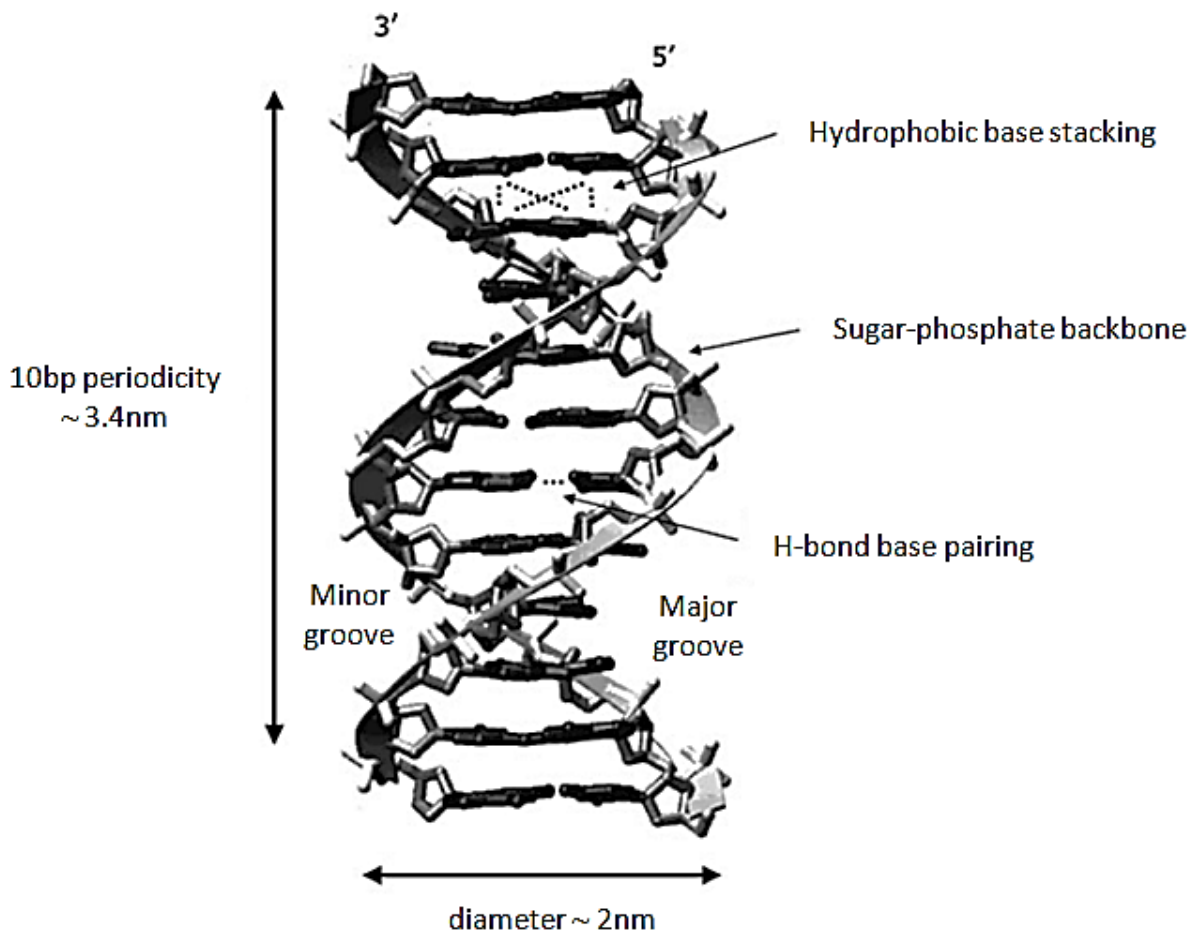


Figure 2.10: The double helix structure of DNA in its B-form, with its relevant dimensions and the main interactions. Adapted and modified <sup>[103]</sup>

Although the genetic information is preserved by the unique chemical nature of DNA, it has been known that DNA suffers from genetic disorders that can impede the growth or introduce abnormalities to the organisms. Various DNA deformities have been identified, such as point mutation, insertion, or deletion in a gene, gene(s) deletion, chromosomal aberrations and trinucleotides repeat disorders. Various sources are known to cause irreversible damage to DNA, for example prolonged UV exposure, x-rays and gamma-rays, intercalating agents (usually aromatic compounds), free radicals etc.<sup>[104]</sup> The physical and chemical agents capable of damaging the DNA are categorized as mutagens, and some of them are carcinogenic, causing anomalous (and often detrimental) tissue growth.<sup>[105]</sup>

## 2.5 Application of LSPR in nucleic acid sensing

In biological sensing, gold and silver nanoparticles have emerged as a robust class of labels as these engineered nanoparticles offer good interface and distinct advantages than other labels to probe for biosystems. Firstly, the plasmon peaks are highly tunable by synthesis. Secondly, the extinctions of gold and silver nanoparticles are exceptionally strong and the light scattered by individual particles are viewable using proper illumination setup such as resonant Rayleigh scattering spectroscopy (Section 2.3). Thirdly, these noble metal nanoparticles do not suffer from photo bleaching and blinking (unlike organic fluorescent dyes<sup>[106]</sup> and semiconductor nanocrystals<sup>[107]</sup>), allowing the observation of biological event over arbitrarily long time intervals. Fourthly, the nanoparticles concentrate incident electromagnetic waves and facilitate efficient light transfer to proximal biomolecules. Finally, the colloidal nanoparticles can be made stable in aqueous solutions that contain many biomolecules of interest.

Gold and silver nanoparticles can be attached readily with biomolecules, such as proteins, antibodies, nucleic acids, and other tracer substances, yet still preserve their optical properties.<sup>[18,108-109]</sup> The successful preparation of stable and benign nanoparticle-bioconjugates has led to their extensive applications in biological detection. In this regard, the nanoparticles can act as transducer and the subsequent biomolecule interaction triggers a measurable optical signal, which can be monitored using LSPR-sensitive devices such as UV-visible extinction spectroscopy,<sup>[110-113]</sup> resonant Rayleigh scattering spectroscopy,<sup>[29,83,114-118]</sup> or even with the unaided eyes.<sup>[112,119-120]</sup> Alternatively, the nanoparticles can behave as light source/sink to modulate energy transfer to/from adjacent biomolecules.<sup>[121-123]</sup>

There are three common sensing platforms utilizing the LSPR of noble metal nanoparticles, namely colloidal homogeneous sensing, surface-confined heterogeneous array sensing, and surface-confined heterogeneous single nanoparticle sensing.<sup>[124]</sup> Each platform

has its own advantages over the others. For example, colloidal methods are fast and simple, whereas single plasmon biosensors enhance the limit of detection (LOD) and enable the study of biological process at molecular level. Nucleic acid sensing is practically important in pathology, genetics, clinical diagnosis, the food & drug industry, and environmental monitoring. The following paragraphs highlight some common applications of the localized surface plasmon resonance (LSPR) of metallic nanoparticles in nucleic acid sensing.

In the mid-1990s, Mirkin and co-workers<sup>[125]</sup> used a strong gold-thiol chemistry to functionalize the surface of spherical gold nanoparticle (nAu) with thiol-capped short ssDNA. When added with dsDNA bearing complementary sticky ends, two batches of such nAu-DNA with non-complementary sequences were self-assembled reversibly into macroscopic aggregates (Figure 2.11a). The hybridization that brought the nanoparticles into close position reduced the concerted plasmon energy, and induced vivid colour change (Figure 2.11b) from red (for finely dispersed nAu in solution) to blue (for aggregates). Due to multiple DNA bridges, the 3-dimensional cross-linked nAu-DNA melted/dehybridized cooperatively with increasing temperature and displayed narrow melting transitions (based on nAu extinction) compared to free DNA (based on DNA absorption).<sup>[126-127]</sup> The work soon invoked numerous applications of DNA tethered gold and silver nanoparticles in nucleic acid sensing<sup>[128-132]</sup> as well as 3-dimensional DNA-guided hierarchical assembly of the nanoparticles.<sup>[133-135]</sup>

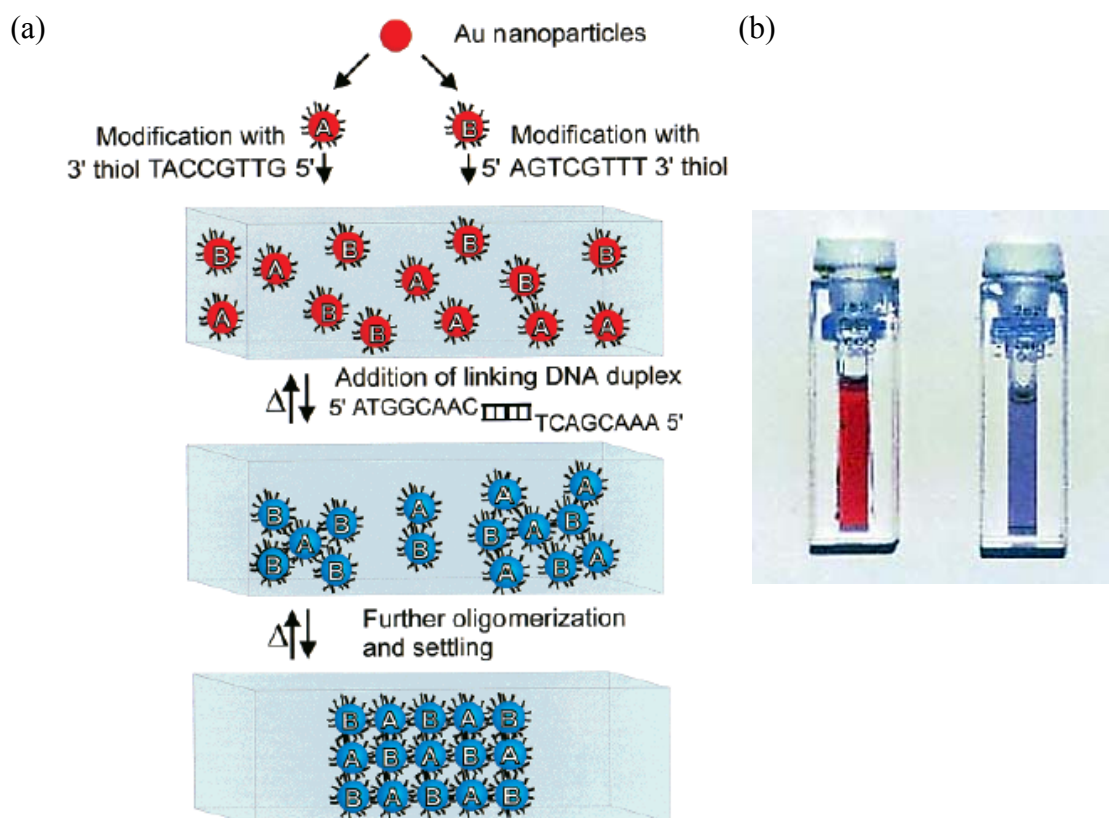


Figure 2.11: (a) ssDNA-modified colloidal AuNS assembled into aggregated structure upon the addition of complementary linker DNA. The assembly took place gradually, forming oligomers of AuNS initially and later massive aggregates. The assembled nanoparticles could be reversibly annealed by applying external heating.  $\Delta$  represents heating above the dissociation temperature of the duplex; (b) The observed colour change from red (monodisperse particles) to purple (aggregated particles) <sup>[125]</sup>

Change in the dispersion state of DNA-modified colloidal nanoparticles was sensitive to discriminate perfectly match DNA from the single-mismatch variants e.g. middle or end mismatches, deletion, and insertion.<sup>[126,136]</sup> To provide better single-base mismatch (SBM) distinction in detecting polymerase chain reaction (PCR) amplified genomic DNA, nAu-DNA probes were designed so that the ends of both the probes ssDNA flanked the mutation site of K-ras oncogene which is of significant value for colorectal cancer diagnosis.<sup>[110]</sup> Subsequent ligation proceeded for complementary target while no ligation occurred for the mismatch ones. Thermal treatment later reverted the assembled aggregates (purple) of single-mismatch samples to well dispersed state (red) while the ligated sample remained purplish.

Instead of ligase, another work adjusted nAu-DNA dispersion by nicking endonuclease (NEase) which recognizes specific dsDNA but cleaves only one ssDNA.<sup>[119]</sup> Target ssDNA was designed to operate solely as substrate to cleave multiple complementary ssDNA linkers which acted as amplifiers. At the end of scission cycles, uncleaved linkers (for single-mismatch targets) triggered complementary nAu-DNA aggregation with concomitant colour change, whereas cleaved linkers (for complementary targets) did not. In that sense, even longer target ssDNA e.g. 80 b could be recognized, as they were not involved in the readout. In short, ligase- and NEase-assisted recognition added to the sequence specificity of dispersion-based colloidal homogeneous assays.

Besides spherical gold nanoparticles (nAu), gold nanorods (AuNR) were utilized in nucleic acid detection. This was demonstrated in the diagnosis of PCR amplified *C. trachomatis* pathogen gene, which is responsible for sexually transmitted disease among human.<sup>[111]</sup> With nanorods, biomolecules could be preferentially controlled to conjugate along either the long or the short axis.<sup>[137-139]</sup> In a similar manner to nAu-based detection, the extensive sandwich aggregation state of AuNR-DNA in the presence of complementary target DNA was visually detected.<sup>[111]</sup> The fact that AuNR possess stronger extinction than nAu and greater longitudinal plasmon tunability and sensitivity, makes it possible to develop AuNR-based multiplex sensors.

One of the prime goals in nucleic acid sensing is to abandon ultimately the need for genomic DNA amplification, which inevitably introduces errors such as contamination. To eliminate the amplifying step, it is highly desirable to develop DNA sensors with improved limit of detection (LOD). From the LSPR perspective, bigger nAu with larger absorptivity<sup>[140]</sup> and nAg that possess vastly greater extinction coefficient than nAu of similar size enable both visual and absorption analyses at much lower target DNA concentrations.<sup>[112,141]</sup> Despite colloidal silver nanoparticles suffer from oxidation and are harder to conjugate, various

efforts have been taken to raise the stability of nAg-DNA, e.g. by using multiple thiol binding<sup>[142]</sup> or phosphorothioate modified DNA,<sup>[143]</sup> regulating the salt<sup>[144]</sup> or pH<sup>[145]</sup> during conjugation, depositing atomic gold layer on nAg,<sup>[146]</sup> and depositing silver layer on nAu-DNA.<sup>[147]</sup>

Besides conventional DNA, gold nanoparticles have been labelled with engineered oligonucleotides, such as locked nucleic acid (LNA)<sup>[113]</sup> and peptide nucleic acid (PNA).<sup>[148]</sup> LNA is analogous to RNA, in which the furanose ribose ring is locked by a methylene bridge between 2'-oxygen and 4'-carbon, resulting in the locked C3'-endo sugar puckering. The conformational restriction gives LNA improved base stacking and therefore increased thermal stability than DNA. These molecular designs allowed the AuNS-LNA/DNA chimerical probes to form even short hybridized duplex (7 bp) with short DNA targets, in which the original melting point would be less than room temperature if AuNS-DNA probes were used instead.<sup>[113]</sup> Together, the synergistic effect of both nAu and LNA enhanced the duplex stability and exhibited exquisite single-mismatch discrimination compared to existing nAu-DNA. Whereas PNA is DNA analogue wherein the entire negatively charged sugar-phosphate backbone is replaced by a neutral polyamide backbone. As the lack of charge repulsion facilitates stronger binding between PNA and DNA/RNA, nAu-PNA probes as short as six nucleotides could hybridize effectively to target DNA, an accomplishment impossible with similar DNA probes.<sup>[148]</sup> Moreover, the smaller interparticle distance as well as the shorter duplex interconnects gave superior mismatch selectivity with clear colour discernment. Therefore, the significant improvements offered by LNA and PNA illustrate the immense potential for these nanoconjugates in bioanalytical and diagnostic applications.

A non-direct nAu aggregation approach towards DNA sensing was through the modulation of aptamer activity by the specific target DNA.<sup>[149-150]</sup> Aptamer is ssDNA or ssRNA that binds to its specific target (small molecules, proteins, or cells etc) via secondary

structure folding with affinity and selectivity comparable to antibodies. While thrombin is capable of cleaving soluble fibrinogen into insoluble fibrin and hence forming clots, thrombin-binding aptamer (TBA) interacts specifically with the protease to suppress its activity. TBA strands have been designed to enhance TBA-thrombin binding in the presence of perfectly match target DNA, thus protecting the fibrinogens attached on nAu from cleavage; whereas single-mismatch targets led to nAu aggregation along with concurrent red-to-blue colorimetric changes.

Immobilized oligonucleotides are known to stabilize the nanoparticles against cationic screening at high salt concentration.<sup>[127,136]</sup> Yet, hybridization of nAu-DNA with equivalent amount of perfectly match target ssDNA without cross-linking the nanoparticles has been shown to induce nAu aggregation at much lower salt concentration (Figure 2.12A and B).<sup>[120]</sup> The colour conversion for such non-cross-linking system was rapid (< 3 min) compared to physical cross-linking system (tens of minutes to hours<sup>[151]</sup>). Different aggregation mechanisms were suggested for the two systems: blunt ends of non-cross-linked duplexes attract each other by helix or coaxial stacking, and London-van der Waals attraction aggregates the nanoparticle rapidly; conversely, cross-linking kinetics is dictated by random collision between the nanoparticles in slow Brownian motion. As non-cross-linked nanoparticles discriminated terminal mismatches superior than middle mismatches (Figure 2.12C),<sup>[120]</sup> and vice versa for cross-linking system, these findings supported the proposed mechanisms to some extent.



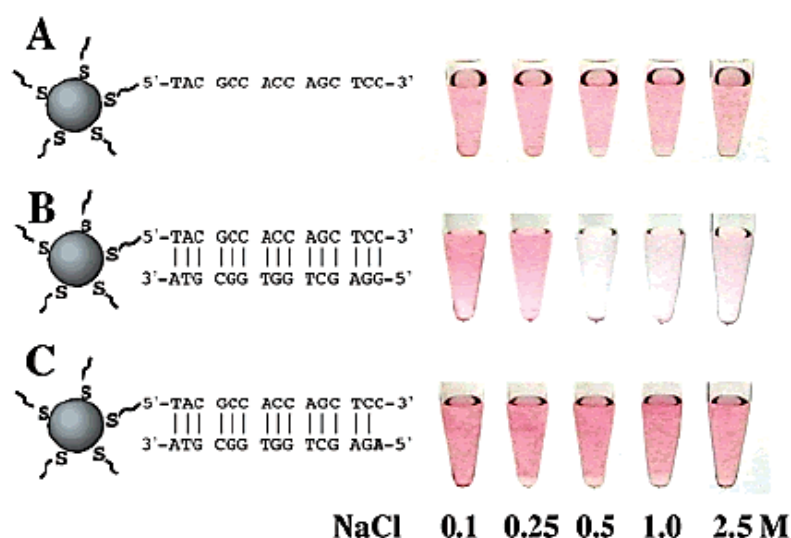


Figure 2.12: Aggregation behaviours of nAu-DNA at various NaCl concentrations at room temperature: (A) without target DNA, (B) with complementary target DNA, and (C) with target DNA possessing single base mismatch at 5' terminus. The final concentrations of nAu, immobilized probe DNA, and the free target DNA were 2.3 nM, 500 nM, and 500 nM respectively <sup>[120]</sup>

Nanoparticles affixed covalently with nucleic acids have the disadvantage of introducing steric constraints to the hybridization kinetics and thermodynamics.<sup>[152]</sup> Thus, some colorimetric DNA sensors avoided conjugation by separating DNA hybridization from the detection step.<sup>[153-155]</sup> Basically, these sensors relied on different adsorption properties of ssDNA and dsDNA onto the charged nanoparticles. While free bases of ssDNA adsorbed on the negatively charged nAu<sup>[153-154]</sup> and exposed the sugar-phosphate backbones outwards, dsDNA that presented both anionic backbones repelled the negative stabilizing ions on the nanoparticle surface. As pristine colloidal nanoparticles were weakly stabilized by repulsive forces from the surface ions, at salt concentration threshold that would ordinarily screen the interparticle repulsion, ssDNA but not dsDNA resisted nanoparticle agglomeration (Figure 2.13a). Likewise, triplex-forming ssDNA that bound to assaying dsDNA via Hoogsteen or reverse Hoogsteen hydrogen bonds could not protect the colloidal nAu from salt-induced aggregation (Figure 2.13b).<sup>[156]</sup> With non-absorbing triplex DNA, salt cations compressed the

electrical double layer of nAu, lowering its zeta-potential and decreasing the interparticle electrostatic repulsion. The successful single nucleotide polymorphism (SNP) assaying by such simple colloidal colour monitoring could be potentially useful, as triplex-forming ssDNA has grown to importance in antigene therapy. Furthermore, immobilization-free detection was successful with AuNR<sup>[155]</sup> and PNA probes.<sup>[141]</sup> In contrast to nAu, anionic backbone of ssDNA probe adsorbed electrostatically to the cationic AuNR (capped by a surfactant bilayer of cetyltrimethylammonium bromide).<sup>[155]</sup> Subsequent target DNA hybridization formed duplex that drew the AuNR into side-by-side aggregation, red- and blue-shifting the transverse and longitudinal LSPR respectively (Figure 2.13c). On the other hand, the mechanism of colorimetric detection using free PNA probes of greater selectivity was reversal of that for DNA probes, because PNA adsorption on nAu alleviated the interparticle repulsion and aggregated nAu aggressively (Figure 2.13d). Only in the presence of complementary target, negative charges of the adsorbed PNA-DNA complexes redispersed the nAu and exerted particle stabilization.<sup>[141]</sup> In brief, by modulating the nanoparticle LSPR, the aforementioned colorimetric techniques could analyse DNA down to the extreme of SNP.

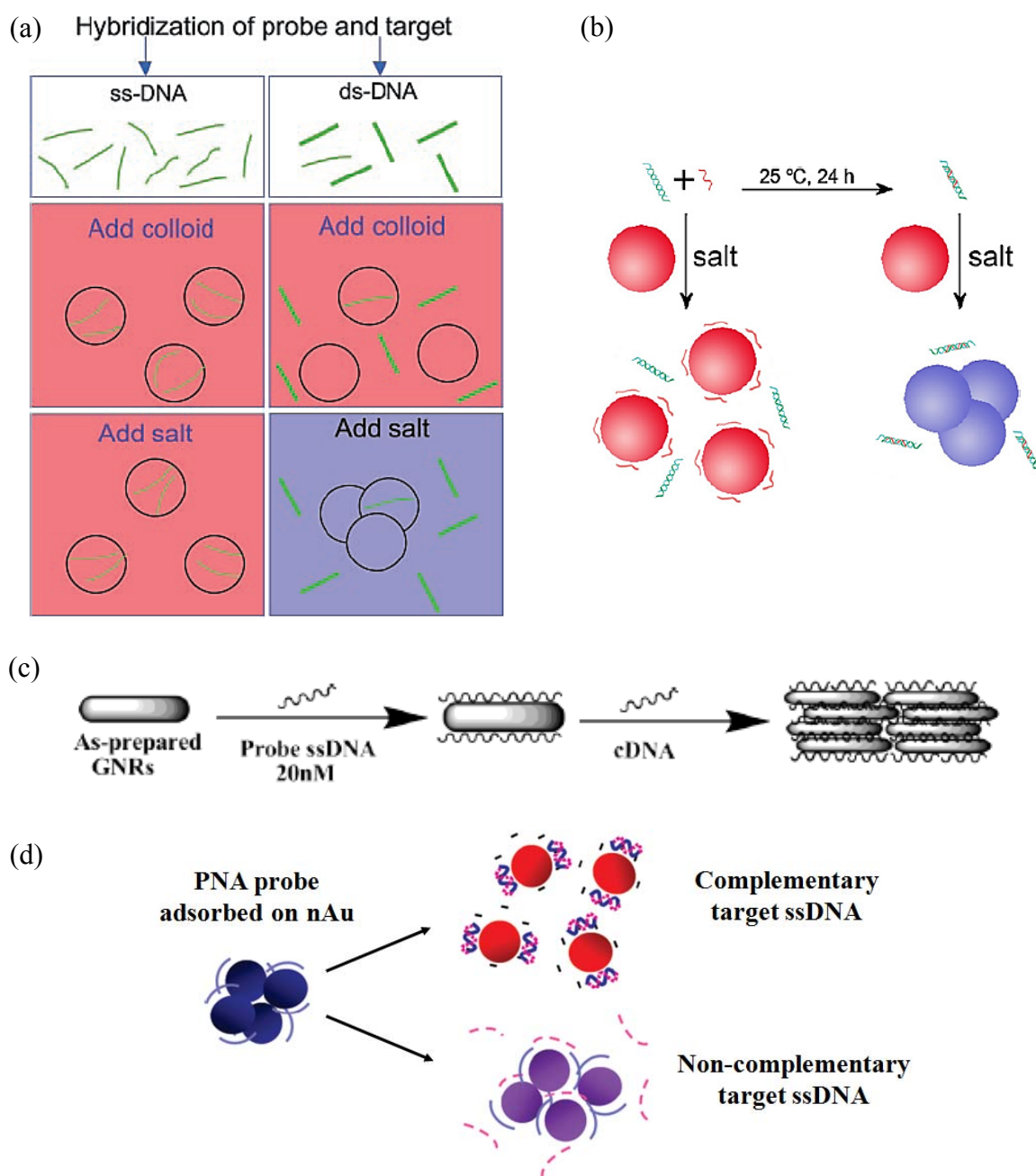


Figure 2.13: Colorimetric method using unmodified colloidal nAu for differentiating between (a) ssDNA and dsDNA,<sup>[153]</sup> (b) dsDNA and triplex DNA,<sup>[156]</sup> and using (c) ssDNA-adsorbed AuNR<sup>[155]</sup> and (d) ssPNA-adsorbed nAu<sup>[141]</sup> for target detection

The intense and localized electromagnetic fields of gold and silver nanoparticles alone have been depicted to be sufficient in nucleic acid detection. For instance, nAu-DNA probes adsorbed on a bead-supported fluid lipid bilayer showed 2-dimensional aggregation due to the hybridization with target ssDNA.<sup>[157]</sup> However, the aggregates were too small to convey

colour change sensible by the naked eyes. Addition of anions selectively desorbed the unstable agglomerates formed by mismatch DNA while retained the stable aggregates of complementary DNA. Thus, the ‘dissolved’ red colour served as the readout signal. In addition, the strong plasmon resonance of nAu has been used to develop non-cross-linked<sup>[120]</sup> microfluidic DNA sensor.<sup>[158-159]</sup>

Surface-confined heterogeneous array coupled with dark field microscopy (Section 2.3) is an ideal platform for multiplex DNA detection using nanoparticles of diverse LSPR peaks. As illustrated in Figure 2.14a, substrate-captured probes allowed precise target DNA binding with additional washing and thermal treatment, which conferred higher selectivity for single-mismatch identification.<sup>[118]</sup> nAg were also employed as signalling agent in microarray DNA assay to screen for a known polymorphism site in breast cancer gene BRCA1 (Figure 2.14b).<sup>[83]</sup> Discrimination DNA facilitated the ligation between nAg-labelled detection DNA and wild type (match) but not mutant type (mismatch) target DNA template. Ligated products immobilized on the microarray site via capture DNA were able to withstand thermal washing. The strong scattering from individual nAg was easily seen as bright diffraction-limited point with standard DFM, allowing direct quantification based on the number of nAg captured. The assay achieved sensitivity of 60× greater than that obtained by fluorescent labels because the counting algorithm eliminated spurious scattering. Importantly, for both synthetic and genomic-amplified ssDNA, a 2 bp deletion in the SNP site associated with the breast cancer onset was successfully discriminated.

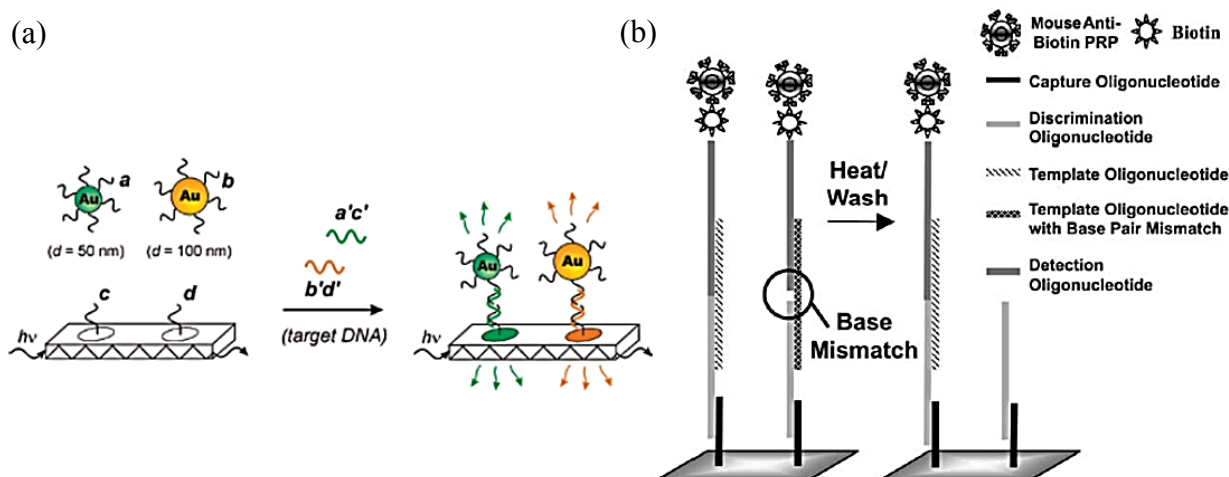


Figure 2.14: Surface-confined heterogeneous array coupled with dark field microscopy (a) Multiplex detection: captured DNA probes, 50 nm and 100 nm nAu-DNA probes and the unlabelled target DNA co-hybridized in a three-component sandwich format according to the specific recognition sequences. Washing at elevated temperature removed the single-mismatch targets <sup>[118]</sup> (b) Ligated products bound to microarray spot containing capture DNA complementary to extension sequence of discrimination DNA. Wash step at elevated temperature removed the non-ligated detection DNA. The quantity of nAg-labelled detection DNA was then counted <sup>[83]</sup>

Apart from synthetic or nuclease-isolated short ssDNA, nanoparticles have been incorporated into *in situ* hybridization of DNA.<sup>[29]</sup> For example, polytene chromosome encoding the specific gene was hybridized with gene-specific probe DNA labelled with gold-silver core-shell nanoparticles. Dark field microscope images (Figure 2.15) simultaneously showed the fluorescence of SYBR Green-stained chromosome as well as the bright scattering of the nanoparticles. The nanoparticles bound to the specific gene, providing individual visualization without further amplification. This practice should be possible for simultaneous DNA-mapping by tuning the nanoparticle LSPR. In short, the strong plasmon resonance of noble metal nanoparticles alone provides the basis for direct DNA analysis that does not require interparticle cross-linking.

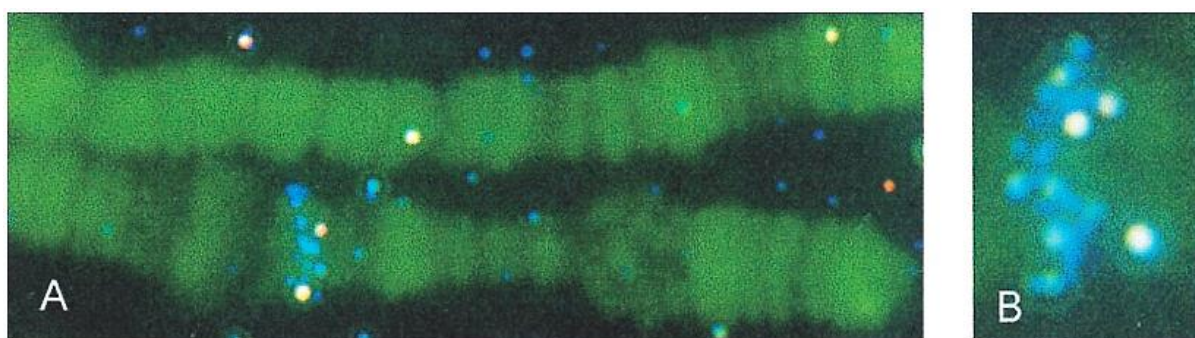


Figure 2.15: (A) Photographs of white gene region in *Drosophila* X chromosome specifically labelled with gold-silver core-shell nanoparticles via *in situ* hybridization. Both the SYBR Green fluorescence of the stained polytene chromosome and the blue light scattered by the nanoparticles were imaged simultaneously. The large number of parallel-aligned copies of DNA present in the polytene chromosome provided multiple target sites for the nanoparticle hybridization (B) A close-up view of the white gene region from another sample, illustrating the large density of nanoparticles that can be clustered yet still be readily identified as individual target site labels. The typical distance between plasmonic nanoparticles is about 2µm. <sup>[29]</sup>

In surface-confined heterogeneous sensing of single nanoparticle, the LSPR peak shift for nAu dimer facilitates optical DNA sensing at single nanostructure level. For instance, immobilized 80 nm nAu showed stepwise plasmon colour change upon binding to freely rotating 40 nm nAu via DNA hybridization (Figure 2.16a).<sup>[114]</sup> Such surface-nAu-assisted DNA detection enabled good LOD with the use of only a dark field microscope without any spectroscopic measurement.<sup>[115]</sup> Nevertheless, the magnitude of plasmon shift was dependent on the number of hybridized 40 nm nAu, the interparticle distance, and the orientation of 40 nm nAu in the confined area around the immobilized 80 nm nAu because the former can rotate dynamically with some restriction. A sensing modality that circumvented these uncertainties used a pre-formed discrete 100 nm - 60 nm nAu dimer that was brought to proximity by ssDNA hairpin, with the 100 nm nAu anchored to the substrate (Figure 2.16b).<sup>[116]</sup> Hybridization of complementary target ssDNA unzipped the hairpin and extended the dimer geometry, increasing the interparticle separation and reducing the plasmon

hybridization, of which the LSPR scattering spectra were monitored by DFM. Spectral blue shift from the reduced symmetric bonding dipole energy (Section 2.1.2) after analyte binding was spectroscopically differentiated from the non-specific binding that resulted in red shift. A comparable assay that leveraged on 40 nm nAu or nAg homodimer along with non-hairpin probe ssDNA showed relatively smaller peak shift magnitudes (Figure 2.16c).<sup>[117]</sup> Based on the significant scattering colour change upon dimer formation, it is feasible to develop multiplex DNA sensor, e.g. using nanoparticles with different compositions to tune the LSPR.<sup>[160]</sup> All these works imply that the actuation of discrete dimeric noble metal nanoparticles, as monitored by single nanostructure scattering spectroscopy i.e. DFM, could be a viable platform in realising single DNA detection.

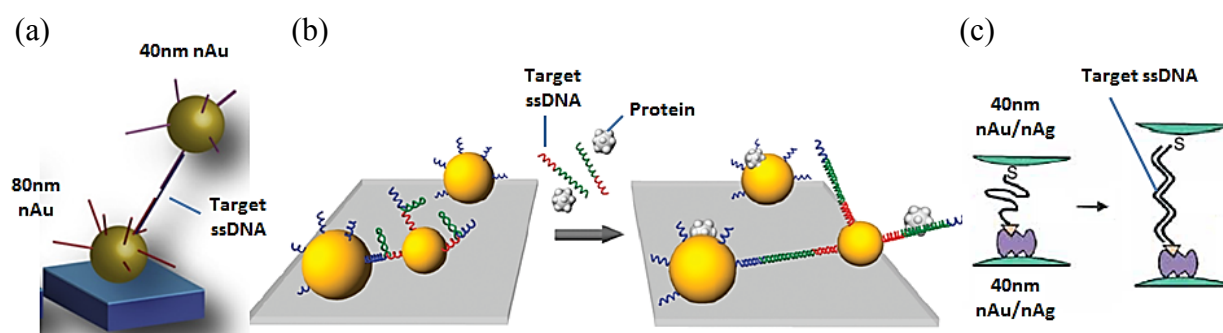


Figure 2.16: Single hybridization event detection (a) 80 nm nAu-DNA probe immobilized on APTES (3-aminopropyltriethoxysilane) surface hybridized to a complementary target ssDNA and 40 nm nAu-DNA probe forming a sandwich structure <sup>[114]</sup> (b) Geometric extension motif for DNA sensing by dimeric 100 nm - 60 nm nAu joined by a probe ssDNA hairpin; 100 nm nAu was anchored to the substrate via aminosilane chemistry; the protein molecules depicted non-specific binding <sup>[116]</sup> (c) 40 nm nAu or nAg homodimer linked by a flexible probe ssDNA aided the sensing of single target ssDNA <sup>[117]</sup>

Plasmon resonance energy could be transferred to chemical or biological molecules adsorbed on the nanoparticles, a phenomenon known as Plasmon Resonance Energy Transfer (PRET). PRET has been suggested to account for surface-enhanced Raman scattering (SERS)<sup>[161]</sup> and fluorescence enhancement<sup>[162]</sup> associated with metallic nanoparticles.<sup>[79]</sup>

Indeed, plasmon scattering spectra actually revealed quenched dips at energy corresponds to the absorption wavelength of the adsorbed biomolecules.<sup>[163]</sup> Therefore, apart from the readout based on the inherent LSPR, some nucleic acid sensors measured the strong plasmonic field-enhanced molecular photoluminescence or Raman signal.

In SERS, the highly confined plasmon energy of metallic nanoparticles amplifies the inelastic scattering of neighbouring molecule vibrational modes. Maximum enhancement is obtained when the plasmon is in resonance with the laser irradiation and overlaps the electronic resonance of chromophore (SERRS).<sup>[164-166]</sup> This was exploited as molecular beacon in DNA sensing,<sup>[121]</sup> in which the ssDNA probes were tagged with nAg at one end and a Raman active molecule at the other end. A probe ssDNA in hairpin configuration (Figure 2.17a) brought both tags close together, yielding strong Raman signal. Once hybridized to complementary DNA, the duplex extended the Raman label far from nAg (Figure 2.17b) and quenched the Raman signal substantially due to the exponential decay of the plasmon field from the nanoparticle surface. Single base mismatches in unmodified target oligonucleotides have also been discriminated based on the SERRS signal from small nanoassemblies of Raman dye-coded nAg-DNA conjugates.<sup>[167]</sup>

Strong electromagnetic enhancement is induced in the gap between two nanoparticles in close proximity (Section 2.1.2), creating a ‘hot spot’ which has been shown to be more efficient than single nanoparticle of similar<sup>[55]</sup> or larger<sup>[165]</sup> size in SERS. This technique has been used in detecting SNP and microRNA involved in breast cancers, wherein massive nAg networks were formed by direct hybridization between two sets of complementary nAg-DNA.<sup>[168]</sup> The Raman dyes tagged on one set of the ssDNA became located between two adjacent nAg upon hybridization. Addition of label-free target DNA disrupted the nanonetworks competitively and reduced the total plasmon coupling, eventually diminishing the Raman scattering effect. SERS response is dependent on the electromagnetic ‘hot spot’



and therefore on the interparticle distance, as portrayed by rigid triplex DNA assembled nAg-LNA.<sup>[122]</sup>

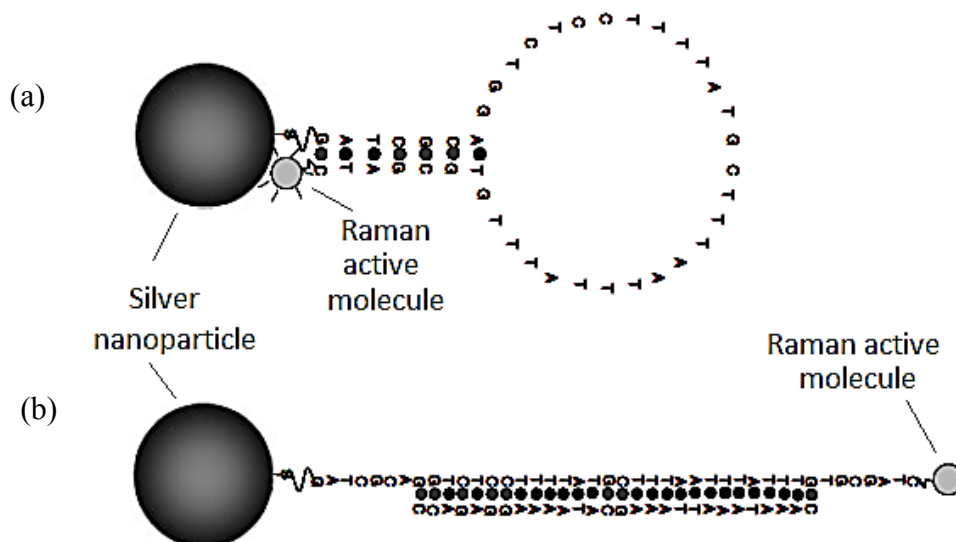


Figure 2.17: Signalling concept of molecular beacon based on surface-enhanced resonant Raman scattering (a) SERRS signal was observed when an nAg-DNA probe formed hairpin, exposing Raman label close to the nAg surface (closed conformation), whereas (b) SERRS signal diminished when target DNA hybridized to the hairpin, pushing the label far from the plasmon decay distance (open conformation)<sup>[121]</sup>

Contrary to SERS, metallic nanoparticles have been illustrated to quench and enhance the luminophores at shorter<sup>[123]</sup> and larger<sup>[123,169]</sup> distances respectively. Metal-quenched luminescence results primarily from non-radiative energy transfer from the organic fluorophores or nanocrystals to the closely spaced metal. For example, when nAu-DNA hybridized to the ssDNA immobilized on graphene oxide (GO) layer, Förster resonance energy transfer (FRET) from donor (GO) to acceptor (nAu) drastically quenched the original GO fluorescence.<sup>[170]</sup> The adsorption of fluorophore-tagged free ssDNA onto colloidal nAu also dissipated the excitation energy, whereas duplex formation regenerated the fluorescent signal.<sup>[171-172]</sup>

On the other hand, metal-enhanced luminescence arises from two contributions. Firstly, nanoparticles concentrate the incident electromagnetic wave to increase the light absorption by luminophores. Secondly, the presence of nanoparticles alters the lifetimes and quantum yields of nearby luminophores by modulating their radiative and non-radiative decay rates. The luminescent quenching and enhancement by metal nanostructures are exploited widely in DNA sensing. A common application is to adhere a luminophore to a metal nanostructure via the terminals of a hairpin ssDNA probe. FRET from the luminophores (e.g. organic fluorophores,<sup>[173]</sup> doped<sup>[123]</sup> or undoped<sup>[174-175]</sup> semiconductor nanocrystal) to proximal metal nanoparticles (e.g. nAu<sup>[123,173-175]</sup>) drastically quenched the photo- or chemiluminescence. Subsequent target DNA hybridization opened the hairpin and introduced large separation distance, enhancing the luminescence by transferring LSPR energy of metal nanoparticles (which has already been excited by the luminescence) to the luminophores.<sup>[123,174-175]</sup> In this regard, substantial spectral overlap between the nanoparticle plasmon absorption and luminophore emission is necessary to ensure efficient energy transfer, and the enhanced luminescence is an excellent gauge towards the presence of DNA.<sup>[176-177]</sup>

In summary, the work discussed above underscores the pragmatic application of LSPR in sequence-specific DNA detection. As nucleic acids are central to expression and conservation of genetic information, being able to detect them at high sensitivity and selectivity has a plethora of implications in biotechnology and medicine such as gene expression profiling, disease diagnosis and treatment, drug discovery and forensic analysis.

## CHAPTER 3: SYNTHESSES OF SPHERICAL GOLD NANOPARTICLES (NAU)

The spherical gold nanoparticles (nAu) used in this research work were synthesized according to the protocols presented in the current chapter.<sup>[178]</sup>

### 3.1 Experimental Section

#### 3.1.1 Materials

Gold (III) chloride trihydrate ( $\text{HAuCl}_4 \cdot 3\text{H}_2\text{O}$ ), trisodium citrate dehydrate ( $\text{C}_6\text{H}_5\text{O}_7\text{Na}_3 \cdot 2\text{H}_2\text{O}$ ), tannic acid ( $\text{C}_{76}\text{H}_{52}\text{O}_{46}$ ), and silver nitrate ( $\text{AgNO}_3$ ) were purchased from Sigma-Aldrich. Prior to the nAu synthesis, all the glassware and magnetic stir bars were cleaned with aqua regia oxidizing solution (3:1 v/v 37%  $\text{HCl}$  : 65%  $\text{HNO}_3$ ) and then rinsed thoroughly with water before use. Milli-Q water with resistance  $> 18 \text{ M}\Omega/\text{cm}$  was used throughout the experiments.

#### 3.1.2 Synthesis of 10 nm nAu

10 nm spherical gold nanoparticles (nAu) were prepared by wet chemistry reduction (adapted from Turkevich). Briefly, 0.01% w/v of gold salt solution was reduced by 0.04% w/v of citrate and 0.001% w/v of tannic acid in total volume of 20 mL at 70 °C. When the reacting solution turned into clear crimson, the temperature was brought to 110 °C, boiled for 5 min, and then cooled slowly in air to room temperature. The as-synthesized 10 nm nAu colloidal solution was filtered by 0.22  $\mu\text{m}$  polyethersulfone syringe filter and stored at 4 °C until further use.

### 3.1.3 Synthesis of 50 nm nAu

In order to synthesize larger nAu that possess uniform shape and narrow size distribution, a 2-stage growth process was employed, in which the highly homogeneous 10 nm nAu (Section 3.1.2) were used as seeds. In short, in the 1<sup>st</sup> stage, 50 mL of 0.1695 mM HAuCl<sub>4</sub>, refluxed at 120 °C with stirring was added with 0.5 mL of the seed solution and let homogenized for 30 s. 1% w/v citrate was then injected quickly into the solution at ratio 0.9/1 of citrate to HAuCl<sub>4</sub> and stirred for 20 min. As the reaction proceeded, the solution turned from clear to blackish, then purple, and finally red, implying the completion of the 1<sup>st</sup> stage growth. Subsequently, 0.1% w/v AgNO<sub>3</sub> was added at ratio 1/50 of Ag<sup>+</sup> to Au<sup>3+</sup> for 10 min under stirring to reshape the polycrystalline nAu into quasi-spherical shape.<sup>[179-180]</sup> In the 2<sup>nd</sup> stage, another set of HAuCl<sub>4</sub> (1.695 mL, 5 mM) and 1% w/v citrate (ratio 0.9/1 of citrate to HAuCl<sub>4</sub>) was added into the nAu solution formed in the 1<sup>st</sup> stage and reacted for 25 min for further nAu growth. The product was then cooled slowly in air to room temperature, filtered by 0.22 µm polyethersulfone syringe filter and stored at 4 °C until further use.

### 3.1.4 Characterization of nAu

UV-vis extinction spectra of nAu were determined by a UV-visible spectrophotometer (Cary Varian 50 Bio) in disposable polystyrene cuvettes of 1 cm path length.

TEM characterization was acquired with a transmission electron microscope (JEOL JEM-3010) operating at 300 kV. 5 µL of nAu solution was dropped on a Formvar-coated copper grid, wicked off after 30 min, and let dried overnight. To obtain the size distribution for nAu, diameters of at least 100 particles were measured from TEM micrographs via graphics software AxioVision 4.8.2 (CarlZeiss).

To analyze the LSPR scattering colour of nAu, diluted nAu solution was introduced by capillary suction into a preformed liquid chamber (borosilicate glass cover slip attached on

microscope glass slide via double-sided tape). The sandwiched sample was then examined under an upright microscope (Nikon Eclipse 50i) with a dark-field oil condenser (oblique angle, NA 1.2-1.43, CytoViva) and a metal halide illuminator (Welch Allyn) as the white light source. Scattered light from nAu was collected by a 100× objective lens (Nikon Plan Fluor 100×, NA 0.5-1.3 oil iris, W.D. 0.16 mm) and directed to colour CCD camera (Nikon Digital Sight DS-Ri1) for real-colour imaging and locating the individual nanoparticles. The image acquisition (24-bit true colour TIF files, 20 ms integration time, and 5.6× gain) was performed using NIS-element AR 3.1 software (Nikon). Imaging experiments were conducted at ambient temperature.

## **3.2 Results and Discussion**

### **3.2.1 Syntheses and characterization of nAu**

In order for the nAu to be functioning as reporter, monodispersity in the nAu size & shape uniformity are of utmost importance.<sup>[181]</sup> Prime weakness of HAuCl<sub>4</sub> reduction by citrate lies in the fact that it promotes nucleation while the existing particles are growing. This introduces polydispersity in the nAu and the effect is even more apparent in large size nAu. New particles nucleation can be opportunely averted by seeding.<sup>[179,182]</sup> To date, the published literatures on seeding-growth which used sodium citrate,<sup>[180,182-184]</sup> ascorbic acid,<sup>[179,185-186]</sup> hydroxylamine,<sup>[183,187]</sup> and hydroxylamine hydrochloride<sup>[188]</sup> as reducing agent produced significant amount of by-products such as ellipsoids or rods, triangles & platelets; whereas those that used strong capping agent<sup>[189]</sup> as stabilizer for eliminating 1- & 2-dimensional particles could not be optimally modified with the delicate thiolated DNA. For the former, incomplete separation of the desired particles would adversely affect the results of LSPR scattering experiments which require meticulously stringent conditions (*vide infra*); for

the later, the nAu stabilized by strong capping agent prevent its further development as nAu-DNA probe in this research.

Consequently, the 50 nm nAu synthesis protocol is developed by performing iterative-seeding growth and optimizing the ratio of citrate to  $\text{HAuCl}_4$  to ensure that the reduction rate of  $\text{Au}^{3+}$  on the surface of existing 10 nm nAu was faster than nucleation rate by boiling sodium citrate, thereby granting homogeneity. It had been reported<sup>[182]</sup> that nanochains & even nanowires form with insufficient reductant, whereas new nuclei start to form if the amount of reductant is in excess. At the low reductant to metal ion ratio used in this synthesis, the presence of seeds made the particle growth rate surpassing nucleation rate, without the hassle of altering the pH for the growth mechanism.<sup>[190]</sup>

TEM images (Figure 3.1) and statistical particle size analysis (Figure 3.2) showed that mean particle diameters for the spherical gold nanoparticles (nAu) synthesized were  $10.03 \pm 1.0$  nm (denoted as 10 nm nAu) and  $51.5 \pm 3.7$  nm (denoted as 50 nm nAu). Both displayed size distributions within 10% of their respective mean diameters. The seed-nAu was prepared by reduction of gold (III) chloride trihydrate using trisodium citrate dehydrate and tannic acid.<sup>[191-192]</sup> The final size of the 50 nm nAu formed by seeding-growth has been predicted using the following equation:<sup>[189]</sup>

$$d_g = d_s \left[ \frac{[M]_a + [M]_s}{[M]_s} \right]^{\frac{1}{3}}, \text{ where}$$

$d_g$  and  $d_s$  represent the diameters of grown- and seed-nAu;  $[M]_s$  and  $[M]_a$  indicate the gold ion concentrations in seeds and in the added  $\text{HAuCl}_4$ , respectively. Thus, the synthesized nAu possessed mean diameter ( $51.5 \pm 3.7$  nm) that were in close agreement with the calculated value (51 nm). The highly homogeneous 50nm nAu were due to (i) the fairly homogeneous seeds, (ii) 2-step seeding-growth, and (iii) silver addition which eliminated the formation of rod- and plate-like gold particles. Optimum silver ion concentration has been found to be

1/50 of the total gold concentration.<sup>[179-180]</sup> Au surface atoms have stronger interaction with Ag than Ag-Ag bond, thus Ag<sup>0</sup> atoms preferred to deposit underpotentially on the (100) and (110) facets of polycrystalline nAu. Although this Ag layer can be oxidized and replaced by Au<sup>3+</sup> later, the preferentially deposited Ag could significantly reduced the growth rate on these facets, and granted the resulting nAu quasi-spherical structure.<sup>[179-180,193]</sup> Besides, the low yet sufficient reductant (citrate) to metal ion (Au<sup>3+</sup>) ratio ensured that the reduction rate of Au<sup>3+</sup> on the surface of 10 nm seeds surpassed the nucleation rate by boiling sodium citrate, thereby granting homogeneity.<sup>[182,190]</sup> In addition, seeding-growth reaction in scrupulously clean glassware helped in the successful production of large nAu with narrow size distribution, because the reduction of Au<sup>3+</sup> on any undesirable small particulates is rapid.

UV-visible spectra (Figure 3.3) of 10 nm and 50 nm nAu exhibited distinct extinction peaks at 520 nm and 527 nm respectively, due to their localized surface plasmon resonance (LSPR) in the visible wavelength region.<sup>[81]</sup> The absence of shoulder peak in the longer wavelength range indicated the absence of aggregated nAu and elongated/hexagonal particles, in accordance with TEM analysis.<sup>[186]</sup> The single peaks displayed by both 10 nm and 50 nm nAu represented the dominating dipole LSPR in small size metal nanoparticles.<sup>[18]</sup> As the nAu diameter increased from 10 nm to 50 nm, retardation effect caused the extinction peak to red shift. The synthesized 50 nm nAu had smaller bandwidth ( $\Gamma = 78$  nm) than some existing protocols in the literature,<sup>[180,182-183,185-187]</sup> signifying the high monodispersity and shape uniformity achieved. The particles retained their stability even after several months of synthesis because no change was observed in the plasmon resonance peak and bandwidth values (data not shown). This suggests that the synthesized nAu were thermodynamically stable at minimum surface energy.

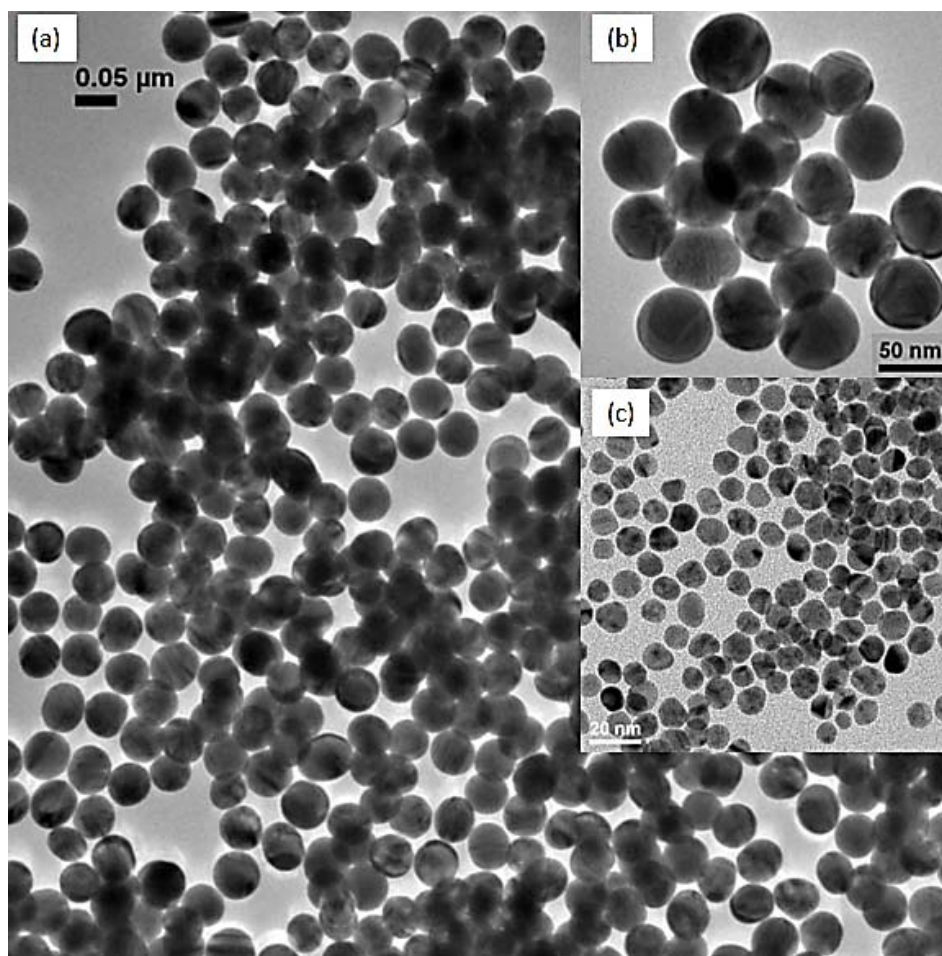


Figure 3.1: TEM images of (a) nAu with mean diameter  $51.5 \text{ nm} \pm 3.7 \text{ nm}$  on a wide field view, (b) its magnified view, and (c) nAu with mean diameter  $10.03 \text{ nm} \pm 1.0 \text{ nm}$ , which also serves as seed for the fabrication of 50 nm nAu.

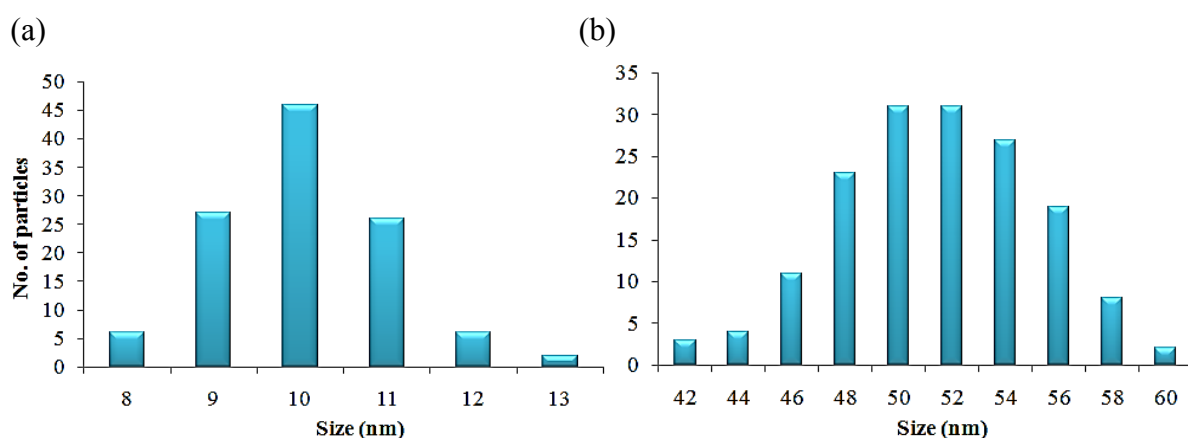


Figure 3.2: Statistical particle diameter analysis. Size distribution of (a) 10 nm nAu with an average diameter of  $10.03 \pm 1.03 \text{ nm}$  and (b) 50 nm nAu with an average diameter of  $51.5 \pm 3.69 \text{ nm}$  by measuring 114 and 159 nanoparticles in the TEM images, respectively.



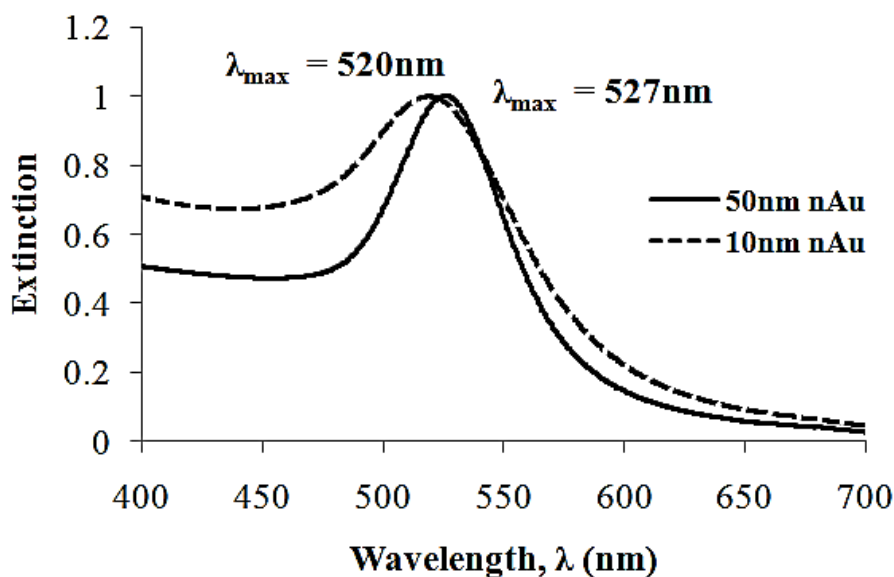


Figure 3.3: UV-visible extinction spectra of nAu solution with mean diameters 10 nm (dashed line) and 50 nm (solid line). Both are normalized to their extinction peak maxima. The bandwidth (FWHM,  $\Pi$ ) for  $51.5 \pm 3.7$  nm nAu is 78 nm.

Compared to existing published articles, the 50 nm nAu developed here based on a 3-step citrate/tannic acid-synthesis with silver ion addition after the completion of 2<sup>nd</sup> growth, has better structural and optical properties.

Jana et al.<sup>[179]</sup> have used  $12 \pm 2$  nm nAu seed produced by the common Frens citrate-reduction to synthesize larger size nAu using ascorbic acid as reducing agent. The reducing agent was added at 10 mL/min in 10 min to the seed solution inoculated with 1/50 ratio of  $\text{AgNO}_3/\text{HAuCl}_4$ . However, they obtained  $49 \pm 10$  nm nAu instead of the calculated 43 nm. The broader size distribution than ours ( $51.5 \pm 3.7$  nm) was most likely due to (1) the use of  $12 \pm 2$  nm seeds, which has broader size distribution than ours ( $10.03 \pm 1$  nm); (2) hydroxylamine and ascorbic acid have been reported to produce non-spherical by-products e.g. nanorods, nanotriangles, hexagonal nanoplates. Thus, even though silver ion has been employed to eliminate rod-shaped particles formation, wider size distribution was obtained.

Xia et al.<sup>[180]</sup> have used sodium citrate and trace amount of AgNO<sub>3</sub> (1/235 AgNO<sub>3</sub>/HAuCl<sub>4</sub>) to synthesize nAu directly (not seeding-growth) in boiling water. While they were able to get narrow size distribution of quasi-spherical nAu i.e.  $36 \pm 3$  nm, no attempt has been made to synthesize larger nAu. Besides, their AgNO<sub>3</sub>/HAuCl<sub>4</sub> ratio is  $\sim 5$ -fold less than ours, most likely to minimize unwanted silver nanoparticles nucleation and growth in one-pot synthesis, but still want to exploit underpotential deposition of Ag<sup>0</sup> on certain facets for shape-controlled growth of nAu.

On the other hand, Qiu et al.<sup>[182]</sup> have used sodium citrate to synthesize  $13 \pm 2$  nm nAu seed, followed by sodium citrate (Cit/Au = 1.32/1) seeded-synthesis of larger nAu ( $\sim 21.6$  nm). The TEM of the as-synthesize nAu indeed showed inhomogeneous shapes of gold nanoparticles, such as the spheroidal and elliptical ones, which might be attributed to the lack of facet-controlled mechanism by silver.

Niu et al.<sup>[189]</sup> have attempted 2-mercaptosuccinic acid (MSA) as the reducing agent to synthesize  $49.5 \pm 3.3$  nm nAu from  $15.3 \pm 1.5$  nm seeds via the careful control of [HAuCl<sub>4</sub>]/[MSA] ratio. The nAu fabricated at ambient temperature were monodisperse and highly reproducible without requiring silver ion addition. While each MSA has a thiol group, it could attach firmly on nAu and function as capping agent as well. However, this Au-S bond between MSA and the nAu surface atom is too strong for downstream conjugation of ssDNA-SH onto nAu. With the strongly tagged MSA at high surface density, unless much more abundance of ssDNA-SH is used to displace the surface MSA, conjugation procedures following the protocols in Chapter 4-6 are not feasible.

The importance of applying the correct surface capping agent has also been demonstrated by another work of Jana et al.<sup>[185]</sup> The  $3.5 \pm 0.7$  nm gold particle seeds obtained via sodium borohydride-reduction of gold salt precursor have been used to synthesize 5 nm - 40 nm nAu with hydroxylamine as the reductant. Nonetheless, gold nanoparticles prepared

this way consisted of a mixture of spheres (e.g.  $37 \pm 5$  nm diameter) and rods (e.g. average major axis 200 nm and minor axis 17 nm). This could largely be caused by the cetyltrimethylammonium bromide that was added as a surface capping agent during the larger nanoparticle synthesis.

Another evidence for the shape uniformity for the nAu synthesized in this work is based on the LSPR scattering imaging. Under the dark field microscope, 99% of the 50 nm nAu exhibited green scattered light (Figure 3.4), which was well preserved for months. 10 nm nAu did not show up as bright as their 50 nm counterparts did because the scattering intensity of a metallic nanoparticle is proportional to the power of six of its effective radius.<sup>[18]</sup> Both 10 nm and 50 nm nAu are versatile for further surface modification as they are stabilized loosely by the citrate ions. The weak capping agent is readily displaceable by molecules having higher bonding energy with the gold atom,<sup>[194]</sup> thereby allowing convenient attachment of DNA carrying thiol group onto the nAu for the studies in the subsequent chapters.

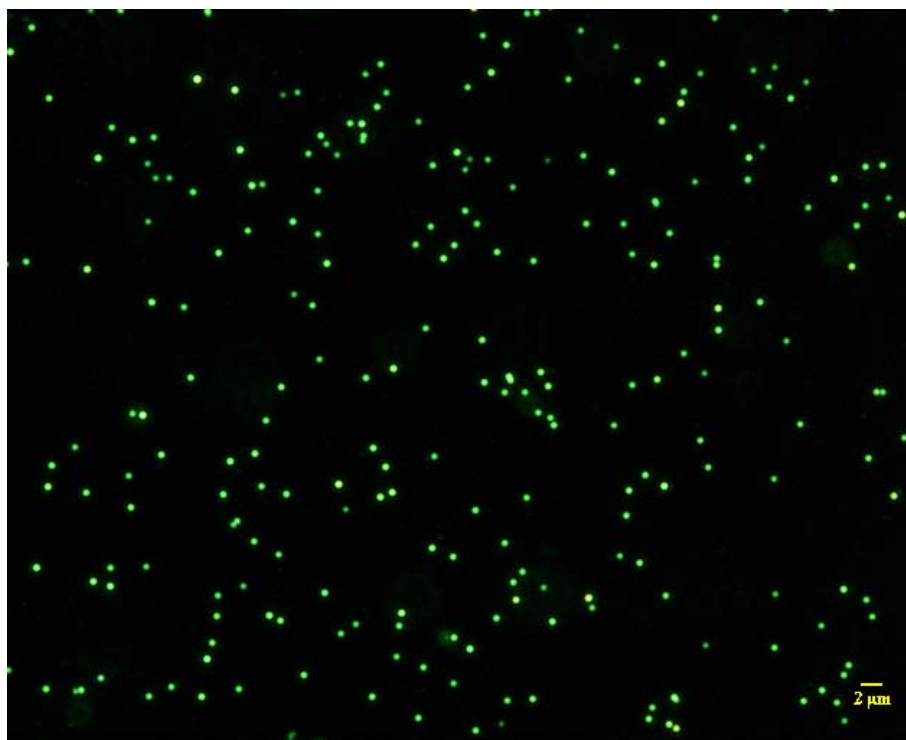


Figure 3.4: Dark field image of as-synthesized nAu with mean diameter  $51.5 \pm 3.7$  nm. The solution was diluted many-fold from the as-synthesized solution to avoid over-crowding and to improve clarity. Each bright dot represents the optical scattering from single nAu.

### 3.3 Conclusion

In this chapter, we describe the synthesis of nAu with desired shape and sizes by wet chemistry reduction technique. The nAu produced are mono-dispersed, possess exceptional stability, display characteristic LSPR peaks, and hold good surface-tunability for further downstream processing. Hereafter, these gold nanoparticles would be used for the research experiments as illustrated in Chapter 4 (*vide infra*).

## CHAPTER 4: ANALYSIS OF METALLIC NANOPARTICLE-DNA ASSEMBLY FORMATION IN BULK SOLUTION VIA LOCALIZED SURFACE PLASMON RESONANCE SHIFT

(Paper reprints from *RSC Advances*<sup>[178]</sup>)

### 4.1 Introduction

In recent years, there has been increasing research on the unique physical and chemical properties of metallic nanoparticles because of their attracting fundamental and technological applications. For example, incident electromagnetic field on a metallic nanoparticle excites the surface conduction electrons collectively, and results in phenomenon generally known as localized surface plasmon resonance (LSPR).<sup>[15,17]</sup> Two neighbouring metallic nanoparticles has been demonstrated to exhibit longitudinal LSPR delocalization that changes exponentially with the interparticle separation distance.<sup>[20,60,66,195]</sup> The corresponding LSPR cross-sectional enhancement has been used routinely as plasmon ruler,<sup>[54,63-64]</sup> the LSPR frequency shift in chemical- and bio-sensing,<sup>[49,117,196-198]</sup> electromagnetic field enhancement<sup>[62]</sup> in Surface-Enhanced Resonant Raman Scattering (SERRS),<sup>[55-56,199]</sup> and near-field surface plasmon coupling in low-loss nano-waveguide to transmit electromagnetic energy.<sup>[52,200-201]</sup>

In the pursuit to discriminate single nucleotide polymorphism (SNP), there have been extensive studies on LSPR-aided detection using gold nanoparticles<sup>[157,159,191,202-206]</sup> that are chemically stable and typically exhibit strong localized surface plasmon resonances (LSPRs) in the visible wavelength region. The commonly employed design mainly relies on two sets of DNA-modified nanoparticle probes, which are complementary to a portion of the non-labelled target DNA sequences (three-component assays).

On the other hand, two-component assays, which involve two sets of complementary DNA-modified nanoparticle probes, receive less attention. Most of the existing research that

utilized this assay concentrated on the search for DNA-binding molecules,<sup>[207-209]</sup> and the investigation of non-Watson-Crick hybridization<sup>[210]</sup> e.g. G-quadruplex interaction.<sup>[211]</sup> Because of the faster hybridization kinetics than three-component assays,<sup>[212]</sup> the two-component assays were also used to design conjugation procedures for reducing conjugation time,<sup>[213]</sup> improving conjugate stability,<sup>[142]</sup> controlling surface DNA density,<sup>[214-216]</sup> mediating the number and space of the bound DNA,<sup>[217]</sup> detecting label-free DNA by displacement,<sup>[168]</sup> and engineering nanoparticle-based superlattice.<sup>[135]</sup> Common readout platforms in detecting the hybridization of DNA-modified nanoparticle probes include the extinction-based colorimetric assay, electrophoresis, electron microscopy, and UV-visible spectroscopy. Optical Rayleigh scattering under dark field microscopy can be another potential readout platform,<sup>[18]</sup> and a few research groups have used the scattering-based two-component assays to detect single DNA enzyme cleavage event<sup>[63]</sup> and to study the LSPR coupling behavior of dimeric or higher-order metal nanoparticles.<sup>[218-219]</sup>

There are two commonly-used schemes constituting the two-component assays: heterogeneous (surface-bound) and homogeneous (in bulk solution) hybridization. For the former, surface bound particles enable real-time observation of the individual hybridization, but are less representative of the ensemble event.<sup>[219]</sup> For the latter, ensemble hybridization provides stronger statistical significance among different populations, at the cost of sacrificing individual binding studies.<sup>[210]</sup> In addition, the kinetics and thermodynamics of duplex formed with a surface-bound nanoparticle deviate from the free duplex formed in bulk solution due to additional interfacial constraints experienced by the hybridizing strand. Moreover, homogeneous hybridization enables annealing to remove any possible secondary structure in the DNA.

While most of the existing studies have focused on the heterogeneous (surface-bound) hybridization system, herein, our work opted for the homogenous (in bulk solution) system

using DNA-modified gold nanoparticles (nAu-DNA). The spherical nanoparticles which have been successfully synthesized and characterized according to protocols in the previous chapter were employed in the DNA conjugation steps. After the hybridization in solution, the hybridized particles were allowed to adsorb on a glass for easy quantification of the hybridization events. The nanoassemblies formed were visualized via Rayleigh scattering with dark field illumination. The abundance of data (i.e. individual hybridized particles on glass) allows us to provide a more statistically representative hybridization event of the ensemble. The objective of this study is to look at the ensemble hybridization behaviour of different populations, which can reflect the whole population more accurately than focusing only on a limited number of individual particles. nAu are preferred over silver nanoparticles because they are chemically more stable, possess better shape controllability, and form stronger bond with thiol functional group that enables easier manipulation. The effect of nAu concentration, the duplex length, the size of nAu, and the DNA surface density in hybridization were studied separately and quantified by LSPR shift. The hybridization development between these quasi-immobilized DNA reiterates the generally agreed hybridization mechanism, while highlighting the importance of surface probe densities on the hybridization efficiency and kinetics. Importantly, we demonstrated standalone small size nanoparticles, with their low light scattering yield, are less useful in probing the nanoassembly formation via dark field scattering.

## **4.2 Experimental Section**

### **4.2.1 Materials**

Gold (III) chloride trihydrate, trisodium citrate dehydrate, tannic acid, silver nitrate, 4,4'-(phenylphosphinidene)-bis-(benzenesulfonic acid) (PPBS), sodium dodecyl sulfate (SDS), sodium chloride, magnesium chloride hexahydrate and poly-L-lysine solution (0.1%)

were purchased from Sigma-Aldrich. Synthetic single-stranded DNA (ssDNA) strands (modified with the terminal 5' alkanethiol group, Table 4.1) were purchased from Proligo. Tris buffer (pH 8.0) was purchased from 1st Base. Milli-Q water with resistance > 18 MΩ/cm was used throughout the experiments.

Table 4.1: List of DNA sequences used to conjugate nAu surface in this study. The underlined portions represent complementary sequences that hybridize. P denotes the main ssDNA probes; cP<sub>27</sub>, cP<sub>18</sub>, and cP<sub>14</sub> denote complementary ssDNA strands which will hybridize with 27 bases, 18 bases, and 14 bases of P to form 27 bp-, 18 bp-, and 14 bp-duplexes.

Name	Oligonucleotide sequences
<b>P</b>	HS - 5'- C <sub>6</sub> - AGC TCG <u>GGA TTA TTG TTA AAT ATT GAT AAG GAT</u> - 3'
<b>cP<sub>27</sub></b>	HS - 5'- C <sub>6</sub> - AGC TCG <u>ATC CTT ATC AAT ATT TAA CAA TAA TCC</u> - 3'
<b>cP<sub>18</sub></b>	HS - 5'- C <sub>6</sub> - AGC TCG TCT TAG <u>TCT AAT ATT TAA CAA TAA TCC</u> - 3'
<b>cP<sub>14</sub></b>	HS - 5'- C <sub>6</sub> - AGC TCG TCT TAG TCT TTC <u>TTT TAA CAA TAA TCC</u> - 3'
<b>dT<sub>5</sub></b>	HS - 5'- C <sub>6</sub> - TTT TT - 3'

#### 4.2.2 Syntheses and characterization of nAu

The synthesis and characterization of 10 nm and 50 nm spherical gold nanoparticles (nAu), as well as the quality of the synthesis are described in detail in Chapter 3.

#### 4.2.3 Fabrication of nAu-DNA probes

The nAu-DNA probes were conveniently derivatized with nucleic acids that have disulfide molecules at the end of their sequences. The sulfur-sulfur (S-S) bond can be cleaved by direct oxidative addition reaction to form high-energy gold-thiolate (Au-S) bonding on the gold surface.<sup>[220-221]</sup> Therefore, all 33-base ssDNA sequences used in this study that carry a thiol group at their 5' terminals (Table 4.1) were received in disulfide format and used



without prior reduction. Strand P is the probe sequence to which complementary strands cP<sub>27</sub>, cP<sub>18</sub>, and cP<sub>14</sub> hybridized to form 27 bp-, 18 bp- and 14 bp-duplexes (bp: base-pair). 50 nm nAu were used in both Scheme 4.1 and Scheme 4.2, whereas 20 nm and 10 nm nAu were only used in Scheme 4.2(a) and 4.2(b), respectively. Prior to conjugation, nAu were passivated with PPBS, and then ssDNA was incubated with 50 nm and 10 nm nAu at 1000:1 and 400:1 ratio (ssDNA:nAu) respectively. After 2 h incubation, for 50 nm nAu, NaCl concentration was increased slowly to 80 mM over 2 days in 0.01% SDS; whereas for 20 nm and 10 nm nAu, NaCl concentration was increased to 600 mM over 2 days. To prepare 20 nm and 10 nm nAu with a low surface-ssDNA density, ssDNA was incubated on 20 nm and 10 nm nAu at 5:1 ratio (ssDNA:nAu), followed by surface passivation with short five thymine bases (dT<sub>5</sub>), and then a gradual NaCl concentration increase to 600 mM over 2 days. Excess reagents were removed by repeated washing and centrifugation.

#### **4.2.4 Formation and analysis of nAu-DNA assemblies**

Two sets of nAu-DNA probes complementary to each other (denoted as nAu-P/nAu-cP<sub>27</sub>, nAu-P/nAu-cP<sub>18</sub>, and nAu-P/nAu-cP<sub>14</sub>) were diluted independently in hybridization buffer (140 mM Tris, 140 mM NaCl, 2 mM MgCl<sub>2</sub>) according to the required concentration. Hybridization was carried out by first mixing 0.5  $\mu$ L of nAu-P probe with 0.5  $\mu$ L of its complements. Then, the sample was heated to 65 °C for 2 min to ensure complete melting of any duplex strands, followed by slow cooling to 24 °C at a rate of 0.5 °C/min for annealing. All the samples were analyzed in time sequence of 1 h, 6 h, and 24 h by sandwiching 1  $\mu$ L of the sample droplets between cover slip and microscope glass slide. Probe hybridization efficiency was examined under an upright microscope (Nikon Eclipse 50i) equipped with a dark-field oil condenser (NA 1.2-1.43, CytoViva) and a metal halide illuminator (Welch Allyn) as the white light source. Scattered light from nAu was collected by a 100 $\times$  objective

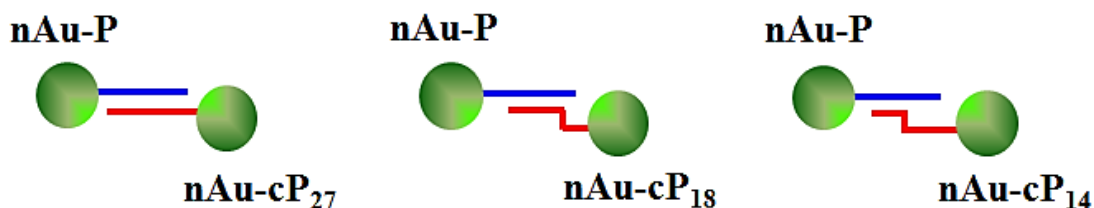
lens (Nikon Plan Fluor 100 $\times$ , NA 0.5-1.3 oil iris, W.D. 0.16 mm) and directed to colour CCD camera (Nikon Digital Sight DS-R1) for real-colour imaging and locating the individual nanoparticles. The image acquisition (24-bit true colour TIF files, 20 ms integration time, and 5.6 $\times$  gain) and analysis were performed using NIS-element AR 3.1 software (Nikon). Spectral measurements were done using an Andor SR-303i-B spectrometer (303 mm focal length, 40-100 s integration times). Statistical analysis, wherever applicable, was done using Student's *t*-test. Imaging and spectra experiments were conducted at ambient temperature.

Three sets of studies, each aiming to investigate the influences of assembly condition on Rayleigh scattering, were carried out using complementary probes (probe = nAu-ssDNA). Scheme 4.1 (using 50 nm nAu only) and Scheme 4.2 (using 50 nm and 20 nm nAu, or 50 nm and 10 nm nAu) were repeated in triplicate and quadruplicate respectively to ensure reproducibility; Student's *t*-test was used for statistical analysis of study A.

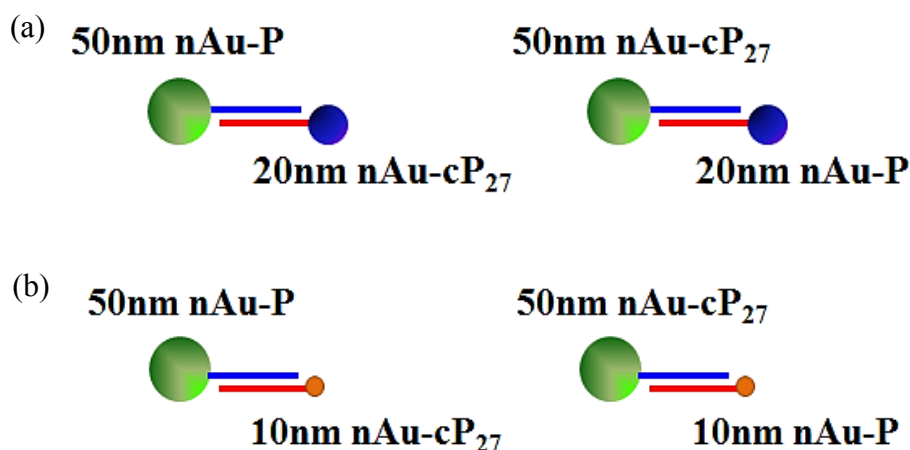
**A. Probe Concentration & Hybridized Duplex Length Study** (Scheme 4.1): By fixing the molar ratio of complementary probes (nAu-P/nAu-cP<sub>27</sub>, nAu-P/nAu-cP<sub>18</sub>, and nAu-P/nAu-cP<sub>14</sub>) at 1/1, hybridization efficiency was examined at probe concentrations of 400 fM, 100 fM, and 10 fM.

**B. Size Effect Study** (Scheme 4.1 vs. Scheme 4.2): Hybridization efficiency was compared at 1/1 molar ratio between 50nm/50nm pair, 50nm/20nm pair, and 50nm/10nm pair using P/cP<sub>27</sub>. The concentration of each probe was fixed at 800 fM, and all the particles were fully saturated with ssDNA.

**C. Surface-ssDNA Density Study** (Scheme 4.2): Hybridization efficiency between two sets of 50nm/20nm pairs at 1/1 molar ratio were compared, where the first set with 20 nm nAu fully saturated with ssDNA on surface and the second set with only 5 strands of ssDNA. The same experiment was repeated for 50nm/10nm pairs at 1/1 molar ratio. The concentration of each probe was fixed at 800 fM.



Scheme 4.1: LSPR coupling between 50 nm nAu with different length in complementary sequence (not drawn to scale). The duplex regions were designed such that the separation between nAu is kept constant to eliminate distance-dependent variable. Note that in reality, each nAu is saturated with ssDNA probes on its surface.



Scheme 4.2: LSPR coupling between (a) 50 nm nAu & 20 nm nAu, (b) 50 nm nAu & 10 nm nAu due to P/cP<sub>27</sub> hybridization (not drawn to scale). Note that in reality, all 50 nm nAu are saturated with ssDNA probe; 20 nm and 10 nm nAu, either bear 5 probe ssDNA sequences each (Surface-ssDNA Density Study) or are saturated with probe ssDNA sequences (Size Effect Study).

#### 4.2.5 DFM and FESEM mapping of nAu and nanoassemblies

To map the LSPR scattering images and nanoparticle/nanoassembly structures, 1  $\mu$ L of pre-hybridized nAu solution was dropped on a poly-L-lysine-coated microscopic glass slide, rinsed gently with copious amount of water, and let dried overnight. Subsequently, a 150 mesh copper grid without any polymer membrane (G200F2 Alphabet Finder, Electron Microscopy Sciences) was secured over the nAu-immobilized spot using nail-polish. This film-free and co-ordinate-marked grid was applied as stencil for DFM-FESEM locating and

mapping purpose. Samples scattering images were first recorded using DFM. Then, the glass substrate of the grid-labelled area was cut and sputtered with a thin layer of platinum particles. The nanoparticle/nanoassembly structures were acquired with a field-emission scanning electron microscope (FESEM, JEOL JSM-6700F) operating at 5 kV. The captured dark field and FESEM micrographs were compared at the same coordinate to locate the nanoparticle/nanoassembly scattering and physical structures.

## **4.3 Results and Discussion**

### **4.3.1 Analysis of nAu-DNA assemblies**



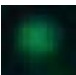















Previous studies have demonstrated that hybridization between short-DNA-modified nAu induces surface plasmon coupling<sup>[218]</sup> and brings upon enhanced plasmon shift and scattering intensities. This plasmon frequency shift can be detected using dark field microscopy (DFM) that analyzes only the scattered light. As observed by DFM in this first part of the doctoral work, upon mixing complementary 50 nm nAu-DNA probes (e.g. nAu-P and nAu-cP<sub>27</sub>), a very significant difference between the unhybridized and hybridized samples is their scattering colours (Figure 4.2), wherein the former consists of mostly green and the latter yellowish-orange. In addition, apart from the dominating green and orange scattered light, yellow scattering is distinctively different from the orange ones. The formation of extensive and co-operative linking between nAu is expected since the nAu used in our system are saturated with oligonucleotides on the surface.<sup>[125]</sup>

We then proceeded to analyze the scattering colours following the procedures outlined in Section 4.2.5. Precise mapping of the individual scattered light in dark field micrographs with respect to the real nanoparticle assembly in electron microscope was done using a copper grid that is membrane-free and labelled with alphabetical or numerical stamps (Figure S4.6a, Appendices) for locating purpose. Typical mappings between DFM and

FESEM are shown in Figure S4.6b-c, as well as in Figure S4.6d-e. Based on the correlation of dark field and FESEM micrographs (Table 4.2) as well as optical scattering spectra (Figure 4.1), we used three categories to quantify conveniently the degree of hybridization, namely ‘green’, ‘yellow’, and ‘orange’ for the sake of ensemble statistics later. The ‘green’ category is composed of unhybridized nAu that scatter wavelength at  $\sim 550$  nm (green) strongly (Figure 4.1). Small nanoassemblies classified as ‘yellow’ comprise either two hybridized 50 nm nAu or three/four 50 nm nAu hybridized in quasi-linear fashion, and with scattered wavelength of 570-580 nm; whereas nanoassemblies termed ‘orange’ consist of three 50 nm nAu in triangular configuration or more than four close-packed 50 nm nAu, and with scattered wavelength of 610-650 nm. The peak maxima of ‘orange’ nanoassemblies span wider wavelength range than ‘yellow’ nanoassemblies because of the varied number of nAu in ‘orange’ nanoassemblies. When complementary nAu-DNA are mixed in the presence of salts, individual nAu (‘green’) hybridize to their complements to form small nanoassemblies (‘yellow’), which further inter-hybridize or added with free individual complementary nAu to form nanoassemblies with significant numbers of nAu (‘orange’). In other words, as hybridization proceeds, the observed plasmon scattering turns from ‘green’ to ‘yellow’, and finally to ‘orange’. To analyze the hybridization of nAu, micrographs were captured at the bottom plane of the liquid chamber. We defined the Red-Green-Blue (RGB) threshold value for ‘green’, ‘yellow’ and ‘orange’ colour categories as  $G = 90-255$ ,  $R = 220-249$  and  $R = 249-255$ , respectively. The image processing software then discerned the scattering points and classified them into one of the aforementioned categories. All the hybridization percentages tabulated are the average of either three or four experimental results, as noted in each figure. Unless stated otherwise, P/cP<sub>27</sub>, P/cP<sub>18</sub>, and P/cP<sub>14</sub> represent hybridization of different complementary nAu-DNA pairs.

We favour larger size nAu (50 nm) which have inherently sufficient scattering intensity and yet not too bulky to slow down the particle diffusion (and hence hybridization). In addition, they are relatively stable in salt buffer required for the hybridization condition. Table 4.2 shows that a dimeric 50 nm nAu pair exhibit sufficient peak shift to cause a distinct plasmonic colour change. We also studied the LSPR coupling ability of small nAu in the subsequent sections (Section 4.3.3 and 4.3.4, Size Effect and Surface-ssDNA Density Studies, respectively), where 10 nm nAu was chosen for its better size contrast against 50 nm nAu, and 20 nm nAu for its lower plasmon scattering contrast against 50nm nAu.

Table 4.2 (Scheme 4.1): Correlation between the plasmon observed under dark field microscope with the inherent structure of the nanoassemblies. The sample is prepared by hybridizing 800 fM of complementary probes nAu-P/nAu-cP<sub>27</sub>, for 1 h at 1/1 molar ratio, in buffer 140 mM Tris, 140 mM NaCl, 2 mM MgCl<sub>2</sub>. FESEM image confirms the change in plasmon colour from green to yellow/yellowish-red when the gold nanoparticles form nanoassemblies due to hybridization. Note that dark field micrographs are taken after the solution dried-up; therefore, the plasmon scattering intensities as well as the plasmon shifts owing to hybridization are not as significant as the dark field micrographs demonstrated in the main article, which are captured with the particles residing in buffer.

Categories	Scattering colour	Nanoassemblies
'Green'		
		
'Yellow'		
		
		
		
'Orange'		
		
		

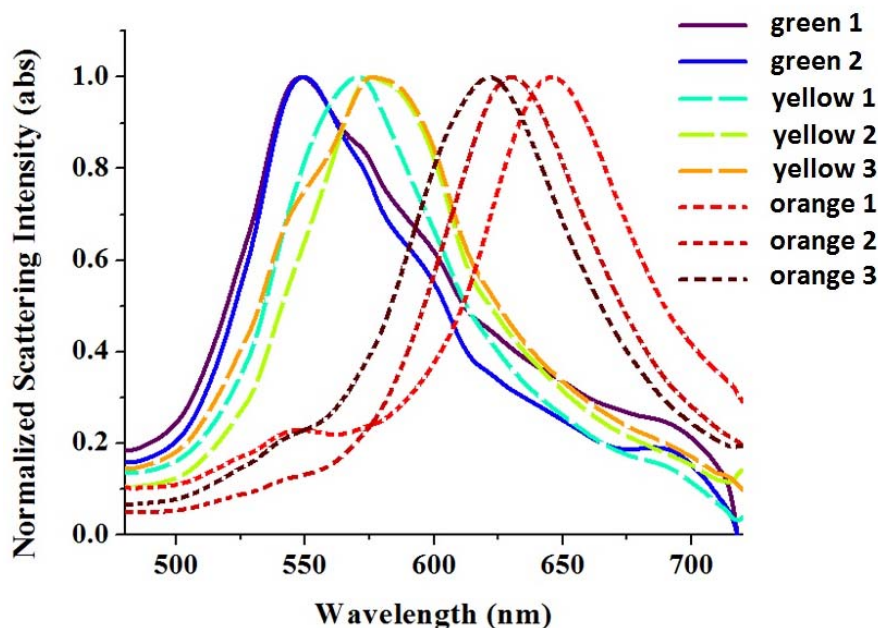


Figure 4.1: Typical light scattering spectra of the particles/nanoassemblies categorized as ‘green’, ‘yellow’, and ‘orange’ showed in Table 4.2, on glass-slides and in buffer (140 mM Tris, 140 mM NaCl, 2 mM MgCl<sub>2</sub>). The spectra were obtained with a dark field microscope, and exposure time 40 s - 100 s on the EMCCD-monochromator. The ranges of peak maxima for each category are around 550 nm, 570-580 nm, and 610-650 nm.

#### 4.3.2 Probe Concentration & Hybridized Duplex Length Study (Scheme 4.1)

In this part of the work, complementary probes P/cP<sub>27</sub>, P/cP<sub>18</sub>, and P/cP<sub>14</sub> were at stoichiometric ratio of 1/1, and the amount of nanoassemblies was determined at various probe concentrations. Besides, hybridization due to the variation in the number of base-pairs involved in nanoassembly formation was examined. The duplex regions have been designed such that the separation between two nAu is kept constant at 39b to eliminate distance-dependent variable. We retained the dangling end in P/cP<sub>18</sub> and P/cP<sub>14</sub> without switching to shorter ssDNA probe to avoid the possible difference in nAu surface-ssDNA densities. In fact, the amount of shorter probe conjugated on same size nAu has been verified to be higher than that for longer probe, due to the smaller steric hindrance from the flexible ssDNA

(contour length =  $0.6 \text{ nm} \times \text{no. of bases}$ ). In addition, the shorter probe often resulted in reduced ionic stability of nAu-DNA, and our 50 nm nAu-DNA system did not withstand the aqueous buffer of high salt concentration applied throughout the whole experiments (data not shown).

Figure 4.2a shows a typical dark field micrograph obtained by hybridization of 400 fM complementary probes P/cP<sub>27</sub> at 1 h, whereas Figure 4.2b represents the control that comprises only single type of probe. LSPR shift analysis showed a general trend of increased hybridization percentage with time (Figure 4.3a-c) relative to the control (Figure 4.3d). For all three duplex structures studied, the percentage of ‘yellow’ category remained low over time (Figure 4.3a-c), suggesting that small nanoassemblies (‘yellow’) are a transition state from unhybridized nAu (‘green’) to nanoassemblies (‘orange’). Note that in reality, each nAu of Scheme 4.1 was saturated with ssDNA probes. Due to the high density of ssDNA functionalized on the nAu surface, the nAu-DNA form very good co-operative hybridization/linking among each other. Besides, the flexible ssDNA enabled nAu to orient flexibly among each other so that more compact nanoassembly formed. It has been proven by other groups who have done 2-component hybridization that over time, plasmon absorption peak shifted gradually towards longer wavelength and TEM revealed increasingly more massive nanoassemblies. From Figure 4.3, at all time points, higher nAu concentration induced more hybridization, which can also be clearly seen in the dark field micrographs (Figure S4.1, Appendices). With more particles per unit volume, the number of effective collision among nAu increases, leading to higher chance of DNA hybridization and nanoassembly formation.



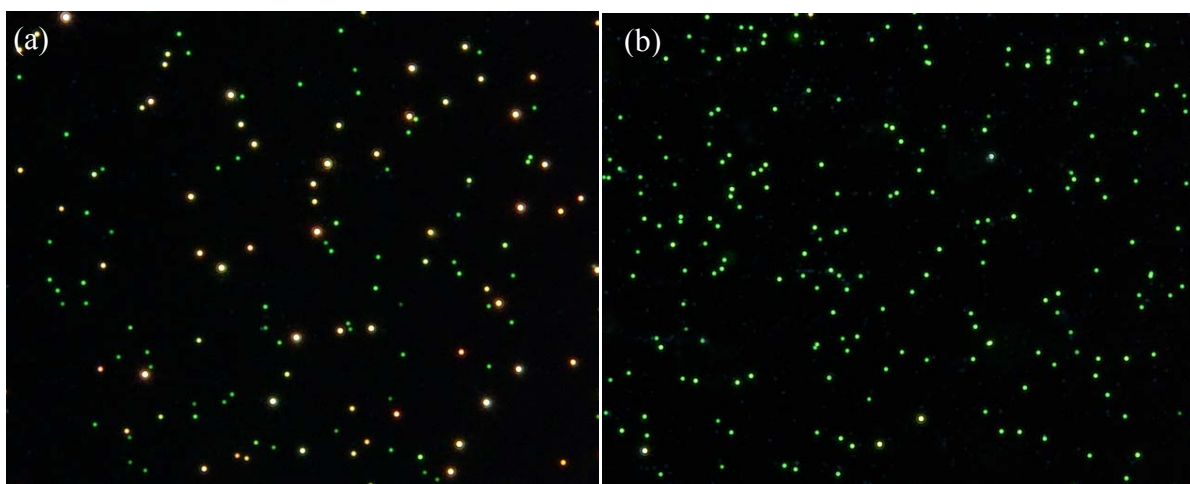
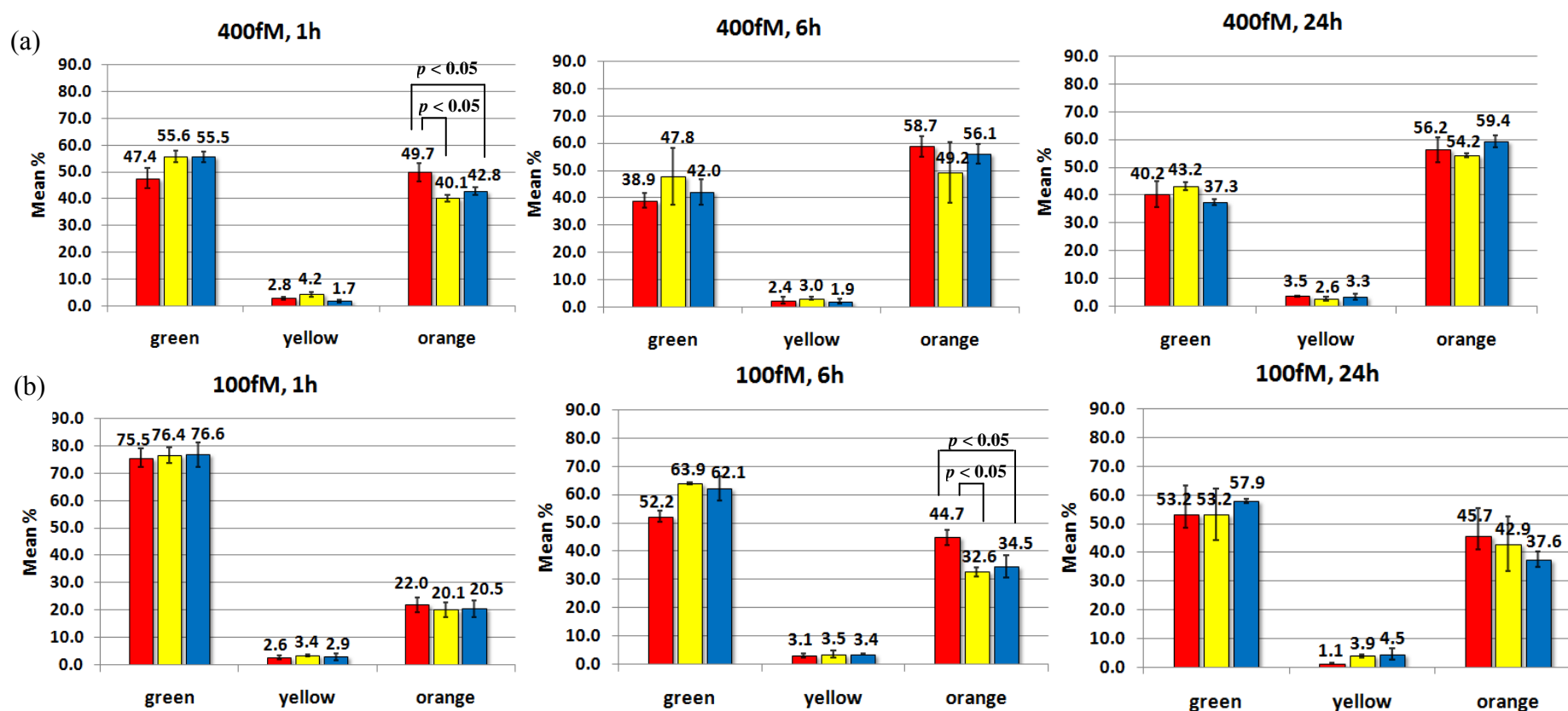


Figure 4.2: Probe Concentration & Hybridized Duplex Length Study (Scheme 4.1). Dark field micrographs on (a) complementary probes nAu-P/nAu-cP<sub>27</sub> hybridized at constant ratio of 1/1 and concentration 400 fM, (b) control comprises only single type of probe, both recorded after 1 h-hybridization. The scattering colour of control remains more than 95% green even after 24 h. Images were taken from the bottom plane of liquid chamber, to which particles settled. Buffer: 140 mM Tris, 140 mM NaCl, 2 mM MgCl<sub>2</sub>.

For the 400 fM probe concentration (Figure 4.3a), P/cP<sub>27</sub> (red bar), with complementary sequences 9 bp more than P/cP<sub>18</sub> (yellow bar) and 13 bp more than P/cP<sub>14</sub> (blue bar), appeared to have higher degree of hybridization than the other two did after 1 h ( $p$ -value < 0.05). These affirmed that the hybridization efficiency increases with longer complementary sequences,<sup>[152,222]</sup> although the distinction between P/cP<sub>18</sub> and P/cP<sub>14</sub> was not clear at this probe concentration. The degree of hybridization for P/cP<sub>27</sub>, P/cP<sub>18</sub>, and P/cP<sub>14</sub> peaked at 6 h and did not exhibit any increase from 6 h to 24 h, indicating that hybridization may have achieved equilibrium within the first 6 h.



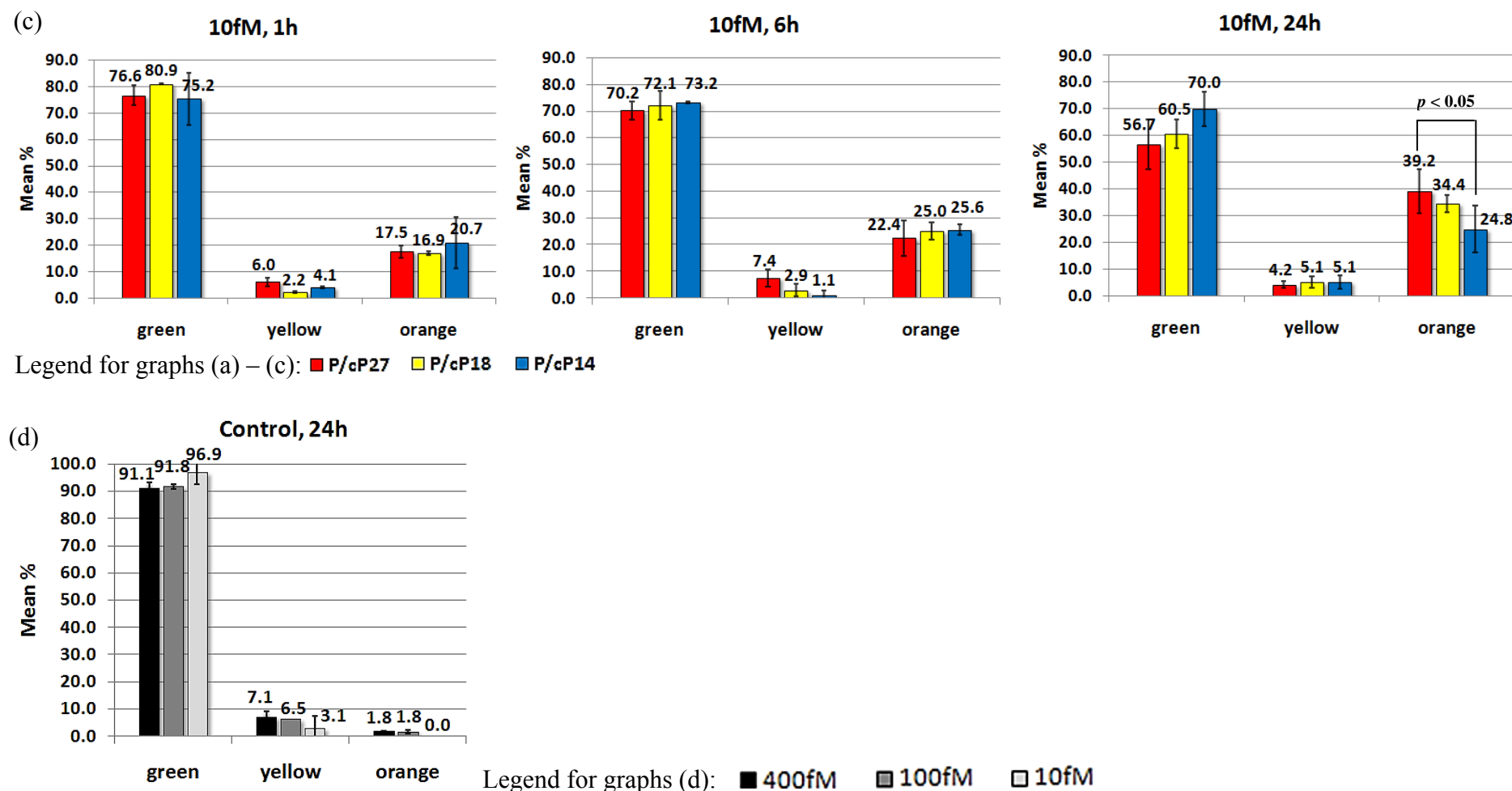


Figure 4.3: Probe Concentration & Hybridized Duplex Length Study (Scheme 4.1). The charts summarize the hybridization percentage between complementary probes nAu-P/nAu-cP<sub>27</sub> (red bars), nAu-P/nAu-cP<sub>18</sub> (yellow bars), and nAu-P/nAu-cP<sub>14</sub> (blue bars), at decreasing concentration of (a) 400 fM, (b) 100 fM, and (c) 10 fM while the ratio is kept at 1/1. The analysis is performed by counting the hybridized-clusters (categorized as ‘yellow’ & ‘orange’ due to their distinct LSPR plasmon shift) vs. the individual probes (categorized as ‘green’). The

corresponding controls are illustrated in (d) for 400 fM (black bars), 100 fM (grey bars), and 10 fM (light-grey bars) where only a single type of probe exists, thus no hybridization take place. Each set of data in (a)-(d) consists of three repeats. Buffer: 140 mM Tris, 140 mM NaCl, 2 mM  $\text{MgCl}_2$ .

The effect of complementary duplex length on hybridization percentage was not obvious at 400 fM, but it was so at 100 fM (Figure 4.3b). After 6 h, P/cP<sub>27</sub> (red bar) showed the highest percentage ( $p$ -value < 0.05), compared with P/cP<sub>18</sub> (yellow bar) and P/cP<sub>14</sub> (blue bar), both of which exhibited similar percentages. At 24 h, however, all three pairs exhibited statistical equivalence in their hybridization percentages.

For the lowest nAu concentration of 10 fM (Figure 4.3c), the hybridization percentages were low even after 24 h incubation. As a result, the effect of duplex lengths on nanoassembly formation shown in Scheme 4.1 was only obvious between P/cP<sub>27</sub> and P/cP<sub>14</sub> at 24 h ( $p$ -value < 0.05). Out of the three duplex structures, P/cP<sub>27</sub> showed faster hybridization kinetics than the other two owing to its more stable duplex linker, which enhance co-operative linking. From the dark field micrographs, we can achieve a detection limit of about 6000 nAu.

Hybridization of free DNA in solution proceeds with relatively fast kinetics and reaches thermodynamic equilibrium in seconds or minutes. The stability of the hybridized DNA duplexes depends mainly on the complementary duplex length. However, the hybridization kinetics slows down substantially when the DNA are covalently bound<sup>[223-224]</sup> on nAu,<sup>[152]</sup> and parameters such as nAu concentration, hybridization time as well as complementary duplex length all affect the degree of hybridization and consequently the nanoassembly formation. As shown in Figure 4.3, the degree of hybridization of DNA-modified nAu in bulk solution decreased with lower nAu concentrations and shorter duplex lengths, but it increased with the progression of time. In addition, system with longer duplex sequence reached equilibrium in shorter time, and the equilibrium was only observed at the highest nAu concentration of 400 fM within the investigation period of 24 h (Figure 4.3a). Although bulkiness of nAu can slow down hybridization kinetics, in our case of homogeneous hybridization (i.e. in bulk solution), appreciable hybridization was observed

within 1 min after mixing of complementary probes in the 400 fM sample and, to lesser extent, in the 100 fM sample (Figure S4.2, Appendices). This is substantially faster compared with the surface-bound hybridization reported in the literature, mostly likely due to additional interfacial restriction by the surface-bound particles.<sup>[219]</sup>

#### **4.3.3 Size Effect Study (Scheme 4.1 vs. Scheme 4.2)**

To gain more information regarding the effect of nAu size on nanoassembly formation, we fixed one 50 nm nAu probe and varied the size of the complementary probe, in which 10 nm nAu was for its better size contrast against 50 nm nAu, and 20 nm nAu for its lower plasmon scattering contrast against 50 nm nAu. Thus, hybridization between complementary 50nm/50nm probes (homo-size system, Scheme 4.1), 50nm/20nm probes (hetero-size system, Scheme 4.2a), and 50nm/10nm probes (hetero-size system, Scheme 4.2b) were carried out at 1/1 molar ratio of 800 fM. All the nAu were fully saturated with ssDNA on their surfaces.

The hybridization percentage for 50nm/50nm homo-size system were high, and the reaction almost reached equilibrium after 1 h (Figure 4.4a); whereas the hybridization percentages for both 50nm/20nm and 50nm/10nm hetero-size system were surprisingly low (Figure 4.4b and 4.4c respectively), and there was a continual increment in hybridization as time elapsed. In addition, the coupled-plasmon colour change due to hybridization of 50nm/10nm probes (Figure S4.3 IIIa, Appendices) was not as significant as that of 50nm/20nm probes (Figure S4.3 IIa), which in turn was not as significant as that of 50nm/50nm probes (Figure S4.3 Ia).

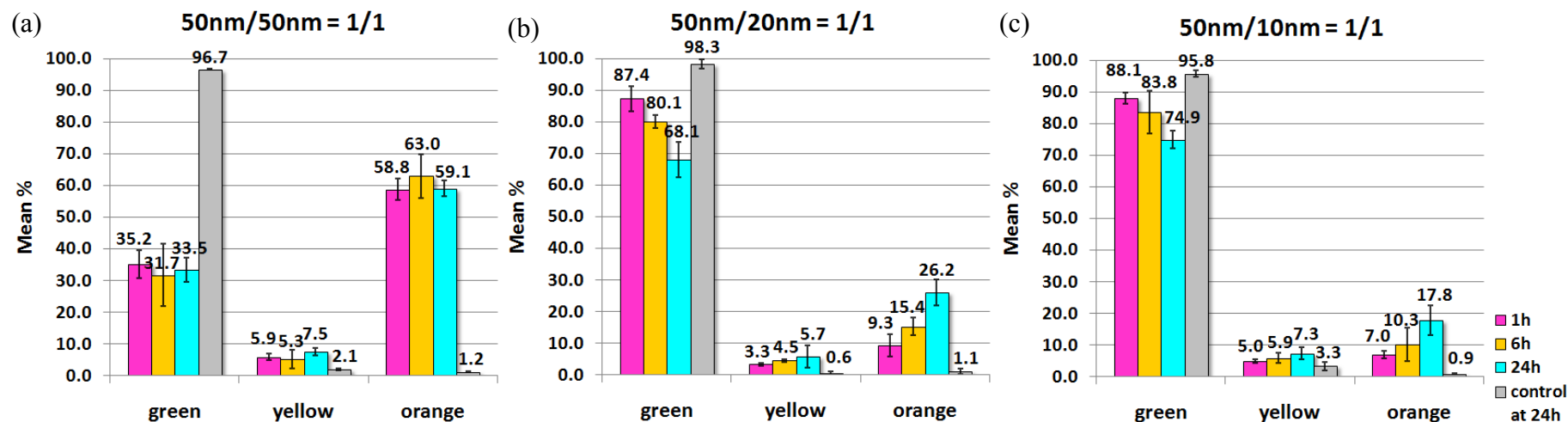


Figure 4.4: Size Effect Study (Scheme 4.1 vs. Scheme 4.2) at 1 h, 6 h, and 24 h. Hybridization percentage between nAu-P/nAu-cP<sub>27</sub> for (a) homo-size system with same probe size (50nm/50nm), (b) hetero-size system with different probe sizes (50nm/20nm), and (c) hetero-size system with different probe sizes (50nm/10nm). Ratio of complementary probes: 1/1; concentrations of all species: 800 fM. Data for homo-size system is the average of three repeats; for hetero-size system, each data reported consists of four repeats, two with 50 nm nAu-P / 20 nm or 10 nm nAu-cP<sub>27</sub>, and the other two with 20 nm or 10 nm nAu-P / 50 nm nAu-cP<sub>27</sub>. Images are quantified by counting the hybridized-clusters ('yellow' & 'orange') vs. the individual probes ('green'). The corresponding controls for (a) homo-size system comprises single type of 50 nm probe at 1.6 pM, and for (b) hetero-size system, comprises 800 fM 50 nm probe & 800 fM 20 nm or 10 nm probe, both carrying the same type of ssDNA sequences. Buffer: 140 mM Tris, 140 mM NaCl, 2 mM MgCl<sub>2</sub>.

It is well known that both the LSPR scattering cross-section and magnitude increase tremendously with the increase in nAu size. Here, 50 nm nAu possess sufficiently high light scattering yield<sup>[18]</sup> and the strong plasmon scattering can be easily detected under the current dark field setup. Besides, the high and nearly saturated ‘orange’ hybridization percentage after 1 h (Figure 4.4a) indicated that hybridization between complementary 50 nm probes was relatively easy. Hill et al.<sup>[225]</sup> have reported that DNA coverage on 60 nm nAu and planar gold films were similar, and this shows that 60 nm nAu exhibit near planar surface curvature in terms of DNA loading. The quasi-planar surface curvature<sup>[225]</sup> of 50 nm nAu can be expected to induce more than one hybridization between two 50 nm nAu to form stable nanoassemblies. This was evidenced by the low percentages of the ‘yellow’ category and high percentages of the ‘orange’ category in the 50nm/50nm system at all time points (Figure 4.4a). Therefore, we deduce that stronger plasmon coupling between complementary 50nm/50nm homo-size probes and more stable links between neighbouring nAu cause more nanoassemblies (‘orange’) to form than small nanoassemblies (‘yellow’), and leave relatively small amount of free ‘green’ particles, which is then reflected as the nearly-saturated high hybridization efficiency. Notice that for the fairly small 50 nm nAu and relatively large interparticle separation, we need not consider the multipole resonance contribution from 50 nm nAu.<sup>[24,218]</sup>

For the 50nm/20nm and 50nm/10nm hetero-size systems, hybridization was originally thought to be easier due to the higher surface curvature (hence higher deflection angle and less DNA crowding)<sup>[225]</sup> and higher mobility exhibited by the smaller 20 nm and 10 nm nAu. However, their observed hybridization percentages (Figure 4.4b, c) were much lower than the 50nm/50nm homo-size system. Based on the size-dependent optical properties of metallic nanoparticles, the plasmon scatterings from a 20 nm and 10 nm nAu are reported to be 240 and 15,000 times weaker than a 50 nm nAu.<sup>[18]</sup> The inherent plasmon scattering from 10 nm



nAu is so weak that by itself alone no visible scattering is detectable under the current condition. As a result, the weak surface plasmon of 10 nm nAu induces relatively weak plasmon coupling between 50 nm and 10 nm nAu, and may cause indiscrete and unobservable plasmon shift even when the 50 nm nAu is hybridized a few 10 nm nAu. We were unable to determine the minimal number of 10 nm and 20 nm nAu required to attach on a 50 nm to bring upon an observable change in the plasmon colour due to the instrumental limitations in our electron microscopy.<sup>[219]</sup> Secondly, a 50 nm nAu with relatively larger surface area is able to hybridize to more 10 nm nAu, and reduces the available free 10 nm nAu<sup>[226]</sup> and may leave many 50 nm nAu unhybridized. It is expected that, most small nAu have already hybridized to large nAu within the first hour owing to the high ssDNA density on the nAu surfaces. However, the weak coupled-plasmon shift results in the low observable hybridization percentage as a whole. This is further supported by the stronger plasmon shift of 50nm/20nm (Figure S4.3 IIa) compared to 50nm/10nm (Figure S4.4 IIIa). We believe that given longer time than 24 h, hybridization percentage of ‘orange’ category for both hetero-size systems would be elevated even higher.

With hybridization between complementary 50nm/10nm probes in 1/3 ratio (Figure S4.4b), more nanoassemblies with multiple 50 nm probes were observed at the same time frame than that of 1/1 ratio (Figure S4.4a). From the structure of nanoassemblies (Figure S4.4), most 10 nm nAu were trapped in between 50 nm nAu, making the 10 nm nAu not accessible to bridge with other 50 nm nAu. When the molar ratio increases, additional 10 nm nAu allow more bridging between the 50 nm nAu and hence results in the observed larger nanoassembly size. Similar binary nAu networks was reported<sup>[227]</sup> using 31nm/8nm probes in 1/120 ratio, and core-satellite structures began to form.

It is important to highlight that all the data tabulated in this work are reproducible. For example, statistics based on 10 frames (Figure S4.5a) or 30 frames (Figure S4.5b) of dark

field images show negligible difference between them, hence proving the validity of our quantification method.

#### **4.3.4 Surface-ssDNA Density Study (Scheme 4.2)**

In this study, the hetero-size systems were compared with the nAu bearing different surface-ssDNA densities. In the first set, all the nAu in both 50nm/20nm and 50nm/10nm hetero-size systems were fully saturated with ssDNA (Figure 4.5 Ia and IIa, denoted as 50nm/20nm and 50nm/10nm respectively). The percentages of nanoassemblies continued to increase from 1 h to 24 h, and the fractions of ‘yellow’ relative to ‘orange’ category at all time frames were small and always less than unity. In the second set, 50 nm nAu were fully saturated with ssDNA but the 20 nm and 10 nm nAu were each conjugated with only 5 ssDNA followed by a monolayer of short oligonucleotides (dT<sub>5</sub>) for surface passivation (Figure 4.5 Ib and IIb, denoted as 50nm/20nm(low) and 50nm/10nm(low) respectively). Consequently, the percentages of 50nm/20nm(low) nanoassemblies (Figure 4.5 Ib) reduced substantially from 1 h to 24 h compared to 50nm/20nm (Figure 4.5 Ia), with the most apparent reduction in the ‘orange’ nanoassemblies. The same trend was observed for 50nm/10nm(low) nanoassemblies (Figure 4.5 IIb) compared to 50nm/10nm (Figure 4.5 Ia). The percentages of 50nm/10nm(low) nanoassemblies also showed negligible change from 1 h to 24 h, and the fraction of ‘yellow’ relative to ‘orange’ category were always high and greater than unity. The low hybridization percentages were most likely due to the ineffective collision between the 50 nm and 20 nm or 10 nm nAu, the latter conjugated with low density of ssDNA.

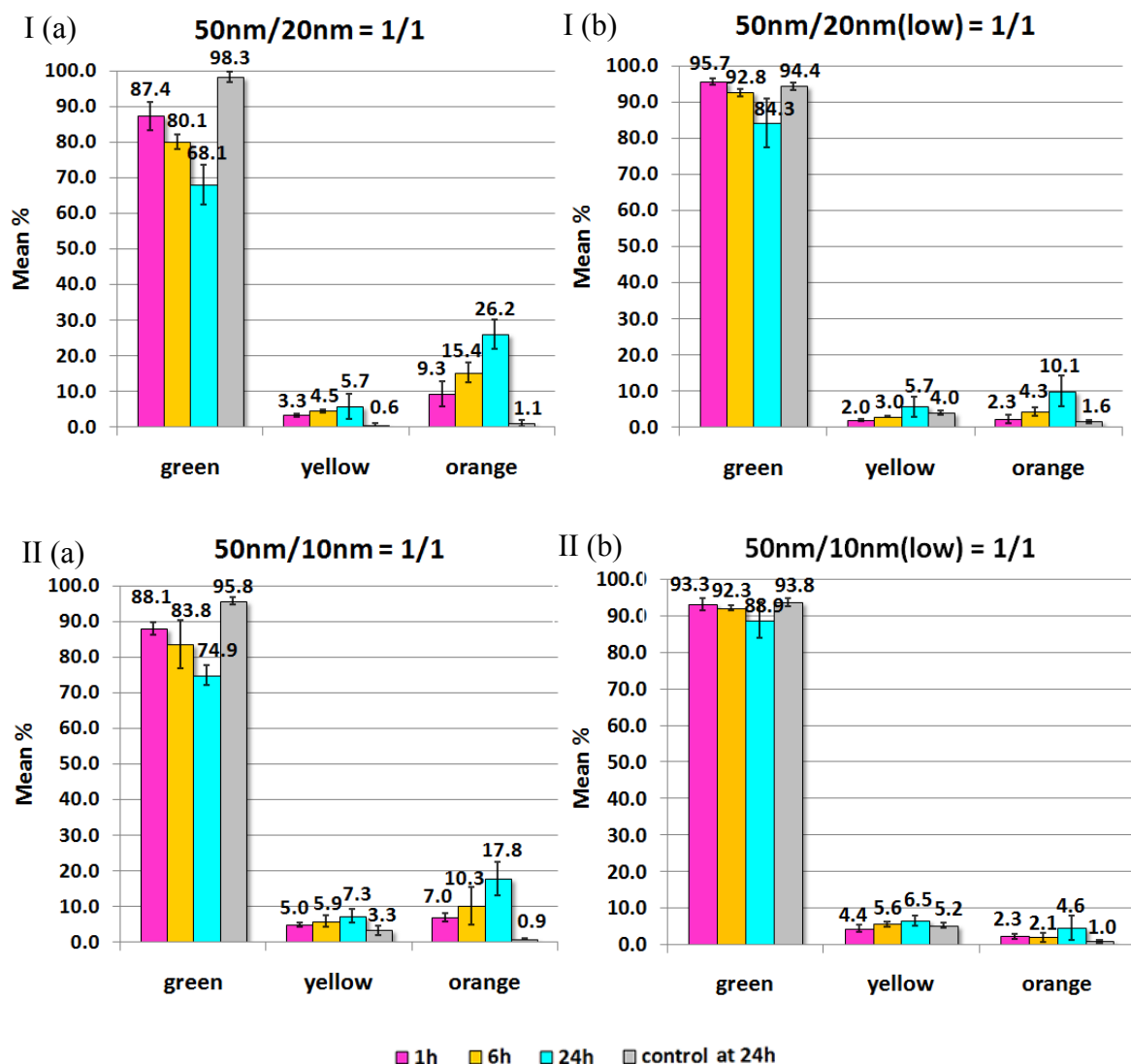


Figure 4.5: Surface-ssDNA Density Study (Scheme 4.2) at 1 h, 6 h, and 24 h. Hybridization percentage between nAu-P/nAu-cP<sub>27</sub> for (I) 50nm/20nm hetero-size system with the 20 nm nAu (a) fully saturated with ssDNA, or (b) bearing only 5 ssDNA, and for (II) 50nm/10nm hetero-size system with the 10 nm nAu (a) fully saturated with ssDNA, or (b) bearing only 5 ssDNA. Ratio of complementary probes: 1/1; concentrations of all species: 800 fM. Each data reported consists of four repeats, two with 50 nm nAu-P / 20 nm or 10 nm nAu-cP<sub>27</sub>, & the other two with 20 nm or 10 nm nAu-P / 50 nm nAu-cP<sub>27</sub>. Images are quantified by counting the hybridized-clusters ('yellow' & 'orange') vs. the individual probes ('green'). The corresponding controls comprise 800 fM 50 nm probe & 800 fM 20 nm or 10 nm probe, both carrying the same type of ssDNA sequences, for (a) fully saturated and (b) 5-ssDNA-bearing 20 nm or 10 nm nAu. Buffer: 140 mM Tris, 140 mM NaCl, 2 mM MgCl<sub>2</sub>.

Apparently, reducing the surface-ssDNA density of 10 nm nAu resulted in the observed extremely low hybridization percentage of 50nm/10nm(low) system compared to 50nm/10nm system. This is not unexpected because the low surface-ssDNA density on 10

nm(low) nAu certainly reduces the number of effective collisions and imposes more steric constraint to form multi-50 nm nanoassemblies. The already weak plasmon coupling between 50 nm and 10 nm nAu (Size Effect Study, *vide supra*) are now aggravated by the even lower hybridization kinetics brought by 10 nm(low) nAu. On the other hand, 10 nm nAu which are fully saturated with ssDNA enable multiple hybridization events to construct multi-50 nm nanoassemblies. This explains why the 50nm/10nm nAu system exhibited faster hybridization than 50nm/10nm(low) system. Finally, 50nm/20nm(low) exhibited the higher degree of nanoassembly formation (Figure 4.5 Ib) compared with 50nm/10nm(low) (Figure 4.5 IIb), most likely due to the stronger scattering yield of 20nm. This shows that small nanoparticles are not as good as their larger counterparts in dark field detection.

#### **4.4 Conclusion**

Using Rayleigh scattering as a signal readout platform, we are able to detect/visualize the progress of nanoassembly formation of complementary nAu-DNA probes at as low as 10 fM concentration. Three studies were conducted to gain knowledge on the hybridization process of the nAu-DNA probes. For the first study, we found that hybridization of the complementary 50 nm nAu at equal amount increased with increasing nAu concentration, longer hybridization time, and longer complementary duplex DNA length. In the second study, due to the size-dependent optical scattering of nAu, higher hybridization percentages were observed in 50nm/50nm homo-size system compared to the 50nm/20nm hetero-size system, which in turn were higher than 50nm/10nm hetero-size system. For the third study, hybridization efficiency of the 50nm/20nm and 50nm/10nm hetero-size systems was significantly reduced by the low surface-DNA density on 20 nm and 10 nm nAu. Added together, our findings showed that the nanoassembly formation can be controlled by various parameters, namely the concentration and molar ratio of complementary nAu-DNA,

hybridization length of duplex DNA, and surface-DNA density of the nanoparticles. Besides, this work highlights the importance of using nanoparticles with sufficient light scattering yield to facilitate the detection of nanoassembly formation by optical scattering. The information carried here is thus useful for the development of a number of assays designing to study conveniently the biomolecule interaction by the aid of specifically chosen nanoparticle system.

## CHAPTER 5: HEAD-TO-TAIL: HYBRIDIZATION AND SINGLE-MISMATCH DISCRIMINATION IN METALLIC NANOPARTICLE-DNA ASSEMBLY

(Paper reprints from *RSC Advances*<sup>[228]</sup>)

### 5.1 Introduction

There are a number of well-established and standard diagnostic methodologies to detect known mismatch base pairing, to name a few, microarray genotyping (hybridization to oligonucleotide arrays), hybridization protection assay, allele-specific oligonucleotide hybridization (hybridization with sequence-specific oligonucleotides), allele-specific amplification, ligase-mediated detection, primer extension and restriction fragment analysis (artificial introduction of restriction sites).<sup>[229-231]</sup> The clever grafting of single-stranded DNA (ssDNA) onto nano-metallics has further inspired the use of wide-ranging DNA-nanoparticle conjugates in the DNA hybridization research.<sup>[125,232-233]</sup> Due to the unique dielectric properties of noble metals, the noble metal nanoparticles exhibit localized surface plasmon resonance (LSPR) in the visible region, an exclusive feature attributable to the collective oscillation of conduction electrons excited at optical frequency.<sup>[81]</sup> Hybridization of complementary ssDNA with the ssDNA conjugated on nanoparticles induces assembling or agglomeration of the nanoparticles<sup>[125,233]</sup> and consequently reduces the energy of the concerted surface plasmon, which then functions as a convenient readout.<sup>[234]</sup>

The strong affinity of sulfur to gold<sup>[194]</sup> has prompted the remarkable use of thiolated DNA-modified gold nanoparticle (nAu-DNA) in the gene detection.<sup>[235]</sup> Because of the relative size, nAu are generally regarded as ‘head’ and the DNA as ‘tail’ in the nAu-DNA conjugates. For three-component or sandwich assays, there are three ways in which the nAu-DNA can bind to the target gene/ssDNA, i.e. tail-to-tail, head-to-tail, and head-to-head.<sup>[127,233]</sup> Despite their sizes in nanometer range, nAu are still much bulkier than the flexible DNA molecules and hence pose movement constraints in the nAu-DNA system compared to the

free-DNA system.<sup>[236]</sup> While head-to-head structure imposes substantial spatial interference to target ssDNA hybridization and thus is scarcely used,<sup>[127,204,237]</sup> tail-to-tail assay that extends the bulky nanoparticles away from each other and introduces the least interparticle repulsion and steric hindrance has been widely applied.<sup>[114,125,127,140,204,238]</sup>

Comparatively fewer works employ head-to-tail structure. Among the existing literatures, head-to-tail alignment has been used mainly in structural templating, such as testing the structural rigidity of DNA-assembled aperiodic nAu dimers and trimers,<sup>[216]</sup> preparation of 4  $\mu\text{m}$  linear-1D nAu-array on a long repetitive 10 kb ssDNA,<sup>[239]</sup> and formation of discrete nAu assemblies on a rigid ring ssDNA templates.<sup>[240-241]</sup> Under certain circumstances e.g. when the target ssDNA templates contain multiple repetitive recognition sequences, the head-to-tail alignment has an advantage of using only a single type of nAu-DNA probe for target hybridization.<sup>[216,239]</sup> Besides structural templating, the head-to-tail structure is also harnessed to perform detection. For instance, 3-dimensional extensive aggregates of a single type of nAu-DNA linked by a DNAzyme served as a colorimetric lead ion sensor upon the  $\text{Pb}^{2+}$ -catalyzed hydrolytic cleavage.<sup>[242]</sup> The use of multiple head-to-tail nAu-DNA alignments has been shown to enhance further the colorimetric shift and scattering intensity, and thus improved the detection sensitivity compared to a single head-to-tail structure.<sup>[243]</sup> Apart from these directions, head-to-tail alignment is less exploited in differentiating complementary vs. mismatch targets DNA. Amidst the existing literatures, this structure has been used to discriminate against targets DNA with base-deletions and multiple-mismatches.<sup>[126,244]</sup> A known work discriminating single-mismatch DNA with the head-probe required precise temperature control to destabilize the nanoassemblies under a thin-layer chromatography (TLC) readout.<sup>[126]</sup> Another work used the Raman dye-coded nAg-DNA to discriminate the single-mismatches at tail-probe at considerably high concentrations of target oligonucleotides (nM).<sup>[167]</sup> To the best of our knowledge, the application of head-to-tail

assays in target DNA detection remains largely unexplored, and little efforts have been paid to examine the relation of head- and tail-probes in the mismatch discrimination.

In this study, we employed the less explored head-to-tail sandwich assay to investigate the hybridization and mismatch-discrimination properties using a readout that does not rely on accurate temperature control. Based on the plasmon coupling results from Chapter 4, only nAu with the strongest LSPR scattering i.e. mean diameter of 50 nm would be used for all the investigations performed henceforth. In particular, this study used head-to-tail alignment with the ssDNA tethered on nAu surface at 5' terminal via strong gold-thiol chemistry, which offers higher stability than the 3' terminal configuration.<sup>[112,245]</sup> We envisage that the nAu alignment in the head-to-tail orientation would render the head- and tail-probes with different target recognition capability against single-mismatch targets ssDNA (different mismatch sites correspond to head- and tail-probes). Our findings confirmed that the tail-probe exhibits greater mismatch-discrimination than the head-probe. Single-mismatches on the tail-probe were further analyzed, and the results showed that both mismatch position and mismatch type influence the nanoassembly formation. Finally, the head-to-tail assay was extended to perform hybridization on targets with non-hybridizing elongated sequences, which is common condition in the detection of endogenous nucleic acids extracted from cells<sup>[246]</sup> and as functional DNA (DNAzyme,<sup>[242]</sup> aptamer,<sup>[247-250]</sup> or aptazymes<sup>[251]</sup>). The results showed that while the non-hybridizing elongated sequence reduces the nanoassembly formation efficiency, it enhances the single-mismatch discrimination. Overall, our findings confirmed that the unique nAu-DNA alignment in head-to-tail structure may be used to enhance the mismatch-discriminations.



## 5.2 Experimental Section

### 5.2.1 Materials

Hydrogen tetrachloroaurate (III) trihydrate, trisodium citrate dehydrate, tannic acid, silver nitrate, 4,4'-(phenylphosphinidene)-bis-(benzenesulfonic acid) (PPBS), sodium dodecyl sulfate (SDS), sodium chloride, magnesium chloride hexahydrate were purchased from Sigma-Aldrich. Synthetic single-stranded DNA (ssDNA) strands (unmodified or modified with the terminal 5' alkanethiol group, Table 5.1) were purchased from Proligo. Tris buffer (pH 8.0) was purchased from 1st Base. Milli-Q water with resistance >18 MΩ/cm was used throughout the experiments.

Table 5.1: List of DNA sequences used in this study. The underlined portions represent complementary sequences that hybridize. T and H denote the main ssDNA probes that were conjugated on nAu surface. P denotes unmodified ssDNA targets that are complementary to a portion of T and H. The bold characters indicate the single-mismatch bases.

Name	Oligonucleotide sequences
<i>Probe DNA conjugated on nAu</i>	
<b>T</b>	HS - 5'- C <sub>6</sub> - TTT TTT TTT TTT TTT CTG <u>TCG TAA TAG TGA GAT</u> - 3'
<b>H</b>	HS - 5'- C <sub>6</sub> - TTT TTT TTT TTT TTT <u>ATG AAT GGT GTA GTG</u> GTC - 3'
<i>Target DNA for hybridization</i>	
<b>P</b>	5' - <u>AC TAC ACC ATT CAT ATC TCA CTA TTA CG</u> - 3'
<b>MH</b>	5' - <u>AC TAC ACA ATT CAT ATC TCA CTA TTA CG</u> - 3'
<b>MT<sup>[a]</sup></b>	5' - <u>AC TAC ACC ATT CAT ATC TCA GTA TTA CG</u> - 3'
<b>MT1</b>	5' - <u>AC TAC ACC ATT CAT TTC TCA CTA TTA CG</u> - 3'
<b>MT2</b>	5' - <u>AC TAC ACC ATT CAT ATA TCA CTA TTA CG</u> - 3'
<b>MT3<sup>[a]</sup></b>	5' - <u>AC TAC ACC ATT CAT ATC TCA GTA TTA CG</u> - 3'

---

<b>MT4</b>	5' - <u>AC TAC ACC ATT CAT ATC TCA CTC TTA CG</u> - 3'
<b>MT5</b>	5' - <u>AC TAC ACC ATT CAT ATC TCA CTA TTA GG</u> - 3'
<b>MT6</b>	5' - <u>AC TAC ACC ATT CAT ATC TCA CTA TTA CT</u> - 3'
<b>P60</b>	5' - <u>AC TAC ACC ATT CAT ATC TCA CTA TTA CG</u> TTT TTT TTT TTT TTT TTT TTT TTT TTT TTT TT - 3'
<b>P61</b>	5' - TTT TTT TTT TTT TTT TTT TTT TTT TTT TTT TTT <u>AC TAC ACC ATT CAT ATC TCA CTA TTA CG</u> - 3'
<b>P90</b>	5' - TTT TTT TTT TTT TTT TTT TTT TTT TTT TTT T T <u>AC TAC ACC ATT CAT ATC TCA CTA TTA CG</u> TTT TTT TTT TTT TTT TTT TTT TTT TTT TTT T - 3'
<b>nc100</b>	5' - TTA CAT TAA CTT TGA TCA TCG TGC TGG CGA TTG ACT TTG GAC AGT TAA TCT AAT CAA AGA GGC TAT GCA GAA AAC TAT TTT ATG AAC AAA AGT CCC AGT A - 3'
<b>MT60</b>	5' - <u>AC TAC ACC ATT CAT ATC TCA GTA TTA CG</u> TTT TTT TTT TTT TTT TTT TTT TTT TTT TTT TT - 3'
<b>MH60</b>	5' - <u>AC TAC ACA ATT CAT ATC TCA CTA TTA CG</u> TTT TTT TTT TTT TTT TTT TTT TTT TTT TTT TT - 3'
<b>MT61</b>	5' - TTT TTT TTT TTT TTT TTT TTT TTT TTT TTT TTT <u>AC TAC ACC ATT CAT ATC TCA TTA TTA CG</u> - 3'
<b>MH61</b>	5' - TTT TTT TTT TTT TTT TTT TTT TTT TTT TTT TTT <u>AC TAC ACA ATT CAT ATC TCA CTA TTA CG</u> - 3'

---

<sup>[a]</sup> MT and MT3 are identical to each other

### 5.2.2 Synthesis and characterization of nAu

The synthesis and characterization of 50 nm spherical gold nanoparticles (nAu), as well as the quality of the synthesis are described in detail in Chapter 3.

### 5.2.3 Fabrication of nAu-DNA probes

Two ssDNA, strand T and H, both carrying an alkanethiol group at their 5' terminals (Table 5.1, *Probe DNA conjugated on nAu*), were used to fabricate two sets of 50 nm nAu-DNA probes by direct oxidative addition in this study.<sup>[220-221]</sup> Prior to conjugation, 50 nm nAu were passivated with PPBS, and then ssDNA was incubated with the nAu at 1000:1 ratio (ssDNA:nAu). After 2 h incubation, NaCl concentration was increased slowly to 80 mM over 2 days in 0.02% SDS. Excess reagents were removed by repeated washing and centrifugation. The resulting conjugates are denoted as nAu-T (corresponds to tail-probe) and nAu-H (corresponds to head-probe) respectively, and they were used as probes in the subsequent target DNA detection studies.

### 5.2.4 Detection of ssDNA targets

The ssDNA sequences used as targets to form head-to-tail structure with the nAu-DNA probes are shown in Table 5.1 (*Target DNA for hybridization*). The probes nAu-T and nAu-H (at concentration of 1 pM nAu each) were allowed to hybridize with the target ssDNA in hybridization buffer (140 mM Tris, 140 mM NaCl, 2 mM MgCl<sub>2</sub>). Briefly, the sample mixture was first heated to 50 °C for two minutes to ensure complete melting of any duplex strands, followed by slow cooling to 24 °C at a rate of 0.2 °C/min for annealing. All the samples were then analyzed at the desired time points, i.e. 1 h and 24 h by sandwiching 1 µL of the sample droplets between cover slip & microscope glass slide. Hybridization among the target with the probes would then direct nAu-T to form the 'tail' and nAu-H 'head' in the head-to-tail sandwich construct. The hybridization efficiency of such construct was next examined under an upright microscope (Nikon Eclipse 50i) equipped with a dark-field oil condenser (NA 1.2-1.43, CytoViva) and a metal halide illuminator (Welch Allyn) as the white light source. Scattered light from nAu was collected by a 100× objective lens (Nikon

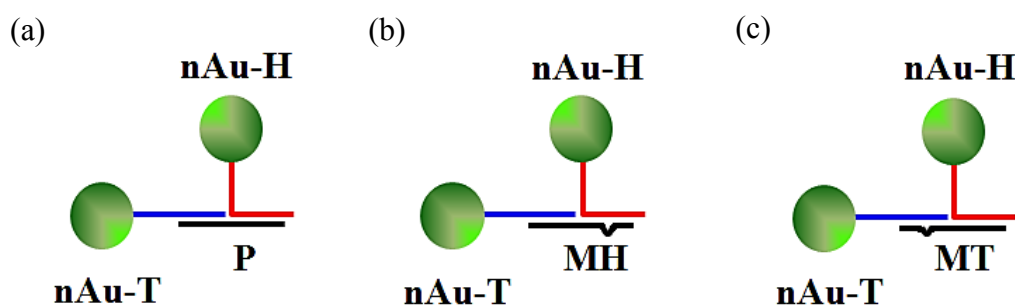
Plan Fluor 100×, NA 0.5-1.3 oil iris, W.D. 0.16 mm) and directed to colour CCD camera (Nikon Digital Sight DS-Ri1) for real-colour imaging and locating the individual nanoparticles. The image acquisition (24-bit true colour TIF files, 20 ms integration time, and 5.6× gain) and analysis were performed using NIS-element AR 3.1 software (Nikon). Statistical analysis, wherever applicable, was done using Student's *t*-test. The imaging process was conducted at ambient temperature. The following three studies, each repeated at least in triplicate to ensure reproducibility, were investigated in this work to assay the head-to-tail alignment.

**A. Perfectly match vs. single-mismatch targets DNA** (Scheme 5.1): Three types of short targets ssDNA were hybridized individually to probes nAu-T and nAu-H: 28 b perfectly match target (P, Scheme 5.1a), 28 b target with a single-mismatch site to H (MH, Scheme 5.1b), and 28 b target having a single-mismatch site to T (MT, Scheme 5.1c). Distinction among P, MH, and MT was examined at target ssDNA concentrations of 4 pM.

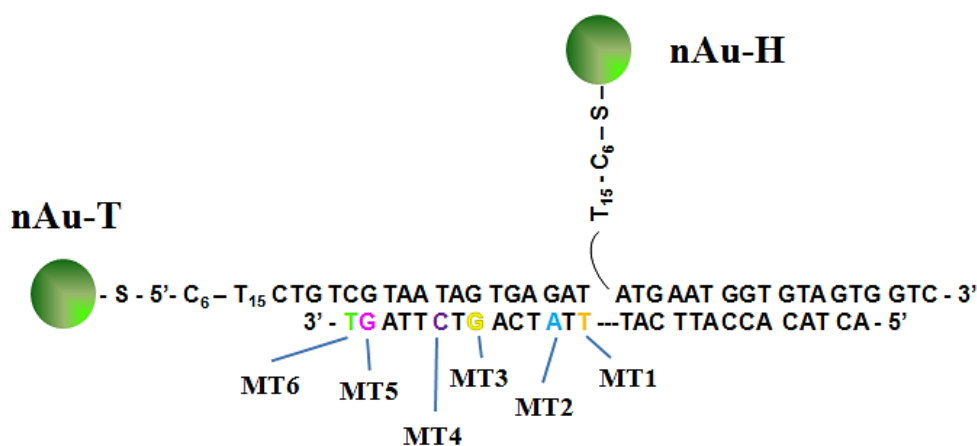
**B. Targets DNA with different single-mismatch sites to tail-probe / nAu-T** (Scheme 5.2): Three groups of 28 b targets ssDNA with different single-mismatch sites to probe nAu-T were studied by analyzing their hybridization efficiency: end-mismatches (MT1 & MT6), near-end-mismatches (MT2 & MT5), and middle-mismatches (MT3 & MT4). Distinction among P and these single-mismatch variants was examined at target ssDNA concentrations of 4 pM.

**C. Targets DNA with non-hybridizing sequence elongation** (Scheme 5.3): Probes nAu-T & nAu-H were hybridized to targets ssDNA akin to Scheme 1, except that the targets now have non-hybridizing base sequences elongated towards nAu-T and/or nAu-H. P60, MT60 and MH60 (Scheme 5.3I) are 60 b targets containing 32 b elongation towards nAu-T; P61, MT61 and MH61 (Scheme 5.3II) are 61 b targets containing 33 b elongation

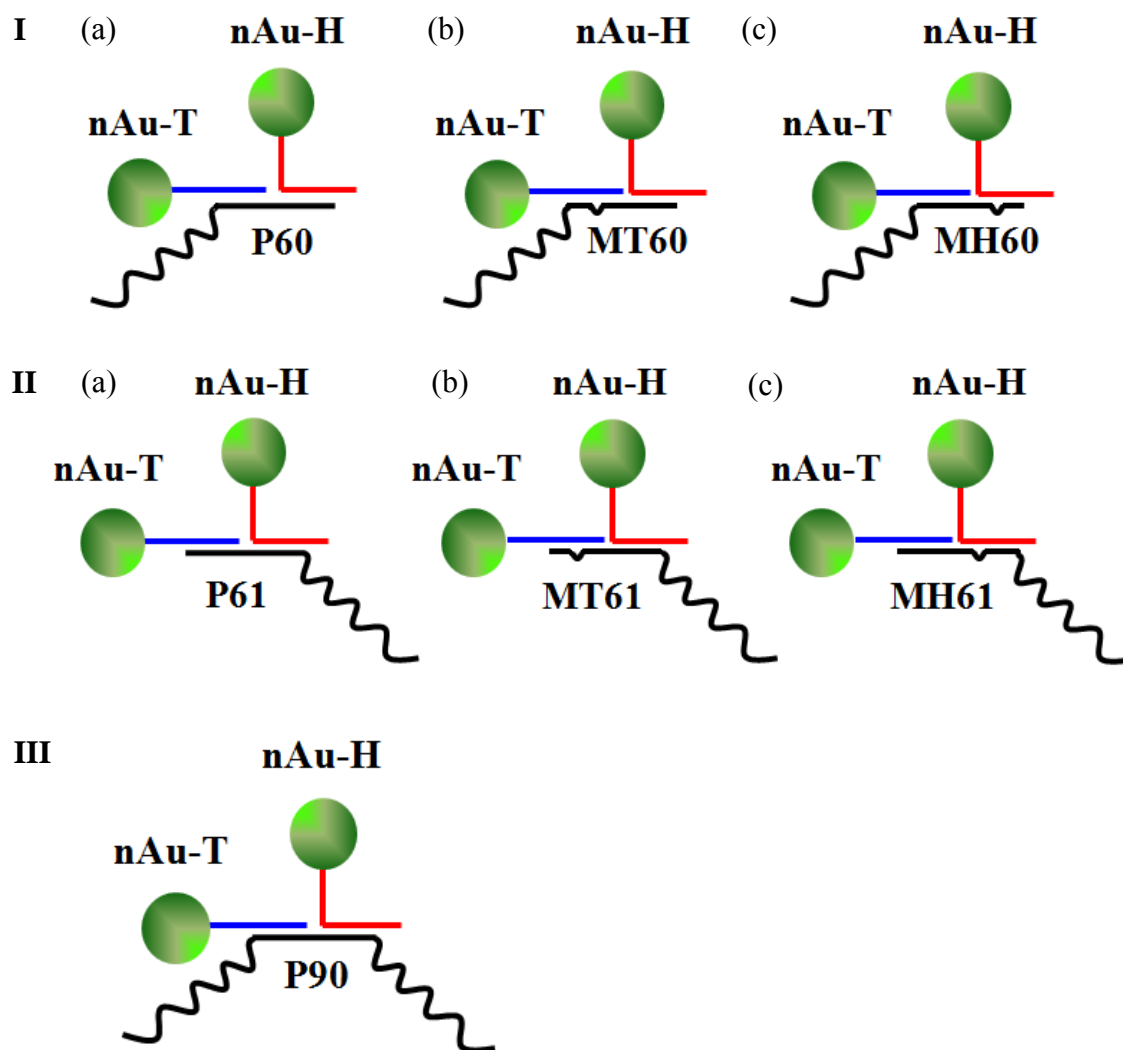
towards nAu-H; whereas P90 (Scheme 5.3III) is a 90 b target containing two 31 b elongated sequences towards both nAu-T and nAu-H. Among the targets, MT60 and MT61 have single-mismatches to T, MH60 and MH61 have single-mismatches to H, while P60, P61, and P90 are perfectly match targets.



Scheme 5.1: Gold nanoparticle conjugates functionalized with ssDNA sequences T (blue line) and H (red line) hybridizing onto (a) perfectly match target P, (b) single-mismatch target MH, and (c) single-mismatch target MT (all in black lines). Note that in reality, each nAu is saturated with ssDNA probes on its surface. The figures are not drawn to scale.



Scheme 5.2: Gold nanoparticle conjugates functionalized with ssDNA sequences T and H hybridizing onto unmodified target ssDNA carrying a single mismatch to probe nAu-T. End-mismatches: MT1 & MT6, near-end-mismatches: MT2 & MT5, middle-mismatches: MT3 & MT4. The figures are not drawn to scale.



Scheme 5.3: Gold nanoparticle conjugates functionalized with ssDNA sequences T (blue line) and H (red line) hybridizing onto (I) unmodified 60 b target (a) P60 (b) MT60 and (c) MH60, (II) unmodified 61 b target (a) P61 (b) MT61 and (c) MH61, (III) unmodified 90 b target P90 (all the targets are in black lines). Non-hybridizing portion of the targets are represented by the winding curves. Note that in reality, each nAu is saturated with ssDNA probes on its surface. The figures are not drawn to scale.

## 5.3 Results and Discussion

### 5.3.1 Probes and hybridization design

The rationale of our readout strategy is based on the unique surface plasmon coupling of spherical gold nanoparticles (nAu). While a single unhybridized nAu-DNA appears as green spot under dark field mode, hybridized nAu-DNA nanoassembly scatters longer

wavelengths and appears as yellow to orange spots. This plasmon red shift enables a distinctive recognition of any possible hybridization in the presence of a complementary DNA. The extent of hybridization for a target DNA can then be quantified by counting the amount of yellow and orange nAu-DNA nanoassemblies from dark field micrographs. To represent better each hybridization event, ten dark field micrographs were taken from different locations of each sample and the numbers of nanoassemblies were summed up. For each data reported, at least three samples were used for averaging the nanoassembly counts. The analysis of nAu-DNA nanoassemblies derived from the surface plasmon resonance shift was detailed in our earlier work.<sup>[178]</sup>

As a common notation in nAu-DNA conjugates,<sup>[233]</sup> nAu are generally assigned as ‘head’ and the DNA as ‘tail’. Thus, in the current head-to-tail sandwich structure, the targets DNA were designed such that upon hybridization, probe nAu-T and nAu-H would bind respectively as the tail-probe and head-probe (see Scheme 5.1). Due to the shorter spacing between nAu, the head-to-tail aligned nAu system is thermodynamically less favored (lower melting temperature) compared to tail-to-tail aligned nAu system.<sup>[249]</sup> This higher steric obstruction property of head-to-tail orientation should therefore aid in the single-mismatch target DNA discrimination.

### **5.3.2 Perfectly match vs. single-mismatch targets DNA (Scheme 5.1)**

The hybridization and single-mismatch discrimination abilities of the head-to-tail assay were evaluated using three targets DNA: 28 b perfectly match P (Scheme 5.1a) to both T and H; 28 b single-mismatch MH (Scheme 5.1b) with a mismatch site to H; and 28 b single-mismatch MT (Scheme 5.1c) with a mismatch site to T.

With a 4 pM target DNA concentration (Figure 5.1), nanoassemblies formed by P (red bar) showed the highest increase from 1 h to 24 h. Within the same period, nanoassemblies

formed by MH (yellow bar) increased moderately, whereas nanoassemblies of MT (blue bar) showed the lowest increase compared to both P and MH. The single-mismatch discrimination factor of the assay can be defined by the ratio  $C_P/C_M$ , in which  $C_P$  and  $C_M$  represent the absolute counted nanoassemblies formed by perfectly match targets and single-mismatch targets respectively. In this regard, a greater discrimination factor indicates higher specificity.  $C_P/C_{MH}$  was measured to be consistently  $\approx 2$  at all time points, whereas  $C_P/C_{MT}$  displayed considerable improvement from 1 h ( $= 1.5$ ) to 24 h ( $> 3$ ). The noise of the sample was found to be low based on the counts of control taken at 24h (pink bar), in which no target DNA was present. The corresponding dark field micrographs for the nanoassemblies formed by hybridization to P, MH, and MT, as well as the control are shown in the Appendices (Figure S5.1).

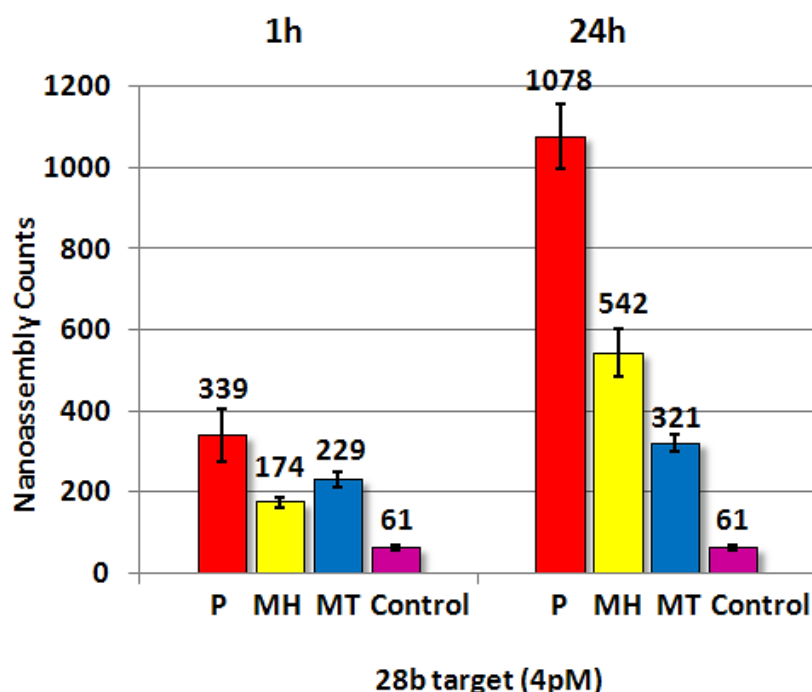


Figure 5.1: (Scheme 5.1) The counted nanoassemblies formed by hybridizing nAu-T and nAu-H to 28 b targets of perfect-match P (red bar), ‘head’-single-mismatch MH (yellow bar), and ‘tail’-single-mismatch MT (blue bar) at 4 pM target concentration. The control (pink bar) was taken at 24 h in the absence of target. Each sample contains 1 pM of nAu-T and 1 pM of nAu-H. Each set of data consists of three repeats. Buffer: 140 mM Tris, 140 mM NaCl, 2 mM  $MgCl_2$



Hybridization of nAu-DNA to the terminus of a long target ssDNA has been shown to be higher than to the centre of the target. This can be attributed to the steric hindrance imposed by the bulky gold probe, which makes it harder for nAu-DNA to gain access to the hybridization site situated at the target centre.<sup>[252]</sup> From the construction of the three-component head-to-tail structure (Scheme 5.1), nAu lying outside the duplex region induces smaller steric hindrance than nAu situated within the duplex. Thus, hybridization of P with nAu-T would be more efficient than that with nAu-H. Hybridization of nAu-T to MT would then be less effective due to the single-mismatch, and for any MT that first binds to nAu-H, the bulky nAu of nAu-H pose a substantial steric hindrance to any incoming nAu-T. When the target is MH, nAu-T that have already bound to MH would impose lesser steric hindrance to any incoming nAu-H. Our results confirm the above statements because less nanoassembly formation was observed with MT than MH after 24 h (Figure 5.1), and the discrimination factor for  $C_P/C_{MT}$  was larger than that for  $C_P/C_{MH}$ . Therefore, the unique head-to-tail nAu alignment validates better discrimination for the single-mismatch site at the tail-probe over head-probe, and this might mostly be the reason for Graham group<sup>[167]</sup> to position the single-mismatches on the tail-probe.

It is noteworthy to point out that the ssDNA spacer between nAu and the recognition sequences plays an important role in facilitating the hybridization and mismatch-discrimination. For instance, replacing the current 15-thymine spacer of H to a shorter 6-thymine spacer impedes much of the nanoassembly formation (data not shown). This is not unexpected considering the bulk size of 50 nm nAu. In addition, nAu with larger size can be applied to improve further the single-mismatch discrimination. The current system was not optimized in terms of the ssDNA spacer length and the nAu size, but both parameters should play critical parts in the hybridization process. At this moment, this unoptimized assay was able to obtain a detection limit of 4-zeptomole of target ssDNA at 4 pM concentration.

### 5.3.3 Target DNA with different single-mismatch sites correspond to tail-probe / nAu-T (Scheme 5.2)

With the findings in Scheme 5.1 demonstrating that the single-mismatch site located at T (tail-probe) has greater sensitivity than single-mismatch located at H (head-probe), in this section, the effect of single-mismatch positions at T was further investigated. As shown in Scheme 5.2, three mismatch positions, namely middle-mismatch (MT3 & MT4), near-end-GC-mismatch (MT2 & MT5), and end-mismatch (MT1 & MT6) were studied. Among the target variants, MT1 and MT4 are AT-mismatches while the rest are GC-mismatches.

In Figure 5.2, a perfectly match target P (red bar) was used as a ruler to compare the effect of various single-mismatch sites, namely end-AT-mismatch MT1 (orange bar), near-end-GC-mismatch MT2 (light blue bar), middle-GC-mismatch MT3 (yellow bar), middle-AT-mismatch MT4 (purple bar), near-end-GC-mismatch MT5 (pink bar), and end-GC-mismatch MT6 (green bar). In the absence of target DNA, the control (grey bar) showed insignificant nanoassembly formation with negligible changes between 1 h and 24 h.

At 1 h (Figure 5.2a), perfectly match target P only exhibited a significant difference against middle-GC-mismatch MT3 ( $p < 0.05$ ) with  $C_P/C_{MT3} \approx 2$ , whereas no difference was observed compared to middle-AT-mismatch MT4. There was no difference between target P and other single-mismatch targets (end-AT-mismatch MT1, near-end-GC-mismatch MT2, near-end-GC-mismatch MT5, and end-GC-mismatch MT6) at 1 h. Therefore, GC-mismatch at middle of the target (MT3) is most destabilizing of all target variants.

At 24 h (Figure 5.2b), target P showed statistical difference against all of its single-mismatch variants ( $p < 0.05$ ), i.e. end-AT-mismatch MT1 ( $C_P/C_{MT1} = 2$ ), near-end-GC-mismatch MT2 ( $C_P/C_{MT2} > 3$ ), middle-GC-mismatch MT3 ( $C_P/C_{MT3} > 3$ ), middle-AT-mismatch MT4 ( $C_P/C_{MT4} > 3$ ), near-end-GC-mismatch MT5 ( $C_P/C_{MT5} > 3$ ), and end-GC-mismatch MT6 ( $C_P/C_{MT6} \approx 3$ ). The lower discrimination for P against MT1 was due to the

least destabilizing effect of AT-mismatch located at the end position. Note that at 6 h (data not shown), target P was still indistinguishable from end-AT-mismatch MT1, whereas it already showed statistical difference ( $p < 0.05$ ) against the rest of the mismatches (MT2 to MT6). At 24 h, among the single-mismatch targets, the effect of middle-mismatch vs. near-end-mismatch was comparable, as evidence by the indistinguishable counts for middle-GC-mismatch MT3, middle-AT-mismatch MT4, near-end-GC-mismatch MT2, and near-end-GC-mismatch MT5. All middle- and near-end-mismatches showed  $C_P/C_{MT} > 3$  relative to target P. Our results also showed that the discrimination factors between AT- and GC-mismatches were not distinctively different, for either the end-mismatches (MT1 & MT6) or middle-mismatches (MT3 & MT4) from 1-24 h. It is noteworthy to point out that, MT1, but not MT6, showed statistically difference ( $p < 0.05$ ) to both middle-mismatches (MT3 & MT4) and near-end-mismatches (MT2 & MT5). The low single-mismatch discrimination factor for MT1 and its significant difference against middle- and near-end-mismatches further support that AT-mismatch located at the end position is least destabilizing. This finding matches well with the absorption-based DNA analysis using LNA-modified gold nanoparticles in a tail-to-tail alignment.<sup>[113]</sup> Note that the results for P and MT/MT3 in Figures 5.1 and 5.2 are from the similar experimental conditions (as both used the same sequences at the same concentrations). The slightly different results could likely be attributed to batch-to-batch variations during the sampling.

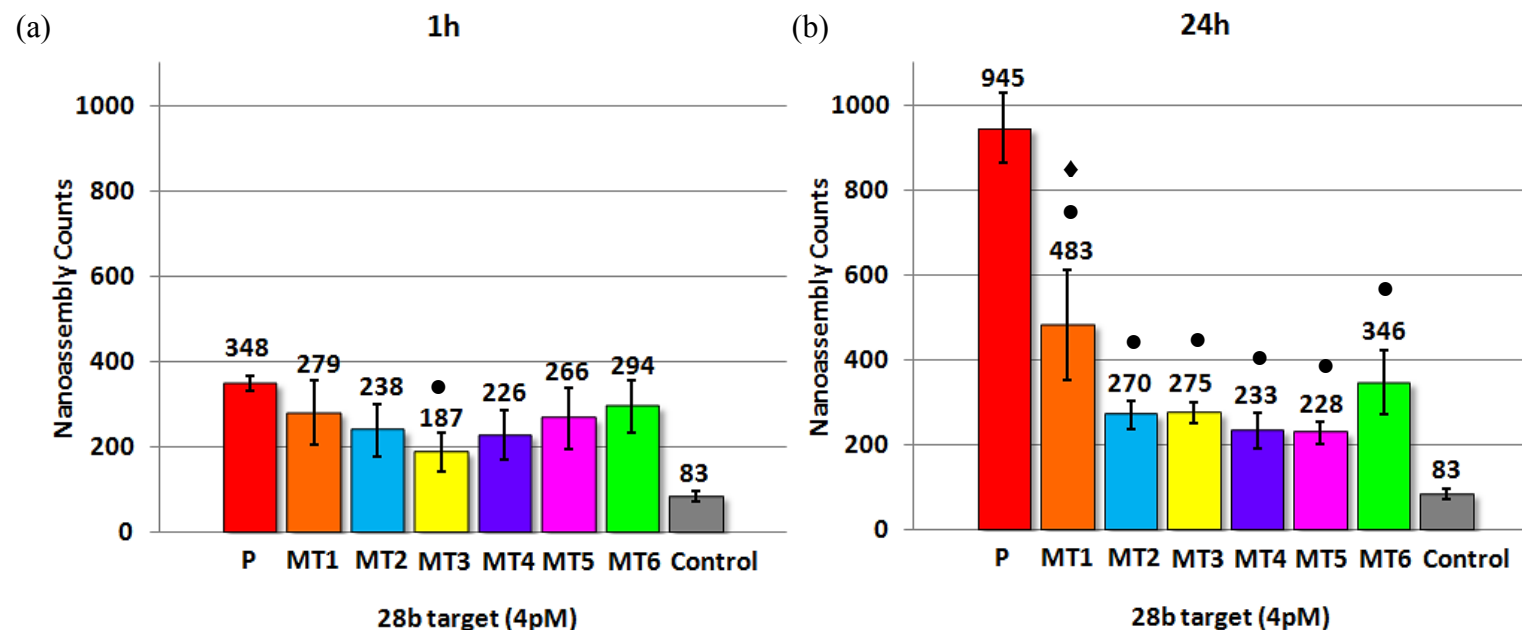


Figure 5.2: The counted nanoassemblies formed by hybridizing nAu-T and nAu-H to 28 b targets of perfect-match P (red bar), end-AT-mismatch MT1 (orange bar), near-end-GC-mismatch MT2 (light blue bar), middle-GC-mismatch MT3 (yellow bar), middle-AT-mismatch MT4 (purple bar), near-end-GC-mismatch MT5 (pink bar), and end-GC-mismatch MT6 (green bar). The data of control (grey bar) is taken in the absence of target. The counts are measured after (a) 1 h, and (b) 24 h of hybridization. Each sample contains 1 pM of nAu-T, 1 pM of nAu-H and 4 pM of target ssDNA. Each data consists of three repeats. Buffer: 140 mM Tris, 140 mM NaCl, 2 mM MgCl<sub>2</sub>

Note: ● Statistical difference ( $p < 0.05$ ) compared to P; ♦ Statistical difference ( $p < 0.05$ ) compared to MT2, MT3, MT4, and MT5

#### 5.3.4 Target DNA with non-hybridizing sequence elongation (Scheme 5.3)

In this section, the head-to-tail assay was extended to detect for longer target DNA with elongated sequences that are non-hybridizing to the nAu-DNA probes (Scheme 5.3). Scheme 5.3Ia shows the hybridization of probes nAu-T and nAu-H to a target DNA with 32 b elongated sequence towards nAu-T (P60). Its corresponding single-mismatch sequences MT60 and MH60 are shown in Scheme 5.3Ib and 5.3Ic respectively. Similarly, Scheme 5.3IIa describes the hybridization of probes nAu-T and nAu-H to a target DNA with 33 b elongated sequence towards nAu-H (P61). Its corresponding single-mismatch sequences MT61 and MH61 are then shown in Scheme 5.3IIb and 5.3IIc respectively. In Scheme 5.3III, the target DNA (P90) possesses two 31 b elongated sequences towards both nAu-T and nAu-H.

At 1 h (Figure 5.3a), P60 (red bar) did not differ markedly from the single-mismatches MT60 (orange bar) and MH60 (yellow bar), whereas P61 (green bar) showed statistically higher nanoassembly counts ( $p < 0.05$ ) than MT61 (blue bar) and MH61 (light blue bar). At 24 h (Figure 5.3b), P60 and P61 showed significant hybridization ( $p < 0.05$ ) compared to their single-mismatch counterparts, i.e. MT60, MH60, MT61, and MH61 with  $C_P/C_M > 3$ . This implies that the non-hybridizing sequences could further improve the mismatch discrimination (compared to Scheme 5.1), albeit with higher target DNA concentration (40 pM) and longer incubation time. The elongated targets DNA were investigated at the higher concentration in which the perfectly match targets formed noticeable nanoassemblies. Increasing the length of non-hybridizing sequences has been reported to reduce the assembly kinetics and melting temperature in a tail-to-tail assay.<sup>[253]</sup> As the non-hybridizing sequences were found to cause a negligible melting temperature change in the free DNA system,<sup>[253]</sup> it indicates that the bulky nAu contributes to the majority steric hindrance in this head-to-tail hybridization assay. We have tested the similar assay at a lower

target concentration of 4 pM (data not shown) but the insignificant nanoassembly formation proved that there exists certain degree of repulsion between the elongated non-hybridizing sequence and the nAu.

Based on the results at 1 h and 24 h, the positions of the elongated sequence at either 5' (for P61) or 3' (for P60) did not seem to have any effect on the nanoassembly formation efficiency. However, extension of non-hybridizing sequence towards the head-probe (Scheme 5.3II) seems to bring better discrimination ability to the system. This is probably due to the greater steric hindrance between the bulky nAu and the non-hybridizing sequence when the sequence is extended towards the tail-probe (Scheme 5.3I). Nevertheless, P90 (purple bar) with a 31 b sequence elongation at both sides showed a considerable drop in the counted hybridized nanoassemblies. Since the hybridization sites are located at the centre of P90, steric hindrance from both sides of the elongated sequences may block both nAu-DNA probes from hybridizing with P90. This result is in agreement with the literature finding, where steric hindrance towards hybridization can become more significant when the nAu-DNA probes hybridize to the centre of a target ssDNA.<sup>[252]</sup> Finally, non-complementary DNA with 100 base-length (nc100) showed negligible nanoassemblies formed (grey bar) compared to the control without targets (pink bar), and this further confirmed the specificity/selectivity of the current assay.

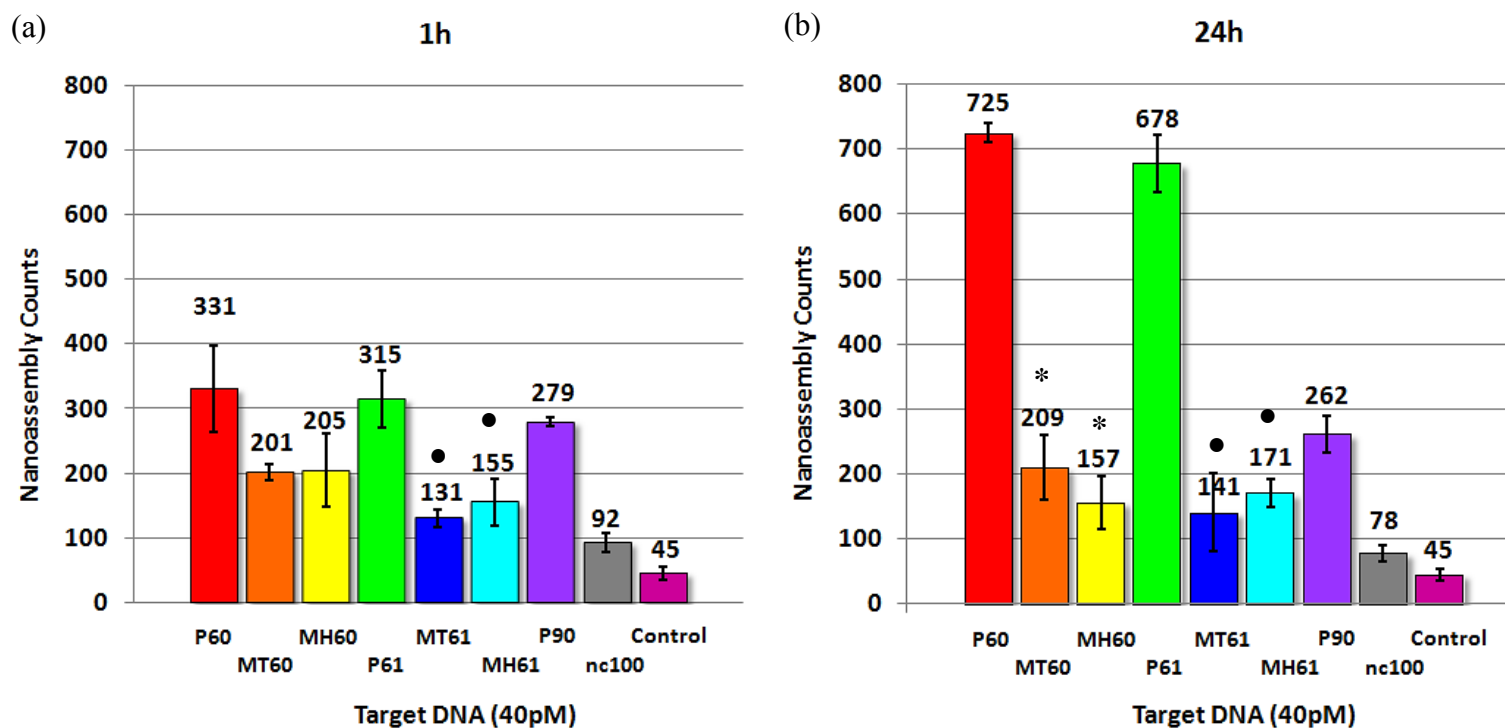


Figure 5.3: The nanoassemblies formed at (a) 1 h and (b) 24 h, by hybridizing nAu-T and nAu-H to targets with non-hybridizing sequences elongated towards nAu-T (P60 - perfect-match, red bar; MT60 & MH60 - single-mismatches, orange & yellow bars respectively), targets with non-hybridizing sequences elongated towards nAu-H (P61 - perfect-match, green bar; MT61 & MH61- single-mismatches, blue & light blue bars respectively), with non-hybridizing sequences elongated towards both nAu-T and nAu-H (P90- perfect-match, purple bar), and with 100 b non-complementary target (grey bar). The data of control (pink bar) is taken in the absence of target. All the targets are at 40 pM while 100 b non-complementary target are at 400 pM. Each of the samples contains 1 pM of nAu-T and 1 pM of nAu-H. Each data consists of three repeats. Buffer: 140 mM Tris, 140 mM NaCl, 2 mM MgCl<sub>2</sub>

Note: • Statistical difference ( $p < 0.05$ ) compared to P61; \* Statistical difference ( $p < 0.05$ ) compared to P60

## 5.4 Conclusion

Based on the unique LSPR coupling properties of nAu, this study investigated the head-to-tail sandwich assay to discriminate perfectly match against single-mismatch targets ssDNA without relying on temperature control. The results showed that nAu-DNA functioning as tail-probe exhibit greater mismatch-discrimination than the head-probe. This can be attributed to the nAu alignment in the sandwich structure, which renders the head- and tail-probes with different target recognition capability. By analyzing the single-mismatches at tail-probe, it was found that both mismatch position and the mismatch type determine the nanoassembly formation. When subjected to hybridization with targets ssDNA having non-hybridizing elongated sequences, the head-to-tail assay differentiated single-mismatches with enhanced efficiency, though with more steric restriction. In summary, the findings provide useful insights to the single-mismatch discrimination ability of the less studied head-to-tail assay.



## **CHAPTER 6: MAGNETIC PARTICLE-ASSISTED SINGLE-MISMATCH DNA DETECTION VIA PLASMONIC SCATTERING OF GOLD NANOPARTICLES**

### **6.1 Introduction**

The search for methods to detect DNA at minute concentration from raw cellular samples has always been challenging. Apart from achieving a low limit of detection (LOD) sensitivity, it is vital to differentiate the fully complementary DNA from their mutants which hold one or more mismatched bases. This ensures the accurate DNA extraction, allowing the identification of genomic alleles and the discovery of coding sequence-related diseases. Hence, various approaches and engineering designs have been researched extensively to bring the LOD and the level of single-base mismatch (SBM) selectivity to as low DNA concentration as possible.<sup>[131,232,254-256]</sup>

One possible way to increase the sensitivity of detection is by amplification of the existing detected signal from the targeting sequence.<sup>[255]</sup> However, this can amplify the undesirable noise signal accordingly and may create false-positive result without further downstream separation. A more effective means to improve the detection sensitivity is by pre-concentrating or selecting the target DNA prior to the assaying events. For this purpose, magnetic microparticles (MMP) e.g. iron, cobalt, nickel, and their oxides<sup>[257]</sup> have been used routinely due to their superparamagnetic feature.<sup>[258-260]</sup> Advances in material technology enable the synthesis of stable MMP with surface-immobilized probe DNA (MMP-DNA), which can capture the targeted free DNA in aqueous easily following the regular Watson-Crick specificity. Then, an external magnetic field is used to induce magnetization in the superparamagnetic MMP and accumulate the originally dispersed MMP (hence the captured DNA) to facilitate the removal of supernatant which includes the interfering DNA. Subsequent magnetic field cut-off immediately decreases the magnetization of MMP to zero and releases them back into aqueous solution. As their magnetism only functions in the

presence of external magnetic field, besides nucleic acids, MMP modified with appropriate affinity molecules have been bestowed to aid in the sensing of other biomolecules such as proteins,<sup>[261]</sup> plant toxins,<sup>[262]</sup> as well as heavy metals such as mercury ions<sup>[263]</sup> in biological and environmental detections respectively.

Table 6.1 summarizes the works carried out in DNA sensing with the assistance from MMP and gold nanoparticles (nAu) or silver nanoparticles (nAg). They are categorized based on the individual readout strategies, namely localized surface plasmon resonance (LSPR), electrochemistry, luminescence, absorbance, atomic spectroscopy, and scanometry. Since the ultimate goal for these detections is to achieve the lowest measurable DNA concentration, the reported concentrations are classified separately as the lowest value at which the fully complementary target DNA can be differentiated from the control (LOD), as well as from the corresponding single-base mismatch DNA (SBM).

Table 6.1: DNA detection strategies with the aid of MMP and noble-metal nanoparticles

Readout	Mechanisms	LOD <sup>c</sup>	SBM <sup>a, c</sup>
Localized surface plasmon resonance (LSPR)	Absorbance Targets ssDNA were co-hybridized in sandwich format by probes MMP-ssDNA and nAu-ssDNA. All the captured nAu were isolated and then deposited with gold layers by reductant- and surfactant-aided autocatalysis of Au <sup>3+</sup> , <sup>[264-265]</sup> or by deposition of Ag <sup>+</sup> . <sup>[266]</sup> Plasmon absorbance of the enlarged nAu was quantified by UV-visible spectroscopy. The salt concentration could be optimized in order to increase the selectivity. <sup>[267]</sup>	1 pM <sup>[264]</sup> 1 fM <sup>[265]</sup> 10 fM <sup>[266]</sup> 0.1 fM <sup>[267]</sup>	100 pM <sup>[264]</sup> 10 pM <sup>[267]</sup>
	Colorimetric Biotinylated targets ssDNA were captured by MMP-streptavidin, which was followed by labeling with the complementary probes nAu-ssDNA or nAg-ssDNA. The isolated MMP-nAu/nAg hybrids were transferred to multi-well plate for visual detection. <sup>[268]</sup>	500 fmol <sup>[268]</sup>	500 fmol (2 b MM) <sup>b, [268]</sup>
	Scattering -	-	-
Electrochemistry	Differential pulse voltammetry (DPV): Targets ssDNA were co-hybridized in sandwich format by probes MMP-ssDNA and (i) ssDNA-biotin followed by labelling with nAu-streptavidin. The anchored nAu was oxidized electrochemically to AuCl <sub>4</sub> <sup>-</sup> . Subsequent potential scanning of DPV recorded the analytical signal of AuCl <sub>4</sub> <sup>-</sup> reduction at +0.4 V. <sup>[269]</sup> (ii) nAu-ssDNA bearing abundant cadmium phosphate-loaded apoferritin (CPLA) nanoparticles. Acidic dissolution of CPLA released the cadmium ions, which were pre-concentrated by anodic stripping to increase the assay sensitivity. The peak current measured by DPV at -0.66 V was correlated to the concentration of target DNA. <sup>[270]</sup>	0.66 μM <sup>[269]</sup> 51 aM <sup>[270]</sup>	26.7 μM <sup>[269]</sup> 2 fM (2 b MM) <sup>[270]</sup>
	Square wave anodic stripping voltammetry (SWASV): Targets ssDNA were co-hybridized in sandwich format by probes	0.5 ng/mL 50 pg/mL <sup>[271]</sup>	

<p>MMP-ssDNA and nAu-ssDNA that carried abundance of barcode ssDNA terminated with quantum dots. Acidic dissolution of the dots released heavy metal ions that were quantified by SWASV. Each type of ions gave its characteristic peak current, enabling simultaneous multiplex DNA detection. The signal was enhanced due to the amplifying quantum dots as well as the anodic stripping.<sup>[271]</sup></p>	1 fM <sup>[272]</sup>	
<p>Cyclic voltammetry (CV): Targets ssDNA were co-hybridized in sandwich format by probes MMP-ssDNA and nAu-ssDNA. The hybrids were deposited onto ferrocene-coated indium-tin oxide (ITO) electrode. Here, the gold functioned as catalyst to initiate the reduction of non-electroactive p-nitrophenol into electroactive p-aminophenol by NaBH<sub>4</sub>. Ferrocene then oxidized p-aminophenol into p-quinoneimine, generating a peak current at 0.35 V. Redox cycling of p-quinoneimine and p-aminophenol by NaBH<sub>4</sub> increased the sensitivity considerably.<sup>[272]</sup></p>		1 nM <sup>[272]</sup>
<p>Potentiometric stripping analysis (PSA): 2-component assay: biotinylated targets ssDNA were hybridized to probe MMP-ssDNA followed by binding with nAu-streptavidin. The captured nAu was deposited with gold/silver, and later dissolved to release the metal ions, which could be pre-concentrated for PSA.<sup>[273]</sup> The gold/silver enhancement could be omitted by replacing the nAu with polystyrene beads (PS) loaded with plentiful of nAu.<sup>[274]</sup> 3-component assay: more practically, unmodified targets ssDNA were co-hybridized as sandwich by probes MMP-ssDNA and PS-ssDNA bearing ample nAu. Gold layers were then deposited onto the nAu to raise the PSA sensitivity.<sup>[274]</sup></p>	<p>1.5 nM (Au precipitation) &amp; pM range (Ag precipitation)<sup>[273]</sup> 6 pM &amp; 150 pM (2- &amp; 3-component assay)<sup>[274]</sup></p>	<p>3.75 μM (no Au or Ag precipitation) (3 b MM)<sup>[273]</sup></p>

Fluorescence	Targets ssDNA were co-hybridized in sandwich format by probes MMP-ssDNA and nAu-ssDNA that is loaded with a surface monolayer of horseradish peroxidase (HRP). HRP amplified the target signal by catalyzing the oxidation of fluorescent substrate <sup>[275]</sup> and chromogenic reagent. <sup>[275]</sup>	1 pM (fluorescence) <sup>[275]</sup>	100 pM (absorbance) <sup>[275]</sup>
Luminescence	Targets ssDNA were co-hybridized in sandwich format by probes MMP-ssDNA and (i) biotinylated ssDNA, followed by labeling with PS-streptavidin, which in turn captured biotinylated nAu. Gold ions (Au <sup>3+</sup> , from the nAu dissolution) catalyzed the luminol oxidation, allowing the quantification of target DNA based on the luminol chemiluminescence signal. <sup>[276]</sup> (ii) probe nAu-ssDNA. The nAu did not require stripping and could directly catalyze the luminol-AgNO <sub>3</sub> chemiluminescence reaction. <sup>[277]</sup> (iii) probe nAu-ssDNA which also bore many barcode DNA terminated with tris-(2,2'-bipyridyl) ruthenium (TBR). Reaction of TBR with tripropylamine (TPA) produced electrogenerated species that emitted light, which constituted the electrochemiluminescence (ECL) signal. <sup>[278]</sup>	1 pM <sup>[276]</sup> 0.5 pM <sup>[277]</sup> 40 pM <sup>[278]</sup>	1 nM <sup>[276]</sup> 500 pM <sup>[277]</sup>
Absorbance	Targets ssDNA were co-hybridized in sandwich format by probes MMP-ssDNA and nAu-ssDNA that is loaded with a surface monolayer of horseradish peroxidase (HRP). HRP amplified the target signal by catalyzing the oxidation of chromogenic substrate in the presence of hydrogen peroxide. By cross-linking the captured nAu-ssDNA with complementary nAu-ssDNA that also carried HRP monolayer, the assay sensitivity could be further improved due to the increased HRP activity. <sup>[279]</sup>	10 pM <sup>[279]</sup>	100 pM <sup>[279]</sup>

Atomic spectroscopy	Mass spectroscopy (MS)	Targets ssDNA were co-hybridized in sandwich format by probes MMP-ssDNA and nAu-ssDNA that was loaded with abundance of disulfide oligo-ethylene glycols (OEG). The mass detection of OEG with different molecular weight enabled multiplex differentiation of DNA from the single-mismatch ones using matrix-assisted laser desorption/ionization time-of-flight mass spectrometry (MALDI-TOF-MS) <sup>[280-281]</sup> Genomic DNA were able to be distinguished from the mutant without the need for polymerase chain reaction (PCR). <sup>[281]</sup>	1 fM <sup>[280]</sup> 0.1 fM <sup>[281]</sup>	10 nM <sup>[280]</sup> 10 nM <sup>[281]</sup>
	Atomic emission spectroscopy (AES)	Targets ssDNA were co-hybridized in sandwich format by probes MMP-ssDNA and nAu-ssDNA. The captured nAu were then dissolved in aqua regia and the gold element signal was detected under inductively coupled plasma atomic emission spectrometry (ICP-AES) <sup>[282]</sup>	350 pM <sup>[282]</sup>	-
Scanometry		Targets ssDNA were co-hybridized in sandwich format by probes MMP-ssDNA and nAu-ssDNA that also carried large amount of barcodes ssDNA. After magnetic separation, barcodes ssDNA were released and formed secondary sandwich between another set of nAu-ssDNA and DNA microarray. Further silver ions nucleation on the bound nAu grew the nanoparticle greyscale intensity. <sup>[246,283-286]</sup>	500 zM <sup>[283]</sup> 500 fM <sup>[284]</sup> 7 aM <sup>[285]</sup> 2.5 fM <sup>[246]</sup> (genomic DNA)	500 aM <sup>[283]</sup>

<sup>a</sup> The concentration values for target DNA detection are based on the single-base mismatch (SBM), unless specified otherwise

<sup>b</sup> MM is an acronym for ‘mismatch’

<sup>c</sup> LOD and SBM are strongly dependent on both the target DNA length and sequence; therefore, comparison among the assays is somewhat tricky without testing them using identical targets and experimental conditions.

To date, the lowest LOD is that from scanometry at 500 zM, equivalent to detecting 15 zmol synthetic target DNA in 30  $\mu$ L sample volume using an abundance of barcode DNA amplification approach.<sup>[283]</sup> Whereas the lowest SBM is also from the same system at 500 aM. Despite the high sensitivities, this 8-year-old DNA detection methodology was costly because 8 types of DNA have been employed. In addition, the assay required lengthy procedures including the barcode DNA dehybridization and collection, readout chip preparation and heterogeneous hybridization, as well as silver enhancement, all of which could introduce inaccuracies easily.<sup>[283]</sup> Even though the assay could be streamlined by utilizing the probe DNA conjugated on the nanoparticles directly (via DTT-liberation) as the barcode DNA for the readout chip, a minimum of 5 types of DNA was still required, along with the similar procedures which were complicated and error-prone, necessitating extreme care.<sup>[286]</sup> Albeit the relatively low LOD (51 aM) attained by the electrochemical detection, the system may not be robust in terms of SBM as only the result from two-base mismatch DNA was reported.<sup>[270]</sup> Likewise, the mass spectroscopic detection showed relatively high SBM (10 nM).<sup>[280-281]</sup> Conversely, homogeneous detection based on the localized surface plasmon resonance (LSPR) absorbance from the probe DNA-modified nAu (nAu-DNA) could reach 100 aM LOD and 10 pM SBM under salt optimizations.<sup>[267]</sup> In spite of the enzymatic catalysis, the luminescent method was not as selective as the strategies relying on the plasmonic characteristics.<sup>[275,277]</sup> All these SBM discrimination detection schemes have their own pros and cons, and no particular approach can reign supreme over the other.

From Table 6.1, the LSPR scattering phenomenon which has been studied comprehensively appears to receive comparatively little application in the MMP-assisted DNA sensing. Therefore, the scattering properties unique to noble metal nanoparticles were used in this work in order to explore the sensitivity level that can be achieved for both LOD and SBM. Also, based on the findings in Chapter 5, homogeneous DNA sensing exploiting

the plasmon coupling has intrinsic limitations in which the number of DNA targets involved in the actual hybridization process was underscored, and interference due to the unhybridized nAu could not be efficiently separated from the nanoassemblies using physical means. Consequently, a simple and direct DNA detection scheme was employed, in which the non-bleaching plasmonic scattering from the gold nanoparticles (nAu) contributed to the signal for assaying LOD and SBM. Owing to the strong LSPR scattering, nAu of average size 50 nm was chosen as reporter. The detected signal is not subjected to further complex development e.g. enzymatic amplification or metallic stripping, and does not require additional barcode DNA or chip-based hybridization. The system which has not been fully optimized yet shows good prospect and presents the LOD and SBM at 2 pM and 20 pM respectively. Further optimization would be able to bring the sensitivity and selectivity even lower than the current obtained values.

## **6.2 Experimental Section**

### **6.2.1 Materials**

Hydrogen tetrachloroaurate (III) trihydrate, trisodium citrate dehydrate, tannic acid, silver nitrate, 4,4'-(phenylphosphinidene)-bis-(benzenesulfonic acid) (PPBS), sodium dodecyl sulfate (SDS), sodium chloride, magnesium chloride hexahydrate, formamide, 2-(N-morpholino)ethane sulfonic acid monohydrate (MES), 1-ethyl-3-(3-dimethylaminopropyl) carbodiimide hydrochloride (EDC·HCl), N-hydroxysulfosuccinimide (NHSS) and synthetic single-stranded DNA (ssDNA) strands (unmodified or modified with the terminal 5' alkanethiol or 3' amino groups, Table 6.2) were purchased from Sigma-Aldrich. Magnetic microparticles with surface carboxyl groups (1  $\mu$ m, Dynabeads MyOne Carboxylic Acid, denoted as MMP-COOH hereafter) were purchased from Life Technologies. Tween-20 was purchased from USB Corporation. Ethylenediaminetetraacetic acid (EDTA) was purchased



from Biological Industries. Tris buffer (pH 8.0) and phosphate buffer saline (10x PBS) were purchased from 1st Base. Milli-Q water with resistance > 18 MΩ/cm was used throughout the experiments. Horizontal and rotational mixings were performed by shaker (Thermomixer Compact, eppendorf) and rotator (Rotator AG, Fine PCR), respectively. Sonication was carried out using an ultrasonicator (S30H Elmasonic).

Table 6.2: List of DNA sequences used in this study. The similar underlined portions represent complementary sequences that hybridize. T, H, C and rC denote the probes ssDNA that were conjugated on nAu, whereas H<sub>M</sub> and T<sub>M</sub> was immobilized on the MMP surface. P denotes unmodified ssDNA that is fully-complementary to T and H<sub>M</sub> or H and T<sub>M</sub>, PM denotes unmodified ssDNA that is fully-complementary to T and H<sub>M</sub>, while MH & MT and SM are single-mismatch variants to P and PM respectively.

Name	Oligonucleotide sequences
<i>Probe DNA conjugated on nAu</i>	
<b>T</b>	HS - 5' - C <sub>6</sub> - TTT TTT TTT TTT TTT CTG <u>TCG TAA TAG TGA GAT</u> - 3'
<b>H</b>	HS - 5' - C <sub>6</sub> - TTT TTT TTT TTT TTT <u>ATG AAT GGT GTA GTG GTC</u> - 3'
<b>C</b>	HS - 5' - C <sub>6</sub> - AGC TCG <u>GGA TTA TTG TTA AAT ATT GAT AAG GAT</u> - 3'
<b>rC</b>	HS - 5' - C <sub>6</sub> - AGC TCG <u>ATC CTT ATC AAT ATT TAA CAA TAA TCC</u> - 3'
<i>Probe DNA conjugated on MMP</i>	
<b>H<sub>M</sub></b>	5' - <u>ATG AAT GGT GTA GTG GTC TTT TTT TTT TTT TTT</u> - C <sub>3</sub> - 3' - NH <sub>2</sub>
<b>T<sub>M</sub></b>	NH <sub>2</sub> - 5' - C <sub>6</sub> - TTT TTT TTT TTT TTT CTG <u>TCG TAA TAG TGA GAT</u> - 3'
<i>Target DNA for hybridization</i>	
<b>P</b>	5' - <u>AC TAC ACC ATT CAT ATC TCA CTA TTA CG</u> - 3'
<b>MH</b>	5' - <u>AC TAC ACA ATT CAT ATC TCA CTA TTA CG</u> - 3'
<b>MT</b>	5' - <u>AC TAC ACC ATT CAT ATC TCA GTA TTA CG</u> - 3'
<b>PM</b>	5' - <u>AAA AAA GAC CAC TAC ACC ATT CAT ATC TCA CTA TTA CGA C</u> - 3'
<b>SM</b>	5' - <u>AAA AAA GAC CAC TAC ACC ATT CAT ATC TCA TTA TTA CGA C</u> - 3'

## 6.2.2 Syntheses and characterization of nAu

The synthesis and characterization of 10 nm and 50 nm spherical gold nanoparticles (nAu), as well as the quality of the synthesis are described in detail in Chapter 3.

## 6.2.3 Fabrication of nAu-DNA probes

ssDNA T, H, C and rC that carry 5'-alkanethiol groups (Table 6.2, *Probe DNA conjugated on nAu*) were used to prepare the nAu-DNA probes in this study. Prior to conjugation, all nAu were passivated with PPBS, and then ssDNA was incubated with 50 nm and 10 nm nAu at 1000:1 and 200:1 ratio (ssDNA:nAu) respectively. After 2 h incubation, for 50 nm nAu, NaCl concentration was increased slowly to 80 mM over 2 days in 0.02% SDS; whereas for 10 nm nAu, NaCl concentration was increased to 600 mM over 2 days. Excess reagents were removed by repeated washing and centrifugation. For 10 nm nAu, equimolar of strands T and C were grafted by adding 100:100:1 ratio of T:C:nAu during incubation and the resulting conjugates are denoted as 10 nm nAu-T·C. Four types of conjugates were prepared for 50 nm nAu, namely nAu-T, nAu-rC, nAu-T·C, and nAu-H·C. For the two conjugates with mixed ssDNA, equimolar of strands T/H and C were grafted by adding 500:500:1 ratio of T/H:C:nAu during conjugation.

## 6.2.4 Surface functionalization of MMP

T<sub>M</sub> and H<sub>M</sub> are ssDNA strands which carry amino groups at the 5' and 3' terminals, respectively (Table 6.2, *Probe DNA conjugated on MMP*). All these DNA-NH<sub>2</sub> were immobilized on the MMP surface via a carbodiimide coupling chemistry. Briefly, 0.5 mg MMP-COOH were washed twice with 100 mM MES buffer pH 4.8. A magnet was used to extract the MMP-COOH to the side of the microcentrifuge tube to facilitate the supernatant

aspiration. Immediately before use, solutions of cross-linking agents were prepared by dissolving the required amounts of EDC and NHSS in MES buffer.

For immobilization using EDC only, 2.5 nmol DNA-NH<sub>2</sub> were added and let homogenized with the MMP-COOH, followed by instantaneous addition of the freshly prepared EDC at COOH/EDC of 1/50.

For immobilization using EDC and NHSS, the freshly prepared EDC and NHSS solutions were added quickly to the MMP-COOH at final concentrations of 1 M each. Then, the mixture was incubated on the rotator for 40 min to convert the carboxyl groups into amine-active intermediates (NHSS-esters). Unreacted excessive reagents were removed subsequently under magnetic separation, and the activated beads were washed twice with PBS buffer pH 7.4. Then, 2.5 nmol DNA-NH<sub>2</sub> were added wherein the secondary amine acted as nucleophile at the slightly basic condition to react spontaneously with the NHSS-ester to form covalent amide bond (amidation), thus attaching the DNA firmly on MMP surface.

The functionalization for both routes were carried out under rotation with an overnight cross-linking development in order to maximize the yield (vigorous and uniform mixing is important for efficient immobilization).<sup>[287]</sup> After that, the surface-modified MMP were washed thrice using buffer of 250 mM Tris, 0.01% Tween-20 to quench any unbound activated carboxyl groups. Finally, the functionalized beads (denoted as MMP-DNA or more specifically, MMP-T<sub>M</sub> and MMP-H<sub>M</sub>) were re-dispersed in storage buffer of 10 mM Tris, 1 mM EDTA, 0.01% Tween-20, and kept at 4 °C until further use.

#### **6.2.5 Detection of target ssDNA**

The ssDNA sequences used as the targets in this MMP- and nAu-assisted detection are tabulated in Table 6.2 (*Target DNA for hybridization*). The target sequences with bold

letters are the single-mismatch DNA. In general, the target DNA forms a sandwich structure with both MMP-DNA and nAu-DNA through the corresponding complementary base-pairs respectively. Prior to the experiment, MMP-DNA were washed three times with the hybridization buffer at the desired salt concentration. A magnet was used to localize and collect the MMP-DNA. Next, hybridization was carried out by incubating the required concentration of target ssDNA and nAu-DNA for the specific time period. After the hybridization, the MMP-target-nAu sandwiches were washed a few times with magnetic separation. 3 min was granted between each wash while the magnet isolated the MMP. The washed sandwiches were then re-dispersed in water, and heated at 65 °C with mild shaking (to avoid MMP settling) for 5 min to detach the hybridized nAu-DNA completely from the MMP surface. The supernatant was collected and sent for quantification using dark field microscopy. Polysorbate surfactant Tween-20 was added in both the hybridization and wash buffers to minimize MMP-DNA sticking on tube wall, allowing easy handling during the experiments and post-experimental treatment. The detail specifications of the experiments are outlined more explicitly in Section 6.3.2, together with their effects on the detection.

#### **6.2.6 Quantification of nAu-DNA**

The collected supernatant samples were analyzed by sandwiching 1  $\mu$ L of droplets between cover slip & microscope glass slide. The probe nAu-DNA released from the MMP-assisted detection experiment was next examined under an upright microscope (Nikon Eclipse 50i) equipped with a dark-field oil condenser (NA 1.2-1.43, CytoViva) and a metal halide illuminator (Welch Allyn) as the white light source. Scattered light from nAu was collected by a 100 $\times$  objective lens (Nikon Plan Fluor 100 $\times$ , NA 0.5-1.3 oil iris, W.D. 0.16 mm) and directed to colour CCD camera (Nikon Digital Sight DS-Ri1) for real-colour imaging and locating the individual nanoparticles. The image acquisition (24-bit true colour

TIF files, 20 ms integration time, and  $5.6\times$  gain) and analysis were performed using NIS-element AR 3.1 software (Nikon). Statistical analysis, wherever applicable, was done using Student's *t*-test. The imaging process was conducted at ambient temperature.

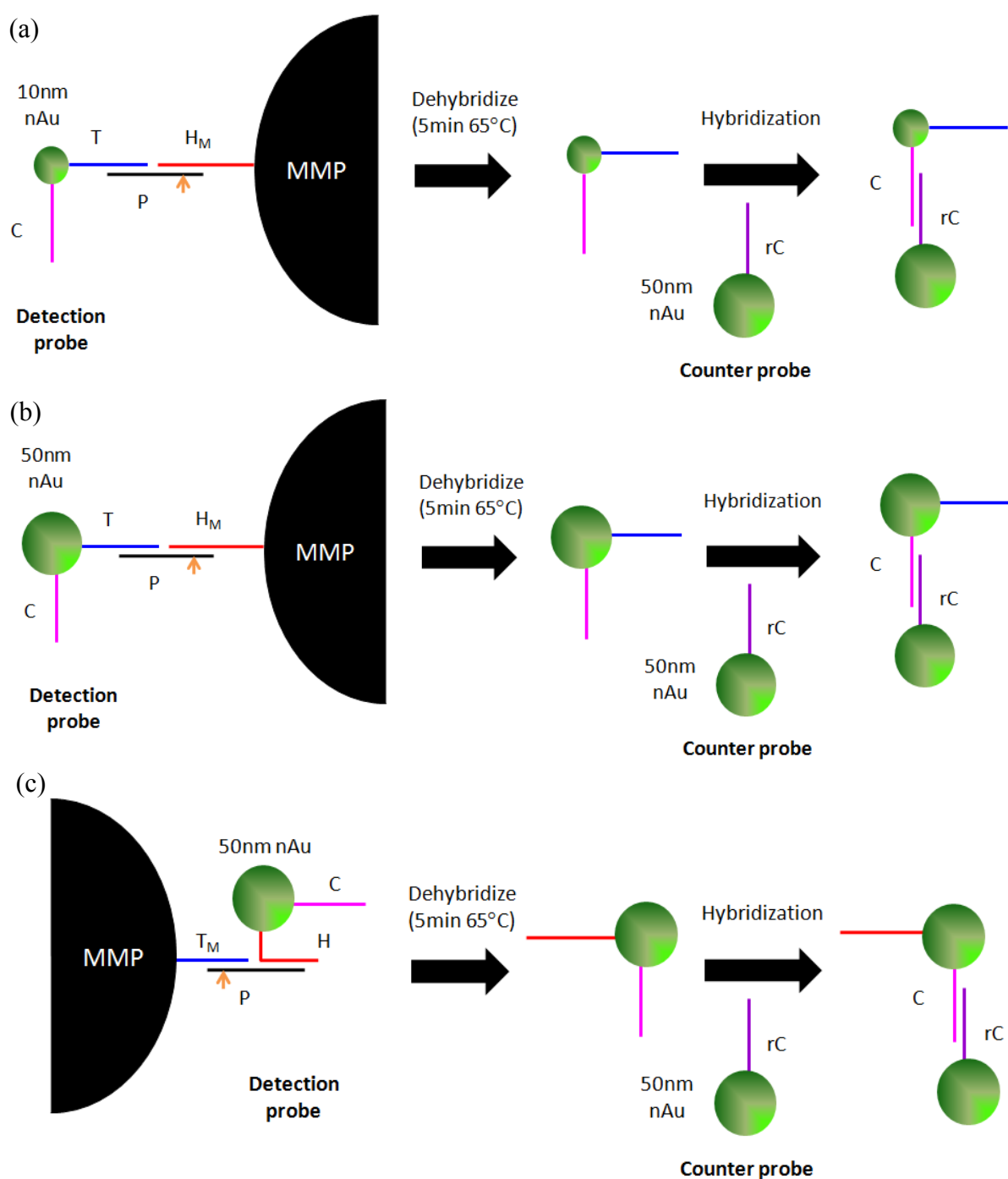
## 6.3 Results and Discussion

### 6.3.1 Design of target ssDNA detection

While a solid magnetic material of 1  $\mu\text{m}$  size displays ferromagnetism, the 1  $\mu\text{m}$  MMP used in this work consists of many nanometre-sized particles (each showing superparamagnetism) crosslinked by polymer into a micrometer-sized aggregate. Therefore, the packed magnetic nanoparticles retains their individual pristine superparamagnetic nature in which low external magnetic field can induce much greater magnetic moment compared to a single magnetic nanoparticle. The probe DNA immobilized magnetic beads (MMP-DNA) provide a unique platform to hybridize with the complementary targets ssDNA in this study. The superparamagnetic nature of MMP allows the beads, and therefore the captured targets ssDNA, to be isolated easily from the solution by using ferromagnetic materials.<sup>[260,288]</sup> The concentrated targets ssDNA could be labelled with complementary probes ssDNA which are tagged with the desired signalling moieties. Here, gold nanoparticles (nAu) have been chosen to function as the reporter. As the nAu display strong localized surface plasmon resonance (LSPR),<sup>[5,16,22,81]</sup> the hybridized nAu-DNA released from the MMP-target-nAu sandwich can be used as readout to quantify the level of hybridization. Particularly, the intense light scattering of nAu under dark field illumination is exploited and the amount of nAu observed on microscopic glass slide accounts for the hybridization efficiency. As the system is challenged with targets ssDNA that bear single-mismatches, a number of parameters have been manipulated to improve the discrimination efficiency between perfectly match and single-mismatch DNA.

### 6.3.2 Analytical performance

A set of preliminary study as shown in Scheme 6.1 was conducted, in which the schemes describe the three approaches of applying two types of nAu-DNA probes, namely detection probes and counter probes, in the detection of targets ssDNA. In Scheme 6.1a, perfectly match target P is captured between the probe  $H_M$  conjugated on MMP (MMP- $H_M$ ) and the probe T conjugated on 10 nm nAu (nAu-T·C, detection probe). 10 nm nAu are chosen based on the consideration that the Brownian motion of metallic particles increases with decreasing dimension. Compared to the sluggish larger nAu, the relatively higher mobility of the small ones would achieve more effective collision between the probe ssDNA and the target ssDNA (more than five correct nucleotides from both collide with each other to initiate the nucleation of hybridization prior to helix zipping<sup>[224,252,289]</sup>). However, the light scattering from individual 10 nm nAu is too weak to be observed clearly under the current dark field setup. To circumvent this issue, besides strands T, another ssDNA, strands C are grafted on the 10 nm nAu as well for second-stage two-component hybridization in order to provide a feasible coupled-scattering readability. After the captured 10 nm nAu-T·C are released from the MMP-target-nAu sandwich, 50 nm nAu-rC (counter probes) which are complementary to the strands C are capable of forming hybridized nanoassemblies with the 10 nm nAu-T·C, as Chapter 4 has shown that P/cP<sub>27</sub> grafted on nAu resulted in robust two-component hybridization (note: C and rC have the same sequences as P and cP<sub>27</sub> in Table 4.1). The nanoassembly formation induces plasmon coupling among the nAu and then changes the colour of light scattering. Nevertheless, the distinction between P (Figure 6.1a), single-mismatch target MH (Figure 6.1b) and the control (Figure 6.1c) was not so obvious. This could largely be attributed to the less pronounced scattering peak shift when the surface plasmons of 10 nm and 50 nm couple together, necessitating more than one 50 nm counter probe to verify for the presence of a 10 nm detection probe.<sup>[178]</sup>



Scheme 6.1: Target ssDNA detection using detection probes and counter probes. (a & b) Tail-to-tail configuration: unmodified target P (black line) hybridizes partially to MMP conjugated with H<sub>M</sub> (red line) and (a) 10 nm nAu or (b) 50 nm nAu conjugated with T (blue line) and C (pink line). After repeated washing, the target ssDNA and probes nAu-T·C (detection probes) are released from the MMP surface by heating. Probes nAu-T·C are then subjected to further hybridization with counter probes nAu-rC (purple line) that are complementary to C. The nanoassemblies are then sent for dark field analysis; (c) Head-to-tail configuration: unmodified target P (black line) hybridizes partially to MMP conjugated with T<sub>M</sub> (blue line) and 50 nm nAu conjugated with H (red line) and C (pink line). After repeated washing, the target ssDNA and probes nAu-H·C (detection probes) are released from the MMP surface by

heating. Probes nAu-H·C are then subjected to further hybridization with counter probes nAu-rC (purple line) that are complementary to C. The nanoassemblies are then sent for dark field analysis. Note that in reality, both MMP and nAu contain multiple ssDNA strands on their surfaces. The beige arrows indicate the single-mismatch sites for targets (a, b) MH and (c) MT.

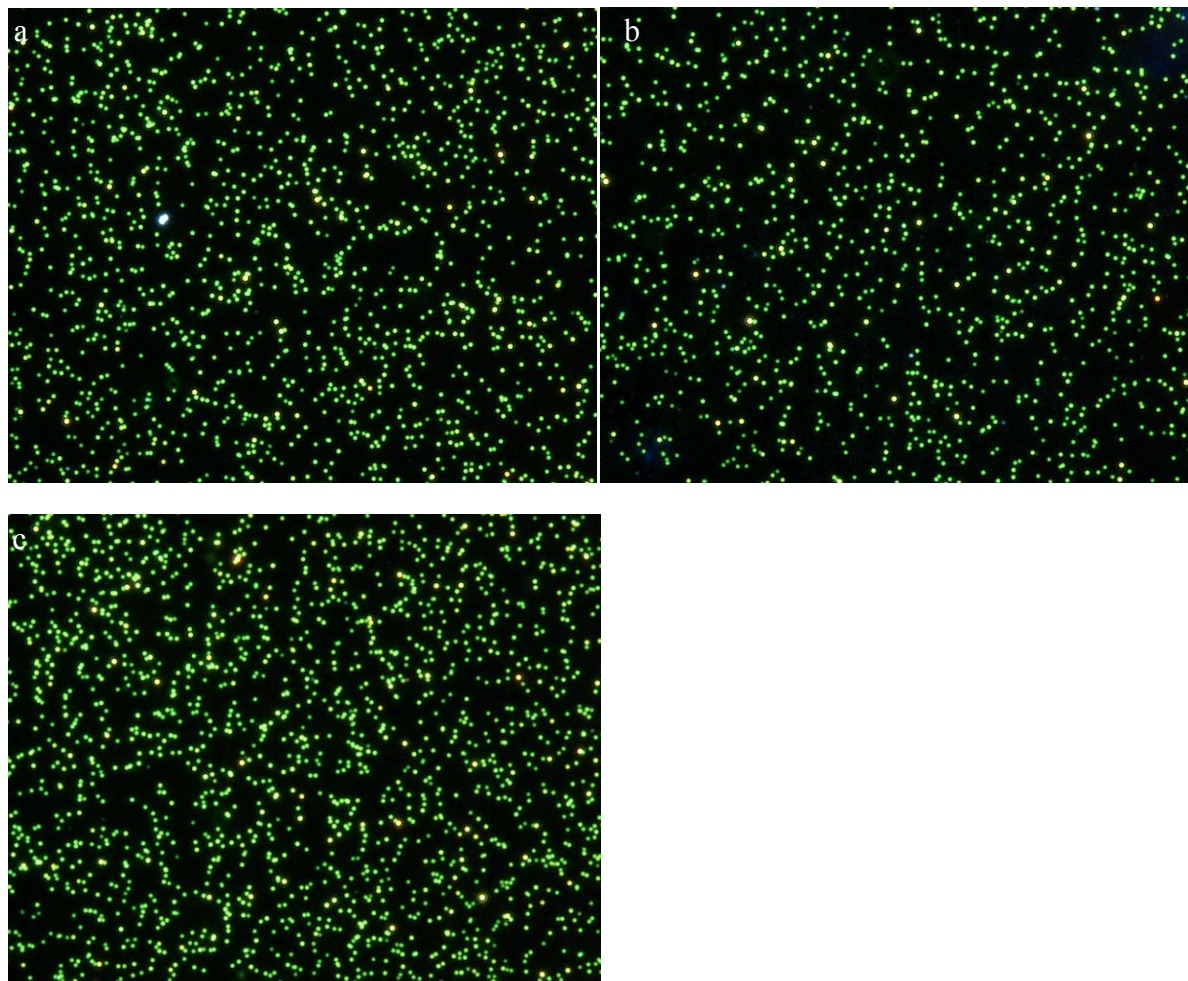


Figure 6.1: Nanoassembly formation based on Scheme 6.1a using 2 pM of target (a) P and (b) MH; (c) the image for control was acquired in the absence of any target DNA. Collective mode condition: incubate 0.172 mg MMP-H<sub>M</sub> with the desired target, together with 3 nM of 10 nm nAu-T·C in 40  $\mu$ L 200 mM NaCl + 10 mM phosphate + 0.005% Tween-20 for 5 h. The samples were then washed five times with 60  $\mu$ L of the buffer, and the magnetically-collected precipitates redispersed in 8  $\mu$ L of water. Dehybridization was performed by heating the mixture at 65  $^{\circ}$ C for 5 min under vigorous shaking. 1.7 pM nAu-rC was then added to hybridize with the released nAu-T·C.

To increase the robustness of detection, 50 nm nAu are deployed as the detection probes in substitution of 10 nm nAu, even though the hybridization efficiency might be



reduced by the bulkier nanoparticles. It has been reported previously that LSPR coupling between two 50 nm nAu incurs distinct scattering peak shift along with substantial colour change in comparison to the single ones and also the 50nm/10nm pairing (Section 4.3.3).<sup>[178]</sup> Thus, it is desirable to use the 50nm/50nm hybridization so that the detection readout could be enhanced.

As this study aims to obtain good discrimination against single-mismatch DNA, two hybridization configurations have been checked using the 50 nm detection and 50 nm counter probes, i.e. tail-to-tail (Scheme 6.1b) and head-to-tail (Scheme 6.1c). Head-to-tail nAu alignment has been demonstrated to possess better single-mismatch discrimination when the mismatch site is located at the ‘tail’ (Chapter 5) due to the steric effect of nAu. On the other hand, MMP which constitute the ‘tail’ in Scheme 6.1c are many-fold larger than the nAu forming the ‘head’. The absolute size of the MMP could be critical in impeding the hybridization of the detection probe nAu-H·C. Indeed, the results show that tail-to-tail configuration (Figure 6.2, I) provides much better hybridization efficiency than the head-to-tail format (Figure 6.2, II) because fewer nanoassemblies were seen in the latter, for both perfectly match P (Figure 6.2, Ia & IIa) and the corresponding single-mismatch targets (Figure 6.2, Ib & IIb). These confirm the reduced steric hindrance encountered by incoming detection probes in the tail-to-tail structure and the inapplicability of MMP-DNA as tail-probe in the head-to-tail format (Scheme 6.1c). Noticeably, the scattering colour change associated with the usage of 50 nm nAu as detection probes (Figure 6.2) was more obvious than those observed when 10 nm nAu were used instead (Figure 6.1).

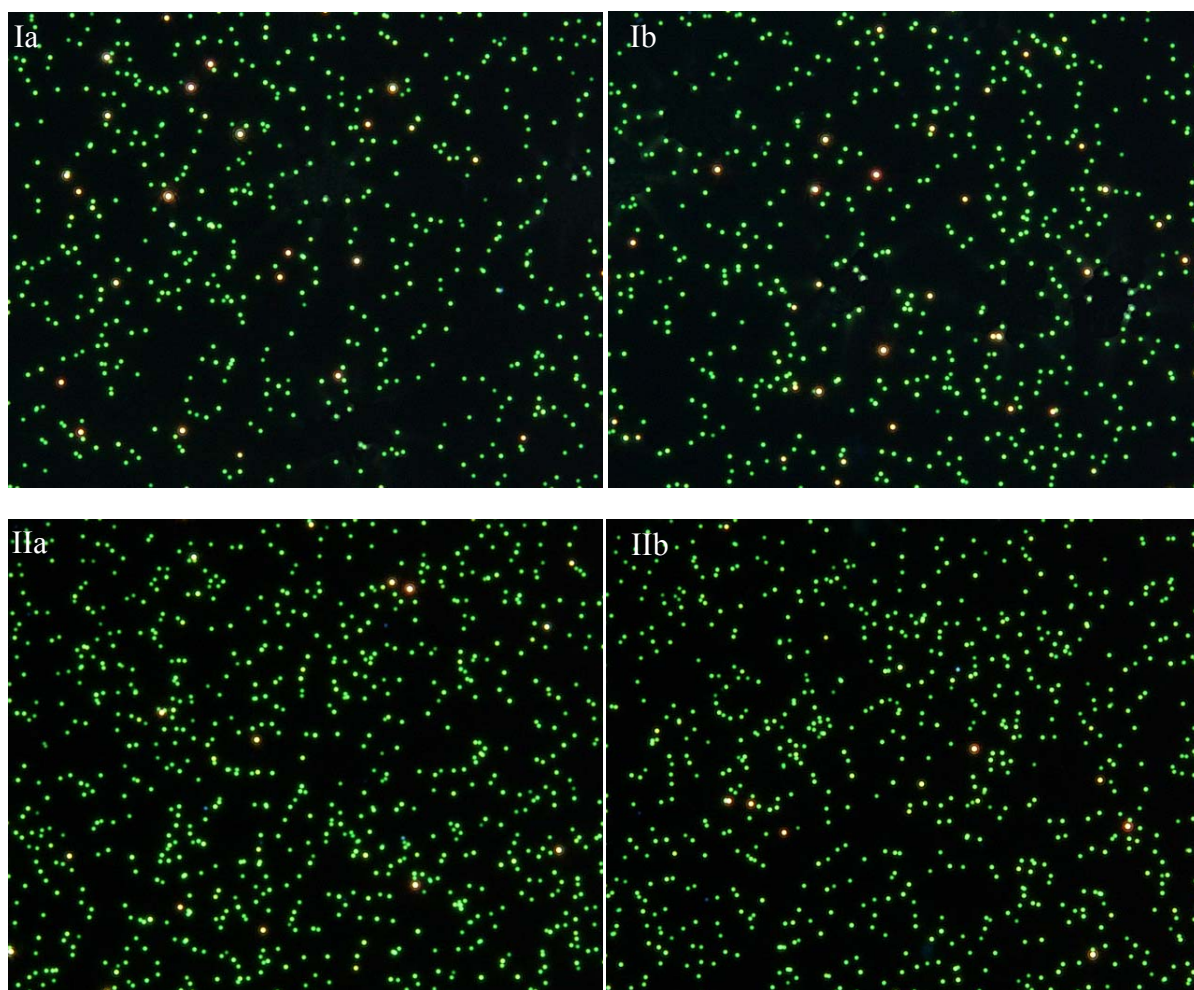
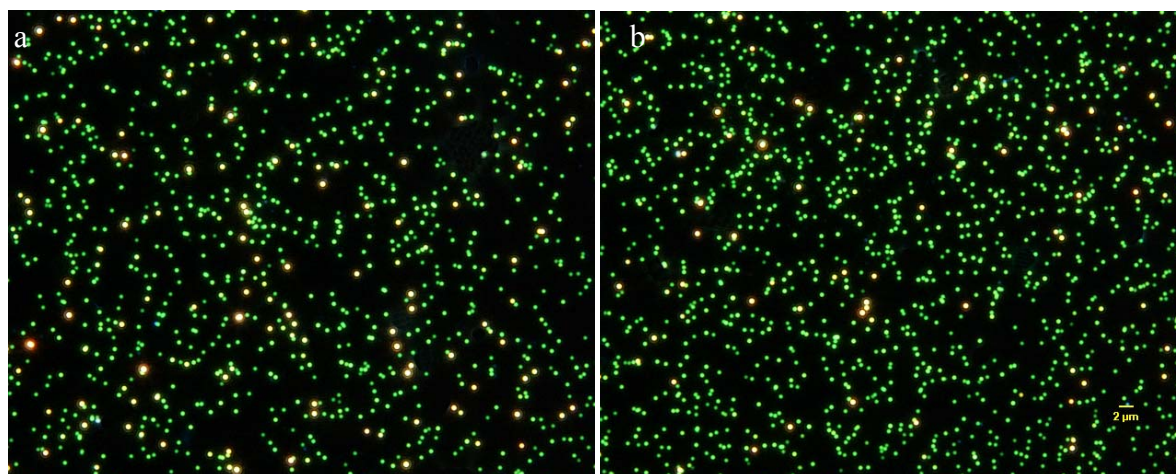


Figure 6.2: Effect of (I) tail-to-tail vs. (II) head-to-tail hybridization conformation based on Scheme 6.1b & c respectively. Stepwise mode condition: incubate 0.2125 mg (I) MMP-H<sub>M</sub> or (II) MMP-T<sub>M</sub> with 333 fM target (Ia) P (Ib) MH (IIa) P (IIb) MT in 60  $\mu$ L 140 mM Tris + 140 mM NaCl + 2 mM MgCl<sub>2</sub> + 0.005% Tween-20 for 3 h, followed by washing twice with 150  $\mu$ L of the buffer, and subsequent 3 h incubation with 1.5 pM of (I) nAu-T·C or (II) nAu-H·C in 30  $\mu$ L of the buffer. The samples were then washed twice with 150  $\mu$ L of the buffer, and the magnetically-collected precipitates redispersed in (I) 20  $\mu$ L (II) 15  $\mu$ L of water. Dehybridization was performed by heating the mixture at 70 °C for 5 min under vigorous shaking. 1 pM nAu-rC was then added to hybridize with the released nAu-T·C or nAu-H·C.

The degree of nanoassembly formation should tally with the number of the target ssDNA used, and therefore should be indicative of the hybridization efficiency. Hence, the tail-to-tail configuration (Scheme 6.1b) was checked for the nanoassembly formation at different concentrations of perfectly match target P (Figure 6.3). As the concentrations of P increased from 2 pM (Figure 6.3c) to 20 pM (Figure 6.3b), and to 200 pM (Figure 6.3a), the amount of nanoassemblies formed were increased as well. However, the system was not

sensitive in differentiating 2 pM P (Figure 6.3c) from the control (Figure 6.3d) despite the significant nanoassemblies formed. The insensitivity could be largely due to the following several reasons. Firstly, in developing the clustering between the detection and counter probes, a rather high concentration of counter probes is beneficial for Scheme 6.1 in order to promote rapid hybridization between the complementary strands C and rC. As there is no separation means for the unhybridized nAu-rC, the excessive counter probes could interfere significantly with the desired nanoassembly scattering signal. Secondly, the ratio and distribution of strands T and C are rather hard to be maintained at exactly the same value and position on each nAu. These variations among individual counter probe might introduce discrepancy during nanoassembly formation. Thirdly, the coexistence of two types of DNA sequences could interfere with the specific hybridization process (between T & target, and between C & rC) and contribute to reduced hybridization efficiency.



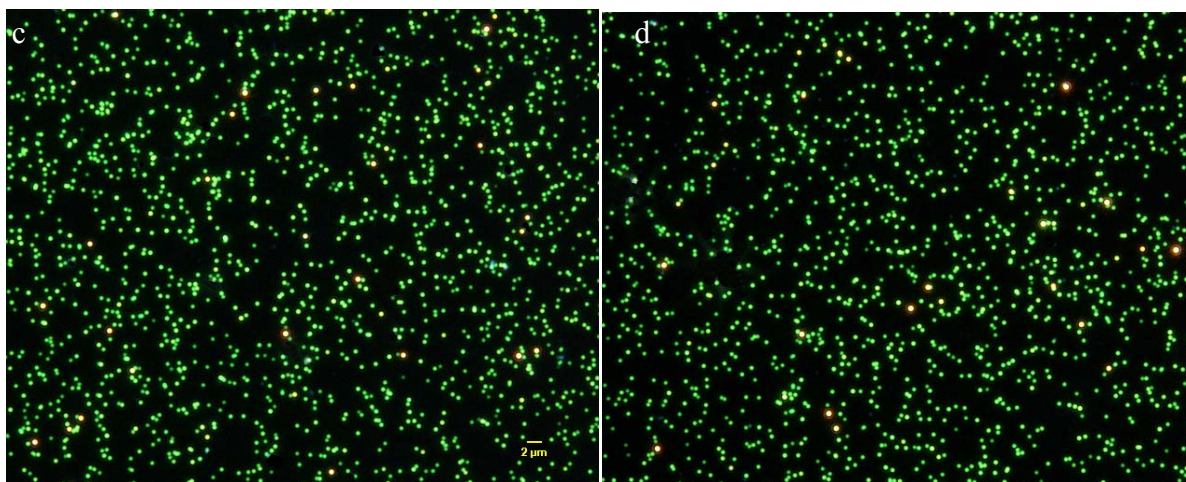
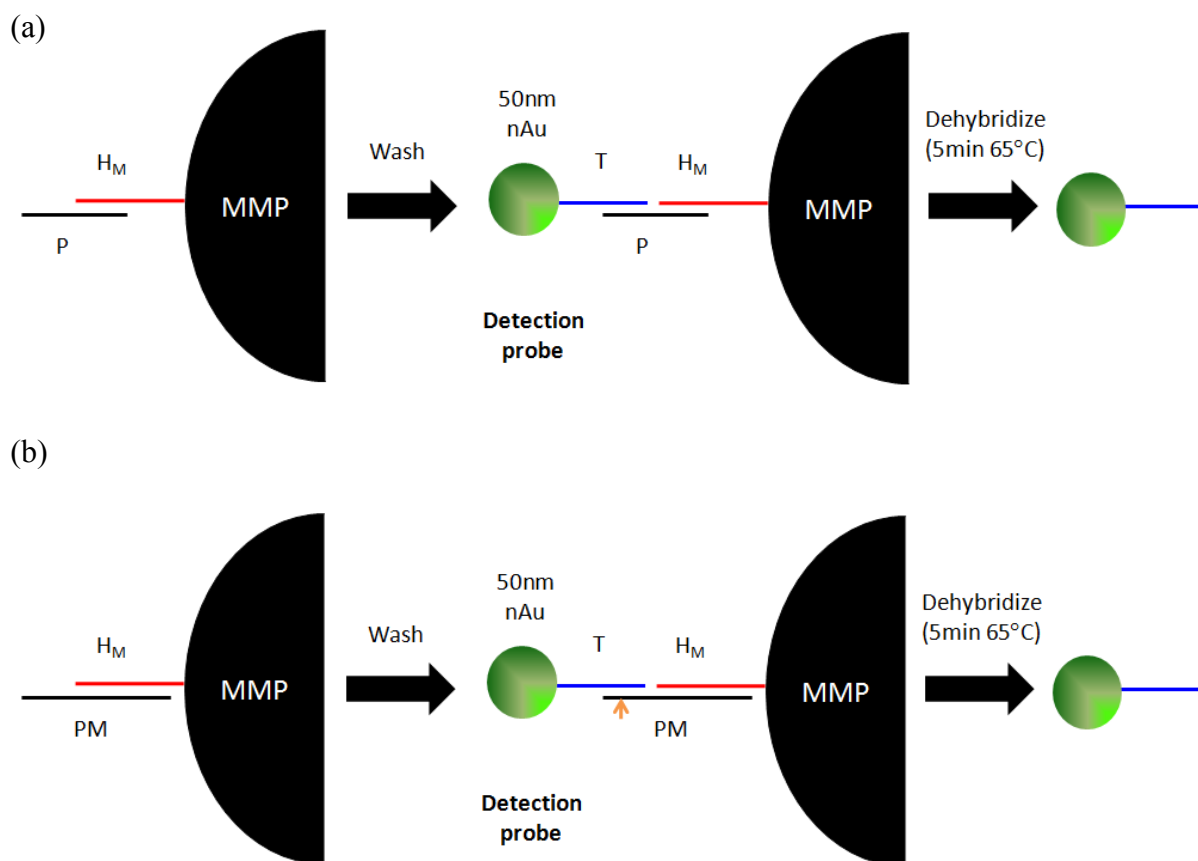


Figure 6.3: Nanoassembly formation based on Scheme 6.1b using (a) 200 pM, (b) 20 pM, and (c) 2 pM of target P; (d) the image for control was acquired in the absence of any target DNA. Collective mode condition: incubate 0.125 mg MMP- $H_M$  with the desired targets, together with 2 pM of 50 nm nAu-T·C in 25  $\mu$ L 140 mM Tris + 140 mM NaCl + 2 mM  $MgCl_2$  + 0.005% Tween-20 for 7 h. The samples were then washed thrice with 40  $\mu$ L of the buffer, and the magnetically-collected precipitates redispersed in 10  $\mu$ L of water. Dehybridization was performed by heating the mixture at 65  $^{\circ}C$  for 5 min under vigorous shaking. 2.5 pM nAu-rC was then added to hybridize with the released nAu-T·C.

After the preliminary study of Scheme 6.1, another detection system is designed wherein only the detection probe is exploited as both the detecting and signalling components (Scheme 6.2a). Here, the 50 nm nAu are conjugated with only one type of ssDNA, i.e. strands T (nAu-T). As individual 50 nm nAu exhibits intense surface plasmon, the light scattering of the hybridized 50nm nAu-T is deployed directly as the readout. The primary detection step involves the construction of a sandwich structure by P co-hybridizing with MMP- $H_M$  and nAu-T (detection probe) through 14 complementary base-pairs on both sides. When subjected to hybridization condition similar to Figure 6.3, indeed, the dark field micrographs as depicted in Figure 6.4 are obtained. The distribution densities of captured nAu-T can be observed to decrease while the concentration of perfectly match target P was reduced from 200 pM (Figure 6.4a) to 20 pM (Figure 6.4b) and to 2 pM (Figure 6.4c). Furthermore, 2 pM P (Figure 6.4c) could now be distinguished from the control (Figure 6.4d) clearly, and this was not easy for the two nAu-DNA probes scheme (Scheme 6.1b, Figure 6.3c-d). Consequently,



the detection scheme based on the use of detection probe alone, besides omitting the need for extra DNA and counter probe hybridization, also turns out to be more sensitive.



Scheme 6.2: Target ssDNA detection using detection probes. MMP conjugated with H<sub>M</sub> (red line) first hybridizes to the unmodified target (a) 28 b P or (b) 40 b PM (both in black lines). After repeated washing, the dangling end of the captured target further hybridizes to 50 nm nAu conjugated with T (blue line). After further repeated washing, the target ssDNA and probe nAu-T (detection probes) are released from the MMP surface by heating. The collected nAu-T are then sent directly for dark field analysis without further treatment. Note that in reality, both MMP and nAu contain multiple ssDNA strands on their surfaces. The beige arrow indicates the single-mismatch sites for target SM. Stepwise mode is described here. For collective mode, the 50 nm nAu-T and targets ssDNA are added simultaneously to the MMP-H<sub>M</sub>.

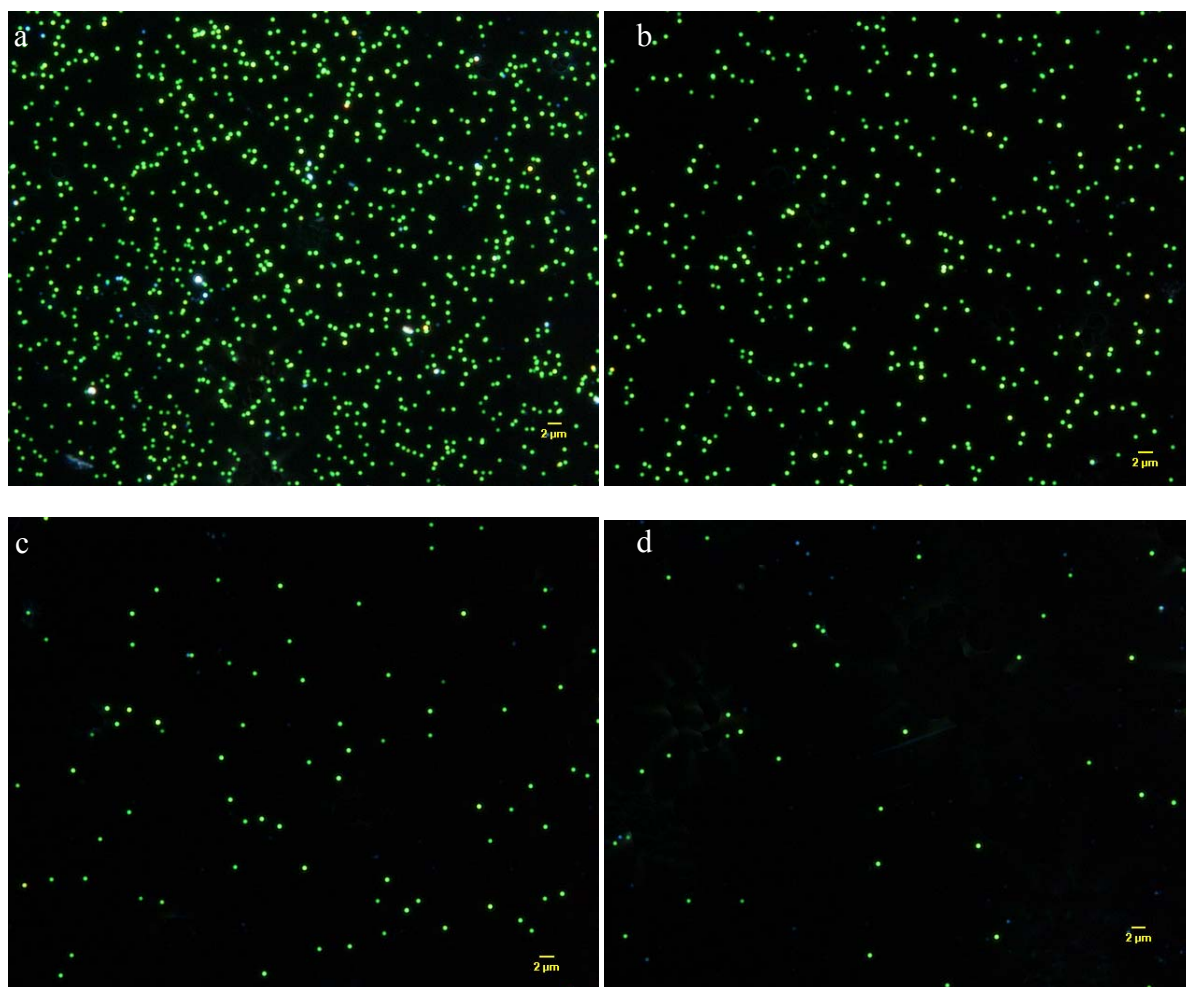


Figure 6.4: Dark field micrographs showing the varied amount of nAu-T released from the sandwich MMP-target-nAu based on Scheme 6.2a using (a) 200 pM, (b) 20 pM, and (c) 2 pM of target P; (d) the image for control was acquired in the absence of any target DNA. Collective mode condition: incubate 0.125 mg MMP- $H_M$  with (a) 200 pM, (b) 20 pM, and (c) 2 pM of target P, together with 2 pM of 50 nm nAu-T in 25  $\mu$ L 140 mM Tris + 140 mM NaCl + 2 mM  $MgCl_2$  + 0.005% Tween-20 for 7 h. The samples were then washed thrice with 40  $\mu$ L of the buffer, and the magnetically-collected precipitates redispersed in 20  $\mu$ L of water. Dehybridization was performed by heating the mixture at 65  $^{\circ}C$  for 5 min under vigorous shaking.

Hybridization among the MMP-DNA, detection probes, and targets ssDNA for both Scheme 6.1 and Scheme 6.2 could be conducted in two modes. For the collective mode, targets ssDNA and detection probes are incubated simultaneously with the MMP-DNA probes; whereas for the stepwise mode, capturing of targets ssDNA by the MMP-DNA, and the binding of detection probes onto the MMP-target hybrids are carried out in two separate hybridizations. This two-stage hybridization allows the unbound targets ssDNA to be

removed by washing before the detection probes are added. Judging from the resulting dark field micrographs (data not shown), the difference between these two modes are insignificant.

Irrespective of the schemes and modes, substantial nonspecific adsorption of the detection probes i.e. nAu-DNA onto the MMP-DNA surface took place in the control samples despite the absence of linking targets ssDNA. The presence of nonspecific nAu-T (Figure 6.5, Ib) could interfere with the reporting detection probes (Figure 6.5, Ia) and reduce the signal to noise ratio (S/N). Therefore, some procedures have been attempted in order to tackle the nonspecific issue.

Initially, the sandwich structures of MMP-target-nAu were subjected to different numbers of washing cycles. Examination under the dark field microscope has depicted that more nAu were removed with increasing washing steps regardless of the target types (data not shown). Hence, the signal to noise ratio (S/N) could not be improved any further with extra washing. Next, sonication was performed during each washing step and its efficacy on treating the nonspecifically-bound detection probes was inspected (Figure 6.5II). Compared to the washing without sonication (Figure 6.5I), washing with sonication reduced the non-specificity more effectively in both perfectly match target P (Figure 6.5, Ia & IIa) as well as the control (Figure 6.5, Ib & IIb). Nonetheless, sonicating force is influenced greatly and directly by the working condition of the sonicator (e.g. water level, sample tube position etc.). Although the same parameters were repeated for each experiment, the amount of nAu-T removed could sometimes be inconsistent. Besides, sonication might disrupt the hybridization because more nAu-T were observed to be removed with longer sonication time. Thus, sonication is not a dependable method to overcome the undesirable nonspecific adsorption.

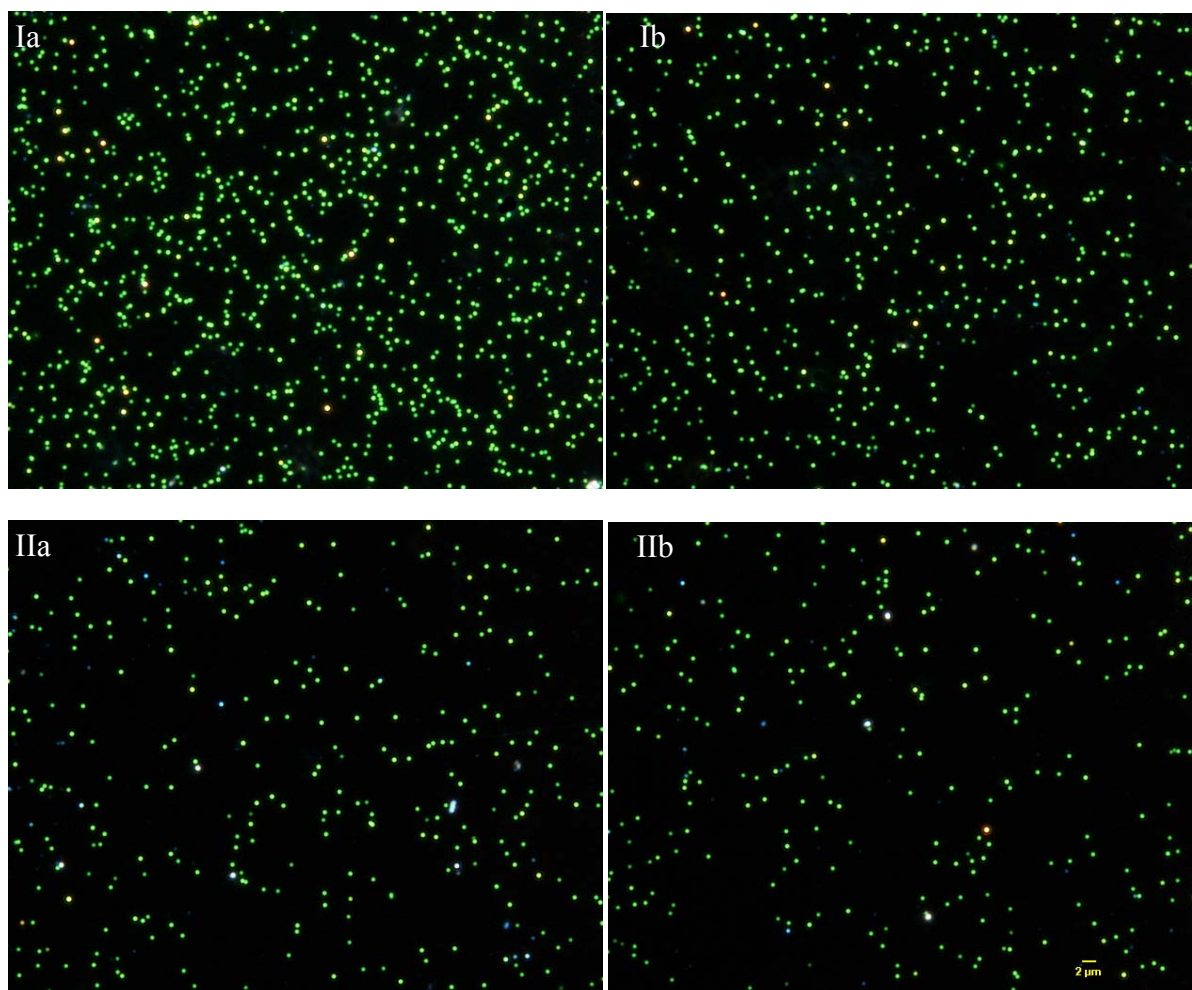


Figure 6.5: Effect of sonication based on Scheme 6.2a (I) without and (II) with sonication for 5 s using (a) 0.2 pM of P and (b) control. Stepwise mode condition: incubate 0.25 mg MMP-H<sub>M</sub> with the desired targets in 200  $\mu$ L 100 mM Tris + 600 mM NaCl + 2 mM MgCl<sub>2</sub> + 0.005% Tween-20 for 3 h, followed by washing twice, and subsequent 4 h incubation with 10 pM of 50 nm nAu-T in 50  $\mu$ L 140 mM Tris + 140 mM NaCl + 2 mM MgCl<sub>2</sub> + 0.005% Tween-20. The samples were then washed with 100  $\mu$ L of the buffer for (I) 5 times without sonication or (II) 4 times with 5 s sonication, and the magnetically-collected precipitates redispersed in 10  $\mu$ L of water. Dehybridization was performed by heating the mixture at 65  $^{\circ}$ C for 5 min under vigorous shaking.

Surface amine, aldehyde, and silica have been reported to adsorb free DNA in aqueous.<sup>[290]</sup> It was then queried that whether the remaining unreacted carboxyl groups present on the MMP surface after DNA functionalization have contributed to the nonspecific binding. Results from the unmodified MMP (MMP-COOH) incubated with the detection probes (nAu-T), however indicated that there was indeed very few nonspecific adsorption (Figure 6.6) compared to the control using similar experimental conditions (Figure 6.8e). The



negative zeta potential of MMP-COOH at  $\text{pH} > 2$  means that the carboxyl groups ( $-\text{COOH}$ ) dissociate into carboxylate ions ( $-\text{COO}^-$ ) at buffer pH 7.9. Unlike the positive charge amine and the neutral aldehyde group, the negative charge carboxylate ions repel the anionic phosphate backbones of ssDNA conjugated on nAu. Furthermore, the relatively low salt concentration during incubation would be less effective in screening the anion-anion repulsion. Additionally, the magnetic beads have been pre-coated with hydrophilic glycidyl ether layer that, apart from concealing the core iron oxide materials, helps to ensure low nonspecific binding. As such, the surface carboxyl was not the root cause for nonspecific adsorption. Comparison among the control samples (data not shown) revealed that when greater amount of MMP-DNA or nAu-DNA was added for hybridization, more nAu-DNA were trapped nonspecifically. Nonspecific adsorption might then have arisen from the interaction between the ssDNA conjugated on both MMP and nAu. The sequences of strands T,  $T_M$ , H, and  $H_M$  listed in Table 6.2 have been cross-checked using an Internet available tool (Integrated DNA Technologies, Oligo Analyzer) prior to the synthesis to ensure little associating properties among each other.

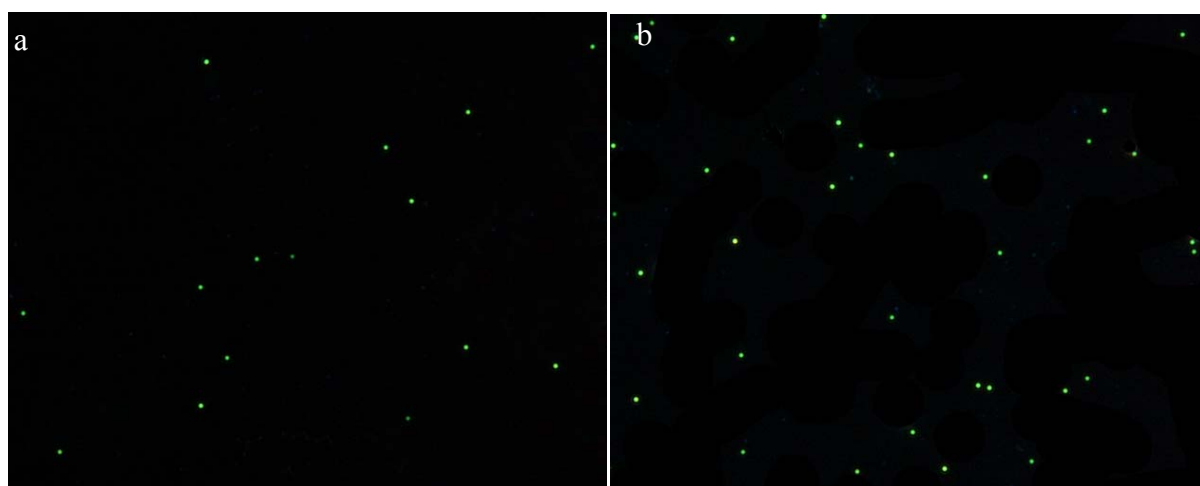
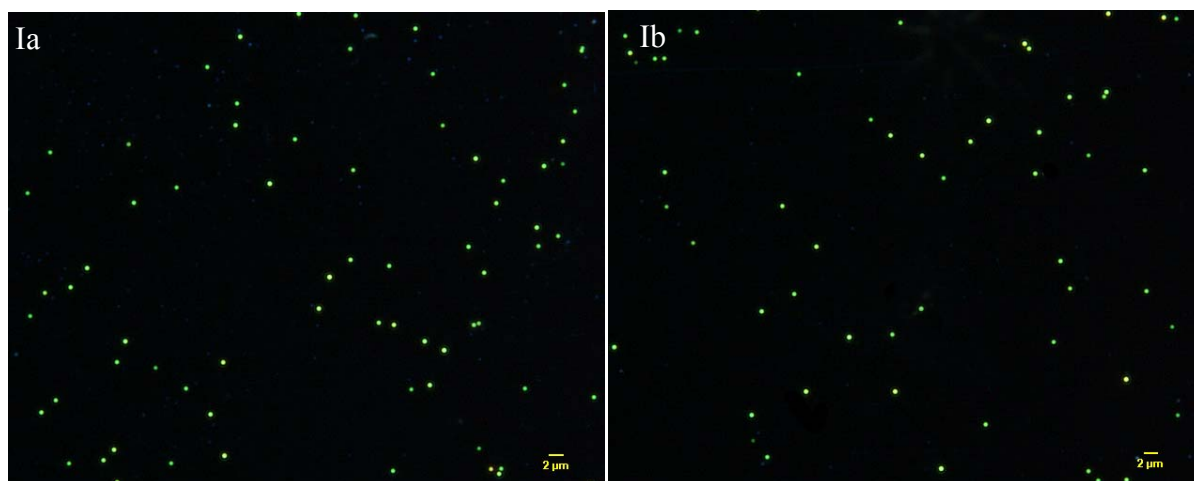


Figure 6.6: (a, b) Dark field micrographs showing the amount of nAu-T adsorbed nonspecifically onto MMP-COOH using experimental condition similar to Figure 6.8.

To incur more stringent hybridization setting, formamide, a strongly associating liquid capable of forming four hydrogen bonds, was evaluated for its potential in eliminating the non-specificity.<sup>[286]</sup> Formamide has been depicted to destabilize the DNA double helix by breaking the hydrogen bonds that hold DNA duplex together.<sup>[291-292]</sup> In fact, dark field micrographs showed that 20% formamide in the hybridization buffer was useful in removing nAu-T (Figure 6.7, I) compared to the one without formamide (Figure 6.7, II), but this also affected seriously the normal hybridization of target P (Figure 6.7, Ia). Whereas lowering the formamide content in hybridization buffer was not effective in reducing the level of nonspecific adsorption. To counteract the competition effect of formamide, alternative route was deployed wherein formamide was introduced only after the hybridization of nAu-DNA by using a washing buffer that contained 20% formamide. Nevertheless, there was not much noise removal by formamide in such circumstance compared to the use of washing buffer alone (data not shown).



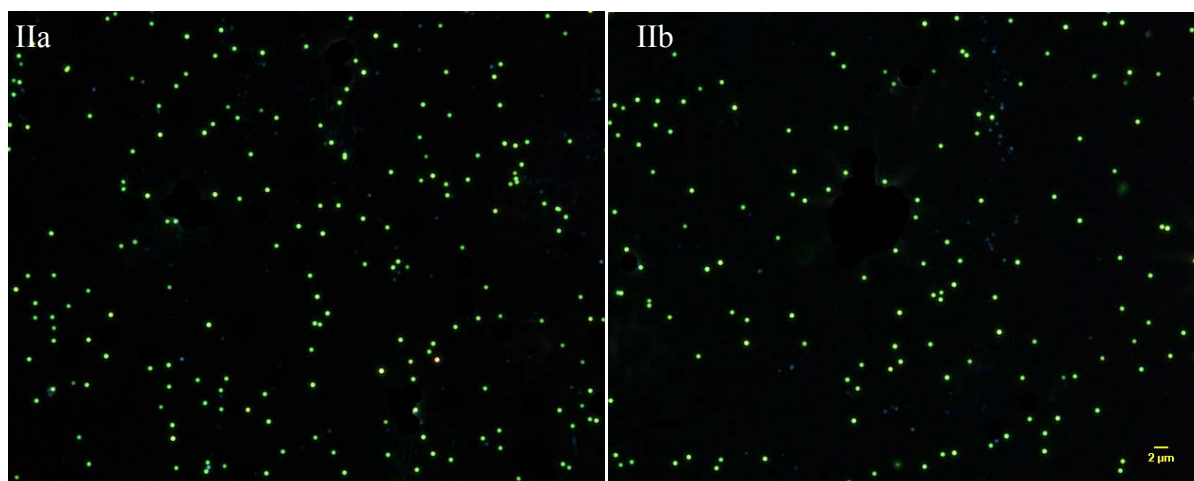


Figure 6.7: Effect of formamide based on Scheme 6.2a (I) with 20% formamide and (II) without formamide using (a) 0.2 pM P and (b) control. Stepwise mode condition: incubate 0.125 mg MMP- $H_M$  with the desired targets in 200  $\mu$ L 100 mM Tris + 600 mM NaCl + 2 mM  $MgCl_2$  + 0.005% Tween-20 for 3 h, followed by washing once, and subsequent 3 h incubation with 10 pM of 50 nm nAu-T in 25  $\mu$ L 140 mM Tris + 140 mM NaCl + 2 mM  $MgCl_2$  + 0.005% Tween-20 (I) with and (II) without 20% formamide. The samples were then washed 5 times with 100  $\mu$ L of the buffer, and the magnetically-collected precipitates redispersed in 10  $\mu$ L of water. Dehybridization was performed by heating the mixture at 65  $^{\circ}C$  for 5 min under vigorous shaking.

Although not completely resolve the non-specificity issue, vigorously mixing the wash buffer-loaded samples on an orbital shaker for two minutes turns out to result in more consistent results than what sonication can achieve in reducing the nonspecifically adsorbed detection probes. Hence, the noise from the undesirable adsorption would be incorporated during the analysis later.

In Scheme 6.2b, 40 b perfectly match target ssDNA (PM) is used in replacement of the 28b target P (Scheme 6.2a). PM co-hybridizes with MMP- $H_M$  and nAu-T through 24- and 16-complementary base-pairs respectively; whereas SM is a mutant that exhibits single-mismatch (beige arrow, Scheme 6.2b) with respect to the detection probe nAu-T. The longer duplex region of the MMP-PM hybrid, and hence the higher melting temperature could increase the hybridization efficiency of PM with probe MMP- $H_M$ . This could also possibly reduce (if any) the nonspecific adsorption of target ssDNA onto MMP- $H_M$ . In addition, when the stepwise mode is employed, hybridization between PM and MMP- $H_M$  is able to be done

at higher salt environment, i.e. from 140 mM to 600 mM NaCl in order to improve the hybridization kinetics. This is not possible for the collective mode as the high salt concentration induces agglomeration of the nAu and hampers the detection. On the other hand, high salt content may promote hydrogen bonding between the non-complementary ssDNA and aggravate the nonspecific adsorption.<sup>[290]</sup> For this reason, the hybridization between PM and MMP-H<sub>M</sub> at 600 mM NaCl is performed at 37 °C. A seemingly trivial drawback from the temperature control is that the stagnant sample tubes residing in the water bath have to be vortex gently every 20 min, in order to re-disperse the rapid settling weighty micrometer-scale MMP (due to gravity) back to form homogeneous solution.<sup>[293]</sup> The need for repeated intermittent dispersion creates less homogeneity in mixing, as compared to the incubation via 360° rotator (ambient temperature) which maintains a better and well-dispersed solution.

When the MMP-target hybrids are added with the detection probes, even though this hybridization is not carried out in buffer of high salt concentration, temperature control at 33 °C is still being utilized. This exerts a more stringent condition for hybridization and enables better discrimination against the single-mismatch target SM. Besides, to promote better hybridization efficiency, the amount of detection probes has been raised, by both increasing the incubating concentration of nAu-T and doubling the final volume of the hybridization mixture. The concentration of nAu-T used was increased from the initial 2 pM (Figure 6.4) to 10 pM (Figure 6.5, 6.6, 6.7, 6.8), while the mixture volume was increased twofold from 25 µL to 50 µL at 10 pM. It is aspired that the greater chances of effective collision could aid to increase the hybridization efficiency, and offset the greater nonspecific adsorption accordingly.

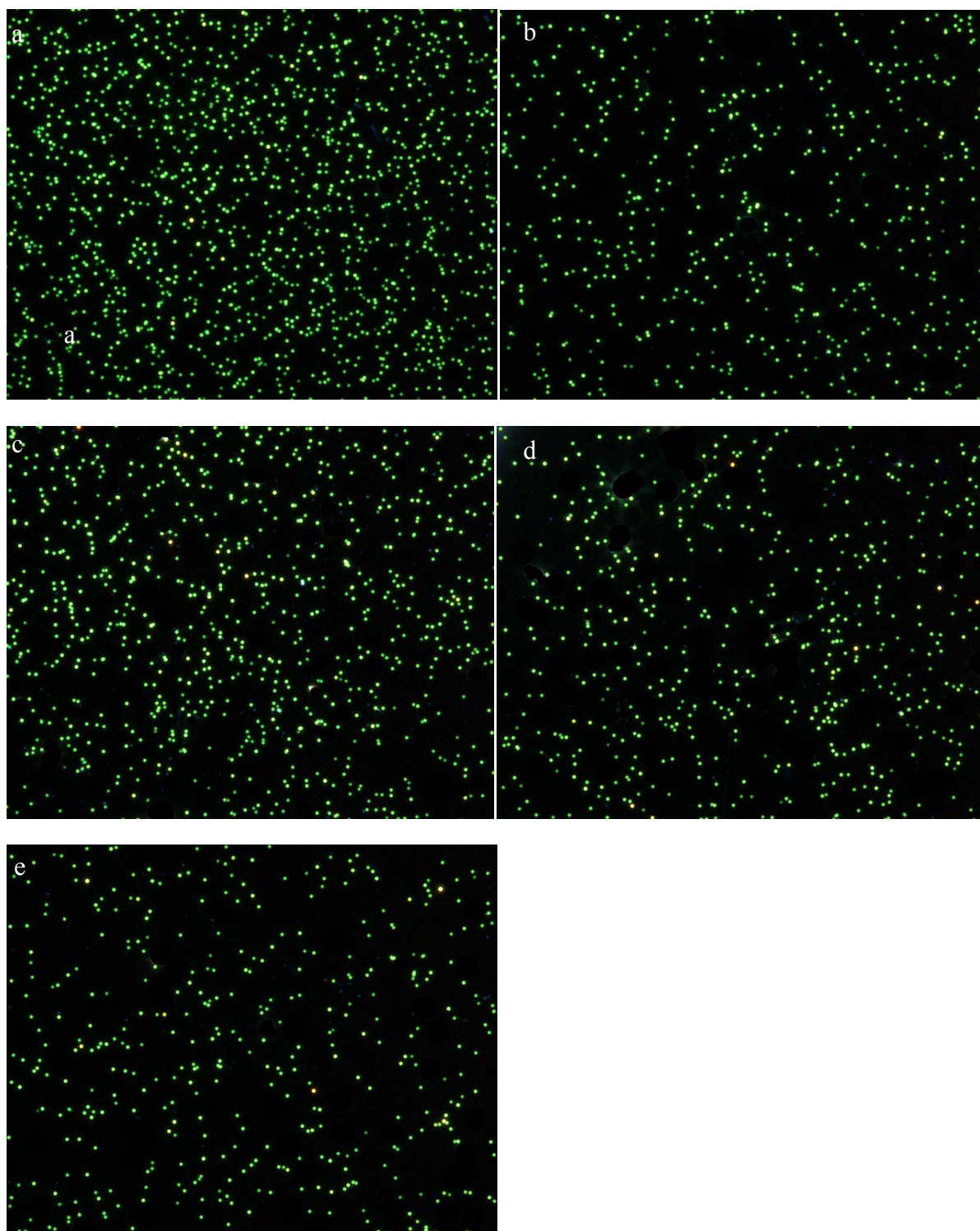


Figure 6.8: Dark field micrographs showing the varied amount of nAu-T released from the sandwich MMP-target-nAu based on Scheme 6.2b using (a) 20 pM PM, (b) 20 pM SM, (c) 2 pM PM, and (d) 2 pM SM; (e) the image for control was acquired in the absence of any target DNA. Stepwise mode condition: incubate 0.25 mg MMP- $H_M$  with the desired targets in 200  $\mu$ L 100 mM Tris + 600 mM NaCl + 2 mM  $MgCl_2$  + 0.005% Tween-20 at 37  $^{\circ}C$  for 2 h, followed by washing twice, and subsequent 6 h incubation with 10 pM of 50 nm nAu-T in 50  $\mu$ L 140 mM Tris + 140 mM NaCl + 2 mM  $MgCl_2$  + 0.005% Tween-20 at 33  $^{\circ}C$ . The samples were then washed 4 times with 100  $\mu$ L of the buffer with 2 min vigorous shaking. The magnetically collected precipitates were finally redispersed in 10  $\mu$ L of water.

Dehybridization was performed by heating the mixture at 65 °C for 5 min under vigorous shaking.

Summarized from the experimental conditions stated above, the distribution of nAu-T released from the magnetically isolated sandwich structures following Scheme 6.2b is shown in Figure 6.8 for two types of targets ssDNA, namely perfectly match PM (Figure 6.8a, c) and single-mismatch SM (Figure 6.8b, d) at concentration values of 20 pM and 2 pM; while the image for control is taken from samples that were devoid of any target ssDNA (Figure 6.8e). The counted amount of nAu-T from the dark field images is tabulated in Figure 6.9 for PM (blue bar) and SM (red bar) at the two concentrations tested, along with the nonspecifically adsorbed nAu retained in the control (green bar). Each displayed data bar is the average of seven repeats, of which the summation of ten frames of dark field micrographs is used for each sample. Importantly, PM showed distinct difference ( $p < 0.05$ ) compared to SM as well as control at 20 pM. Conversely, the distinction between PM and SM dropped when the concentration of target ssDNA was lowered by one-order of magnitude to 2 pM; yet PM was still statistically different ( $p < 0.05$ ) compared to the control. Thus, the limit of detection achieved is 2 pM, and the single-mismatch distinction is at 20 pM. Judged against the literature reported values, the single-mismatch limit obtained here is fairly reasonable, considering that in the current protocol, no further amplifying steps have been taken.

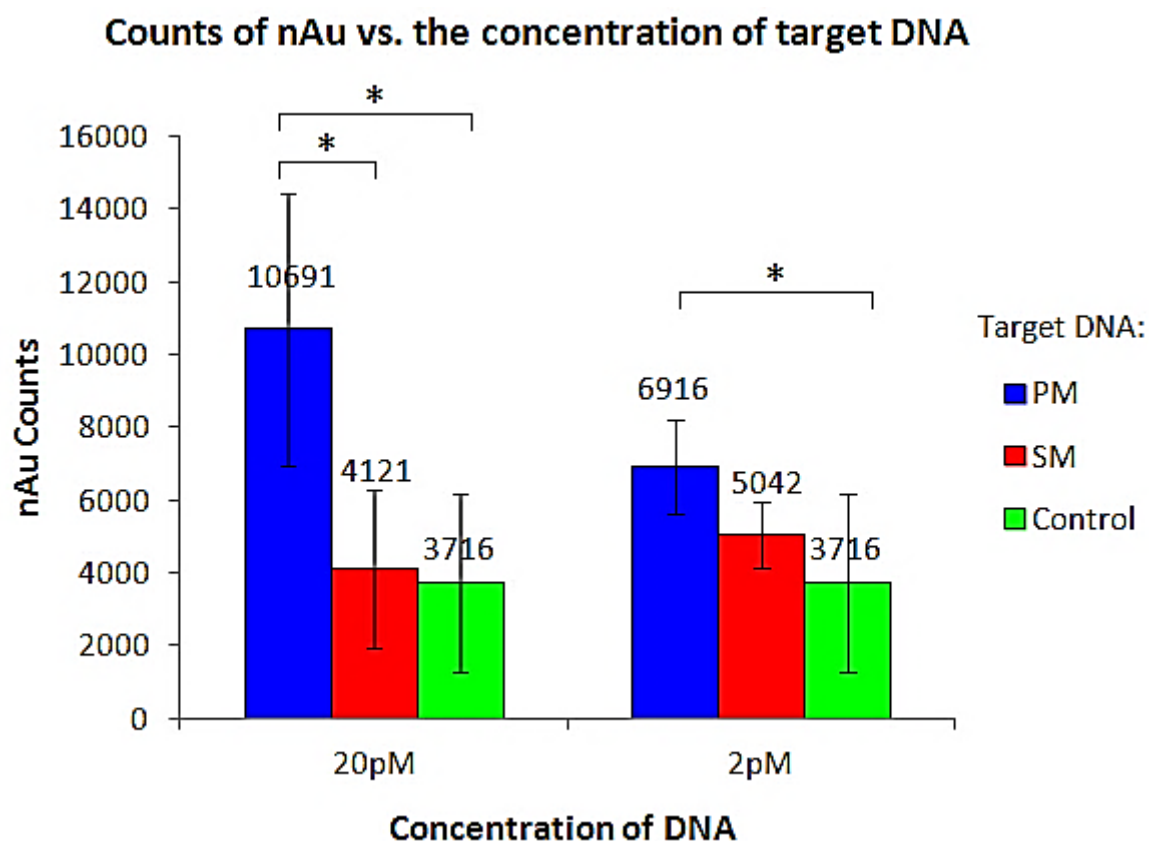


Figure 6.9: The amount of nAu-T released from MMP surface during dehybridization, for 20 pM and 2 pM of perfectly match (PM, blue bar) and single-mismatch (SM, red bar) captured target DNA, counted from total of ten frames of dark field micrographs for each sample. The data of control (green bar) is taken in the absence of any DNA target. The experimental condition is as described in Figure 6.8. The asterisk symbol (\*) denotes statistical difference ( $p < 0.05$ ) between two data.

### 6.3.3 Issues on cross-linking

Immobilization of DNA-NH<sub>2</sub> onto MMP-COOH requires the formation of covalent amide bond between the carboxyl groups of MMP and the amino groups of DNA (amidation). The manufacturer has recommended the use of 1-ethyl-3-(3-dimethylaminopropyl) carbodiimide (EDC) as the sole cross-linking agent, but the resulting MMP-DNA were associated with abundant nonspecific adsorption. In fact, the efficiency of EDC-mediated amidation has been reported to be low<sup>[294]</sup> because the reaction can be affected by several issues, and we believe that the problem aroused from the inefficient surface conjugation of



probe DNA-NH<sub>2</sub> onto MMP-COOH. Despite EDC chemistry is considered robust in general, under the reaction condition recommended by the supplier, the following constraints to the reaction efficacy could not be avoided.

Although EDC is considerably more reactive in aqueous media of low pH, the half-life of EDC decreases to 3.9 h at pH 5 (25 °C, 50 mM MES).<sup>[295]</sup> At the conjugation pH 4.8 according to the manufacturer protocol, without carboxylate ions, EDC could lost its activity rapidly by water hydrolysis into the corresponding urea derivative.<sup>[296]</sup> The reactive intermediate of EDC and carboxylate ion is a highly unstable O-acylisourea. This compound suffers protonation easily at the Schiff base to form unstable carbocation that is susceptible to nucleophilic attack. It is known that attack from carboxylate ion (a strong base) produces carboxylic anhydride, an intermediate essential for amidation; and cyclizable carboxylic acids facilitate the formation of carboxylic anhydride significantly.<sup>[296]</sup> O-acylisourea derived from the non-cyclizable carboxylic acids has been demonstrated to undergo rapid water hydrolysis, turning into urea derivative despite with the presence of amine.<sup>[296]</sup> It remains confidential information regarding the carboxyl types for the commercial MMP-COOH, and the amidation efficiency would be low if they do not bear cyclizable carboxyl groups. Furthermore, COOH/EDC ratio of 1/30 has been reported to form by-products which prevent the coupling with amines.<sup>[296]</sup> The excess EDC used in the current work (1/50) may have already produced markedly stable N-acylurea from the undesired side reaction. Most importantly, since the carboxyl activation by EDC was performed at pH 4.8, and the DNA-NH<sub>2</sub> were incubated directly with the reaction mixture, the amines were probably in protonated state. Formation of amide bond is generally more efficient at higher pH, in which the amines retain their unionized state. Protonated amines are relatively ineffective nucleophiles to attack the O-acylisourea derived carbocation, hence reducing the amidation efficiency considerably.<sup>[296]</sup>



According to the manufacturer, the coupling efficiency for their MMP-COOH is not improved with the use of N-hydroxysuccinimide (NHS), a reagent commonly exploited to raise the efficiency of EDC-mediated amidation. With these concerns, more polar N-hydroxysulfosuccinimide (NHSS) is employed in this work because the derived intermediate preserves water-solubility compared to that of NHS, by virtue of the charged sulfonate group. NHSS converts the carboxyl group to amine-reactive NHSS-ester which is less labile and possesses longer lifetime. The NHSS-ester has sufficient stability to permit even two-step cross-linking, i.e. carboxyl activation at more acidic condition, and subsequent amidation at slightly basic medium which allow nucleophilic attack from the unionized amines. Note that NHSS-ester has longer lifespan while the hydrolysis of NHSS-ester compete with amidation at acidic and basic aqueous media, respectively.<sup>[294]</sup> Overnight cross-linking is therefore feasible for EDC/NHSS-mediated coupling to enhance the amide bond formation efficiency.<sup>[294]</sup>

It was found that more nAu adsorbed nonspecifically onto the MMP-DNA fabricated via EDC cross-linking, whereas less nAu bound on the MMP-DNA with EDC/NHSS coupling. The high adsorptivity associated with EDC cross-linking might partly be due to the by-product N-acylurea since excess EDC has been used. The N-acylurea which is rich in carbonyl oxygen, amine nitrogen and hydrogen may contribute to the adverse hydrogen bonding with nAu-DNA. Whereas more successful coupling could be attributed to the EDC/NHSS cross-linking chemistry, wherein more DNA-NH<sub>2</sub> were grafted onto MMP than that with EDC alone, granting the MMP-DNA better repulsion against nonspecific adsorption and consequently trapped less nAu-DNA on the surface. As such, the efficiency of EDC-mediated coupling has been improved with the assistance of NHSS.

Nevertheless, nonspecific adsorption persisted even for EDC/NHSS cross-linking. In contrast to protein-NH<sub>2</sub> conjugation onto the MMP-COOH, each ssDNA only carries one

NH<sub>2</sub> compared to protein macromolecules that often contain multiple NH<sub>2</sub>. As the lifetime of each NHSS-ester in PBS is short, most reported works that involved MMP & DNA conjugation have indeed employed other conjugation chemistry. For instance, via cross-linker succinimidyl-4-(p-maleimidophenyl) butyrate (SMPB) to immobilize thiolated DNA on MMP-NH<sub>2</sub> in medium of anhydrous dimethyl sulfoxide (DMSO); or via streptavidin-biotin chemistry to immobilize biotinylated DNA on MMP with streptavidin surface.

#### 6.3.4 Suggested improvements

Several procedures, as listed below in this section, are recommended in order to implement the assay successfully and to improve the single-mismatch sensitivity.

Bovine serum albumin (BSA) is a macromolecule blocker which has been employed widely in the passivation of solid surfaces (e.g. glass,<sup>[297]</sup> magnetic beads,<sup>[265,267,298]</sup> polystyrene well plates,<sup>[299-301]</sup> etc) to provide sufficient resistance for undesirable biomolecular adsorption. In MMP-assisted DNA detection, 0.05% (w/v) BSA in the hybridizing medium has reduced considerably the quantity of 25 b polyadenine adsorbed nonspecifically on the MMP conjugated with 25 b polythymine.<sup>[290]</sup> 1mg/mL BSA in the hybridization medium also provided the highest detectable DNA signal compared to the samples incubated without or with less/more BSA.<sup>[302]</sup> The enhancement effect from BSA has been attributed to the minimization of nonspecific adsorption for both detection probes (carbon nanotube-DNA) and targets ssDNA onto the MMP-DNA in the collective hybridization.

As the MMP-DNA in the current schemes are capable of trapping nAu-DNA (Figure 6.5Ib, 6.5IIb, 6.7IIb, 6.8e), the incorporation of BSA may be practical to effectively block the nonspecific adsorption and further enhance the hybridization efficiency. BSA can be applied in various steps. For example, freshly conjugated MMP-DNA have been washed with

BSA<sup>[267]</sup> or incubated with BSA<sup>[264-265,275,298,303-304]</sup> for 15-60 min prior to storage; hybridized MMP-target could be washed with BSA<sup>[304]</sup> or incubated with BSA<sup>[305]</sup> for 15 min before the washing.

On the other hand, freshly conjugated nAu-DNA could be passivated with BSA because the BSA-free nAu-DNA probes showed strong adsorption toward MMP and caused high background.<sup>[275]</sup> Although the nAu-DNA probes used in this system are passivated with short oligonucleotides comprising five thymine bases (dT<sub>5</sub>), the resistance might not be sufficient to withhold the strong attraction towards MMP-DNA, thus leading to nonspecific adsorption. It has also been found that the bigger passivating components confer better stability to the nAu (data not shown). Thus, BSA (66 kDa) can be used to substitute the short oligonucleotides in passivating the remaining nAu surface to prevent nonspecific adsorption.

When BSA is employed as the blocking agent during hybridization, it is critical to optimize the BSA concentration because excessive BSA imparts undesirable crowding or steric hindrance, and leads to reduced hybridization efficiency.<sup>[302]</sup> When BSA is exploited for surface passivation of either MMP or nAu, the probes ssDNA then require mute spacer of adequate length to expose the recognition sequence outside the BSA region to ensure that the normal base-pairing process is not interrupted.<sup>[279]</sup> It is aspired that the optimized BSA blocking or loading could be advantageous to suppress the nonspecific signals.

As an alternative to BSA, non-complementary DNA and transfer-RNA have been utilized as the blocking agents during collective hybridization<sup>[279]</sup> and protein detection,<sup>[287,306]</sup> respectively. The function of blocking DNA is to further block the nAu-DNA and MMP-DNA and prevent any nonspecific adsorption between them. Therefore, in this system, about 10-100 fold of non-cognate ssDNA can be added to the hybridization mixture in which the detection probes are present.

The spacer comprising 15 deoxythymidine triphosphates (T15) for probes T and H (Table 6.2) immobilized on the nAu may be replaced with 15 deoxyadenosine triphosphates (A15). The spacer gives enough space for complementary DNA to come in and hybridize with the recognition site. As thymine has the least adsorption propensity for gold surface among the nucleobases,<sup>[307]</sup> T15 could minimize the probe adsorption on the dT<sub>5</sub>-passivated nAu. On the other hand, adenine base that exhibits the highest adsorption affinity could possibly induce weak interaction between the adenine and gold surface and hence minimize the nonspecific binding during the detection assay.<sup>[287]</sup> Additionally, the dT<sub>5</sub> passivation may also be substituted with dA<sub>5</sub> or even longer dA<sub>10</sub>, for the same rationale as above.

Nonspecific adsorption is not unique to DNA detection system only as it is also prevalent for MMP-assisted protein detection assay.<sup>[287]</sup> For the latter, applying higher concentrations of MMP and nAu probe captured more targets protein, along with more nonspecific binding. It is suggested to lower the probe concentration when significant nonspecific adsorption is observed, as the probe concentration is an important factor to reduce nonspecific binding.<sup>[306]</sup>

In order to improve the selectivity between PM and SM, the salt concentration during the hybridization of probe nAu-DNA with the target DNA could be optimized, as the salt condition has been demonstrated to play an important role in maximizing the sensitivity level for both LOD and SBM.<sup>[267]</sup>

There is serious concern on the reusability of MMP-DNA. Home-made MNP-DNA has been verified to exhibit good reproducibility for DNA detection up to 16 times in the presence of optimum BSA content and storage at 4 °C.<sup>[302]</sup> However, reuse of the biomolecule-conjugated MMP is not recommended by the supplier for the commercial MMP. Besides, there was gradual increase in the amount of nonspecifically adsorbed nAu-DNA in the control sample with increasing cycle of usage, which could mean that the quality of

MMP-DNA has deteriorated. Therefore, by preparing the fresh batch of MMP-DNA for each experiment, the data analysis would probably yield less discrepancy among each repeats, though at the higher expense. It should be noted that the used MMP-DNA were only washed by copious amount of pure water to denature the hybridized DNA.

For cross-linking employing either EDC or EDC/NHSS routes, the structure of probes MMP-DNA co-hybridizing with probes nAu-DNA in the presence of ample complementary targets DNA could not be obtained from the TEM analysis, such as those illustrated in the literatures.<sup>[268,274,277,282]</sup> This indicates that the coupling of DNA-NH<sub>2</sub> with MMP-COOH by both chemistries are not efficient. Furthermore, the level of nonspecific adsorption increased with more cycles of MMP-DNA usage, despite the beads have been washed with copious pure water for multiple times after each cycle.

A few measures may be undertaken to attain better functionalization and ultimately higher sensitivity in detection. For example, during the EDC/NHSS coupling reaction, the ratio of COOH/EDC should be controlled at 1/5-1/10 to avoid the side reaction of producing N-acylurea.<sup>[296]</sup> Also, instead of the NHSS/EDC ratio of 1/1 used throughout the current work, the ratio can be tuned to 1/10 due to the extremely short life-span and hydrolysis-prone EDC.<sup>[294]</sup> Besides, carboxyl activation could be carried out at 0 °C in order to improve the stability of the amine-reactive intermediates, while the amidation be done at 25 °C.<sup>[296]</sup> Another point for concern may lie in the types of buffers used during the cross-linking process. A commonly used buffer, the phosphate solution, is incompatible because the phosphate ions could react with carbodiimide to form O-phosphoisourea that hydrolyzes rapidly into the corresponding urea.<sup>[294-295]</sup> In this work, carboxyl activation has been performed in MES buffer pH 4.8 to obtain the NHSS-ester, while the amidation was done in the common PBS buffer pH 7.4 to render the amino groups in unionized state. Thus, PBS should be substituted with MES buffer pH 6.5 in the beads washing as well as in the

subsequent amidation, as this would eliminate the phosphate effect and improve the coupling. Also, acetate and citrate buffers should be avoided as they are carboxylated and are able to form mixed anhydrides with MMP-COOH and drive towards side reactions with by-products.<sup>[294,308]</sup>

If the coupling efficiency could not be improved after the aforementioned modification, it is advisable to use different linkage (e.g. streptavidin-biotin) to immobilize the DNA onto the MMP. Streptavidin-biotin binding has been the most commonly used cross-linking method, although the materials are considerably more expensive, and the bonding is not as strong as the amide bond.

## **6.4 Conclusion**

In this study, the superparamagnetic MMP have been exploited to concentrate and separate the target ssDNA in the LSPR-assisted detection. As the surface plasmon scattering seems to receive relatively little application in the MMP-aided DNA sensing, this study is undertaken to investigate the robustness of such combination. After some modification on the experimental techniques, a simple DNA detection scheme is employed, in which the non-bleaching plasmonic scattering from the gold nanoparticles (nAu) is used directly as the signal to quantify the assay sensitivity by LOD and the selectivity by SBM. No further amplification on the detected signal is carried out e.g. enzymatic reaction or metallic stripping, and no additional barcode DNA or chip-based hybridization is required. The system that has not been fully optimized shows the LOD and SBM at 2 pM and 20 pM respectively. There are two main factors affecting the detection sensitivity and selectivity, i.e. the nonspecific adsorption along with the inefficient probe ssDNA immobilization onto the MMP surface. These two major issues have yet to be completely resolved. Further optimization should bring the sensitivity and selectivity to a lower level compared to the

current reported values. Therefore, the combination of superparamagnetic MMP and LSPR scattering is a potentially useful recipe in the DNA sensing and hence deserves more in-depth study.

## CHAPTER 7: CONCLUSIONS AND FUTURE PROSPECT

### 7.1 Conclusions

Throughout this doctoral research, the LSPR scattering inherent to noble metal nanoparticles and their plasmonic coupling effect have been exploited to study the nanoassembly formation as well as the quantitative characterization of DNA hybridization. The thesis work started with the successful fabrication of spherical gold nanoparticles (nAu) of various sizes that possessed high stability, good homogeneity and versatile surface that allowed easy downstream functionalization. By facily conjugating appropriate probe ssDNA on the nAu via covalent bond, the feasibility of such bio-nanometallic hybrids in the aforementioned studies has been investigated systematically.

Most of the existing studies focusing on the chip-based heterogeneous (surface-bound) hybridization encountered interference arising from glass-aqueous interface. The application of a homogenous (in bulk solution) hybridization system for all works in this thesis could circumvent the problem. This has also enabled a more accurate and statistical representation of the ensemble hybridization behaviour for the whole populations of hybridization components. Moreover, subsequent permanent binding of nanoparticles and nanoassemblies on the glass substrates has facilitated multiple analyses including the spectroscopically-resolved LSPR wavelength shift, the DFM-visualized plasmon colour change, and the FESEM-identification of the nanoassembly structures, hence allowing correlations to be established.

Applying a simple two-component hybridization of complementary nAu-DNA probes, the formation of nanoassemblies in bulk solution was effectively assessed. Indeed, the LSPR from nAu having sufficiently strong scattering cross-section ( $C_{sca}$ ) was found to be a crucial factor to grant the success of scattering-based nanoassembly formation detection. The study demonstrated that the dimensions for nAu influenced drastically the nanoassembly



readout level, because the smaller nAu showed limited observable LSPR shift. The nanoassembly formation efficiency, as quantified in terms of the LSPR shift, showed that the Watson-Crick recognition ability of DNA was well retained because the hybridization percentage of the complementary 50 nm nAu increased with rising nAu concentration, longer hybridization time, and longer complementary duplex DNA length. Additionally, the nAu surface-ssDNA density was shown to play an important role in forming the nanoassemblies of the conjugates.

Having established the proper hybridization condition (e.g. dimension, concentration, surface density, hybridization period etc) from the previous work that affected the assembling process, the LSPR coupling from the nAu nanoassembly formation was tailored to detect DNA. In a three-component assembly, the asymmetry construct from a less thermodynamically favourable and less popular head-to-tail nAu-DNA alignment, together with the bulk size of nAu, was found to confer the head- and tail-probes different recognition dominance. The tail-probe was depicted to exhibit considerably higher single-base mismatch discrimination ability than the head-probe at sites corresponded to their individual recognizing sequences. Specifically, analysis of single-mismatch loci on the tail-probe showed that the GC-mismatch located at the middle of recognition site gave the greatest distinction against perfectly match targets. The assay was not limited to short target ssDNA; when extended to perform hybridization with targets having non-hybridizing elongated sequences, the head-to-tail assay displayed better single-mismatch discrimination, despite at reduced nanoassembly formation efficiency, which is ubiquitous even for the widely-used tail-to-tail alignment.

Although the optical LSPR scattering phenomenon has been studied comprehensively, it receives comparatively little application in the MMP-assisted DNA sensing. Therefore, by employing the non-bleach LSPR scattering from nAu as the sole signal reporter, the

sensitivity and single-base mismatch selectivity that can be achieved in the MMP-aided DNA detection was explored. A simple and direct DNA detection scheme was designed, in which the detected signal used for quantification was not subjected to further amplification. The current system has not been entirely optimized, yet it showed good prospect and presented the sensitivity and single-base mismatch selectivity at 2 pM and 20 pM respectively. Full/More optimization would be able to bring the sensitivity and selectivity to a lower level compared to the current obtained values.

Overall, this research has demonstrated a facile usage of LSPR as well as the plasmon coupling, in order to account for the nanoassembly construction and DNA detection by homogeneous hybridization. Such simple and straightforward nAu and nanoassembly-based quantification can be exploited in driving towards simpler, more sensitive, and more selective DNA sensing strategies.

## 7.2 Future Prospect

Due to the isotropic spherical shape, it is noticed from Work 1 that hybridized nAu-DNA within a low-order nanoassembly (e.g. trimer, tetramer, pentamer) could align in different angle relative to each other and result in very different scattering spectra. For instance, compactly packed trimeric nAu-DNA scatters rather strongly and their scattering colour is classified into ‘orange’ category; whereas trimeric nAu-DNA hybridized in quasi-linear fashion can only be categorized as ‘yellow’ due to its weaker LSPR coupling. As such, measuring the spectral peak shift of nAu-DNA assembled in low-order manner using a monochromator or spectrometer coupled to the dark field microscopy could provide valuable in-depth understanding on the influence of nanoassembly alignment to the scattering spectra. In addition, while the monochromator can analyse the wavelength spectrum of single particles or single nanoassemblies, the DFM is able to simultaneously examine the LSPR scattering colour and determine the corresponding colour category.

Genomic DNA extracted from the cell is of hundreds to thousands of base length, and generally requires PCR amplification for downstream detection. Therefore, it is of great interest to detect the genomic DNA by integrating the site-selective head-to-tail assay in conjunction with the concentrating ability of MMP into one system. This would be a useful platform for high sensitivity and site-specific selectivity detection. Micro RNAs (miRNAs) are a class of non-protein-coding regulatory ssRNA typically of 18-25b. Recent advances in miRNAs expression profiling have implied their emerging potential as biomarkers for cancer diagnostics and classifications.<sup>[309-311]</sup> Consequently, miRNA detection using plasmonic head-to-tail assay is another research direction worth to pursue.

An ideal sensor should give negative response to all single-mismatch DNA, regardless of the mismatch location. Thus, the deployment of a simple flash cell will be appealing, wherein the target DNA and the tail-probe can be incubated in stepwise manner to the head-

probe pre-immobilized on a glass substrate. Apart from flashing to minimize false positive signal, the cell also enables real-time observation of hybridization by DFM as well as real-time measurement of LSPR spectral change upon hybridization using a monochromator. Furthermore, the presence of substrate encourages lower-order nanoassemblies to form (e.g. dimer, trimer) rather than massive/elaborated nanoassemblies, and hence improves the LOD sensitivity. Therefore, the substrate might be able to work together with the head-to-tail alignment to enhance the LOD sensitivity and to incur more stringent SBM selectivity. Depending on the purpose of analysis, if RGB threshold is to be used for nanoassembly classification in hybridization quantification, abundance of dark field micrographs can still be obtained from the flash cell. The substrate-based quantification can then be compared to the existing homogenous data in Work 2 to analyse the substrate effect on the head-to-tail hybridization. And if single particle or single nanoassembly data (e.g. scattering spectrum in correlation to RGB classification) and real-time hybridization kinetics or nanoassembly formation rate is to be examined, then special focus can be paid to the selected particles for in-depth characterization.

Recent study has shown that multiple ssDNA can cooperatively fold a long template DNA strand rapidly into nanoscale DNA objects at constant temperature, with absolute yield that approached 100%.<sup>[312]</sup> For future studies, it is interesting to investigate how the nAu-DNA staples hybridize with the templating strand to affect the DNA folding into 2- and 3-dimensional nanoscale structures. The reaction progress, influenced by the duplex and nanoparticle designs, can be monitored by cryogenic quenching followed by agarose gel electrophoresis or DFM and scattering spectroscopy for plasmon coupling study. The information on the details of these interactions may pave the way towards rapid self-assembly of nanoparticles onto DNA origami which are currently hampered by the low yield and long time scale (order of tens of hours).<sup>[133,313-315]</sup> The DNA-directed assembly of nanoparticles

into DNA objects can thus be a candidate route towards facile generation of future nanodevices such as nanorobots and nanoswitches.<sup>[316-317]</sup>

Besides DNA, MMP in combination with the LSPR scattering can be a potentially versatile biosensor for antibody-antigen,<sup>[29,261,318-320]</sup> aptamer-ligand,<sup>[321]</sup> and lectin-carbohydrate<sup>[322-323]</sup> through their specific interaction. These LSPR-based optical sensors may find useful application in laboratorial diagnostics.

## BIBLIOGRAPHY

1. Jain, P. K.; Lee, K. S.; El-Sayed, I. H.; El-Sayed, M. A., *J. Phys. Chem. B* **2006**, *110*, 7238-7248.
2. Turkevich, J.; Garton, G.; Stevenson, P. C., **1954**, *9*, 26-35.
3. Burda, C.; Chen, X.; Narayanan, R.; El-Sayed, M. A., *Chem. Rev.* **2005**, *105*, 1025-1102.
4. Wiley, B.; Sun, Y.; Xia, Y., *Acc. Chem. Res.* **2007**, *40*, 1067-1076.
5. Jain, P. K.; Huang, X.; El-Sayed, I. H.; El-Sayed, M. A., *Plasmonics* **2007**, *2*, 107-118.
6. Mock, J. J.; Hill, R. T.; Degiron, A.; Zauscher, S.; Chilkoti, A.; Smith, D. R., *Nano Lett.* **2008**, *8*, 2245-2252.
7. Chicanne, C.; David, T.; Quidant, R.; Weeber, J. C.; Lacroute, Y.; Bourillot, E.; Dereux, A.; Colas des Francs, G.; Girard, C., *Phys. Rev. Lett.* **2002**, *88*, 974021-974024.
8. Yamamoto, N.; Araya, K.; García de Abajo, F. J., *Phys. Rev. B: Condens. Matter* **2001**, *64*, 2054191-2054199.
9. Chaturvedi, P.; Hsu, K. H.; Kumar, A.; Fung, K. H.; Mabon, J. C.; Fang, N. X., *ACS Nano* **2009**, *3*, 2965-2974.
10. García De Abajo, F. J., *Rev. Mod. Phys.* **2010**, *82*, 209-275.
11. Bosman, M.; Keast, V. J.; Watanabe, M.; Maarroof, A. I.; Cortie, M. B., **2007**, *18*.
12. Mayer, K. M.; Hafner, J. H., *Chem. Rev.* **2011**, *111*, 3828-3857.
13. Ghosh, S. K.; Pal, T., *Chem. Rev.* **2007**, *107*, 4797-4862.
14. Johnson, P. B.; Christy, R. W., *Phys. Rev. B: Condens. Matter* **1972**, *6*, 4370-4379.
15. Kreibig, U.; Vollmer, M. *Optical Properties of Metal Clusters*; Springer: New York, **1995**.
16. Henry, A. I.; Bingham, J. M.; Ringe, E.; Marks, L. D.; Schatz, G. C.; Van Duyne, R. P., *J. Phys. Chem. C* **2011**, *115*, 9291-9305.
17. Bohren, C. F.; Huffman, D. R. *Absorption and Scattering of Light by Small Particles*; Wiley: New York, **1983**.
18. Yguerabide, J.; Yguerabide, E. E., **1998**, *262*, 137-156.
19. Lee, K.-S.; El-Sayed, M. A., *J. Phys. Chem. B* **2006**, *110*, 19220-19225.
20. Jain, P. K.; El-Sayed, M. A., *Chem. Phys. Lett.* **2010**, *487*, 153-164.
21. Link, S.; El-Sayed, M. A., *J. Phys. Chem. B* **1999**, *103*, 8410-8426.
22. Myroshnychenko, V.; Rodríguez-Fernández, J.; Pastoriza-Santos, I.; Funston, A. M.; Novo, C.; Mulvaney, P.; Liz-Marzán, L. M.; García De Abajo, F. J., *Chem. Soc. Rev.* **2008**, *37*, 1792-1805.
23. Kelly, K. L.; Coronado, E.; Zhao, L. L.; Schatz, G. C., *J. Phys. Chem. B* **2003**, *107*, 668-677.
24. Tcherniak, A.; Ha, J. W.; Dominguez-Medina, S.; Slaughter, L. S.; Link, S., *Nano Lett.* **2010**, *10*, 1398-1404.
25. Berciaud, S.; Cognet, L.; Tamarat, P.; Lounis, B., *Nano Lett.* **2005**, *5*, 515-518.
26. Doremus, R. H., *J. Chem. Phys.* **1964**, *40*, 2389-2396.
27. Link, S.; El-Sayed, M. A., *J. Phys. Chem. B* **1999**, *103*, 4212-4217.
28. Schultz, D. A., *Curr. Opin. Biotechnol.* **2003**, *14*, 13-22.
29. Schultz, S.; Smith, D. R.; Mock, J. J.; Schultz, D. A., *Proc. Natl. Acad. Sci. USA* **2000**, *97*, 996-1001.
30. Yguerabide, J.; Yguerabide, E. E., *Anal. Biochem.* **1998**, *262*, 157-176.
31. Pelton, M.; Aizpurua, J.; Bryant, G., *Laser Photonics Rev.* **2008**, *2*, 136-159.

32. Sönnichsen, C.; Franzl, T.; Wilk, T.; Von Plessen, G.; Feldmann, J.; Wilson, O.; Mulvaney, P., *Phys. Rev. Lett.* **2002**, *88*, 774021-774024.
33. Nehl, C. L.; Grady, N. K.; Goodrich, G. P.; Tam, F.; Halas, N. J.; Hafner, J. H., *Nano Lett.* **2004**, *4*, 2355-2359.
34. Prodan, E.; Radloff, C.; Halas, N. J.; Nordlander, P., *Science* **2003**, *302*, 419-422.
35. Mock, J. J.; Barbic, M.; Smith, D. R.; Schultz, D. A.; Schultz, S., *J. Chem. Phys.* **2002**, *116*, 6755-6759.
36. Tao, A.; Sinsermsuksakul, P.; Yang, P., *Angew. Chem. Int. Ed.* **2006**, *45*, 4597-4601.
37. Halas, N. J.; Lal, S.; Chang, W. S.; Link, S.; Nordlander, P., *Chem. Rev.* **2011**, *111*, 3913-3961.
38. Ringe, E.; Langille, M. R.; Sohn, K.; Zhang, J.; Huang, J.; Mirkin, C. A.; Van Duyne, R. P.; Marks, L. D., *J. Phys. Chem. Lett.* **2012**, *3*, 1479-1483.
39. Mukherjee, S.; Sobhani, H.; Lassiter, J. B.; Bardhan, R.; Nordlander, P.; Halas, N. J., *Nano Lett.* **2010**, *10*, 2694-2701.
40. Hao, F.; Sonnefraud, Y.; Van Dorpe, P.; Maier, S. A.; Halas, N. J.; Nordlander, P., *Nano Lett.* **2008**, *8*, 3983-3988.
41. Orendorff, C. J.; Sau, T. K.; Murphy, C. J., *Small* **2006**, *2*, 636-639.
42. Haynes, C. L.; Van Duyne, R. P., *J. Phys. Chem. B* **2001**, *105*, 5599-5611.
43. McFarland, A. D.; Van Duyne, R. P., *Nano Lett.* **2003**, *3*, 1057-1062.
44. Pierrat, S.; Zins, I.; Breivogel, A.; Sönnichsen, G., *Nano Lett.* **2007**, *7*, 259-263.
45. Miller, M. M.; Lazarides, A. A., *J. Opt. A* **2006**, *8*, S239-S249.
46. Miller, M. M.; Lazarides, A. A., *J. Phys. Chem. B* **2005**, *109*, 21556-21565.
47. Petryayeva, E.; Krull, U. J., *Anal. Chim. Acta* **2011**, *706*, 8-24.
48. Hövel, H.; Fritz, S.; Hilger, A.; Kreibig, U.; Vollmer, M., *Phys. Rev. B: Condens. Matter* **1993**, *48*, 18178-18188.
49. Novo, C.; Funston, A. M.; Pastoriza-Santos, I.; Liz-Marzán, L. M.; Mulvaney, P., *J. Phys. Chem. C* **2008**, *112*, 3-7.
50. Habteyes, T. G.; Dhuey, S.; Wood, E.; Gargas, D.; Cabrini, S.; Schuck, P. J.; Alivisatos, A. P.; Leone, S. R., *ACS Nano* **2012**, *6*, 5702-5709.
51. Chen, S. Y.; Mock, J. J.; Hill, R. T.; Chilkoti, A.; Smith, D. R.; Lazarides, A. A., *ACS Nano* **2010**, *4*, 6535-6546.
52. Bradshaw, J. T.; Mendes, S. B.; Saavedra, S. S., *Anal. Chem.* **2005**, *77*.
53. Willander, M.; Al-Hilli, S., *Methods Mol. Biol. (Clifton, N.J.)* **2009**, *544*, 201-229.
54. Reinhard, B. M.; Siu, M.; Agarwal, H.; Alivisatos, A. P.; Liphardt, J., *Nano Lett.* **2005**, *5*, 2246-2252.
55. Svedberg, F.; Li, Z.; Xu, H.; Käll, M., *Nano Lett.* **2006**, *6*, 2639-2641.
56. Ringler, M.; Klar, T. A.; Schwemer, A.; Susha, A. S.; Stehr, J.; Raschke, G.; Funk, S.; Borowski, M.; Nichtl, A.; Kürzinger, K.; Phillips, R. T.; Feldmann, J., *Nano Lett.* **2007**, *7*, 2753-2757.
57. Martin-Moreno, L., *Nat. Phys.* **2009**, *5*, 457-458.
58. Lee, J. H.; Wu, Q.; Park, W., *Opt. Lett.* **2009**, *34*, 443-445.
59. Wei, Q. H.; Su, K. H.; Durant, S.; Zhang, X., *Nano Lett.* **2004**, *4*, 1067-1071.
60. Nordlander, P.; Oubre, C.; Prodan, E.; Li, K.; Stockman, M. I., *Nano Lett.* **2004**, *4*, 899-903.
61. Rechberger, W.; Hohenau, A.; Leitner, A.; Krenn, J. R.; Lamprecht, B.; Aussenegg, F. R., *Opt. Commun.* **2003**, *220*, 137-141.
62. Yim, T. J.; Wang, Y.; Zhang, X., *Nanot.* **2008**, *19*, 435605.
63. Reinhard, B. M.; Sheikholeslami, S.; Mastroianni, A.; Alivisatos, A. P.; Liphardt, J., *Proc. Natl. Acad. Sci. USA* **2007**, *104*, 2667-2672.
64. Wang, H.; Reinhard, B. M., *J. Phys. Chem. C* **2009**, *113*, 11215-11222.

65. Tamaru, H.; Kuwata, H.; Miyazaki, H. T.; Miyano, K., *Appl. Phys. Lett.* **2002**, *80*, 1826.
66. Su, K. H.; Wei, Q. H.; Zhang, X.; Mock, J. J.; Smith, D. R.; Schultz, S., *Nano Lett.* **2003**, *3*, 1087-1090.
67. Gunnarsson, L.; Rindzevicius, T.; Prikulis, J.; Kasemo, B.; Käll, M.; Zou, S.; Schatz, G. C., *J. Phys. Chem. B* **2005**, *109*, 1079-1087.
68. Crow, M. J.; Seekell, K.; Wax, A., *Opt. Lett.* **2011**, *36*, 757-759.
69. Schmeits, M.; Dambly, L., *Phys. Rev. B: Condens. Matter* **1991**, *44*, 12706-12712.
70. Atay, T.; Song, J. H.; Nurmikko, A. V., *Nano Lett.* **2004**, *4*, 1627-1631.
71. Prikulis, J.; Svedberg, F.; Käll, M.; Enger, J.; Ramser, K.; Goksör, M.; Hanstorp, D., *Nano Lett.* **2004**, *4*, 115-118.
72. Jares-Erijman, E. A.; Jovin, T. M., *Nat. Biotechnol.* **2003**, *21*, 1387-1395.
73. Kelbauskas, L.; Woodbury, N.; Lohr, D., *Biochem. Cell Biol.* **2009**, *87*, 323-335.
74. Vogel, S. S.; Thaler, C.; Koushik, S. V., *Sci. STKE* **2006**, 2006.
75. Stoeva, S.; Klabunde, K. J.; Sorensen, C. M.; Dragieva, I., *J. Am. Chem. Soc.* **2002**, *124*, 2305-2311.
76. Nagpal, P.; Lindquist, N. C.; Oh, S. H.; Norris, D. J., *Science* **2009**, *325*, 594-597.
77. Yin, Y.; Alivisatos, A. P., *Nature* **2005**, *437*, 664-670.
78. Turkevich, J.; Stevenson, P. C.; Hillier, J., *Discuss. Faraday Soc.* **1951**, *11*, 55-75.
79. Rycenga, M.; Cobley, C. M.; Zeng, J.; Li, W.; Moran, C. H.; Zhang, Q.; Qin, D.; Xia, Y., *Chem. Rev.* **2011**, *111*, 3669-3712.
80. Zsigmondy, R. A. In *Nobel Lectures, Chemistry 1922-1941*; Elsevier Publishing Company: Amsterdam, 1966.
81. Hu, M.; Novo, C.; Funston, A.; Wang, H.; Staleva, H.; Zou, S.; Mulvaney, P.; Xia, Y.; Hartland, G. V., *J. Mater. Chem.* **2008**, *18*, 1949-1960.
82. Murphy, C. J.; Gole, A. M.; Stone, J. W.; Sisco, P. N.; Alkilany, A. M.; Goldsmith, E. C.; Baxter, S. C., *Acc. Chem. Res.* **2008**, *41*, 1721-1730.
83. Oldenburg, S. J.; Genick, C. C.; Clark, K. A.; Schultz, D. A., *Anal. Biochem.* **2002**, *309*, 109-116.
84. Butler, J. M.; Elsevier Academic Press: San Diego, CA, 2012.
85. Jin, J.-I.; Grote, J.; Taylor & Francis: Boca Raton, FL, 2012.
86. Berg, J. M.; Tymoczko, J. L.; Stryer, L. *Biochemistry*; W H Freeman: New York, **2002**.
87. Watson, J. D.; Crick, F. H. C., *Nature* **1953**, *171*, 737-738.
88. Clausen-Schaumann, H.; Rief, M.; Tolksdorf, C.; Gaub, H. E., *Biophys. J.* **2000**, *78*, 1997-2007.
89. Yakovchuk, P.; Protozanova, E.; Frank-Kamenetskii, M. D., *Nucleic Acids Res.* **2006**, *34*, 564-574.
90. Rich, A., *Gene* **1993**, *135*, 99-109.
91. Casey, B. P.; Glazer, P. M. *Progress in Nucleic Acid Research and Molecular Biology: Gene Targeting via Triple-Helix Formation*, **2001**; Vol. 67. 163-192.
92. Burge, S.; Parkinson, G. N.; Hazel, P.; Todd, A. K.; Neidle, S., *Nucleic Acids Res.* **2006**, *34*, 5402-5415.
93. Roh, Y. H.; Ruiz, R. C. H.; Peng, S.; Lee, J. B.; Luo, D., *Chem. Soc. Rev.* **2011**, *40*, 5730-5744.
94. Saenger, W.; Hunter, W. N.; Kennard, O., *Nature* **1986**, *324*, 385-388.
95. Mandelkern, M.; Elias, J. G.; Eden, D.; Crothers, D. M., *J. Mol. Biol.* **1981**, *152*, 153-161.
96. Wing, R.; Drew, H.; Takano, T.; Broka, C.; Tanaka, S.; Itakura, K.; Dickerson, R. E., *Nature* **1980**, *287*, 755-758.



97. Smith, S. B.; Cui, Y.; Bustamante, C., *Science* **1996**, 271, 795-799.
98. Kanaar, R.; Cozzarelli, N. R., *Curr. Opin. Struct. Biol.* **1992**, 2, 369-379.
99. Koster, D. A.; Crut, A.; Shuman, S.; Bjornsti, M. A.; Dekker, N. H., *Cell* **2010**, 142, 519-530.
100. Wang, J. C., *Sci. Am.* **1982**, 247, 94-109.
101. Wang, J. C., *Nat. Rev. Mol. Cell Biol.* **2002**, 3, 430-440.
102. Alberts, B.; Johnson, A.; Lewis, J.; Raff, M.; Roberts, K.; Walter, P. *Molecular Biology of the Cell*; Garland Science: New York, **2002**.
103. Bellini, T.; Cerbino, R.; Zanchetta, G. *DNA-Based Soft Phases*, **2012**; Vol. 318. 225-280.
104. Nagao, M.; Sugimura, T.; Matsushima, T., *Annu. Rev. Genet.* **1978**, 12, 117-159.
105. Sugimura, T.; Wakabayashi, K.; Nakagama, H.; Nagao, M., *Cancer Sci.* **2004**, 95, 290-299.
106. Tinnefeld, P.; Sauer, M., *Angew. Chem. Int. Ed.* **2005**, 44, 2642-2671.
107. Lee, S. F.; Osborne, M. A., *Chem. Phys. Chem.* **2009**, 10, 2174-2191.
108. Liu, G. L.; Yin, Y.; Kunchakarra, S.; Mukherjee, B.; Gerion, D.; Jett, S. D.; Bear, D. G.; Gray, J. W.; Alivisatos, A. P.; Lee, L. P.; Chen, F. F., *Nat. Nanotechnol.* **2006**, 1, 47-52.
109. Raschke, G.; Kowarik, S.; Franzl, T.; Sönnichsen, C.; Klar, T. A.; Feldmann, J.; Nichtl, A.; Kürzinger, K., *Nano Lett.* **2003**, 3, 935-938.
110. Li, J.; Chu, X.; Liu, Y.; Jiang, J. H.; He, Z.; Zhang, Z.; Shen, G.; Yu, R. Q., *Nucleic Acids Res.* **2005**, 33, 1-9.
111. Parab, H. J.; Jung, C.; Lee, J. H.; Park, H. G., *Biosensors Bioelectron.* **2010**, 26, 667-673.
112. Thompson, D. G.; Enright, A.; Faulds, K.; Smith, W. E.; Graham, D., *Anal. Chem.* **2008**, 80, 2805-2810.
113. McKenzie, F.; Faulds, K.; Graham, D., *Small* **2007**, 3, 1866-1868.
114. Verdoold, R.; Gill, R.; Ungureanu, F.; Molenaar, R.; Kooyman, R. P. H., *Biosensors Bioelectron.* **2011**, 27, 77-81.
115. Verdoold, R.; Ungureanu, F.; Wasserberg, D.; Kooyman, R. P. H. In *Proceeding of SPIE 2009*; Vol. 7312.
116. Chen, J. I. L.; Chen, Y.; Ginger, D. S., *J. Am. Chem. Soc.* **2010**, 132, 9600-9601.
117. Sönnichsen, C.; Reinhard, B. M.; Liphardt, J.; Alivisatos, A. P., *Nat. Biotechnol.* **2005**, 23, 741-745.
118. Taton, T. A.; Lu, G.; Mirkin, C. A., *J. Am. Chem. Soc.* **2001**, 123, 5164-5165.
119. Xu, W.; Xue, X.; Li, T.; Zeng, H.; Liu, X., *Angew. Chem. Int. Ed.* **2009**, 48, 6849-6852.
120. Sato, K.; Hosokawa, K.; Maeda, M., *J. Am. Chem. Soc.* **2003**, 125, 8102-8103.
121. Wabuyele, M. B.; Yan, F.; Vo-Dinh, T., *Anal. Bioanal. Chem.* **2010**, 398, 729-736.
122. Guerrini, L.; McKenzie, F.; Wark, A. W.; Faulds, K.; Graham, D., *Chem. Sci.* **2012**, 3, 2262-2269.
123. Shan, Y.; Xu, J. J.; Chen, H. Y., *Chem. Commun.* **2009**, 905-907.
124. Haes, A. J.; Stuart, D. A.; Nie, S.; Van Duyne, R. P., *J. Fluores.* **2004**, 14, 355-367.
125. Mirkin, C. A.; Letsinger, R. L.; Mucic, R. C.; Storhoff, J. J., *Nature* **1996**, 382, 607-609.
126. Elghanian, R.; Storhoff, J. J.; Mucic, R. C.; Letsinger, R. L.; Mirkin, C. A., *Science* **1997**, 277, 1078-1081.
127. Jin, R.; Wu, G.; Li, Z.; Mirkin, C. A.; Schatz, G. C., *J. Am. Chem. Soc.* **2003**, 125, 1643-1654.

128. Anker, J. N.; Hall, W. P.; Lyandres, O.; Shah, N. C.; Zhao, J.; Van Duyne, R. P., *Nat. Mater.* **2008**, *7*, 442-453.
129. Bichenkova, E. V.; Lang, Z.; Yu, X.; Rogert, C.; Douglas, K. T., *Biochim. Biophys. Acta* **2011**, *1809*, 1-23.
130. Saha, K.; Agasti, S. S.; Kim, C.; Li, X.; Rotello, V. M., *Chem. Rev.* **2012**, *112*, 2739-2779.
131. Zanolli, L. M.; D'Agata, R.; Spoto, G., *Anal. Bioanal. Chem.* **2012**, *402*, 1759-1771.
132. Peng, H. I.; Miller, B. L., *Analyst* **2011**, *136*, Analyst436-447.
133. Nykypanchuk, D.; Maye, M. M.; Van Der Lelie, D.; Gang, O., *Nature* **2008**, *451*, 549-552.
134. Jones, M. R.; MacFarlane, R. J.; Lee, B.; Zhang, J.; Young, K. L.; Senesi, A. J.; Mirkin, C. A., *Nat. Mater.* **2010**, *9*, 913-917.
135. Macfarlane, R. J.; Lee, B.; Jones, M. R.; Harris, N.; Schatz, G. C.; Mirkin, C. A., *Science* **2011**, *334*, 204-208.
136. Storhoff, J. J.; Elghanian, R.; Mucic, R. C.; Mirkin, C. A.; Letsinger, R. L., *J. Am. Chem. Soc.* **1998**, *120*, 1959-1964.
137. Pan, B.; Ao, L.; Gao, F.; Tian, H.; He, R.; Cui, D., *Nanot.* **2005**, *16*, 1776-1780.
138. Yang, D. P.; Cui, D. X., *Chem. Asia. J.* **2008**, *3*, 2010-2022.
139. Xu, L.; Kuang, H.; Xu, C.; Ma, W.; Wang, L.; Kotov, N. A., *J. Am. Chem. Soc.* **2012**, *134*, 1699-1709.
140. Reynolds Iii, R. A.; Mirkin, C. A.; Letsinger, R. L., *J. Am. Chem. Soc.* **2000**, *122*, 3795-3796.
141. Kanjanawarut, R.; Su, X., *Anal. Chem.* **2009**, *81*, 6122-6129.
142. Lee, J. S.; Lytton-Jean, A. K. R.; Hurst, S. J.; Mirkin, C. A., *Nano Lett.* **2007**, *7*, 2112-2115.
143. Pal, S.; Sharma, J.; Yan, H.; Liu, Y., *Chem. Commun.* **2009**, 6059-6061.
144. Tokareva, I.; Hutter, E., *J. Am. Chem. Soc.* **2004**, *126*, 15784-15789.
145. Vidal Jr, B. C.; Deivaraj, T. C.; Yang, J.; Too, H. P.; Chow, G. M.; Gan, L. M.; Lee, J. Y., *New J. Chem.* **2005**, *29*, 812-816.
146. Cao, Y.; Jin, R.; Mirkin, C. A., *J. Am. Chem. Soc.* **2001**, *123*, 7961-7962.
147. Lim, D. K.; Kim, I. J.; Nam, J. M., *Chem. Commun.* **2008**, 5312-5314.
148. Chakrabarti, R.; Klibanov, A. M., *J. Am. Chem. Soc.* **2003**, *125*, 12531-12540.
149. Chen, C. K.; Shiang, Y. C.; Huang, C. C.; Chang, H. T., *Biosensors Bioelectron.* **2011**, *26*, 3464-3468.
150. Jian, J. W.; Huang, C. C., *Chem. Eur. J.* **2011**, *17*, 2374-2380.
151. Storhoff, J. J.; Lazarides, A. A.; Mucic, R. C.; Mirkin, C. A.; Letsinger, R. L.; Schatz, G. C., *J. Am. Chem. Soc.* **2000**, *122*, 4640-4650.
152. Xu, J.; Craig, S. L., *J. Am. Chem. Soc.* **2005**, *127*, 13227-13231.
153. Li, H.; Rothberg, L., *Proc. Natl. Acad. Sci. USA* **2004**, *101*, 14036-14039.
154. Ray, P. C., *Angew. Chem. Int. Ed.* **2006**, *45*, 1151-1154.
155. Ma, Z.; Tian, L.; Wang, T.; Wang, C., *Anal. Chim. Acta* **2010**, *673*, 179-184.
156. Zhu, X.; Liu, Y.; Yang, J.; Liang, Z.; Li, G., *Biosensors Bioelectron.* **2010**, *25*, 2135-2139.
157. Charrier, A.; Candoni, N.; Liachenko, N.; Thibaudau, F., *Biosensors Bioelectron.* **2007**, *22*, 1881-1886.
158. Hosokawa, K.; Sato, K.; Ichikawa, N.; Maeda, M., *L. Chip* **2004**, *4*, 181-185.
159. Sato, Y.; Sato, K.; Hosokawa, K.; Maeda, M., *Anal. Biochem.* **2006**, *355*, 125-131.
160. Xiao, L.; Wei, L.; He, Y.; Yeung, E. S., *Anal. Chem.* **2010**, *82*, 6308-6314.
161. Nie, S.; Emory, S. R., *Science* **1997**, *275*, 1102-1106.
162. Das, P.; Metiu, H., *J. Phys. Chem.* **1985**, *89*, 4680-4687.

163. Liu, G. L.; Long, Y. T.; Choi, Y.; Kang, T.; Lee, L. P., *Nat. Methods* **2007**, *4*, 1015-1017.
164. Hill, R. T.; Mock, J. J.; Urzhumov, Y.; Sebba, D. S.; Oldenburg, S. J.; Chen, S. Y.; Lazarides, A. A.; Chilkoti, A.; Smith, D. R., *Nano Lett.* **2010**, *10*, 4150-4154.
165. Larmour, I. A.; Argueta, E. A.; Faulds, K.; Graham, D., *J. Phys. Chem. C* **2012**, *116*, 2677-2682.
166. McNay, G.; Eustace, D.; Smith, W. E.; Faulds, K.; Graham, D., *Appl. Spectrosc.* **2011**, *65*, 825-837.
167. Thompson, D. G.; Faulds, K.; Smith, W. E.; Graham, D., *J. Phys. Chem. C* **2009**, *114*, 7384-7389.
168. Wang, H. N.; Vo-Dinh, T., *Small* **2011**, *7*, 3067-3074.
169. Maye, M. M.; Gang, O.; Cotlet, M., *Chem. Commun.* **2010**, *46*, 6111-6113.
170. Liu, F.; Choi, J. Y.; Seo, T. S., *Biosensors Bioelectron.* **2010**, *25*, 2361-2365.
171. Ray, P. C.; Fortner, A.; Griffin, J.; Kim, C. K.; Singh, J. P.; Yu, H., *Chem. Phys. Lett.* **2005**, *414*, 259-264.
172. Wang, H.; Li, J.; Wang, Y.; Jin, J.; Yang, R.; Wang, K.; Tan, W., *Anal. Chem.* **2010**, *82*, 7684-7690.
173. Dubertret, B.; Calame, M.; Libchaber, A. J., *Nat. Biotechnol.* **2001**, *19*, 365-370.
174. Zhou, H.; Liu, J.; Xu, J. J.; Chen, H. Y., *Chem. Commun.* **2011**, *47*, 8358-8360.
175. Zhou, H.; Liu, J.; Xu, J. J.; Chen, H. Y., *Anal. Chem.* **2011**, *83*, 8320-8328.
176. Chen, Y.; Munechika, K.; Jen-La Plante, I.; Munro, A. M.; Skrabalak, S. E.; Xia, Y.; Ginger, D. S., *Appl. Phys. Lett.* **2008**, *93*.
177. Zhao, W. W.; Wang, J.; Xu, J. J.; Chen, H. Y., *Chem. Commun.* **2011**, *47*, 10990-10992.
178. Fong, K. E.; Yung, L.-Y. L., *RSC Adv.* **2012**, *2*, 5154-5163.
179. Jana, N. R.; Gearheart, L.; Murphy, C. J., *Chem. Mater.* **2001**, *13*, 2313-2322.
180. Xia, H.; Bai, S.; Hartmann, J.; Wang, D., *Langmuir* **2010**, *26*, 3585-3589.
181. Zhang, Q.; Xie, J.; Yu, Y.; Lee, J. Y., **2010**, *2*, 1962-1975.
182. Qiu, P.; Mao, C., *J. Nanopart. Res.* **2009**, *11*, 885-894.
183. Brown, K. R.; Walter, D. G.; Natan, M. J., *Chem. Mater.* **2000**, *12*, 306-313.
184. Kimling, J.; Maier, M.; Okenve, B.; Kotaidis, V.; Ballot, H.; Plech, A., *J. Phys. Chem. B* **2006**, *110*, 15700-15707.
185. Jana, N. R.; Gearheart, L.; Murphy, C. J., *Langmuir* **2001**, *17*, 6782-6786.
186. Sau, T. K.; Pal, A.; Jana, N. R.; Wang, Z. L.; Pal, T., *J. Nanopart. Res.* **2001**, *3*, 257-261.
187. Brown, K. R.; Natan, M. J., *Langmuir* **1998**, *14*, 726-728.
188. Volkert, A. A.; Subramaniam, V.; Haes, A. J., *Chem. Commun.* **2011**, *47*, 478-480.
189. Niu, J.; Zhu, T.; Liu, Z., *Nanot.* **2007**, *18*.
190. Ji, X.; Song, X.; Li, J.; Bai, Y.; Yang, W.; Peng, X., *J. Am. Chem. Soc.* **2007**, *129*, 13939-13948.
191. Qin, W. J.; Yim, O. S.; Lai, P. S.; Yung, L. Y. L., *Biosensors Bioelectron.* **2010**, *25*, 2021-2025.
192. Handley, D. A. *Colloidal Gold: Principles Methods and Applications*; Academic Press: New York, **1989**.
193. Personick, M. L.; Langille, M. R.; Zhang, J.; Mirkin, C. A., *Nano Lett.* **2011**, *11*, 3394-3398.
194. Capek, I., *Adv. Colloid Interface Sci.* **2011**, *163*, 123-143.
195. Funston, A. M.; Novo, C.; Davis, T. J.; Mulvaney, P., *Nano Lett.* **2009**, *9*, 1651-1658.
196. Sebba, D. S.; Mock, J. J.; Smith, D. R.; LaBean, T. H.; Lazarides, A. A., *Nano Lett.* **2008**, *8*, 1803-1808.

197. Jain, P. K.; El-Sayed, M. A., *Nano Lett.* **2008**, *8*, 4347-4352.
198. Ling, J.; Li, Y. F.; Huang, C. Z., *Anal. Chem.* **2009**, *81*, 1707-1714.
199. Xu, H.; Käll, M., *Phys. Rev. Lett.* **2002**, *89*, 2468021-2468024.
200. De Waele, R.; Koenderink, A. F.; Polman, A., *Nano Lett.* **2007**, *7*, 2004-2008.
201. Koenderink, A. F.; De Waele, R.; Prangsma, J. C.; Polman, A., *Phys. Rev. B: Condens. Matter* **2007**, *76*.
202. Tokonami, S.; Shiigi, H.; Nagaoka, T., *Anal. Chem.* **2008**, *80*, 8071-8075.
203. Wang, L.; Li, P. C. H., *Biomicrofluidics* **2010**, *4*, 1-9.
204. Du, B. A.; Li, Z. P.; Liu, C. H., *Angew. Chem. Int. Ed.* **2006**, *45*, 8022-8025.
205. Zhang, J.; Song, S.; Zhang, L.; Wang, L.; Wu, H.; Pan, D.; Fan, C., *J. Am. Chem. Soc.* **2006**, *128*, 8575-8580.
206. Li, J.; Jiang, J. H.; Xu, X. M.; Chu, X.; Jiang, C.; Shen, G.; Yu, R. Q., *Analyst* **2008**, *133*, 939-945.
207. Hurst, S. J.; Min, S. H.; Lytton-Jean, A. K. R.; Mirkin, C. A., *Anal. Chem.* **2007**, *79*, 7201-7205.
208. Xu, X.; Han, M. S.; Mirkin, C. A., *Angew. Chem. Int. Ed.* **2007**, *46*, 3468-3470.
209. Han, M. S.; Lytton-Jean, A. K. R.; Oh, B. K.; Heo, J.; Mirkin, C. A., *Angew. Chem. Int. Ed.* **2006**, *45*, 1807-1810.
210. Hill, H. D.; Hurst, S. J.; Mirkin, C. A., *Nano Lett.* **2009**, *9*, 317-321.
211. Hurst, S. J.; Hill, H. D.; Macfarlane, R. J.; Wu, J.; Dravid, V. P.; Mirkin, C. A., *Small* **2009**, *5*, 2156-2161.
212. Qin, W. J.; Yung, L. Y. L., *Bioconjugate Chem.* **2008**, *19*, 385-390.
213. Zhao, W.; Lin, L.; Hsing, I. M., *Bioconjugate Chem.* **2009**, *20*, 1218-1222.
214. Zhao, W.; Hsing, I. M., *Chem. Commun.* **2010**, *46*, 1314-1316.
215. Claridge, S. A.; Liang, H. W.; Basu, S. R.; Fréchet, J. M. J.; Alivisatos, A. P., *Nano Lett.* **2008**, *8*, 1202-1206.
216. Loweth, C. J.; Brett Caldwell, W.; Peng, X.; Alivisatos, A. P.; Schultz, P. G., *Angew. Chem. Int. Ed.* **1999**, *38*, 1808-1812.
217. Suzuki, K.; Hosokawa, K.; Maeda, M., *J. Am. Chem. Soc.* **2009**, *131*, 7518-7519.
218. Sheikholeslami, S.; Jun, Y. W.; Jain, P. K.; Alivisatos, A. P., *Nano Lett.* **2010**, *10*, 2655-2660.
219. Sannomiya, T.; Hafner, C.; Voros, J., *Nano Lett.* **2008**, *8*, 3450-3455.
220. Dubois, L. H.; Nuzzo, R. G., *Annu. Rev. Phys. Chem.* **1992**, *43*, 437-463.
221. Biebuyck, H. A.; Whitesides, G. M., *Langmuir* **1993**, *9*, 1766-1770.
222. Lytton-Jean, A. K. R.; Mirkin, C. A., *J. Am. Chem. Soc.* **2005**, *127*, 12754-12755.
223. Peterson, A. W.; Heaton, R. J.; Georgiadis, R. M., *Nucleic Acids Res.* **2001**, *29*, 5163-5168.
224. Peterson, A. W.; Wolf, L. K.; Georgiadis, R. M., *J. Am. Chem. Soc.* **2002**, *124*, 14601-14607.
225. Hill, H. D.; Millstone, J. E.; Banholzer, M. J.; Mirkin, C. A., *ACS Nano* **2009**, *3*, 418-424.
226. Park, S. J.; Lazarides, A. A.; Storhoff, J. J.; Pesce, L.; Mirkin, C. A., *J. Phys. Chem. B* **2004**, *108*, 12375-12380.
227. Mucic, R. C.; Storhoff, J. J.; Mirkin, C. A.; Letsinger, R. L., *J. Am. Chem. Soc.* **1998**, *120*, 12674-12675.
228. Fong, K. E.; Yung, L.-Y. L., *RSC Adv.* **2013**, *3*, 6076-6084.
229. Cotton, R. G. H., *Mutat. Res.* **1993**, *285*, 125-144.
230. Kwok, P. Y.; Chen, X., *Curr. Issues Mol. Biol.* **2003**, *5*, 43-60.
231. Nelson, N. C., *Crit. Rev. Clin. Lab. Sci.* **1998**, *35*, 369-414.

232. Adams, N. M.; Jackson, S. R.; Haselton, F. R.; Wright, D. W., *Langmuir* **2012**, 28, 1068-1082.
233. Alivisatos, A. P.; Johnsson, K. P.; Peng, X.; Wilson, T. E.; Loweth, C. J.; Bruchez Jr, M. P.; Schultz, P. G., *Nature* **1996**, 382, 609-611.
234. Jain, P. K.; Huang, W.; El-Sayed, M. A., *Nano Lett.* **2007**, 7, 2080-2088.
235. Cutler, J. I.; Auyeung, E.; Mirkin, C. A., *J. Am. Chem. Soc.* **2012**, 134, 1376-1391.
236. Chen, C.; Wang, W.; Ge, J.; Zhao, X. S., *Nucleic Acids Res.* **2009**, 37, 3756-3765.
237. Chak, C. P.; Lai, J. M. Y.; Sham, K. W. Y.; Cheng, C. H. K.; Leung, K. C. F., *RSC Adv.* **2011**, 1, 1342-1348.
238. Xue, X.; Xu, W.; Wang, F.; Liu, X., *J. Am. Chem. Soc.* **2009**, 131, 11668-11669.
239. Deng, Z.; Tian, Y.; Lee, S. H.; Ribbe, A. E.; Mao, C., *Angew. Chem. Int. Ed.* **2005**, 44, 3582-3585.
240. Aldaye, F. A.; Sleiman, H. F., *Angew. Chem. Int. Ed.* **2006**, 45, 2204-2209.
241. Aldaye, F. A.; Sleiman, H. F., *J. Am. Chem. Soc.* **2007**, 129, 4130-4131.
242. Liu, J.; Lu, Y., *J. Am. Chem. Soc.* **2003**, 125, 6642-6643.
243. Storhoff, J. J.; Lucas, A. D.; Garimella, V.; Bao, Y. P.; Müller, U. R., *Nat. Biotechnol.* **2004**, 22, 883-887.
244. Chen, Y. T.; Hsu, C. L.; Hou, S. Y., *Anal. Biochem.* **2008**, 375, 299-305.
245. Dillenback, L. M.; Goodrich, G. P.; Keating, C. D., *Nano Lett.* **2006**, 6, 16-23.
246. Hill, H. D.; Vega, R. A.; Mirkin, C. A., *Anal. Chem.* **2007**, 79, 9218-9223.
247. Liu, J.; Lu, Y., *Angew. Chem. Int. Ed.* **2006**, 45, 90-94.
248. Liu, J.; Lu, Y., *Adv. Mater.* **2006**, 18, 1667-1671.
249. Liu, J.; Lu, Y., *J. Am. Chem. Soc.* **2007**, 129, 8634-8643.
250. Liu, J.; Mazumdar, D.; Lu, Y., *Angew. Chem. Int. Ed.* **2006**, 45, 7955-7959.
251. Liu, J.; Cao, Z.; Lu, Y., *Chem. Rev.* **2009**, 109, 1948-1998.
252. Takeda, Y.; Kondow, T.; Mafuné, F., *J. Phys. Chem. C* **2008**, 112, 89-94.
253. Smith, B. D.; Dave, N.; Huang, P. J. J.; Liu, J., *J. Phys. Chem. C* **2011**, 115, 7851-7857.
254. Rosi, N. L.; Mirkin, C. A., *Chem. Rev.* **2005**, 105, 1547-1562.
255. Jeon, J.; Lim, D. K.; Nam, J. M., *J. Mater. Chem.* **2009**, 19, 2107-2117.
256. Dolatabadi, J. E. N.; Mashinchian, O.; Ayoubi, B.; Jamali, A. A.; Mobed, A.; Losic, D.; Omid, Y.; de la Guardia, M., *TrAC, Trends Anal. Chem.* **2011**, 30, 459-472.
257. Kouassi, G. K., *Curr. Nanosci.* **2011**, 7, 510-523.
258. Ngomsik, A. F.; Bee, A.; Draye, M.; Cote, G.; Cabuil, V., *C. R. Chim.* **2005**, 8, 963-970.
259. Thurm, S.; Odenbach, S., *J. Magn. Magn. Mater.* **2002**, 252, 247-249.
260. Huber, D. L., *Small* **2005**, 1, 482-501.
261. Nam, J. M.; Thaxton, C. S.; Mirkin, C. A., *Science* **2003**, 301, 1884-1886.
262. Zhuang, J.; Cheng, T.; Gao, L.; Luo, Y.; Ren, Q.; Lu, D.; Tang, F.; Ren, X.; Yang, D.; Feng, J.; Zhu, J.; Yan, X., *Toxicon* **2010**, 55, 145-152.
263. Hsu, I. H.; Hsu, T. C.; Sun, Y. C., *Biosensors Bioelectron.* **2011**, 26, 4605-4609.
264. Fan, A.; Cai, S.; Cao, Z.; Lau, C.; Lu, J., *Analyst* **2010**, 135, 1400-1405.
265. Zhan, Z.; Cao, C.; Sim, S. J., *Biosensors Bioelectron.* **2010**, 26, 511-516.
266. Xu, X.; Georganopoulou, D. G.; Hill, H. D.; Mirkin, C. A., *Anal. Chem.* **2007**, 79, 6650-6654.
267. Zhan, Z.; Ma, X.; Cao, C.; Sim, S. J., *Biosensors Bioelectron.* **2012**, 32, 127-132.
268. Chen, Y.; Aveyard, J.; Wilson, R., *Chem. Commun.* **2004**, 2804-2805.
269. Castañeda, M. T.; Merkoçi, A.; Pumera, M.; Alegret, S., *Biosensors Bioelectron.* **2007**, 22, 1961-1967.
270. Yu, F.; Li, G.; Qu, B.; Cao, W., *Biosensors Bioelectron.* **2010**, 26, 1114-1117.

271. Zhang, D.; Huarng, M. C.; Alocilja, E. C., *Biosensors Bioelectron.* **2010**, *26*, 1736-1742.
272. Selvaraju, T.; Das, J.; Jo, K.; Kwon, K.; Huh, C. H.; Kim, T. K.; Yang, H., *Langmuir* **2008**, *24*, 9883-9888.
273. Wang, J.; Xu, D.; Kawde, A. N.; Polsky, R., *Anal. Chem.* **2001**, *73*, 5576-5581.
274. Kawde, A. N.; Wang, J., *Electroanalysis* **2004**, *16*, 101-107.
275. Li, J.; Song, S.; Liu, X.; Wang, L.; Pan, D.; Huang, Q.; Zhao, Y.; Fan, C., *Adv. Mater.* **2008**, *20*, 497-500.
276. Fan, A.; Lau, C.; Lu, J., *Analyst* **2008**, *133*, 219-225.
277. Cai, S.; Xin, L.; Lau, C.; Lu, J., *Analyst* **2010**, *135*, 615-620.
278. Zhu, D.; Tang, Y.; Xing, D.; Chen, W. R., *Anal. Chem.* **2008**, *80*, 3566-3571.
279. Li, J.; Song, S.; Li, D.; Su, Y.; Huang, Q.; Zhao, Y.; Fan, C., *Biosensors Bioelectron.* **2009**, *24*, 3311-3315.
280. Qiu, F.; Gu, K.; Yang, B.; Ding, Y.; Jiang, D.; Wu, Y.; Huang, L. L., *Talanta* **2011**, *85*, 1698-1702.
281. Yang, B.; Zhou, G.; Huang, L. L., *Anal. Bioanal. Chem.* **2010**, *397*, 1937-1945.
282. Wu, L.; Qiu, L.; Shi, C.; Zhu, J., *Biomacromolecules* **2007**, *8*, 2795-2800.
283. Nam, J. M.; Stoeva, S. I.; Mirkin, C. A., *J. Am. Chem. Soc.* **2004**, *126*, 5932-5933.
284. Stoeva, S. I.; Lee, J. S.; Thaxton, C. S.; Mirkin, C. A., *Angew. Chem. Int. Ed.* **2006**, *45*, 3303-3306.
285. Thaxton, C. S.; Hill, H. D.; Georganopoulou, D. G.; Stoeva, S. I.; Mirkin, C. A., *Anal. Chem.* **2005**, *77*, 8174-8178.
286. Hill, H. D.; Mirkin, C. A., *Nat. Protocols* **2006**, *1*, 324-336.
287. Nam, J. M.; Jang, K. J.; Groves, J. T., *Nat. Protocols* **2007**, *2*, 1438-1444.
288. Tai, Y.; Wang, L.; Yan, G.; Gao, J. M.; Yu, H.; Zhang, L., *Polym. Int.* **2011**, *60*, 976-994.
289. Peterson, A. W.; Heaton, R. J.; Georgiadis, R., *J. Am. Chem. Soc.* **2000**, *122*, 7837-7838.
290. Bruce, I. J.; Sen, T., *Langmuir* **2005**, *21*, 7029-7035.
291. Sadhu, C.; Dutta, S.; Gopinathan, K. P., *J. Biosci. (Bangalore)* **1984**, *6*, 817-821.
292. Blake, R. D.; Delcourt, S. G., *Nucleic Acids Res.* **1996**, *24*, 2095-2103.
293. Haun, J. B.; Yoon, T. J.; Lee, H.; Weissleder, R., *Wiley Interdis. Rev.: Nanomed. Nanobiotechnol.* **2010**, *2*, 291-304.
294. Sehgal, D.; Vijay, I. K., *Anal. Biochem.* **1994**, *218*, 87-91.
295. Gilles, M. A.; Hudson, A. Q.; Borders Jr, C. L., *Anal. Biochem.* **1990**, *184*, 244-248.
296. Nakajima, N.; Ikada, Y., *Bioconjugate Chem.* **1995**, *6*, 123-130.
297. Pierrat, S.; Hartinger, E.; Faiss, S.; Janshoff, A.; Sönnichsen, C., *J. Phys. Chem. C* **2009**, *113*, 11179-11183.
298. Liu, G.; Lin, Y., *J. Am. Chem. Soc.* **2007**, *129*, 10394-10401.
299. Liu, C. H.; Li, Z. P.; Du, B. A.; Duan, X. R.; Wang, Y. C., *Anal. Chem.* **2006**, *78*, 3738-3744.
300. Niu, Y.; Zhao, Y.; Fan, A., *Anal. Chem.* **2011**, *83*, 7500-7506.
301. Zhang, Y.; Tang, Z.; Wang, J.; Wu, H.; Maham, A.; Lin, Y., *Anal. Chem.* **2010**, *82*, 6440-6446.
302. Hu, P.; Cheng, Z. H.; Yuan, F. L.; Ling, J.; Yu, L. L.; Liang, R. F.; Jian, P. X., *Anal. Chem.* **2008**, *80*, 1819-1823.
303. Dong, X.; Zhao, W.; Xu, J.; Chen, H., *Sci. China Chem.* **2011**, *54*, 1304-1310.
304. Miao, J.; Cao, Z.; Zhou, Y.; Lau, C.; Lu, J., *Anal. Chem.* **2008**, *80*, 1606-1613.
305. Abbaspour, A.; Noori, A., *Biosensors Bioelectron.* **2012**, *37*, 11-18.

306. Stoeva, S. I.; Lee, J. S.; Smith, J. E.; Rosen, S. T.; Mirkin, C. A., *J. Am. Chem. Soc.* **2006**, *128*, 8378-8379.
307. Hurst, S. J.; Lytton-Jean, A. K. R.; Mirkin, C. A., *Anal. Chem.* **2006**, *78*, 8313-8318.
308. Wrobel, N.; Schinkinger, M.; Mirsky, V. M., *Anal. Biochem.* **2002**, *305*, 135-138.
309. Iorio, M. V.; Croce, C. M., **2012**, *4*, 143-159.
310. Mo, Y. Y., **2012**, *69*, 3529-3531.
311. Pritchard, C. C.; Cheng, H. H.; Tewari, M., **2012**, *13*, 358-369.
312. Sobczak, J.-P. J.; Martin, T. G.; Gerling, T.; Dietz, H., **2012**, *338*, 1458-1461.
313. Pal, S.; Deng, Z.; Wang, H.; Zou, S.; Liu, Y.; Yan, H., *J. Am. Chem. Soc.* **2011**, *133*, 17606-17609.
314. Shen, X.; Asenjo-Garcia, A.; Liu, Q.; Jiang, Q.; García de Abajo, F. J.; Liu, N.; Ding, B., *Nano Lett.* **2013**.
315. Zhao, Z.; Liu, Y.; Yan, H., *Org. Biomol. Chem.* **2013**, *11*, 596-598.
316. Gu, H.; Chao, J.; Xiao, S.-J.; Seeman, N. C., **2010**, *465*, 202-205.
317. *Nanorobotics, Current Approaches and Techniques*; Springer New York, **2013**.
318. Kim Thanh, N. T.; Rosenzweig, Z., *Anal. Chem.* **2002**, *74*, 1624-1628.
319. Georganopoulou, D. G.; Chang, L.; Nam, J. M.; Thaxton, C. S.; Mufson, E. J.; Klein, W. L.; Mirkin, C. A., *Proc. Natl. Acad. Sci. USA* **2005**, *102*, 2273-2276.
320. Haes, A. J.; Chang, L.; Klein, W. L.; Van Duyne, R. P., *J. Am. Chem. Soc.* **2005**, *127*, 2264-2271.
321. Wang, J.; Shan, Y.; Zhao, W. W.; Xu, J. J.; Chen, H. Y., *Anal. Chem.* **2011**, *83*, 4004-4011.
322. Otsuka, H.; Akiyama, Y.; Nagasaki, Y.; Kataoka, K., *J. Am. Chem. Soc.* **2001**, *123*, 8226-8230.
323. Yonzon, C. R.; Jeoung, E.; Zou, S.; Schatz, G. C.; Mirksich, M.; Van Duyne, R. P., *J. Am. Chem. Soc.* **2004**, *126*, 12669-12676.

## **APPENDICES**

**Dark field micrographs, TEM micrographs, DFM-FESEM mappings and relevant statistics in Chapter 4 and Chapter 5**



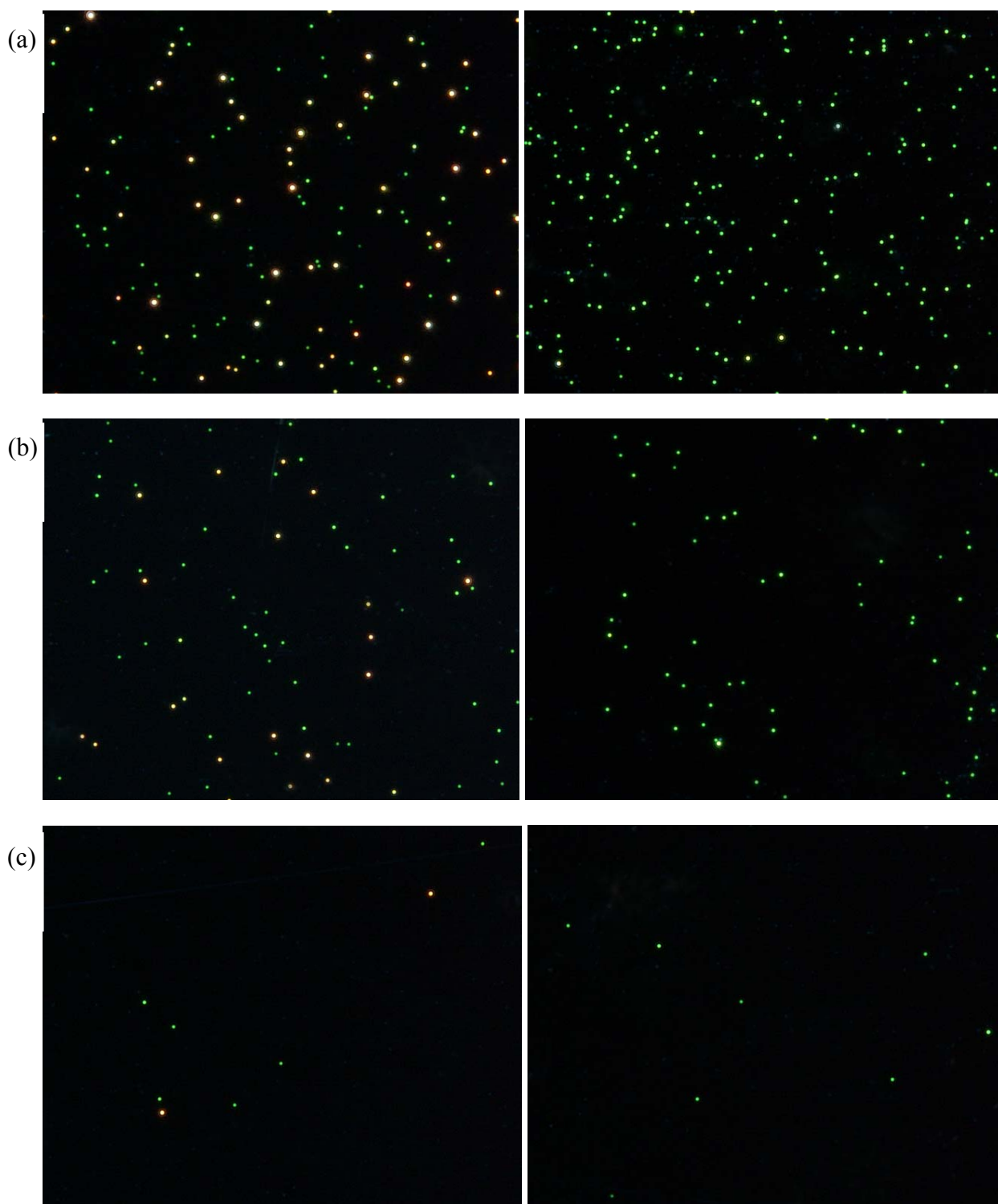


Figure S4.1: Probe Concentration & Hybridized Duplex Length Study (Scheme 4.1). Comparison of the dark field micrographs on hybridization percentage between complementary probes nAu-P/nAu-cP<sub>27</sub> at decreasing concentration (a) 400 fM, (b) 100 fM, and (c) 10 fM, recorded after 1h-hybridization. For each set of concentration, left panel constitutes of probes nAu-P & nAu-cP<sub>27</sub> at constant ratio of 1/1; right panel is control comprises only single type of probe. The scattering color of all controls remains more than 95% green even after 24 h. Images were taken from the bottom plane of liquid chamber, to which particles settled. Buffer: 140 mM Tris, 140 mM NaCl, 2 mM MgCl<sub>2</sub>.

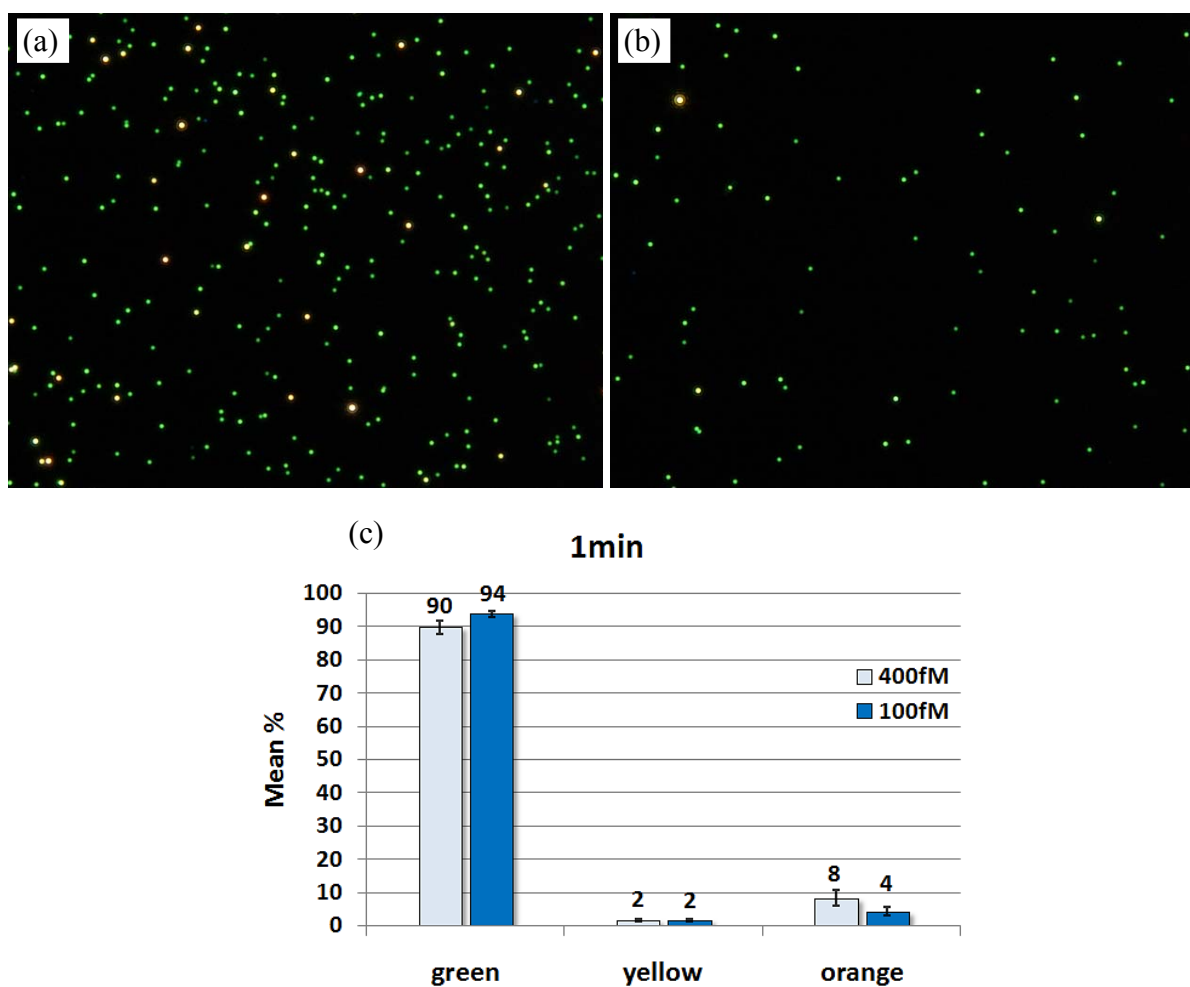


Figure S4.2: Nanoassemblies formed at 1 min for (a) 400 fM (b) 100 fM of complementary probes 50 nm nAu-P / 50 nm nAu-cP<sub>27</sub>, both at constant ratio of 1/1, and (c) the corresponding hybridization percentages for 400 fM (light blue), and 100 fM (blue). Images were taken from the bottom plane of liquid chamber, to which particles settled. Buffer: 140 mM Tris, 140 mM NaCl, 2 mM MgCl<sub>2</sub>.

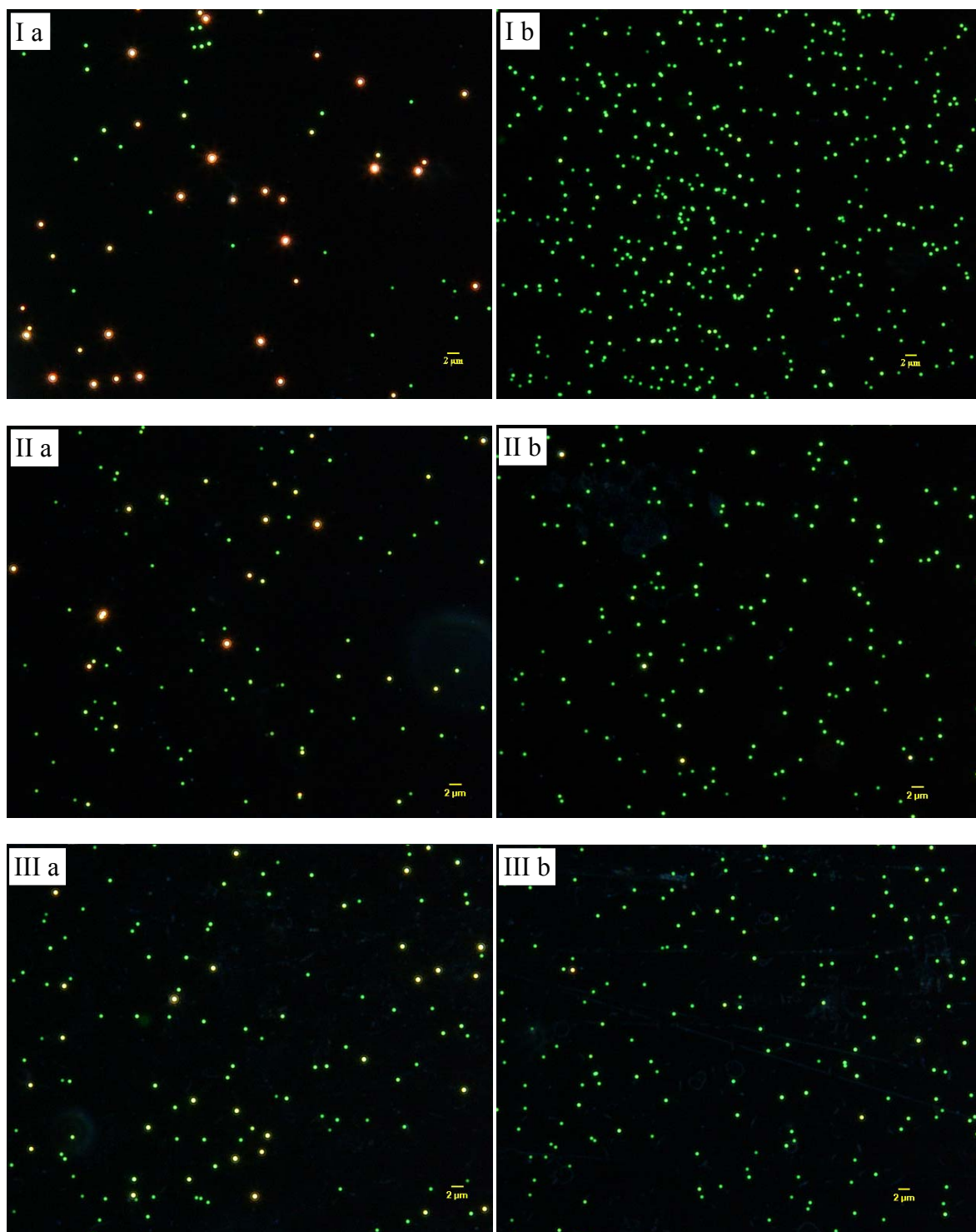


Figure S4.3: Size Effect Study (Scheme 4.1 vs. Scheme 4.2). Comparison of the dark field micrographs on hybridization percentage between complementary probes nAu-P/nAu-cP<sub>27</sub> for I(a) homo-size system with same probe size 50nm/50nm, and hetero-size systems with different probe sizes II(a) 50nm/20nm, III(a) 50nm/10nm, all at constant ratio of 1/1 (800 fM each), recorded after 6 h-hybridization. The corresponding controls are shown for I(b) homo-size system which comprises single type of 50 nm probe at 1.6 pM, and hetero-size systems which comprise 800 fM 50 nm probe & II(b) 800 fM 20 nm probe, III(b) 800 fM 10 nm probe, all carrying the same type of ssDNA sequences. Images were taken from the bottom

plane of liquid chamber, to which particles settled. Buffer: 140 mM Tris, 140 mM NaCl, 2 mM MgCl<sub>2</sub>.

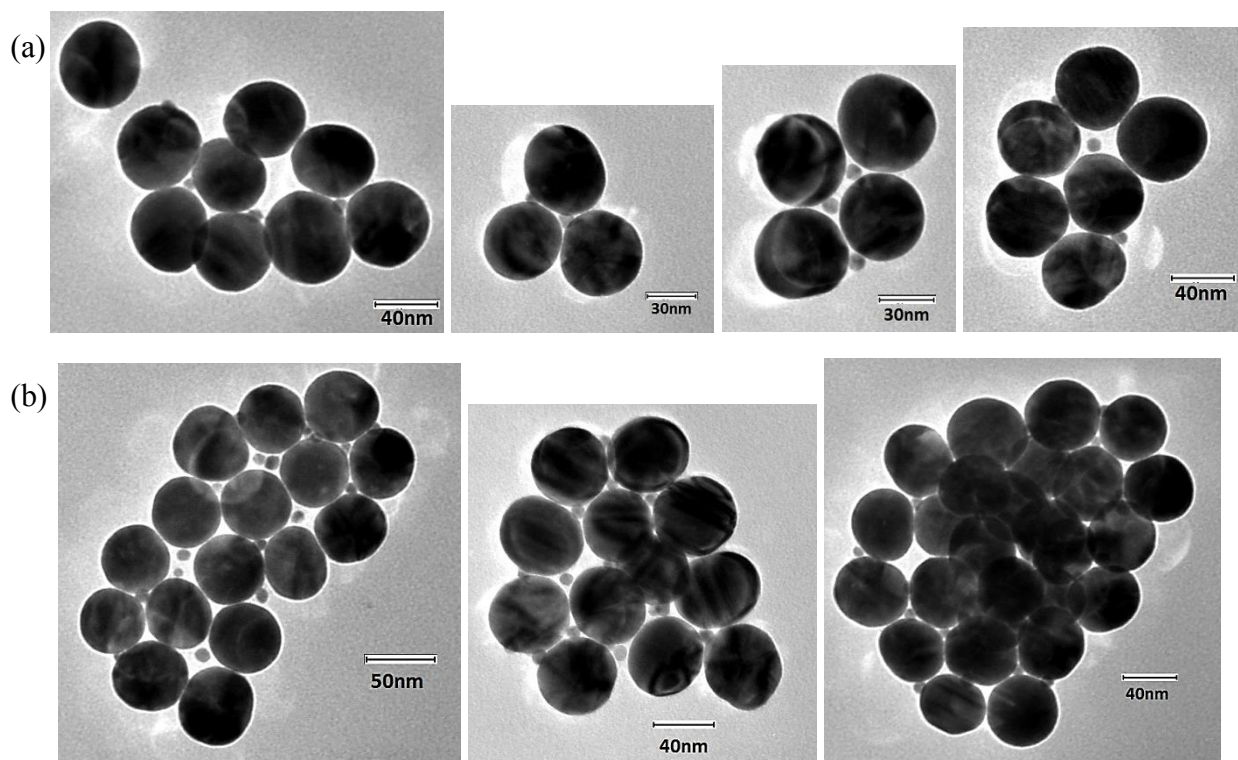


Figure S4.4: Size Effect Study (Scheme 4.1 vs. Scheme 4.2). Comparison of the TEM micrographs on hybridization efficiency between complementary probes nAu-P/nAu-cP<sub>27</sub> for hetero-size system with different probe sizes (50nm/10nm) at molar ratio (a) 1/1 (b) 1/3, recorded after 6 h-hybridization in buffer of 140 mM Tris, 140 mM NaCl, 2 mM MgCl<sub>2</sub>. The concentration of 50 nm nAu-P is 800 fM.

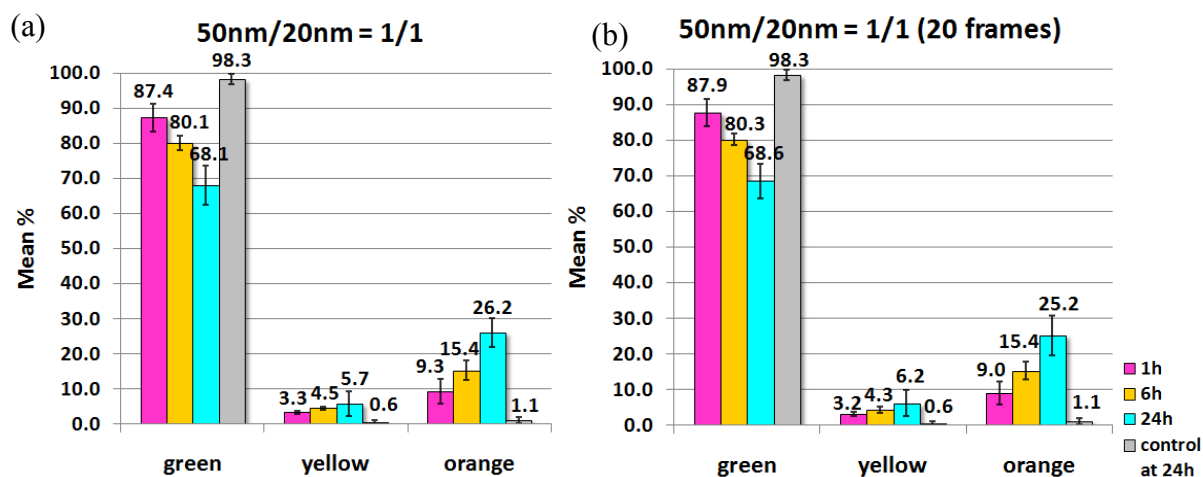
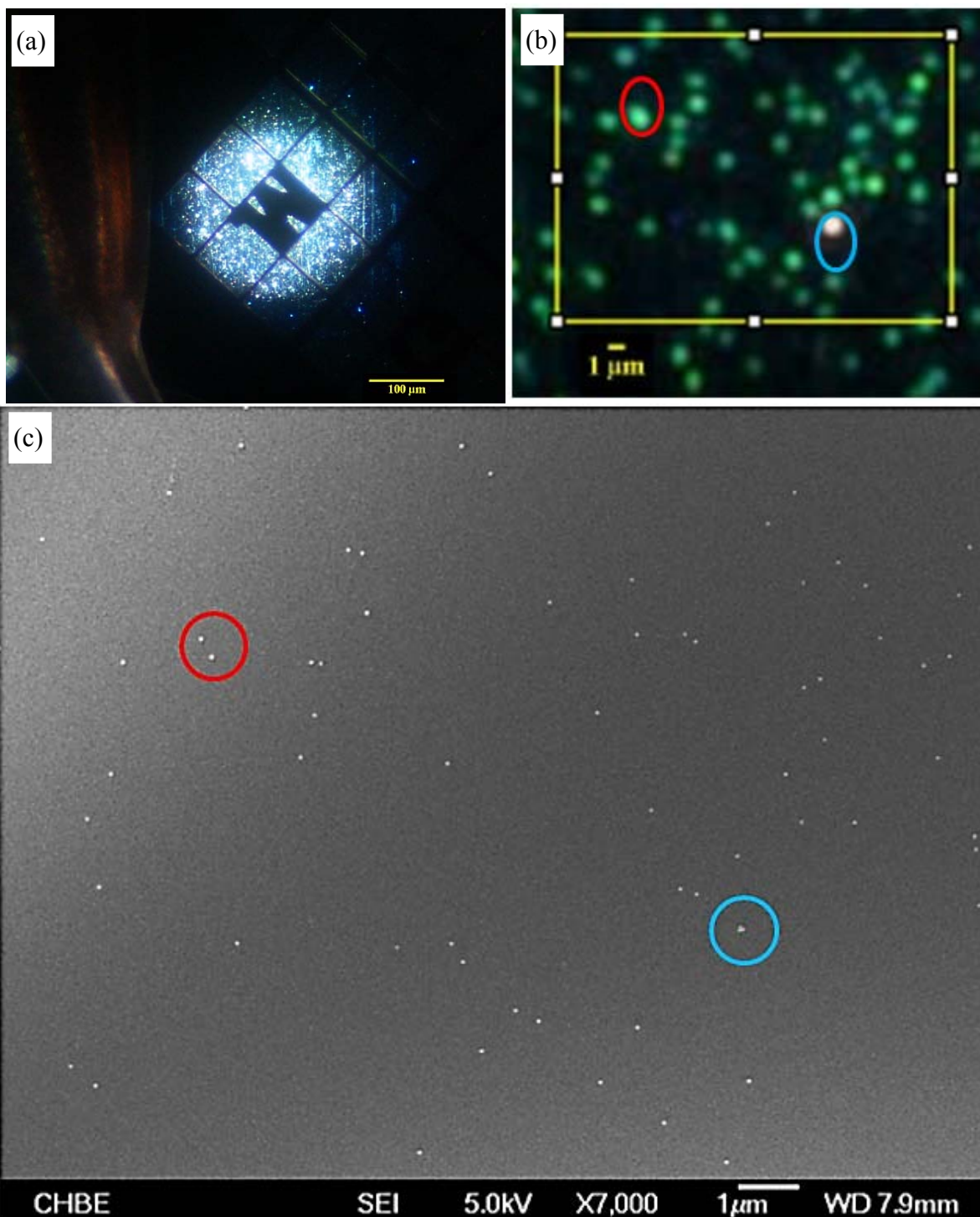


Figure S4.5: Comparison of the statistical distributions based on (a) 10, and (b) 30 dark field images. The data show the hybridization percentages between nAu-P/nAu-cP<sub>27</sub> for hetero-size system with different probe sizes (50nm/20nm) in Size Effect Study. Ratio of complementary probes: 1/1; concentrations of all species: 800 fM. Each bar reported consists of four repeats, two with 50 nm nAu-P / 20 nm nAu-cP<sub>27</sub>, & the other two with 20 nm nAu-P / 50 nm nAu-cP<sub>27</sub>. Images are quantified by counting the hybridized-clusters ('yellow' & 'orange') vs. the individual probes ('green'). Buffer: 140 mM Tris, 140 mM NaCl, 2 mM MgCl<sub>2</sub>.





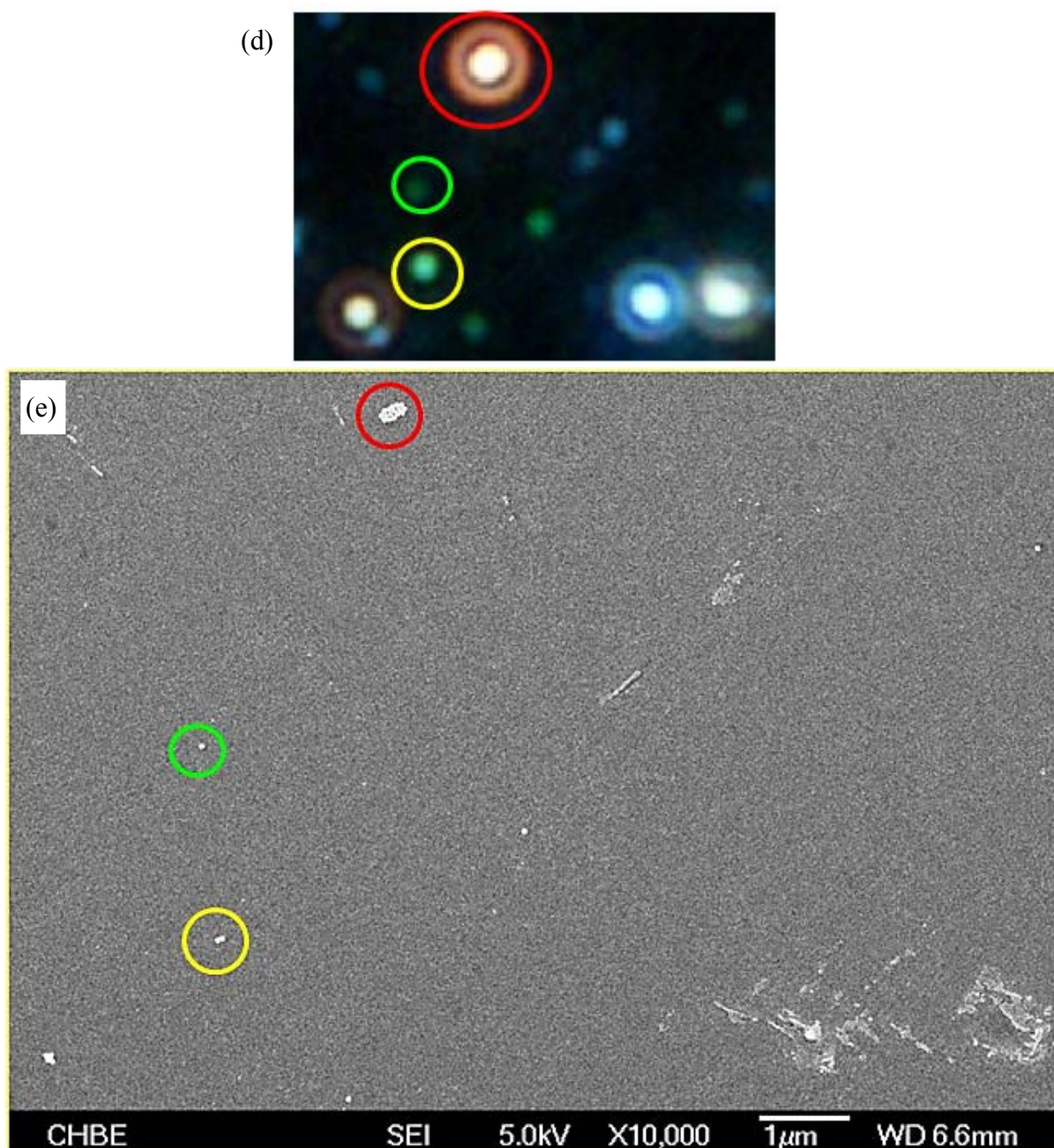


Figure S4.6: (a) A typical Alphabet Finder copper grid under DFM. Mapping of (b, d) scattered plasmon resonance under DFM with (c, e) the corresponding inherent structure of the nanoparticles or nanoassemblies in FESEM. (b & c) Red circles showed that 2 nAu with separation distance  $< 1 \mu\text{m}$  were electronically but not optically resolved; whereas blue circles showed that 3 closely-spaced 50 nm nAu gave a strong LSPR coupling with orange colour scattering. (d & e) Green, yellow and red circles highlighting the single nAu, dimeric nAu, and nanoassemblies that exhibited 'green', 'yellow' and 'orange' scattering colours, respectively. Ratio of complementary 50 nm nAu-P/nAu-cP<sub>27</sub> probes: 1/1 under dried condition.



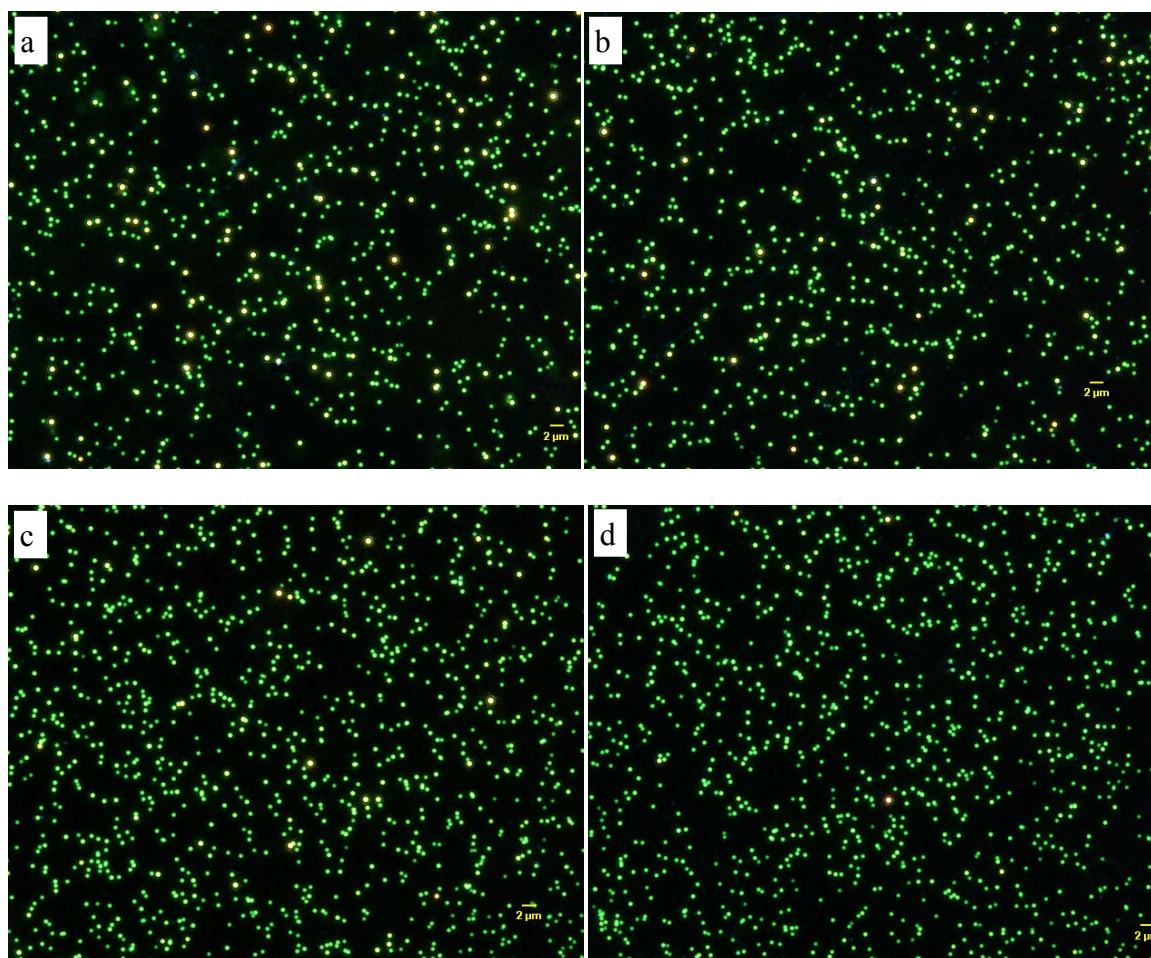


Fig S5.1. Dark field micrographs of Scheme 1, recorded after 24 h hybridization. The nanoassemblies were formed by hybridizing nAu-T and nAu-H to 28 b targets of (a) perfect-match P, (b) H-single-mismatch MH, and (c) T-single-mismatch MT at 4 pM target concentration; (d) The control is absence of any target DNA. Each sample contains 1 pM of nAu-T and 1 pM of nAu-H. Images were taken from the bottom plane of the liquid chamber where the particles had settled. Buffer: 140 mM Tris, 140 mM NaCl, 2 mM  $\text{MgCl}_2$



## Publications

### Publications in peer-reviewed journals

1. Fong, K. E. and Yung, L.-Y. L. Analysis of metallic nanoparticle-DNA assembly formation in bulk solution via localized surface plasmon resonance shift. *RSC Advances* **2**, 5154-5163 (2012)
2. Fong, K.E. and Yung, L.-Y. L. Head-to-Tail: Hybridization and Single-Mismatch Discrimination in Metallic Nanoparticle-DNA Assembly. *RSC Advances* **3**, 6076-6084 (2013)
3. Fong, K. E. and Yung, L.-Y. L. Localized Surface Plasmon Resonance: A Unique Property of Plasmonic Nanoparticles for Nucleic Acid Detection. *Nanoscale* (accepted, 2013)
4. Chen, X., Chen, C-B., Udalgama, C. N. B., Ren, M., Fong, K. E., Yung, L.-Y. L., Giorgia, P., Bettiol, A. A. & Watt, F. High resolution 3D imaging and quantification of gold nanoparticles in a whole cell. *Biophys. J.* (104:7), 1419 (2013)

### Publications in scientific conference

1. Fong, K. E. & Yung, L. Y. L. in *International Conference on Materials for Advanced Technologies (ICMAT 2011)*. 'Localized Surface Plasmon Resonance Shift of Small Clusters of Metallic Nanoparticles via DNA Hybridization', 26 June - 1 July, Singapore